Observation of
the strongly-coupled Higgs sector
in the CMS detector at the LHC

Paweł Zych

Institute of Experimental Physics

Warsaw University

A thesis submitted in partial fulfilment
for the degree of

Doctor of Philosophy in Physics

Written under the supervision of

Prof. Krzysztof Doroba

Warsaw, July 2007

Abstract

This thesis is devoted to studying prospects for observation of hypothetical strong interaction between intermediate vector bosons at 1-TeV scale. This scenario is able to naturally solve hierarchy problem and also to replace light standard Higgs boson in breaking electroweak symmetry. Simulation studies has been done for the CMS detector that will start data taking at the LHC at CERN laboratory in 2008. The indications of the strongly-coupled sector are searched for in vector boson fusion process with $WW \rightarrow \mu\nu q\bar{q}$ final state. Realistic estimation of background by consideration of multi-jet processes, the most recent model for showering of generated particles, full detector simulation and event reconstruction are included in the study. Selection procedure optimized for high luminosity conditions has been constructed using simulated data. It was estimated that discovery of the strongly-coupled sector scenario would require at least about 700 fb^{-1} of integrated luminosity. Unless there were indications of the signal of interest, the exclusion of this scenario would be possible with at least about 300 fb^{-1} of collected data. These limits are biased by large uncertainty; nevertheless, are still significantly much more pessimistic than the previous estimates.

Contents

List of Figures

List of Tables

Chapter 1

Introduction

The Large Hadron Collider (LHC) is currently being built at the European Organization for Nuclear Research (CERN) in Geneva, Switzerland. In 2007, two general-purpose detectors located at this collider, the A Toroidal LHC ApparatuS (ATLAS) and the Compact Muon Solenoid (CMS), will start their operation detecting interactions of protons. One of the main goals of these experiments is to find the Higgs boson, the most wanted piece in particle physics.

The 20th century was very successful for particle physics. This branch of physics was born, when electron, the first elementary particle, was discovered by J.J. Thomson in 1890s [1]. Afterward, other particles were observed, what triggered development of their mathematical description. Eventually, the Glashow-Salam-Weinberg (GSW) model [2, 3, 4, 5], currently known as the Standard Model (SM), was established in the beginning of 1970s. It classified the known elementary particles and was able to describe unified electroweak interactions between them. Now, we see it cannot be a complete theory of fundamental physics; however, predictive power is its credit. The GSW model and its developments anticipated the existence of W and Z bosons, gluons, top and charm quarks. Unfortunately, the SM lacks experimentally supported mechanism of electroweak symmetry breaking (EWSB) that is believed to be also responsible for giving mass to quarks and leptons, and to W and Z bosons, whereas leaving massless the photon. This is fundamental question of particle physics. Without this mechanism, the scattering amplitudes of longitudinally polarized vector bosons would violate unitarity for invariant masses around 1 TeV. This indicates that the answer to the question about the source of the masses is near. The most serious candidate is the mechanism of spontaneous breaking. The most popular procedure of this kind is known as the Higgs-Kibble mechanism [6, 7, 8, 9] (also known as Higgs mechanism). Unfortunately, it has not been confirmed because the Higgs boson, the only physical element of symmetry-breaking sector, has not been discovered yet. Present precision electroweak (EW) data favors theories based on the light Higgs boson and connected with it weakly-coupled

symmetry breaking sector. However, one cannot definitively rule out other scenarios. It is possible to construct models of new physics with good quality of the global fit to precision electroweak data and relaxed the strong upper limit on the Higgs mass. Therefore, there is still a room for heavy Higgs boson case and phenomenologically very similar to it so-called strongly-coupled symmetry-breaking sector [10]. Although, this sector does not contain fundamental Higgs particle, it can be still called Higgs sector [11, 12] because it plays the same role.

The subject of this thesis is the ability of the CMS detector, and the LHC in general, to experimental confirmation of hypothetical models with strongly-interacting Higgs sector. It is used one of the most characteristic signals of this type of models, *i.e.* the enhanced production of longitudinally polarized vector boson pairs ($V_L V_L$) and resonant behavior in vector-boson fusion processes [13, 14, 15]. Model-independent approach provided by the Electroweak Chiral Lagrangian (EWChL) and final states with two W bosons decaying into $l\nu q\bar{q}$ were chosen for this study.

The main results of this thesis are the following. For the first time, the background is properly estimated by the use of multi-jet event samples and the most recent model for showering of generated particles. This method is supported by the advanced generation-level studies. In the data processing chain, the author has included trigger and optimized event selection. A number of new requirements in the event selection path were proposed. Additionally, the results were obtained with the use of precise detector simulation, realistic detector conditions and original event reconstruction. The results of this thesis show that it will be difficult to observe strongly-coupled symmetry-breaking sector with heavy resonances. The integrated luminosity of about 700 fb⁻¹ collected by the CMS experiment, *i.e.* around 7 years of running with high luminosity, is required for the discovery and about 300 fb⁻¹ will be enough for experimental exclusion of this model. These limits are, however, biased by large uncertainty.

This thesis is organized as follows. In Chapter 2, the Standard Model with standard Higgs mechanism is reviewed. Chapter 3 introduces strongly-coupled symmetry-breaking sector and EWChL approach to it. The way, in which physics processes are generated, is described in Chapter 4. The CMS experiment, its expected performance and reconstruction method of collected and simulated events is presented in Chapter 5. Chapter 6 is devoted into the method of data analysis. The results are discussed in Chapter 7 and conclusions are given in Chapter 8. In order not to overload the main stream of the text with additional or detailed information, some of the subjects, pictures and tables are presented in dedicated appendixes that are given in the end of this thesis. At the end, one can also find Glossary, used notation, acronyms and the list of references.

Chapter 2

The Standard Model

This chapter introduces the reader to the subject of electroweak symmetry breaking. First, the theory of particle physics, the Standard Model, is presented. Next, it is discussed the subject of spontaneous symmetry breaking that is suspected to be a procedure giving particles their masses. The most popular procedure of this kind is Higgs mechanism with elementary Higgs boson. The Higgs mechanism is reviewed in more details including its shortcomings, effective formulation and current experimental status.

2.1 Structure

The Standard Model describes the known subatomic world with the use of

$$SU(3)_{color} \times SU(2)_L \times U(1)_Y \tag{2.1}$$

gauge group symmetries.

The component of the theory invariant under $SU(3)_{color}$ is called Quantum Chromodynamics (QCD) [16]. It introduces the quantum number, color, appearing in three species. Interactions between colored quarks are mediated by the exchange of eight colored gauge bosons, gluons. Because gluons are massless, the $SU(3)_{color}$ symmetry is unbroken. The strength of color interaction is strong for energy transferred of the order of 1 GeV; however, at high energies it exhibits *asymptotic freedom* [17, 18]. The coupling constant is thus small in the latter case, enabling the use of perturbation theory.

The $SU(2)_L \times U(1)_Y$ part of the SM symmetry describes the unified electroweak (EW) interactions [2, 3, 4]. $SU(2)_L$ is the group of the left-handed weak isospin I, and $U(1)_Y$ is connected with the weak hypercharge Y. Additional requirement of local $SU(2)_L \times U(1)_Y$ symmetry invariance for the theory triggers off the appearance of gauge bosons through according definition of covariant derivatives $\mathcal{D}_\mu$. These bosons

are: the $\vec{W}_\mu = (W_\mu^1, W_\mu^2, W_\mu^3)$ triplet connected with $SU(2)_L$ gauge group and B_μ field connected with $U(1)_Y$ group. Neutral B_μ and W_μ^3 boson fields mix with the use of weak mixing angle θ_W to form fields for physical Z^0 boson and photon. This phenomenon and the relation between the couplings: $\frac{1}{e^2} = \frac{1}{g^2} + \frac{1}{g'^2}$ are indications of electroweak unification. W^1 and W^2 fields also mix to observable W^+ and W^- bosons. Weakness of EW couplings allows for perturbative approach in calculations. The electroweak part of the Standard Model is of special interest for this thesis; therefore, whenever gauge sector, symmetries and other related issues are not explicitly specified, they will refer to electroweak sector.

The Standard Model successfully describes most of the observed phenomena and experimental data collected at LEP, SLC and Tevatron colliders [19, 20, 21]. Predicted values are consistent with the measurements in some cases with an accuracy of one part in a thousand or better, *e.g.* *Z*-pole observables. The new particles have been discovered, where they had been predicted to give the proper radiative corrections, *e.g.* direct and indirect top quark mass measurements. It all makes the Model self-consistent. The data really confirms that $SU(3)_{color} \times SU(2)_L \times U(1)_Y$ is a gauge symmetry of Nature.

2.2 Spontaneous symmetry breaking

The only item still not confirmed and understood is the mechanism of electroweak symmetry breaking. Nevertheless, the SM still fits to the data with this undetermined sector and is even able to provide indirect limits on it. Mechanism of EWSB is believed to be the procedure allowing description of massive particles since simple introduction of mass terms into the Lagrangian would directly break the electroweak $SU(2)_L \times U(1)_Y$ gauge symmetry. In reality, all particles, but the photon, are massive, so the symmetry must be broken. Explicit mass terms would, however, also result in non-renormalizable theory, what means that infinities appearing in calculations could not be controlled with a finite number of subtractions or redefinitions. The preferred mechanism of electroweak symmetry breaking is thus spontaneous symmetry breaking that guarantees renormalizability of the resulting model [22, 23, 24, 25].

Spontaneous symmetry breaking requires addition of a potential to the SM Lagrangian, which ground state (vacuum) is infinitely degenerate and does not respect the global symmetry. According to the Goldstone theorem [26, 27], the consequence is presence of massless particle in the spectrum of the theory, the so-called Goldstone boson. The number of Goldstone bosons is equal to the number of broken-symmetry generators[1] [28]. Goldstone bosons for spontaneously broken electroweak symmetry

---

[1]this statement is limited to Lorentz-invariant theories

are often called unphysical particles since because of their zero mass they should have already been discovered. Therefore, they can not be distinct particles. It is interpreted that the massless Goldstone bosons combine with the massless gauge bosons[1], what results in massive gauge bosons[2].

Massive vector bosons, by definition, have three degrees of freedom that are called polarizations or helicities. Disappearing massless Goldstone boson could be, therefore, identified with appearing longitudinal polarization state of becoming massive vector boson. For massive vector boson W moving in z direction (with $p^\mu = (E, \vec{p})$, $\vec{p} = (0, 0, p)$), the polarization four-vectors can be chosen as:

$$\varepsilon_\pm^\mu \quad = \quad \frac{1}{\sqrt{2}}(0, 1, \pm i, 0) \ , \tag{2.2}$$

$$\varepsilon_L^\mu \quad = \quad \frac{1}{M}(p, 0, 0, E) \ , \tag{2.3}$$

where ε_+^μ and ε_-^μ are positive (right-handed) and negative (left-handed) helicities that both are also denoted as ε_T^μ and called transverse polarizations (helicities). Longitudinal polarization ε_L^μ is called zero helicity as well. The names of both polarizations refer to the directions of their three-vectors with respect to the four-momentum: $\vec{\varepsilon_T}\vec{p} = 0$, $\vec{\varepsilon_L}\vec{p} \neq 0$. For boosted bosons, the longitudinal polarization four-vector becomes parallel to four-momentum p^μ [3]:

$$\varepsilon_L^\mu = \frac{p^\mu}{M_W} \quad \text{for } E \gg M_W \ . \tag{2.4}$$

This feature leads to different interactions of transverse and longitudinal components (decoupling) in high energy regime. Additionally, it could also cause high energy divergences in calculations of processes involving longitudinally polarized gauge bosons. However, because of gauge cancellations between subprocesses, the resulting cross-section may still behave properly for all energies, *i.e.* does not grow as a positive power of E.

The other consequence of Eq. (2.4) is the Goldstone boson equivalence theorem [13, 14, 15, 29, 30], abbreviated as Equivalence Theorem (ET), which says that on-mass-shell amplitudes with longitudinally polarized vector bosons $\mathcal{M}(V_L(p_1), V_L(p_2), ...)$ can be approximated by amplitudes for the same processes with corresponding massless Goldstone bosons $w(p_i)$:

$$\mathcal{M}(V_L(p_1), V_L(p_2), ...) = \mathcal{M}(w(p_1), w(p_2), ...) + \mathcal{O}(\frac{M_W}{E_i}) \ . \tag{2.5}$$

---

[1] commonly it is said that the massless Goldstone bosons are *eaten* by gauge bosons

[2] It can happen only if the broken symmetries in the global symmetry correspond to a gauge symmetry

[3] $\varepsilon_L^\mu = \frac{p^\mu}{M_W} + \frac{M_W}{E+p}(-1, 0, 0, 1)$

This relation implies, what was only suggested before, that the Goldstone scalars behave as corresponding longitudinal components of massive vector bosonsin high-energy limit. As a result, scattering amplitudes of Goldstone bosons can be used in place of those for longitudinally polarized gauge bosons. These longitudinal components are not only the consequence of symmetry breaking mechanism, but processes with them can be also used as a probe of symmetry breaking model.

Two particular examples of spontaneous symmetry breaking models are Higgs mechanism [6, 7, 8, 9] and dynamical symmetry breaking [31, 31, 32]. The first class predicts the appearance of new particles - Higgs bosons. Although not confirmed, the simplest Higgs model with one such boson is the most popular, and frequently regarded as the intrinsic part of the SM. It will be discussed in more details as an example of model with spontaneous symmetry breaking because some aspects are common to all models.

2.3 Higgs mechanism

In the minimal Higgs model, the symmetry breaking sector consists of four scalars (h and $\vec{w} = (w_1, w_2, w_3)$) that most often are represented as a complex doublet under the $SU(2)_L$ group:

$$\Phi = \frac{1}{\sqrt{2}} \left(\begin{array}{c} w_1 + i w_2 \\ h + i w_3 \end{array} \right) . \tag{2.6}$$

The w_1 and w_2 are mixed to obtain $w^{\pm} = \frac{1}{\sqrt{2}}(w_1 \pm i w_2)$ with definit electric charge. Fields h and w_3 are electrically neutral. The symmetry-breaking Lagrangian for field Φ is given by:

$$\mathcal{L}_{SB} = (\mathcal{D}_\mu \Phi)^{\dagger} (\mathcal{D}^\mu \Phi) - V(\Phi^{\dagger} \Phi) . \tag{2.7}$$

The *ad hoc* potential:

$$V(\Phi^{\dagger}\Phi) = \frac{1}{2}\lambda \left(\Phi^{\dagger}\Phi + \frac{\mu^2}{\lambda} \right)^2 \tag{2.8}$$

for $\mu^2 < 0$ introduces the spontaneous symmetry breaking since it acquires $U(1)$ symmetric degenerated minimum for $\Phi^{\dagger}\Phi = -\frac{\mu^2}{\lambda} = \frac{v^2}{2}$, with

$$v = (\sqrt{2}\,G_F)^{-1/2} \approx 246 \text{ GeV} \tag{2.9}$$

called the vacuum expectation value (*vev*). After substitution of h field for $H + v$, the minimum occurs for all scalar fields vanishing. They may be regarded as degrees of freedom in expansion around the vacuum. Resulting potential looks like:

$$V = \frac{\lambda}{8} \left(\vec{w}^2 + H^2 + 2Hv \right)^2 . \tag{2.10}$$

The $\vec{w}$ fields are massless (expected three Goldstone bosons). The H field, called the Higgs field, has a mass:

$$M_H = \sqrt{\lambda v^2} = \sqrt{-2\mu^2} \qquad (2.11)$$

that is related to unknown scalar quartic self-coupling λ. This makes M_H theoretically undetermined.

The Higgs boson is the only particle in the SM that has got a mass term. The masses of all other particles are generated through spontaneous symmetry breaking and interactions with the Higgs boson. Mass terms for gauge bosons appear due to the couplings of the scalar Higgs doublet to gauge bosons, which are present in Eq. (2.7) in the term with covariant derivatives $\mathcal{D}_\mu$. The result is massless photon and massive Z^0 and $W^\pm$ bosons. Mass terms for charged fermions result from gauge invariant couplings between these fermions and symmetry breaking scalars (Yukawa couplings). The Higgs model is unfortunately not able, except for M_W/M_Z ratio, to predict values of the masses.

The potential in Eq. (2.8) provides spontaneous breaking of $SU(2)_L \times U(1)_Y$ symmetry to $U(1)_{EM}$. The Higgs potential is also invariant under larger global $SU(2)_L \times SU(2)_R$ symmetry. This is because it admits four-dimensional rotations of four scalar fields $(\vec{w}, h)$, i.e. it is invariant under $SO(4)$ symmetry that is isomorphic to $SU(2)_L \times SU(2)_R$ [33]. After spontaneous symmetry breakdown, the symmetry of the potential in Eq. (2.10) is $SO(3)$ that is isomorphic to $SU(2)_C$ [33], the diagonal part of $SU(2)_L \times SU(2)_R$. The unbroken global $SU(2)_C$ symmetry is called the "custodial symmetry" [31, 32, 34].

The $SU(2) \times SU(2)$ symmetry[1], and as a result custodial symmetry as well, makes that the mass relation between the W and Z gauge fields, i.e. :

$$\rho \equiv \frac{M_W^2}{M_Z^2 \cos^2 \theta_W} \qquad (2.12)$$

reads [32]:

$$\rho = 1 . \qquad (2.13)$$

This relation is automatically obtained for Higgs mechanism with scalar field doublet, and is experimentally satisfied to very high accuracy [21]:

$$\rho(\exp) = 1.0002^{+0.0007}_{-0.0004}. \qquad (2.14)$$

It can be used to restrict alternative mechanisms of spontaneous symmetry breaking and the new physics beyond the SM. Another motivation for $SU(2) \times SU(2)$ symmetry

---

[1] $SU(2) \times U(1)$ is not enough

is that the $SU(2)_C$ symmetry plays a role of isospin symmetry, under which Goldstone boson fields $\vec{w}$ make a triplet.

The Higgs boson is not only an artifact of the Higgs potential, but is also an important ingredient of the whole SM. It plays a key role in regularization of high-energy behavior of amplitudes for scatterings of longitudinal vector bosons. Higgs boson contribution cancels the bad high energy behavior coming from four-point contact interaction $V_L V_L V_L V_L$ [14, 35, 36]. Resulting partial-wave amplitude a_0 [1] for $V_L V_L \to V_L V_L$ scattering process is in high-energy limit ($s \gg M_H^2$) dependent only on Higgs boson mass. Unitarity[2] requirement (e.g. Eq. (A.3) in App. A) can thus play a role of theoretical limitation on this mass [37]:

$$M_H \leq \sqrt{\frac{8\pi\sqrt{2}}{5 G_F}} = 4\sqrt{\pi/5}\; v \approx 780 \text{ GeV} .$$ (2.15)

This is the perturbative[3] unitarity bound on the Higgs boson mass [14, 36].

Unless elementary Higgs boson exists, unitarity in partial waves for $W_L^+ W_L^- \to Z_L Z_L$ scattering will be violated for energies above the scale [38]:

$$\Lambda_{\text{unit}} = \sqrt{\frac{4\pi\sqrt{2}}{G_F}} = \sqrt{8\pi}\; v \approx 1.2 \text{ TeV} .$$ (2.16)

The SM without the Higgs boson can not thus be a fundamental theory, but only an effective theory below the above scale. Indications of new physics have to appear at Λ_{unit} scale at the latest.

The SM couplings of longitudinally and transversely polarized bosons (V_L and V_T) to the Higgs boson and fermions are given in Table 2.1. The couplings of V_T's are given by the structure of the Standard Model gauge sector and are completely independent on EWSB mechanism. For low energies, both helicity components (longitudinal and transverse) couple with the same force. In $E \gg M_V$ limit, equivalence theorem can be applied; therefore, the couplings of V_L's are

	V_T	V_L (for $E \gg M_V$)
H	$\sim M_V$	$\sim \lambda\ (\sim M_H^2)$
fermions	$\sim g$	$\sim m_f$

Table 2.1: The SM couplings of longitudinal and transverse components of vector bosons (V_L and V_T) to the Higgs boson and fermions. Couplings for V_L's are given in $E \gg M_V$ limit. Couplings of V_L's for low energies are the same as the couplings for V_T's.

provided by symmetry-breaking sector (Higgs sector or its alternatives). The couplings of V_L's and V_T's differ much in this limit.

---

[1] a_J is the amplitude for J-th partial wave
[2] The subject of scattering amplitude unitarity is reviewed in App. A.
[3] obtained for tree level amplitude

The Higgs boson mass M_H can be treated as a parameter that controls the strength of weak interactions between gauge bosons in high energies [14]. In electroweak scale energies (*e.g.* LEP collider energies), the amplitudes for these processes are of the same order regardless the polarizations of participating bosons. On the other hand at TeV energies and for heavier Higgs boson, the process with only longitudinally polarized vector bosons dominate over the processes with mixed polarizations [39]. This is caused by the form of the polarization vectors in Eqs. (2.2)–(2.3). Additionally, the partial-wave tree level unitarity in $V_L V_L \to V_L V_L$ scattering processes, apart from the region around resonance pole, is never violated for M_H lower than the critical value in Eq. (2.15)[1]. If M_H exceeds the critical value, the unitarity will not be respected for $s > M_H^2$. Therefore, in the former case the weak interactions are effectively always weak, and in the latter one become strong in the TeV energy regime. The same results can be obtained with equivalence theorem and analogous processes with Goldstone bosons within the theory given by Eq. (2.10).

Considering one loop corrections to quartic coupling λ, one gets a relation $\lambda = \lambda(\mu)$ [38] (μ is cut-off energy scale) that blows up for a certain value of the scale μ (Landau pole). This behavior can be avoided by imposing constant $\lambda = 0$ coupling. This way not interacting, *i.e.* trivial, theory with $M_H = 0$ is obtained. Such possibility is, however, unacceptable. The alternative for this is limitation of the running coupling $\lambda(\mu)$ and the Higgs mechanism only to $\mu < \Lambda$, where Λ is the scale where the model breaks down and new physics appears. Maximum value of Λ may be identified with the energy, for which perturbative unitarity with Higgs boson is saturated. As a result, one gets for $\Lambda \geq M_H$ the bound as in Eq. (2.15). For $\Lambda \gg M_H$, the upper bound is much lower [38]. This is, originally considered in Ref. **??**, so-called triviality bound on the Higgs boson mass.

There is also a lower bound on M_H (vacuum stability bound [40, 41, 42]) that follows from the requirement that $\lambda(\mu)$ stays positive[2] for all $\mu < \Lambda$.

Both requirements limit the allowed range for the Higgs boson mass as it is presented in Figure 2.1.

2.4 Shortcomings and alternatives for Higgs mechanism

Despite the great success of electroweak theory, the use of Higgs mechanism for symmetry breaking is still only a proposal, in addition not ideal. The three main problematic

---

[1] it is true also for calculations without the use of equivalence theorem

[2] for negative coupling self interaction of Higgs fields is attractive and new minimum of the potential appears

Figure 2.1: Bounds on the Higgs boson mass as function of cut-off scale Λ (scale at which the Standard Model breaks down). Triviality bounds the M_H from above and vacuum stability from below. m_t is top quark mass. Picture from Ref. [43].
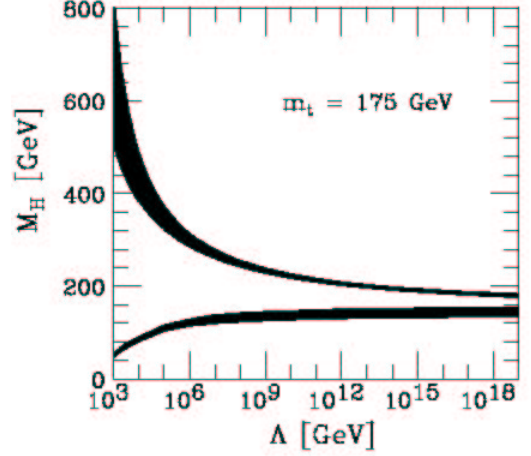
points are:

1. arbitrariness,

2. naturalness,

3. limitation to low energies.

The Higgs mechanism seems to correctly describe symmetry breaking, but should be regarded as theoretically not yet understood since its origin is not known. Postulating the existence of scalar multiplets with appropriate quantum numbers and couplings is completely arbitrary. They are introduced just for the sake of electroweak symmetry breaking. The potential in Eq. (2.8) is simply assumed and additionally requires tachyonic mass for scalars. The other drawback is lack of explanation, why the lightest Higgs boson could be so light as preferred by experiments (*cf.* Sec. 2.6).

Higgs mechanism does not tend to solve hierarchy problem of the SM [44], *i.e.* there is no connection between fundamental scale in physics, the Planck scale $M_{Pl} = 10^{18}$ GeV, and the electroweak scale (*vev* of the Higgs field or masses of gauge bosons). On the contrary, it introduces the other problem, naturalness [45, 46, 47], that is common to all theories with fundamental scalars. Namely, quantum 1-loop corrections to squared bare Higgs boson mass are quadratically[1] dependent on Λ - the cut-off scale regarded as validity scale of the SM:

$$\Delta M_H^2 = \sum_i A_i m_i^2 \frac{\Lambda^2}{v^2} \ , \tag{2.17}$$

where i runs over fermions and bosons, and A_i is multiplicative factor. If one wants the SM to be valid to high scale, the mass shift is substantial; however, it can be canceled in renormalization procedure to keep M_H at the EW scale. Desired counterterms

---

[1]in unbroken theories, like QCD or Quantum Electrodynamics (QED), divergences are at most logarithmic [48] what is acceptable

should be, however, unnaturally very precise in 1 part to Λ/M_H. If $\Lambda = M_{Pl}$ was assumed, extremely (unnaturally) exact fine-tuning would be required.

The third problem is connected with triviality bound [45, 46], and means that the Higgs mechanism cannot be used as EWSB mechanism at appropriately high energies. The Higgs model can thus be only regarded as an effective low-energy theory[1].

The troubles with the Higgs mechanism hint at more general or even alternative mechanisms of spontaneous symmetry breaking. Candidates should play the same role, but also be better motivated. Complying with certain general properties required by the SM characteristics is also needed. These requirements are:

1. respecting of at least $SU(2) \times U(1)$ global symmetry;

2. spontaneous breakdown of this global symmetry with appearance of at least three massless Goldstone bosons;

3. symmetry properties of the vacuum state: at least $U(1)$, preferred $SU(2)$ symmetry to obey and explain standard $SU(2)_C$ symmetry being satisfied to high precision by Eq. (2.14);

4. providing interactions connecting the symmetry breaking sector with the SM gauge sector to cause spontaneous breaking of $SU(2)_L \times U(1)_Y$ gauge symmetry down to $U(1)$;

5. the energy of vacuum state (*vev*) should equal $v \equiv 246$ GeV
   (determined by the known values of gauge boson masses and the electroweak coupling constants);

6. mass scale of symmetry breaking sector is bounded from above by the cut-off [38]:

$$\Lambda_{SB} \approx 1.2 \text{ TeV} \tag{2.18}$$

   originating from unitarity bound in Eq. (2.16). The symmetry breaking must intervene before this scale to restore unitarity in scattering amplitudes. The best known method of such intervention are resonances in the scattering. The examples are hypothetical Higgs boson and pion resonances. The lightest symmetry breaking sector resonance with mass M_{SB} should appear at latest around the scale of the cut-off: $M_{SB} \approx \Lambda_{SB}$ [2].

---

[1] the subject of effective field theories will be further discussed in Section 2.5

[2] in specific example of the Higgs model, the resonance (as Higgs boson) appears earlier with mass obeying Eq. (2.15)

7. the symmetry breaking sector that appears before the scale Λ_{SB} should regularize divergent high-energy behavior of $V_L V_L \rightarrow V_L V_L$ scattering amplitudes (amplitudes should obey unitarity condition).

The Higgs mechanism with minimal Higgs sector is likely the simplest mechanism that can confront with these requirements. The alternatives realize two general scenarios for the EWSB sector: either weakly-coupled light resonances exist or this sector is strongly coupled at around 1 TeV scale. The first class includes more complicated Higgs models but also higgs-less models. Very popular are supersymmetric models [49, 50, 51] with two complex Higgs doublets resulting in three neutral and two charged Higgs bosons. If the supersymmetry was exact[1], the naturalness problem would be overcome thanks to approximate cancellation of the quadratic divergences between boson and fermion loop contributions in Eq. (2.17)). However, scalar masses can only be protected from large corrections if the supersymmetry is broken at scale not much larger than 1 TeV. Unfortunately, supersymmetry does not explain the reason of electroweak symmetry breaking that is only parametrized with the use of fundamental scalars and assumed arbitrary potential. Completely new dynamics of EWSB, that is most often inspired by extra dimensions [52, 53], is provided by higgs-less models. The unitarity violation in scatterings of longitudinally polarized bosons is in these models postponed by introduction of new resonances, *e.g.* Kaluza-Klein excitations of gauge bosons.

Unless there are low mass fundamental states resonantly produced in $V_L V_L$ scattering, unitarity is violated in this process at Λ_{unit} scale, and longitudinally polarized bosons are strongly interacting at TeV scale because of high energy limit of polarization vector in Eq. (2.4). This is the second scenario with sector of new particles that interact strongly at TeV energy scale. The result of this strong interaction could be natural mechanism for EWSB similar to the one existing for strongly-coupled pions. This mechanism is known as dynamical spontaneous symmetry breaking. The most characteristic manifestations would be heavy resonances of strong interactions or increased cross-section, both for TeV scale energy. This scenario is also able to explain the smallness of the EW scale in comparison to the Planck scale, *i.e.* hierarchy problem. These models are of main interest for this thesis; therefore, will be further discussed in Section 3.

The realized in Nature scenario of EWSB may be determined by observation and identification of low mass fundamental particles or heavy resonances, but also by the measurement of the cross-section for production of longitudinal gauge boson pairs.

---

[1]it is not true since superpartners have not been found

2.5 Electroweak Chiral Lagrangian approach to the SM with heavy elementary Higgs boson

It can be very instructive to consider initially the case of strongly-coupled symmetry-breaking sector that is available in the SM for high Higgs boson mass.

The Goldstone bosons make a triplet under $SU(2)_C$ group, and because of this are similar to the pions making in the limit of vanishing mass a triplet under isospin $SU(2)$. After substitution of v for f_π in $\pi\pi$ scattering amplitudes[1] [54] and assuming that simple scaling in energy is valid, one obtains the low-energy theorem for Goldstone bosons of broken EW symmetry in the form of the following amplitudes:

$$\mathcal{M}(w^+ w^- \to zz) = \frac{s}{v^2} \, , \tag{2.19}$$

$$\mathcal{M}(w^+ w^- \to w^+ w^-) = -\frac{u}{v^2} \, , \tag{2.20}$$

$$\mathcal{M}(zz \to zz) = 0 \, , \tag{2.21}$$

$$\mathcal{M}(w^\pm z \to w^\pm z) = \frac{t}{v^2} \, , \tag{2.22}$$

$$\mathcal{M}(w^\pm w^\pm \to w^\pm w^\pm) = -\frac{s}{v^2} \, . \tag{2.23}$$

These amplitudes are valid in low-energy domain:

$$s \ll \min\{M_{SB}^2, (4\pi v)^2\} \, . \tag{2.24}$$

The amplitudes are applicable to energies much lower than M_{SB} - a mass scale where states of symmetry-breaking sector appear (*e.g.* Higgs boson), and much below $4\pi v$ - the scale determined by validity of perturbative approach [55, 56]. These equations can be applied to longitudinally-polarized vector bosons for $\sqrt{s} \gg M_W$. In this limit they are consistent with the exact calculations for Goldstone bosons and longitudinal vector bosons.

The low-energy theorem is limited to low energies, and contains no sensitivity to M_{SB}. This limitation can be overcome and a dependence on M_{SB} appears in effective field theory method.

The effective field theory is applicable to the problem with two distant mass scales. Most often considered case is an influence of unknown physics from higher energy Λ on experimentally accessible domain. The effective field theory can be seen as an expansion in $1/\Lambda$. Non-standard terms are thus suppressed by Λ scale and integrated out in coupling constants and self-energies. Beneath effective approach lies fundamental renormalizable theory of interactions, *e.g.* QCD, that is eventually able to determine all free parameters.

---

[1] physics of pions will be further discussed in this section and in Section 3.1

The most well-known example of an effective field theory is the Fermi model of beta decay that was applied to energies much lower than M_W. Another example is the effective field theory of QCD being used for low energy pions.

The Standard Model, that appears to be an exact theory for the Fermi model and correctly describes the interactions of particles up to energies of the order v, can be also considered as an effective field theory at energies E$\ll$1 TeV with new phenomena expected at higher energies. An example is symmetry breaking sector with energy scale much higher than electroweak scale. Here, heavy Higgs boson with large M_H will be considered. Higgs boson mass of the order of 1 TeV implies $\lambda/\pi^2 \approx 1$ [1]. Symmetry breaking sector is thus strongly interacting. This situation is similar to the case of strong interactions within pion sector, for which effective chiral Lagrangian [57, 58, 59, 60], also called chiral perturbation theory, approach was used as well. Effective approach was very successful in description of light quarks interacting by the pion exchange and pion scattering processes. The strength of the interaction is not the only similarity between Higgs sector and the sector of pions. Although the basic symmetries of the Lagrangians are different [$SU(2)_L \times U(1)_Y$ vs $SU(2)_L \times SU(2)_R$ respectively for Higgs and pion sectors], in both of these cases this is $SU(2)$ symmetry that is spontaneously broken giving rise to three massless Goldstone bosons (non-physical massless scalars vs approximately massless pions, respectively) and one massive scalar (not found Higgs boson vs not found σ particle [2], respectively) with vev's: $v = 246$ GeV and $f_\pi = 93$ MeV, respectively.

The effective formulation of the SM with very heavy Higgs boson is called the Electroweak Chiral Lagrangian (EWChL) [61, 62, 63]. By definition, it can completely determine the impact of heavy and strongly interacting Higgs sector on the low-energy structure of the SM. As a result, it enables specification of acceptable Higgs boson masses.

The theory of Higgs sector can be realized with the use of linear σ model [64] with $SU(2)_L \times SU(2)_R$ symmetry, *i.e.* using 2×2 matrix $U(x)$ [61, 62, 63]:

$$U(x) = \sigma(x) + i\vec{\tau} \cdot \vec{\pi}(x) , \qquad (2.25)$$

linearly parametrized by scalar fields ($\sigma(x)$ - the Higgs field, $\vec{\pi}(x) = (\pi_1(x), \pi_2(x), \pi_3(x))$ - a triplet of would-be Goldstone boson fields), where $\vec{\tau} = (\tau_1, \tau_2, \tau_3)$ are the Pauli matrices. This representation of scalars is alternative to usually used one in Eq. (2.6) that uses the complex $SU(2)_L$ doublet. It leads to the following most general form

---

[1]in formulation of effective Higgs sector for the SM it is commonly used definition $\lambda \equiv \frac{M_H^2}{2v^2}$ that slightly differs from definition used in Section 2.3 for Higgs scalar potential

[2]the candidate for this particle is $f_0(600)$ state [21]

for the scalar potential $V(U)$ consistent with the requirements of renormalizability and $SU(2)_L \times U(1)_Y$ gauge invariance:

$$V(U) = \frac{1}{4}\lambda \left(\frac{1}{2}Tr(U^\dagger U) + \frac{\mu^2}{\lambda} \right)^2 . \tag{2.26}$$

The theory of scalar sector can be defined by the following Lagrangian:

$$\mathcal{L} = \frac{1}{4}Tr(\partial_\mu U^\dagger \partial^\mu U) - V(U) . \tag{2.27}$$

In addition to being invariant under the global $SU(2) \times U(1)$ group, this Lagrangian is also invariant under the global chiral $SU(2)_L \times SU(2)_R$ transformation of fields. Vacuum state of the potential for the scalar system in Eq. (2.26) breaks this symmetry to $SU(2)_{L+R}$ (automatically yielding ρ=1 and implying that the photon remains massless since $U(1)_{EM}$ is contained in $SU(2)_{L+R}$), what can drive spontaneous symmetry breaking $SU(2)_L \times U(1)_Y \rightarrow U(1)_{EM}$ of the gauged groups.

For the representation as in Eq. (2.25), the potential in Eq. (2.26) has the following form in terms of scalar fields:

$$V = \frac{1}{4}\lambda \left(\sigma^2 + \vec{\pi}^2 + \frac{\mu^2}{\lambda} \right)^2 . \tag{2.28}$$

For $\mu^2 < 0$ its minimum is degenerated, and $\sigma(x)$ and $\vec{\pi}(x)$ fields lie on a three-dimensional hypersphere of radius $\sqrt{\frac{-\mu^2}{\lambda}}$. Similarly as for Higgs mechanism in Section 2.3, components of $\vec{\pi}$ become three massless Goldstone bosons and eventually third (longitudinal) polarization states of W and Z bosons. The only massive scalar particle σ is identified with the Higgs particle.

We are, however, interested in the heavy Higgs boson limit. The easiest method for studying this case is to take the limit $M_H \rightarrow \infty$ explicitly (keeping v fixed) [61, 62, 63]. As a result one obtains scalar Lagrangian being non-linear σ model [64]. It is by definition non-renormalizable, *i.e.* one-loop corrections contain divergences; therefore, it requires addition of a sufficient number of counterterms to original tree level Lagrangian. Counterterms are made of all possible structures obeying the symmetries of the Lagrangian [$SU(2) \times U(1)$] and can be found by power-counting arguments. A list of all independent $SU(2) \times U(1)$ and CP-invariant counterterms can be found in Ref. [63]. They provide a complete description and enable determination of the low-energy sensitivity of the SM to heavy scalar sector.

Among the counterterms are the terms, which contribute to $VVVV$ vertices. Thanks to them, standard tree-level vertices $WWWW$ and $ZZWW$ obtain additional anomalous pieces, but $ZZZZ$ vertex is entirely new. These new radiatively induced self-interactions are summarized by the effective Lagrangian terms:

$$\frac{1}{16\pi^2}\frac{1}{12}\ln\frac{M_H}{M_W}[Tr(V_\mu V^\mu)]^2 + \frac{1}{16\pi^2}\frac{2}{12}\ln\frac{M_H}{M_W}[Tr(V_\mu V_\nu)]^2 , \tag{2.29}$$

where V_μ field is a function of scalar U fields. Dependence on the Higgs boson mass appears after identification of the cut-off with M_H. Since V_μ contribute with single power of the gauge coupling g, each of these terms is characterized by a strength that is quartic in g and logarithmically dependent on M_H.

It is worth mentioning, that consideration of the one-loop corrections is sufficient. Higher order corrections to Eq. (2.26) are not important even though the loop expansion factor λ/π^2 tends to 1 for large M_H. This is because the higher corrections are relatively suppressed by at least one power of the weak coupling constant $g^2/16\pi^2$ [61, 65].

Low-energy observables weakly (only logarithmically) depend on M_H; therefore, optimal quantities and precise experiments are necessary in order to isolate heavy Higgs boson effects. Such M_H-dependent corrections can be found in natural relations like $\rho = 1$, in values of W and Z vector boson masses, in values of anomalous magnetic and quadrupole moments of W boson and in VVV ($VVVV$) coupling. Except for the corrections to the $\rho = 1$ relation, all of these measurements are feasible only with actually produced vector bosons. For $M_H \approx 1$ TeV, the correction to ρ reads 0.006 [62].

The formalism presented in this section allowed for discussion of all heavy Higgs effects in a systematic and complete manner. This discussion can be treated as an introduction to Section 3.2, where effective consideration of general strongly-coupled sector will be presented.

2.6 Experimental status of Higgs mechanism

As was shown in the previous section, the SM dependence on M_H appears to be weak. Nevertheless, precision measurements performed at the LEP, SLC and Tevatron colliders have succeeded in ruling out heavy Higgs bosons and giving a significant constraint on it.

The experimental bound on the Higgs boson mass is obtained from a global fit of the SM predictions to precision measurements of Z-pole data (mass, width, asymmetries and others), W-pole data (mass, width) and to the top quark mass. This is indirect search for the Higgs boson since it enters only through one-loop corrections. The result is 95% confidence level (CL) upper limit [19]:

$$M_H \leq 166 \; GeV \; . \tag{2.30}$$

The result of direct searches for the Higgs boson at LEP provides a 95% CL lower bound $M_H > 114.4$ GeV [66]. Inclusion of this bound increases the upper limit to 199 GeV.

The global fit to electroweak data assumes, however, that there is no other new physics, and that the SM terms with minimal Higgs sector are valid up to large scale

(*e.g.* GUT scale $\Lambda \sim 10^{16}$ GeV), where new physics may eventually appear. If one assumes scale $\Lambda \lesssim 10$ TeV, so that the triviality limit is met, the experimental bounds on the Higgs boson mass can be raised to about 400-500 GeV [67]. This is a general feature that consistency of a heavier Higgs boson case with precision measurements requires conspiracy of new physics with experimental signatures at the TeV scale [68]. Such new physics is also motivated by lower fine-tuning (satisfaction of naturalness requirement) preferring $\Lambda < 30$ TeV [69].

Chapter 3

Symmetry breaking by
the strongly-coupled sector

This Chapter is focused on a concept of the strongly-coupled sector being responsible for electroweak symmetry breakdown. First follows the introduction to this scenario with realistic examples of models at 1 GeV and 1 TeV scales. Because of variety of models for EW scale and since no one of them is currently confirmed, the effective approach to strongly-coupled models is proposed. Subsequently, it is discussed in detail and considered with respect to the precision measurements.

3.1 Models with symmetry breaking by
the strongly-coupled sector

The precision measurements do not really exclude heavy Higgs with the mass even as high as the triviality limit provided that the scale of new physics is $\Lambda \lesssim 10$ TeV (Section 2.6). However, if one increased the Higgs mass or completely removed it from symmetry breaking sector, longitudinally polarized gauge bosons (symmetry breaking sector composed of Goldstone bosons) would be strongly-coupled at energy scale of around 1-2 TeV (*cf.* Secs. 2.3 and 2.5). These are standard examples of strongly-coupled symmetry breaking sectors. Because unitarity is broken in scattering processes of longitudinally polarized W_L and Z_L bosons in both of these cases, the Higgs model with heavy Higgs boson is not a perfect candidate for symmetry breaking mechanism. There must be some other regulator of amplitude that would enable satisfaction of unitarity requirement in the case of the strongly-coupled sector breaking EW symmetry. The most popular regulators are still, naturally induced by strong dynamics, resonances.

3.1.1 Strong interactions at around 1 GeV scale - an example

The only presently know interactions of strong strength are strong (color) interactions described by the QCD. This example can illustrate how the possible new strong interactions may look like.

Properties of the QCD pion sector after a proper energy rescaling fulfill the requirements imposed in Sec. 2.4 on candidates for electroweak symmetry breaking sector. Pions, the lightest pseudoscalar mesons, are commonly identified as the Goldstone bosons associated with the spontaneous breaking of the global $SU(2)_L \times SU(2)_R$ chiral symmetry that is the symmetry of the Lagrangian for two flavors of massless quarks $(\Psi \equiv (u, d))$ [31][1]. The $SU(2)_L \times SU(2)_R$ symmetry is another, apart from gauge $SU(3)_{color}$, symmetry of the QCD. The running QCD coupling constant becomes large at scale around $\Lambda_{QCD} \approx 210$ MeV, where quark-anti-quark pairs are bounded into a composite field $\bar{\Psi}\Psi$ (quark condensate) with nonzero *vev* $\langle 0|\bar{\Psi}\Psi|0\rangle$. The vacuum state spontaneously break chiral $SU(2)_L \times SU(2)_R$ symmetry to $SU(2)$. The breakdown is thus caused by the strong interaction itself; thus, called dynamical symmetry breaking. This mechanism was invented by the authors of Refs. [31, 32, 71]. The scale of symmetry breaking is determined by $f_\pi = 92$ MeV - the pion decay constant. The $SU(2)$ symmetry of the vacuum introduces quantum number, isospin I, and is denoted by $SU(2)_I$. Under this symmetry, the pions make a triplet (π^-, π^0, π^+). Because of nonzero masses of the quarks, $SU(2)_L \times SU(2)_R$ is only an approximate symmetry. Thus, $SU(2)_I$ is as well approximate, and pions have nonzero masses.

The symmetry breaking sector of the QCD, the pion sector, is strongly-coupled in the region of resonances appearing at M_{SB} mass (of the order of 1 GeV). The lightest of these states, a σ meson, is regarded as hypothetical counterpart of the Higgs boson in pion sector, and is identified with $\pi\pi$ resonant state $f_0(600)$ of mass

$$M_\sigma = 513 \pm 32 \text{ MeV} \tag{3.1}$$

and width $\Gamma_\sigma = 335 \pm 67$ MeV [21]. At energies lower than M_σ, interactions of pions are of weak strength, and the use of perturbation theory is allowed. It is not in contradiction with the QCD coupling constant that at low energies (energies lower than Λ_{QCD}) limit is strong since the QCD describes interactions between quarks and not between pions (strong interaction bound states). This treatment of strong interactions is known as quasiparticle approach [72, 73, 74, 75].

---

[1] pedagogical review is also given in [70]

3.1.2 Strong interactions at around 1 TeV scale

Dynamical spontaneous symmetry breaking can be also used to break EW $SU(2)_L \times U(1)_Y$ symmetry. At first, it can be expected that the strongly-coupled symmetry breaking sector, that is to be used for the SM, is a scaled QCD strongly-coupled pion sector. It would require introduction of the novel strong force and new fermions with phenomenology similar to the QCD strong interactions and quarks. The interaction should be of strong strength at Λ_{QCD}^{new} scale that would be approximately

$$v/f_\pi \approx 2700 \qquad (3.2)$$

times higher than QCD strong interaction Λ_{QCD} [1]. After this scaling, symmetry breaking of novel strong interaction occurs around electroweak scale. The novel strong interaction would thus naturally break $SU(2)_L \times SU(2)_R \to SU(2)$ and incidentally is able to cause $SU(2)_L \times U(1)_Y \to U(1)_{EM}$ breaking. Goldstone bosons are generated in accurate number to make, within the limits of the equivalence theorem application, the longitudinal components of the gauge bosons. Presented mechanism does not influence the masses of W and Z bosons since the value of *vev* is preserved. The $SU(2)$ symmetry of the vacuum state plays a role of accidental $SU(2)_C$ custodial symmetry. Results of the experiments summarized in Eq. (2.14) are thus satisfied and understood. This suggests that both $SU(2)_L \times SU(2)_R$ and $SU(2)_C$ symmetries are exact. Such defined strongly-coupled symmetry breaking sector would be able to substitute the Higgs sector in breaking the symmetry in the SM.

The masses of symmetry breaking sector resonances (M_{SB}) and thus the region of strong interaction within this sector can be estimated by scaling hadronic spectrum. The first resonance could be observed around

$$M_{SB} \sim v/f_\pi \times M_\sigma \approx 1400 \text{ GeV} . \qquad (3.3)$$

As in the case of QCD, the strongly-coupled symmetry breaking sector (longitudinally polarized gauge bosons) would be weakly-coupled for energies lower than M_{SB}, and perturbative theory would work there. In analogy to pions, such behavior of the coupling would probably require Goldstone bosons to be composite particles.

One of the most important advantages of strong interaction theories is that they do not have the hierarchy problem if interaction is asymptotically free. For the case of QCD, its natural scale Λ_{QCD} is determined by the scale, where running strong coupling constant $\alpha_s(\mu)$ becomes strong (close to unity). Thus, renormalization can naturally generate the tiny ratio $\Lambda_{QCD}/M_{Planck} \sim 10^{-20}$. The hierarchy problem of the SM

---

[1] Λ_{QCD}^{new} scale might be significantly higher than v if extra special scalars are present [55, 56]

could similarly be solved if electroweak scale (v) was around Λ_{QCD}^{new} of the novel strong interaction. Meeting of these scales would of course require according particle spectrum of this interaction.

Unfortunately, the novel strong interactions can not be a scaled-up version of QCD since such model is not consistent with precision measurements[1] [11, 12, 76, 77]. It can be only considered as an unrealistic simple example illustrating the phenomenology of models with EW-scale strongly-coupled sector.

3.1.3   Examples of realistic EWSB strongly-coupled models

The simplest example of strongly-coupled EWSB model is Higgs sector with Higgs boson mass of the order of 1 TeV. It was already discussed in Sec. 2.5.

The most popular class of models for EW scale with strongly-coupled symmetry breaking sector are technicolor (TC) models. They have basic phenomenology similar to QCD. It is predicted the existence of techniquarks that interact by the exchange of technicolor[2] technigluons. The interaction is strong at energy scale of the order of 1 TeV. The effective Lagrangian of their bound states (condensates) contains potential similar to the Higgs potential in Eq. (2.8) with spontaneously broken $SU(2) \times SU(2)$ symmetry. Since the techniquarks also couple to the electroweak bosons, the $SU(2)_L \times U(1)_Y$ symmetry is also broken. The TC, as the QCD, predicts existence of technihadrons - technicolor bound states, namely: technipions (Goldstone bosons of the spontaneously broken symmetry), spin-1 technimesons ($\rho_T^{\pm,0}$, ω_T) and others. Original pure TC has been extended to more realistic, so-called extended, TC model allowing the generation of fermion masses. This in turn evolved to walking TC [3] that respects the absence of flavor-changing neutral-currents. The walking TC could not, however, confront with large mass of the top quark. In the next generation of TC models, so-called topcolor, a separate mechanism for the top mass was proposed. This final model is complicated, but consistent with the precision measurements. There are many other technicolor-like models that are realistic. The introduction to the subject may be found in Refs. [78, 79], whereas a more detailed review is presented in Refs. [80, 81, 82].

Technicolor models are commonly disfavored because usually there is no natural limit, in which they reduce to the Standard Model. This condition is satisfied in the degenerate BESS model [83, 84] that uses dynamical symmetry breaking, but does not provide large corrections to EW precision observables if masses of the new particles

---

[1]this statement actually concerns simple QCD-like technicolor model

[2]technicolor is new quantum number

[3]the name originates from the coupling constant that changes very slowly (walks) between two basic scales of walking TC

are large. This model is characterized by the extended strongly-coupled gauge sector with enhanced global symmetries.

The models with strong dynamics at some scale are also inspired by the idea of extra dimensions. Some of them provide higgs-less explanation for the EWSB. The examples are breaking the symmetry by deconstructed dimensions [85], by large top quark mass [86], or by boundary conditions of the gauge fields [52]. Another possibility is light Higgs boson being a composite state bound by new strong interactions [87, 88, 89]. This idea is also used in so-called *Little Higgs* models [90, 91, 92], in which Higgs bosons are pseudo-Goldstone bosons of symmetry broken dynamically at a TeV energy scale. The main advantage of these models is Higgs boson mass that is stable with respect to loop corrections and the effective theory that is weakly interacting up to energies significantly beyond the TeV scale. Disadvantage is much larger gauge group that is needed.

There is a variety of models with strong dynamics at TeV scale that enable EWSB. Therefore, it is worth to apply phenomenological (effective) approach that has already been used in the case of pion interactions. It would enable the most general description of the strongly-coupled symmetry breaking sector dynamics and the general study of the new colliders' sensitivity to models with such EWSB. This can eventually lead to establishing a complete renormalizable field theory. The framework of Electroweak Chiral Lagrangian (EWChL) is a realization of this approach.

3.2 Electroweak Chiral Lagrangian approach

Effective field theory language for EW scale energies was initially used to describe the impact of a heavy Higgs boson on low energy observables. Here a general class of models with strongly-coupled symmetry breaking sector will be considered. Particular models are represented by characteristic values of the effective couplings. The effective approach is able, as in the case of QCD, to describe low energy ($E \ll M_{SB}$) physics of symmetry breaking sector strongly-coupled at M_{SB} scale. In this limit interactions are weak since influences from TeV scale are generated through loops. After a special treatment (*e.g.* unitarization), the EWChL amplitudes are applicable even in the region of M_{SB} and beyond. However, regardless the origin of spontaneous symmetry breakdown, amplitudes are always the same in very low energy limit and given by Eqs. (2.19)–(2.23).

3.2.1　The Lagrangian

The EWChL is the most general way of the Standard Model development if TeV-scale symmetry breaking physics is assumed. The EWChL is the complete set of $SU(2)_L \times SU(2)_R$, Lorentz and CP invariant operators up to dimension four. This section only overviews the EWChL. More details can be found for example in Refs. [55, 93, 94, 95, 96, 97].

The full model is described by the Lagrangian:

$$\mathcal{L} = \mathcal{L}_{SM} + \mathcal{L}_{EWChL} - V(U) , \qquad (3.4)$$

where $\mathcal{L}_{SM}$ denotes the SM Lagrangian. The EWChL and the potential $V(U)$ are expressed in terms of 2×2 unitary matrix U:

$$U = \exp(i\frac{\vec{\tau}.\vec{\pi}}{v}) . \qquad (3.5)$$

This matrix is non-linearly parametrized with the use of three fields π_i that will appear to be would-be Goldstone bosons of the broken symmetry. $\vec{\tau}$ are the Pauli matrices. Matrix U transforms under $SU(2)_L \times SU(2)_R$ symmetry as $U \to LUR^{\dagger}$[1]. There is no explicit fundamental Higgs scalar field here like in linear representation in Eq. (2.25); however, resonant behavior in scattering processes can still, as will be shown later, be indirectly obtained. Potential $V(U)$ of π_i fields breaks spontaneously $SU(2)_L \times SU(2)_R$ symmetry to $SU(2)$.

The EWChL can be decomposed into two main parts:

$$\mathcal{L}_{\text{EWChL}} = \mathcal{L}_{\text{NL}} + \sum_{i=1}^{5} \mathcal{L}_i^{(4)} . \qquad (3.6)$$

The $\mathcal{L}_{NL}$ term:

$$\mathcal{L}_{NL} = \frac{v^2}{4} Tr[D_{\mu}U(D^{\mu}U)^{\dagger}] \qquad (3.7)$$

is the most general effective Lagrangian that can be written with only two derivatives. Covariant derivative $D_{\mu}U$, laws of transformation under symmetry groups and further details can be found for example in Refs. [94, 96]. With the representation in Eq. (3.5) the $\mathcal{L}_{NL}$ term is the Lagrangian of so-called non-linear sigma model [64].

The remaining terms in Eq. (3.6) [94, 96]:

$$\mathcal{L}_1^{(4)} = \frac{1}{2}g^2 a_1 B_{\mu\nu} Tr(TF^{\mu\nu}) , \qquad (3.8)$$

$$\mathcal{L}_2^{(4)} = \frac{1}{2}iga_2 B_{\mu\nu} Tr(T[V^{\mu}, V^{\nu}]) , \qquad (3.9)$$

---

[1]L and R are $SU(2)$ matrices

$$\mathcal{L}_3^{(4)} \;=\; iga_3 Tr(F_{\mu\nu}[V^\mu, V^\nu]) \;, \tag{3.10}$$

$$\mathcal{L}_4^{(4)} \;=\; a_4 \left[\text{Tr}\,(V_\mu V_\nu)\right]^2 \;, \tag{3.11}$$

$$\mathcal{L}_5^{(4)} \;=\; a_5 \left[\text{Tr}\,(V_\mu V^\mu)\right]^2 \;, \tag{3.12}$$

for $T \equiv U\tau^3 U^\dagger$ and $V_\mu \equiv (D_\mu U)U^\dagger$, complete the list of terms[1]. The superscript in $\mathcal{L}_i^{(n)}$ notation refers to the dimension of operators.

Among $\mathcal{L}_i^{(n)}$ terms are the counterterms that cancel the divergences generated in a one-loop calculation with the $\mathcal{L}_{NL}$ Lagrangian. Whereas the latter term is universal part of the EWChL, the $\mathcal{L}_i^{(n)}$ terms have model-dependent effective coefficients a_i that can be calculated within the underlying symmetry breaking model. Such calculations has been performed for example for the SM with a heavy Higgs boson [98, 99, 100, 101, 102, 103], for technicolor models in the large N_{TC} limit [104], and for chiral models within the resonance saturation hypothesis [105, 106, 107]. Commonly, one is limited only to first order corrections. Higher order corrections would require additional counterterms, what testifies that EWChL is really non-renormalizable.

The typical size of effective coefficients can be anticipated from naive dimensional analysis [60, 108]:

$$a_i \sim (\frac{v}{\Lambda})^2 \;. \tag{3.13}$$

For Λ (energy scale of the strongly-coupled sector) of the order of 2-3 TeV, coefficients a_i are of the order of 10^{-2}.

Chiral parameters contribute to two-point boson functions (self-energies) (a_1), triple gauge coupling (TGC)'s (a_2 and a_3), and to quartic gauge coupling (QGC)'s (a_4 and a_5). The a_4 and a_5 parameters have not been directly probed, yet. They will be attainable in $VV \to VV$ ($V = Z, W^+, W^-$) scattering processes just at the LHC. Study of these processes can be a novel method for determination of a possible symmetry breaking mechanism by the strongly-coupled sector.

3.2.2 Calculations

Assuming that custodial $SU(2)_C$ symmetry is conserved, calculations for $V_L V_L \to V_L V_L$ processes can be done similarly to the ones performed for the pion scattering with the isospin $SU(2)_I$ symmetry.

The amplitudes for scattering processes of isospin states W_L^a ($a = 1, 2, 3$):

$$W_L^a \, W_L^b \;\to\; W_L^c \, W_L^d \;; \tag{3.14}$$

---

[1]Unless $SU(2)_C$ invariance is assumed (like it is done here), one should consider the Lagrangian with $SU(2) \times U(1) \to U(1)$ symmetry breaking pattern. Thus, additional $\mathcal{L}_0^{(2)}$, $\mathcal{L}_6^{(4)}$, ..., $\mathcal{L}_{11}^{(4)}$ terms with extra parameters a_0, a_6, ..., a_{11} appears in the most general Lagrangian. Those terms parametrize custodial symmetry breaking; therefore, corresponding parameters should be small.

can be expressed in terms of a single amplitude function $\mathcal{A}(s, t, u)$ [54]:

$$\mathcal{M}(W_L^a W_L^b \to W_L^c W_L^d) = \mathcal{A}(s, t, u)\delta^{ab}\delta^{cd} + \mathcal{A}(t, s, u)\delta^{ac}\delta^{bd} + \mathcal{A}(u, t, s)\delta^{ad}\delta^{bc}, \quad (3.15)$$

where s, t, and u are the usual Mandelstam variables. Individual physical amplitudes for $W_L^\pm = (1/\sqrt{2})(W_L^1 \mp iW_L^2)$ and $Z_L = W_L^3$ are the following:

$$
\begin{aligned}
\mathcal{M}(W_L^+ W_L^- \to Z_L Z_L) &= \mathcal{A}(s, t, u) , \\
\mathcal{M}(Z_L Z_L \to W_L^+ W_L^-) &= \mathcal{A}(s, t, u) , \\
\mathcal{M}(W_L^+ W_L^- \to W_L^+ W_L^-) &= \mathcal{A}(s, t, u) + \mathcal{A}(t, s, u) , \\
\mathcal{M}(Z_L Z_L \to Z_L Z_L) &= \mathcal{A}(s, t, u) + \mathcal{A}(t, s, u) + \mathcal{A}(u, t, s) , \\
\mathcal{M}(W_L^\pm Z_L \to W_L^\pm Z_L) &= \mathcal{A}(t, s, u) , \\
\mathcal{M}(W_L^\pm W_L^\pm \to W_L^\pm W_L^\pm) &= \mathcal{A}(t, s, u) + \mathcal{A}(u, t, s) . \quad (3.16)
\end{aligned}
$$

Because of $SU(2)_I$ symmetry, there are three possible weak isospin channels $I = 0, 1, 2$ in $V_L V_L \to V_L V_L$ processes with isospin eigenamplitudes $\mathcal{A}_I$ [14, 35, 36]:

$$
\begin{aligned}
\mathcal{A}_0(s, t, u) &= 3\mathcal{A}(s, t, u) + \mathcal{A}(t, s, u) + \mathcal{A}(u, t, s) , \\
\mathcal{A}_1(s, t, u) &= \mathcal{A}(t, s, u) - \mathcal{A}(u, t, s) , \\
\mathcal{A}_2(s, t, u) &= \mathcal{A}(t, s, u) + \mathcal{A}(u, t, s) . \quad (3.17)
\end{aligned}
$$

The scattering partial wave amplitudes $a_{IJ}(s)$ with definite angular momentum J and isospin I are thus the following:

$$a_{IJ}(s) = \frac{1}{64\pi} \int_{-1}^{1} d(\cos\theta) \, P_J(\cos\theta) \, \mathcal{A}_I(s, t, u) , \quad (3.18)$$

where θ is the center of mass system (c.m.s.) scattering angle, and $P_J(\cos\theta)$ is Legendre polynomial. Such computed partial wave amplitudes in Eq. (3.18) can be approximated for low energies by the first two terms in the expansion[1]:

$$a_{IJ}(s) = a_{IJ}^{(2)}(s) + a_{IJ}^{(4)}(s) , \quad (3.19)$$

where the superscripts refer to the corresponding powers of c.m.s. energy $\sqrt{s}$. The amplitude $a_{IJ}^{(2)}$ exhibits s/v^2 behavior. The dependence on a_4 and a_5 parameters appears just in $a_{IJ}^{(4)}$ that is of the order of s^2/v^4. The Bose symmetry implies that even J are allowed only for $I = 0$ and 2, whereas odd J only for $I = 1$ [2]. Only three partial wave amplitudes: a_{00}, a_{11}, a_{20} will be subsequently taken into account. The higher partial waves are of order s^2/v^4, but they are numerically small and can be neglected.

---

[1] expansion terms are given for example in Ref. [96]
[2] precisely Bose symmetry allows for even values of $I + J$

Having truncated amplitude as in Eq. (3.19) one can ones again compute isospin amplitudes $\mathcal{A}_I$ using formula reverse to that in Eq. (3.18). They reads:

$$\mathcal{A}_I(s,t) = 32\pi \sum_{J=0}^{\infty} (2J+1)\, a_{IJ}(s)\, P_J(1 + \frac{2t}{s})\,. \tag{3.20}$$

where $1 + \frac{2t}{s} = \cos\theta$. These amplitude can be used to calculate the physical $\mathcal{A}(V_L V_L \to V_L V_L)$ amplitudes according to the recipe:

$$
\begin{aligned}
\mathcal{A}(W_L^+ W_L^- \to W_L^+ W_L^-) &= \frac{1}{3}\mathcal{A}_0 + \frac{1}{2}\mathcal{A}_1 + \frac{1}{6}\mathcal{A}_2\,, \\
\mathcal{A}(W_L^+ W_L^- \to Z_L Z_L) &= \frac{1}{3}\mathcal{A}_0 \qquad\quad - \frac{1}{3}\mathcal{A}_2\,, \\
\mathcal{A}(Z_L Z_L \to Z_L Z_L) &= \frac{1}{3}\mathcal{A}_0 \qquad\quad + \frac{2}{3}\mathcal{A}_2\,, \\
\mathcal{A}(W_L Z_L \to W_L Z_L) &= \qquad\qquad \frac{1}{2}\mathcal{A}_1 + \frac{1}{2}\mathcal{A}_2\,, \\
\mathcal{A}(W_L^\pm W_L^\pm \to W_L^\pm W_L^\pm) &= \qquad\qquad\qquad\quad \mathcal{A}_2\,.
\end{aligned}
\tag{3.21}
$$

The amplitude function $\mathcal{A}(s,t,u)$ is given by particular models of strongly-coupled sector. The EWChL yields the following formula [93]:

$$
\begin{aligned}
\mathcal{A}(s,t,u) = &\; \frac{s}{v^2} + \frac{4}{v^4}\left[2a_5(\mu)s^2 + a_4(\mu)(t^2+u^2)\right] \\
&- \frac{1}{96\pi^2 v^4}\left[t(s+2t)\log(\frac{-t}{\mu^2}) + u(s+2u)\log(\frac{-u}{\mu^2}) + 3s^2\log(\frac{-s}{\mu^2})\right]\,,
\end{aligned}
\tag{3.22}
$$

where $\log(-s) = \log(s) - i\pi$ if $s > 0$. Dependent on renormalization scale μ chiral couplings are [99]:

$$
\begin{aligned}
a_4(\mu) &= a_4(\mu') - \frac{1}{12}\frac{1}{16\pi^2}\log\frac{\mu^2}{\mu'^2}\,, \\
a_5(\mu) &= a_5(\mu') - \frac{1}{24}\frac{1}{16\pi^2}\log\frac{\mu^2}{\mu'^2}\,.
\end{aligned}
\tag{3.23}
$$

Amplitude in Eq. (3.22) can be used for direct calculation of physical amplitudes $\mathcal{A}(V_L V_L \to V_L V_L)$ in Eq. (3.16). Alternatively one can follow the sequence of equations: (3.22)$\to$(3.17)$\to$(3.18)$\to$(3.19)$\to$(3.20)$\to$(3.21). The only difference for now between these two recipes is the use of truncated expansion in Eq. (3.19) in the second case. The reason for using the second recipe will become clear in Section 3.2.3.

Physical amplitudes $\mathcal{A}(V_L V_L \to V_L V_L)$, when folded with initial $V_L V_L$ luminosities, can be used for obtaining the cross-sections for $pp \to VVjj$ processes with intrinsic $V_L V_L \to V_L V_L$ scatterings [97].

3.2.3   Unitarization of amplitudes and resonances

As in the case of low-energy theorem for Goldstone bosons in Eqs. (2.19)-(2.23) the perturbative predictions made with the effective Lagrangian can also be used only at low energies:

$$s \ll \Lambda_{SB}^2 \,, \quad \Lambda_{SB} = min\{M_{SB}, 4\pi v\} \,, \tag{3.24}$$

Because M_{SB} is lower than $4\pi v$ (*cf.* Eq. (3.3)), this limitation can be translated to $\sqrt{s} \ll 1400$ GeV. There is also lower bound on EWChL application:

$$s \gg M_W^2 \tag{3.25}$$

that is connected with usage of equivalence theorem. This last limitation is, however, only required if the effective Lagrangian is to be used for processes with longitudinal components of gauge bosons.

   If the upper limit of the effective Lagrangian application is approached, the amplitudes in the form of truncated series in powers of invariant mass in Eq. (3.19) violate the unitarity condition given in Eqs. (A.4) and (A.5), and perturbation theory ceases to work. This energy region is, however, especially interesting since will be accessible at the LHC. Truncated amplitudes satisfy only the following perturbative unitarity relation:

$$\mathrm{Im}\, a_{IJ}^{(4)}(s) = \mid a_{IJ}^{(2)}(s) \mid^2 \tag{3.26}$$

for partial wave amplitudes with fixed power of energy. Unfortunately this condition is not equivalent to the exact unitary relation in the TeV energy region.

   Assuming that the amplitude satisfies unitary relation and using approximation in Eq. (3.19), for which Eq. (3.26) is satisfied, one arrives at the following expression for the amplitude [96, 109, 110]:

$$a_{IJ}(s) = \frac{a_{IJ}^{(2)}(s)}{1 - a_{IJ}^{(4)}(s)/a_{IJ}^{(2)}(s)} \,, \tag{3.27}$$

This approximation of amplitude respects strict elastic unitarity at all energies. Additionally, when Eq. (3.27) is re-expanded in powers of s, low energy expansion presented in Eq. (3.19) is recovered. This formula should, therefore, substitute truncated expansion in Eq. (3.19). This method is called Inverse Amplitude Method (IAM) or Padé unitarization[1] [111, 112, 113, 114, 115, 116, 117].

---

[1] called as well *1,1* Padé approximant

Figure 3.1: The $a_4 \times a_5$ parameter space of EWChL with regions of various resonant behaviors as provided by Padé unitarization. Points represent the scenarios that are studied in this thesis. These scenarios are scalar models (S1, S4, S6), vector models (V1, V2), vector-scalar models (VS, VS1) and model without resonance (NR). Plot prepared basing on that in Ref. [110].
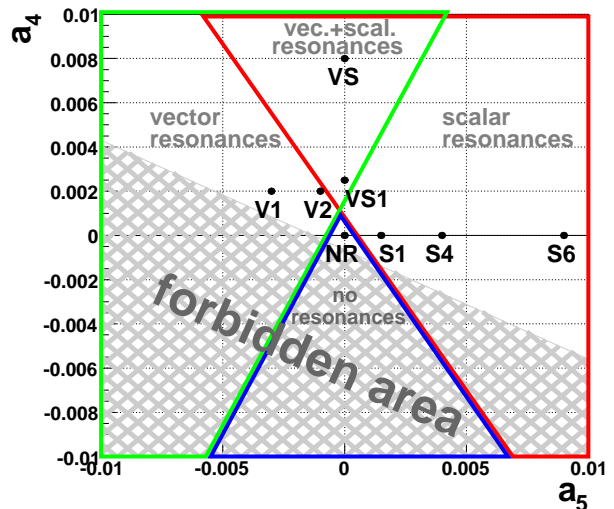
The tree-level amplitudes in general do not obey the unitarity relation. However, inclusion of higher-loop corrections provide approximate satisfaction of unitarity condition [112]. The IAM can be, therefore, regarded as a substitution of complicated calculations and a special resummation of one-loop series [115].

Formalism of EWChL with Padé unitarization can describe resonances, one of the signatures of the new strongly interacting physics. It is done without increasing the number of parameters. Resonant behavior in scattering amplitudes is obtained for invariant masses s, for which a phase-shift:

$$\delta_{IJ}(s) = \frac{\text{Im } a_{IJ}(s)}{\text{Re } a_{IJ}(s)} \qquad (3.28)$$

equals $\pi/2$. This is the condition for partial wave pole, which is interpreted as dynamically generated resonance. For phase-shifts δ_{00} and δ_{11} passing $\pi/2$, one obtains scalar and vector resonance, respectively. Similar behavior for δ_{20} can not be called resonance since $I = 2$, $J = 0$ partial wave is repulsive and the pole is only called saturation effect.

Since amplitudes depend only on a_4 and a_5, the resonant characteristics is also fully determined by these parameters. This can be used to build a map of resonances in the $a_4 \times a_5$ parameter space. It is presented in Figure 3.1. Depending on the values of these parameters, one obtains different resonant behaviors. The type of resonance can thus be used for model classification. There is also region allowing models with two types of resonances (scalar and vector). The complete theoretical study of the resonances that are generated has been performed in [110]. Resonant behavior for points marked in Fig. 3.1 can be seen in $d\sigma/ds$ differential cross-section for $V_L V_L \to W_L W_L$ scatterings. It is presented in Fig. 3.2.

(a) Resonant behaviors for scalar models.

(b) Resonant behaviors for non-scalar models (vector, vector-scalar and non-resonant).
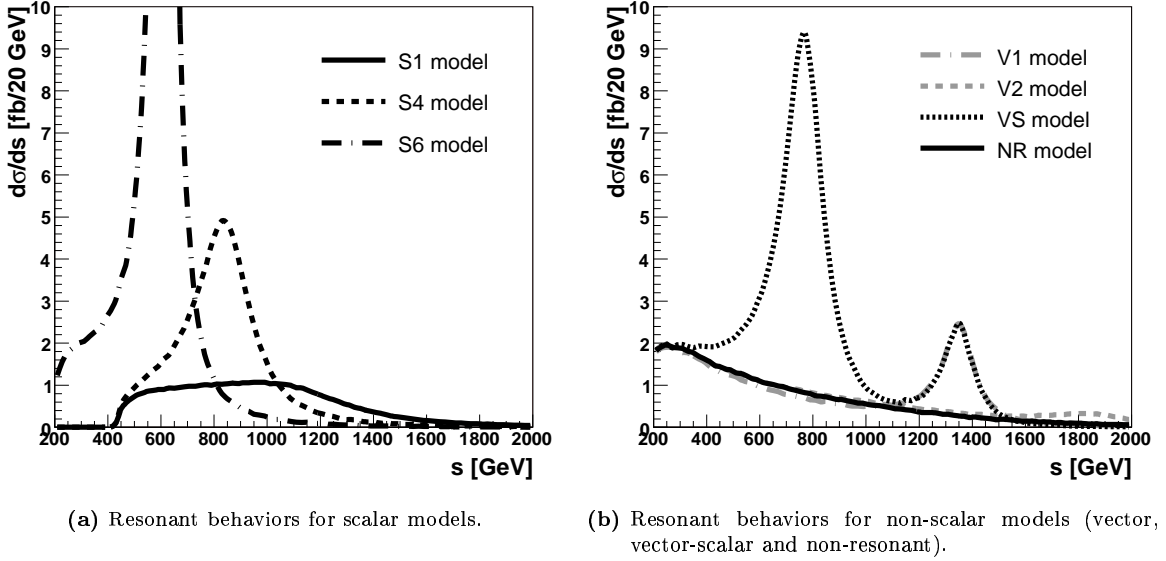
Figure 3.2: Resonant behavior seen in $d\sigma/ds$ differential cross-section for $V_L V_L \rightarrow W_L W_L$ scatterings for various models accessible within EWChL approach with Padé unitarization.

Values of masses and half-widths for resonances are identified with real and imaginary parts of pole positions. For scalar channel ($J{=}0$), the following expressions for the mass M_S and the width Γ_S of scalar resonance are obtained [96]:

$$M_S^2 = \frac{12\,v^2}{16\left(11a_5(M_S) + 7a_4(M_S)\right) + \frac{101}{3(4\pi)^2}} \,, \tag{3.29}$$

$$\Gamma_S = \frac{M_S^3}{16\,\pi\,v^2} \,, \tag{3.30}$$

where coefficients $a_4(\mu)$ and $a_5(\mu)$ are calculated at scale $\mu = M_S$. The mass of neutral scalar resonance and partial wave amplitude a_{00} [1] actually depend only on $7a_4 + 11a_5$ combination of parameters. Thus, the points lying on the line in $a_4 \times a_5$ space with definite value of $7a_4 + 11a_5$ combination represent the same physical model.

There is actually no direct correspondence between scalar models and Higgs model, *i.e.* one is not able, at least within the unitarization procedure that is used here, to reproduce resonance that could be identified with the Higgs boson. This is because scalar resonance is narrower than the standard Higgs boson, for which the width above ZZ threshold reads:

$$\Gamma_H^{SM} = \frac{3M_H^3}{32\pi v^2} \,. \tag{3.31}$$

This potentially enables distinguishing strongly-coupled symmetry breaking sector resonance from standard heavy Higgs boson.

---

[1]the formula for a_{00} can for example be found in Ref. [96]

For vector channel (J=1), the following expressions for the mass M_V and the width Γ_V of vector resonance are obtained [96]:

$$M_V^2 \;\; = \;\; \frac{v^2}{4(a_4 - 2a_5) + \frac{1}{9(4\pi)^2}} \;, \tag{3.32}$$

$$\Gamma_V \;\; = \;\; \frac{M_V^3}{96\,\pi\,v^2} \;. \tag{3.33}$$

The mass, unlike in Eq. (3.29), does not depend on the scale since it is fully determined by $a_4 - 2a_5$ combination that is scale independent (*cf.* Eq. (3.23)). This also leads to an ambiguity in receiving particular physical model with combination of parameters that gives the same value of $a_4 - 2a_5$.

The forbidden region in Figure 3.1 is excluded by causality constraint [110]. The region for saturation effects in $I = 2$ wave is very limited and is not considered here. The allowed region in the very center of Fig. 3.1 corresponds to models without resonances.

The points in Fig. 3.1 represent the scenarios that will be further studied in this thesis. These scenarios are scalar models (S1, S4, S6), vector models (V1, V2), vector-scalar models (VS, VS1) and the model without resonance (NR). These points allow, thanks to symmetries observed for scalar and vector resonances, to access most of the presented space of parameters. The prediction for $V_L V_L \to V_L V_L$ amplitudes in this section is limited to $\sqrt{s} \gtrsim 500$ GeV (*cf.* Eq. (3.25)). Therefore, most of the space in Figure 3.1 is allowed, and no models (points) from outside of this space need to be considered. Details on the values of parameters, obtained masses of resonances and cross-sections are collected in Table 3.1. The general rule is that as both a_4 and a_5 parameters tend to zero, the resonances become heavier and broader. The signal is simultaneously less significant because the cross-section drops down due to the limited phase-space (c.m.s. energy) at collider experiments.

The Padé approximant used here is not the only unitarization method; therefore, this choice is somehow arbitrary[1]. It is also possible with accordingly defined amplitude function $\mathcal{A}(s, t, u)$ (alternative to that in Eq. (3.22)) to obtain resonances directly [120]. Additionally, various methods lead to different predictions. However, the IAM seems to be the best method since it is very well motivated by theory [113, 116] and low energy data for unitarization of meson-meson amplitudes, and is also the most popular. Padé approximants have been very successful not only in description of meson dynamics, but also in reproduction of the first resonances in each I, J channel up to 1.2 GeV [115, 116, 117, 121, 122, 123], for example the $\rho(770)$ resonance in $\pi\pi$ scattering and the K*(892) in πK scattering. Nevertheless, this does not guarantee correct performance in the case

---

[1]comparison of different methods is presented for example in Refs. [97, 118, 119]

model	a_4(1 TeV)	a_5(1 TeV)	scalar resonance $M_S(\mu = M_S)$ [GeV]	Γ_S	vector resonance M_V [GeV]	Γ_V	$\sigma*$BR [fb]
S1	0.0	0.0015	1189	552	-	-	6.5
S4	0.0	0.0040	901	240	-	-	11.4
S6	0.0	0.0090	652	91	-	-	30.4
V1	0.002	-0.003	-	-	1360	138	4.9
V2	0.002	-0.001	-	-	1903	378	4.9
VS	0.008	0.0	824	184	1360	138	21.9
VS1	0.0025	0.0	1174	531	2378	737	6.8
NR	0.0	0.0	-	-	-	-	4.3

Table 3.1: Definitions of selected study models within EWChL. Models (also shown in Fig. 3.1) are identified by the values of a_4 and a_5 parameters at the fixed scale of $\mu = 1$ TeV. Theoretical masses $M_S(\mu = M_S)$ and widths Γ_S of the scalar resonances are calculated according to Eqs. (3.29) and (3.30) for $\mu = M_S$. Theoretical masses M_V and widths Γ_V of the vector resonances are calculated according to Eqs. (3.32) and (3.33). The total LHC cross-sections σ for $pp \rightarrow W_L W_L qq$ with intrinsic $V_L V_L \rightarrow W_L W_L$ scattering and included branching ratios for $W_L W_L \rightarrow q\bar{q}\mu\nu$ decays of final states ($\sigma*$BR) are calculated in PYTHIA with cuts presented in App. D.

of electroweak Goldstone bosons. Therefore, results with Padé unitarization should only be treated as an example that enables studying the experimental reach of the CMS experiment in observation of $V_L V_V L \rightarrow V_L V_L$ scattering processes for invariant masses of the order of 1 TeV in this thesis.

3.2.4   Consistency with precision data

Are the models predicted with the use of EWChL realistic? This question concerns consistency with the precision measurements done at LEP, SLC and Tevatron. It turns out that even though some of the processes predicted by EWChL (*e.g.* gauge boson scatterings) are not directly accessible yet, presently available data can constrain the values of EWChL parameters. A whole set of chiral parameters $a_0, \ldots, a_{11}$ is considered below with inclusion of $a_0, a_6, \ldots, a_{11}$ parameters that measure $SU(2)_C$-violating effects. They are constrained by precision measurements of oblique parameters (vector boson two-point functions) (a_0, a_1, a_8), TGC's (a_2, a_3, a_9, a_{11}) and by loop corrections to oblique parameters or by QGC's ($a_4, \ldots, a_7, a_{10}$).

The precision electroweak data concerning Z^0 and W bosons are analyzed with the use of sets of variables describing possible deviations from the Standard Model. The most popular approach uses three observables S, T and U [11, 12], called oblique parameters. This set parametrizes the corrections to the gauge boson self-energies

(propagators). Since EWChL parameters contribute to the Z-pole physics at the one-loop level, measured values of oblique parameters can be used for restriction of chiral parameters.

The latest fit [21] to EW data with assumed $M_H = 300$ GeV gives:

$$
\begin{aligned}
S &= -0.21 \pm 0.10 \,, \\
T &= -0.04 \pm 0.11 \,, \\
U &= 0.21 \pm 0.12 \,,
\end{aligned}
\tag{3.34}
$$

In order to extract the value of the oblique parameters due to strongly-coupled symmetry breaking sector, one first must subtract the impact of the standard Higgs boson. After this procedure, one obtains the following 90% CL (2σ-level) intervals[1]:

$$
\begin{aligned}
-0.0003 &< a_0 < 0.0133 \,, \\
0.0019 &< a_1 < 0.0099 \,, \\
-0.0006 &< a_8 < 0.0090 \,.
\end{aligned}
\tag{3.35}
$$

The a_2, a_3, a_9, a_{11} parameters are in turn connected with $WW\gamma$ and WWZ TGC's [104] that were directly probed at LEP2 collider. The measured values of g_1^Z, g_5^Z, κ_Z and κ_γ couplings [21] provide the following 2σ-level constrains on the anomalous chiral couplings:

$$
\begin{aligned}
\Delta\kappa_\gamma, \Delta\kappa_Z &\implies -0.266 < a_2 < 0.287 \,, \\
\Delta g_1^Z &\implies -0.097 < a_3 < 0.050 \,, \\
\Delta\kappa_\gamma, \Delta\kappa_Z, \Delta g_1^Z &\implies -0.326 < a_9 < 0.020 \,, \\
\Delta g_5^Z &\implies -0.451 < a_{11} < 0.198 \,.
\end{aligned}
\tag{3.36}
$$

Loop corrections to the T parameter through EWChL couplings have been evaluated in Ref. [124]. With the T value used in Ref. [125][2], the 90% CL constraints on the couplings of interest are the following [125][3]:

$$
\begin{aligned}
-0.17 &< a_4 < 0.17 \,, \\
-0.42 &< a_5 < 0.42 \,, \\
-0.021 &< a_6 < 0.021 \,, \\
-0.17 &< a_7 < 0.17 \,, \\
-0.023 &< a_{10} < 0.023 \,.
\end{aligned}
\tag{3.37}
$$

---

[1]these values are recalculated results of Ref. [96] with the use of the latest values of oblique parameters given in Ref. [21]

[2]the difference from the latest value given in Eq. (3.34) is not significant and is neglected

[3]Ref. [125] actually gives constrains on ℓ_i chiral parameters that are connected with a_i parameters by the relation $\ell_i(v/\Lambda)^2 \equiv a_i$

The above quoted constrains on chiral parameters show that there is room for the EWChL models. However, it needs to be remembered that particular model predicts values for every parameter. It can be, therefore, difficult to invent the model that could confront all constraints in Eqs. (3.35)-(3.37), but such models can not be presently excluded. In particular the whole space presented in Fig.3.1 for $V_L V_L \rightarrow W_L W_L$ scattering is allowed, and resonances in scattering processes with mass starting particularly from about 500 GeV are not excluded. Indeed, as is calculated in Ref. [10], TeV-scale strongly interacting new physics is allowed by precision measurements, and it does not contradict the limits for models with fundamental Higgs boson resonance.

Chapter 4

Signal and background processes

This chapter is devoted to the subject of physics processes that are of interest for this thesis. First, the simulation methods are introduced. Next, processes leading to experimental signal of the strongly-coupled sector are presented. Vector boson fusion will be chosen as optimal signal process and calculation methods, which were used for its generation, will be reviewed. The signal signature will be established, and background processes that can mimic the signal will be subsequently presented. Special emphasis will be put on multi-jet processes. It will be presented original method of this background consideration.

4.1 Monte-Carlo generation methods

The total cross-section for the interaction of protons that will be observed by the CMS detector at the LHC (minimum bias events) is about 100 mb [21]. It is thus impossible to simulate any reasonable fraction of the events that occur during for example one year of expected data taking. Moreover, the bulk of these events origin from soft processes being well known. This is the reason, why simulations are often limited only to rare hard processes with high p_T final state particles. This limitation is also motivated by the searches for new particles and phenomena of new physics that that are expected for high masses and transverse momenta.

Proton collisions happening at the LHC are approximated in the simulation by elementary interaction of only one parton from each of two colliding protons. The result of two parton interaction is production of n hard fermions or bosons in the final state $(2 \rightarrow n$ processes$)$[1]. Simple $2 \rightarrow 1$ (e.g. $gg \rightarrow h$), $2 \rightarrow 2$ (e.g. $gg, q\bar{q} \rightarrow t\bar{t}$) and $2 \rightarrow 3$ (e.g. $gg, q\bar{q} \rightarrow t\bar{t}h$) processes can be generated in general-purpose Monte-Carlo (MC) generators, like for example PYTHIA and HERWIG. These programs are so-called parton-shower generators, *i.e.* besides generation of the hard process, they are

---

[1]examples of diagrams for various processes can be found in Sec. B.2

able to process further its results. They accordingly radiate secondary soft partons from primary partons (initial-state radiation (ISR) and final-state radiation (FSR)), perform fragmentation (also called hadronization, which is transition of the partons into observable particles) and eventually decay particles if this action is needed. Among more complicated 2→ n (n is less than 5-6, *e.g.* $gg \rightarrow t\bar{t}g$) processes, most commonly considered are 2→2 processes with additional generation-level jets (partons, *i.e.* gluons or light quarks) in the final state. They are called multi-jet processes. The 2→ n processes are attainable with the use of tree level matrix-element (ME) generators like CompHEP, MadGraph, AlpGen and others[1]. The ME generators automatically include all contributing parton-level subprocesses, calculate amplitudes including interference between subprocesses and generate events according to the desired phase space. As a result one obtains cross-section together with a set of 4-momenta for final states. Such event has subsequently to be processed by parton-shower generator.

Secondary partons (from ISR and FSR) are additions to simulated hard process and are usually calculated within parton-shower recipe. In this approach, one sums, in the collinear limit, the perturbative series of QCD $a \rightarrow bc$ branchings to all orders in the coupling constant. This procedure is hard-process independent. It is performed by backward evolution for ISR and the forward one for FSR. If radiations are switch-off, parton-shower part of generator is only responsible for showering of final state quarks and gluons. The result of showering are showers of partons that appear as groups of particles after hadronization. These groups will be called here clusters. They are defined as neighboring $\Delta\eta \times \Delta\phi$ cells with particle energy deposits. Throughout this work, UA1 clusterization algorithm [127, 128] is used as provided by PYTHIA routine `PYCELL` with configuration presented in Appendix C.3. Clusters are generation-level representatives of combining particle deposits in calorimeters reconstruction-level (or detector-level) jets (jets in classical meaning). Therefore, they are often in literature not distinguished and both referred to as jets. In this thesis it is put stress on terminological differentiation of these objects. The following terms will be used: generation-level jet, cluster, reconstruction-level jet. The term generation-level jet will be used for partons contributing to basic $2 \rightarrow n$ process. After showering they are reconstructed as clusters. When generated event is processed through detector simulation, generation-level jets and clusters appears (are reconstructed) as reconstruction-level jets.

It will be used CompHEP matrix-element and PYTHIA parton-shower generators. Event samples generated in CompHEP are processed with PYTHIA exactly in the same way as events generated in PYTHIA. This processing includes already mentioned showering and hadronization. Apart from a single parton-parton interaction

---

[1]generators are described and references to them are given in Ref. [126]

of protons, multiple interactions (MI) (also known as underlaying events (UE)), *i.e.* QCD interactions of remaining partons of the same pair of protons, are included as well. The model that is used for this purpose is described in Ref. [129] and references therein. The partons that do not interact are treated by the default PYTHIA beam remnant model. Another effect is overlapping of the events from different proton-proton collisions. This phenomenon is called pile-up (PU). It is taken into account at the digitization level of event processing (*cf.* Section 5.3). The distributions of incoming partons are obtained from CTEQ5L [130] set for both used generators. CompHEP and PYTHIA are leading-order (LO) generators. In order to include next-to-leading-order (NLO) corrections (virtual and soft QCD radiations), the cross-sections are multiplied by K-factors - ratios of the NLO cross-sections to the LO cross-sections. It is done for processes, for which K-factors are significantly different than 1.0, and of course if K-factors are available.

As generators the author used PYTHIA 6.2 [129] for Wj, $t\bar{t}$ and signal processes and CompHEP 4.2p1 [131, 132] for processes of W and $t\bar{t}$ production together with a given number of generation-level jets. Additionally, also PYTHIA 6.3 [133] with the new approach to parton-shower (p_T-ordered) was used. Cuts on p_T, η and on a separation between generated final state particles were applied to limit waste of central processing unit (CPU) time on events that surely will be rejected in the selection and as well to remove soft and collinear singularities that can appear in calculations. This is especially important for processes that were generated in CompHEP and have a very complicated kinematics due to 3-4 particles in the final state (*e.g.* $t\bar{t}j$, $t\bar{t}jj$, Wjj and $Wjjj$, where j stands for generation-level jet). High multiplicity of contributing subprocesses and limited phase space in generation make generation very CPU time demanding; therefore, they were mostly performed in parallel in the LHC Computing Grid [134] with the use of scripts specially written by the author. Configuration of the generators is described in Appendix C for PYTHIA and in Appendix F for CompHEP.

4.2 Experimental signal of the strongly-coupled sector

As was argued in preceding chapters, the new strong interaction at electroweak scale, that can be responsible for symmetry violation, influences mainly only the production and interactions of longitudinally polarized vector bosons (V_L). There are three general classes of high energy processes (potential signal processes) at hadron colliders, which involve interactions of strongly-coupled V_L bosons [15, 56, 135, 136]:

1. $q\bar{q}$ annihilation and gg fusion, *e.g.* $q\bar{q} \to V_L V_L$;

2. vector-boson fusion (VBF) also referred to as scattering, *i.e.* $V_L V_L \rightarrow V_L V_L$ process;

3. multiple V_L production.

Diagrams for them are presented in Figure 4.1.

(a) $q\bar{q} \rightarrow V_L V_L$ process is realized in leading-order (left) and in next-to-leading order by rescattering process (right).

(b) $gg \rightarrow V_L V_L$ fusion

(c) vector boson fusion

(d) multiple V_L production
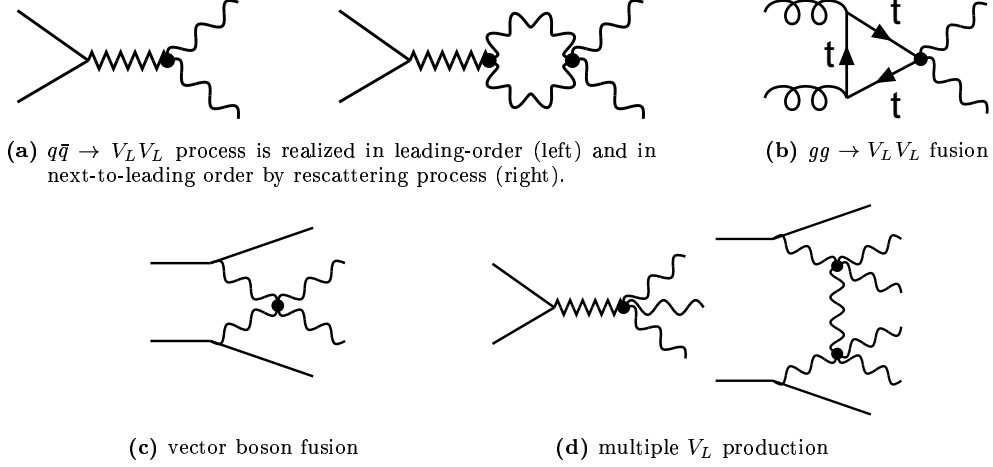
Figure 4.1: Hadron collider high energy signal processes of the strongly-coupled symmetry breaking sector. Diagrams represent the most important types of processes. Full dots denote the couplings influenced by the strongly-coupled sector dynamics. Wavy lines represent V_L's and zigzag ones V_T's.

The expected experimental signal of new strong interactions is in general enhanced cross-section for large invariant masses (around 1 TeV). The aim of this section is to select optimal (for experimental observation) signal process and corresponding event characteristics.

4.2.1 $q\bar{q}$ annihilation and gg fusion

Processes of $q\bar{q}$ annihilation and gg fusion are the two most important sources of $V_L V_L$ pairs at the LHC [39]. The $q\bar{q}$ annihilation is realized via anomalous trilinear and quartic EWChL couplings that lead to the processes illustrated in Fig. 4.1(a). Contribution from intermediate state of transversely polarized V boson (V_T) is leading since its coupling to incoming quarks dominate over coupling of V_L to quarks. The chiral Lagrangian next-to-leading contribution to the annihilation process (rescattering in the second picture in Fig. 4.1(a)) [39] can also be interpreted as mixing of virtual V_T with chiral vector resonance. Therefore, this contribution is suppressed with respect to the leading order process. Only vector resonances are accessible in $q\bar{q} \rightarrow V_L V_L$ annihilation. The most important background is standard $q\bar{q} \rightarrow VV$ process with $V_L V_T$ and

$V_T V_T$ pairs in the final state. It belongs to the background since it is mostly independent on signal strong interactions. Nevertheless, this process overwhelms the signal. Because the methods differentiating between longitudinally and transversely polarized gauge bosons are not efficient, the only chance is to look at $V_L V_L$ pairs of high invariant masses, where the impact of new strongly-coupled physics is more pronounced. Another background of importance similar to $q\bar{q} \to V_T V_T$ is gg fusion that goes through heavy quark loop and contribute to $W^+ W^-$ and ZZ channels [39]. Process of gg fusion could also contribute to the signal-like $V_L V_L$ final state [137] according to the diagram presented in Fig. 4.1(b), but it has not been much studied, yet.

4.2.2   Vector boson fusion

The vector-boson fusion (VBF) is realized in hadron colliders, when incoming quarks emit bosons that subsequently scatter on each other (Fig. 4.1(c)).

For practical reasons, the discussion of VBF will be limited to WW final state and its decay to $\mu\nu q\bar{q}$. In general the scattering goes through unknown part predicted by a particular model and represented by the oval in diagram in Figure 4.2(a). The Standard Model diagrams contributing to $VV \to WW$ scattering are shown in Figure B.1. In chiral Lagrangian language, there is only one term with quartic coupling. This scattering can be also considered as a subprocess of $pp \to WWjj$ class of processes. One can even define more general class that are $pp \to \mu\nu q\bar{q}jj$ processes, where $\mu\nu q\bar{q}$ final states represent four fermions that can be obtained from decays of two final-state vector bosons.

Therefore, the anomalies caused by the strongly-coupled sector can be searched for in the following classes of processes ($j = q, \bar{q}, g$):

1. vector boson scattering, *i.e.* $qq \to WWqq$ processes with ingredient process of boson fusion (scheme in Figure 4.2(a));

2. $jj \to WWjj$ processes (scheme in Figure 4.2(b));

3. $jj \to q\bar{q}\mu\nu jj$ processes (scheme in Figure 4.2(c)).

Exact contents of the ovals in Fig. 4.2 represent the parts that can be dependent on new physics, in particular on the strongly-coupled sector. Every class of processes in Fig. 4.2 is contained in the class that follows it. Moving from the simplest class of vector boson scattering (Fig. 4.2(a)) to the one with $jj \to WWjj$ process (Fig. 4.2(b)) quantum interference between VV scattering and non-scattering diagrams is included. Hence, the third class ($jj \to q\bar{q}\mu\nu jj$ process in Fig. 4.2(c)) is the closest to the real process; however, simultaneously conceptually the most complicated and CPU time consuming.

(a) The $jj \rightarrow q\bar{q}\mu\nu jj$ process going through model-dependent vector boson scattering $VV \rightarrow WW$.

(b) The $jj \rightarrow q\bar{q}\mu\nu jj$ process going through model-dependent $jj \rightarrow WWjj$ process.

(c) The most general model-dependent $jj \rightarrow q\bar{q}\mu\nu jj$ process.
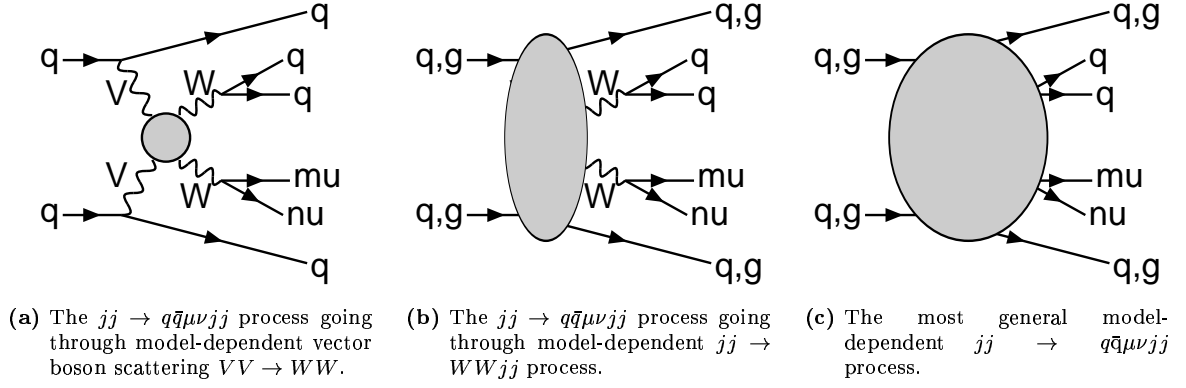
Figure 4.2: Schemes presenting three classes (from the least to the most general) of $jj \rightarrow q\bar{q}\mu\nu jj$ processes containing model dependent $VV \rightarrow WW$ scattering with subsequent $W \rightarrow q\bar{q}$ and $W \rightarrow \mu\nu$ decays.

4.2.3 Multiple V_L production

This process was considered as the signal of new strongly-coupled EWSB sector in fermion colliders in Ref. [15]. The examples are production of $2n$ longitudinally polarized gauge bosons in fusion process and production of $V_L V_L V_L$ in $q\bar{q}$ annihilation (Fig. 4.1(d)). Low production rate for the first and big background for the second process do not encourage to study such signatures.

4.2.4 Review of previous studies

The subject of 1-TeV scale strongly-coupled sector has been theoretically and phenomenologically studied in many papers; however, most of them are restricted to generation level. More realistic studies with showering of generated particles, or with artificially included detector effects are very rare.

Strongly coupled symmetry-breaking sector was initially studied in the case of massive Higgs boson [109, 138, 139, 140, 141, 142, 143, 144, 145, 146, 147, 148]. The techniques established then were later applied for studies on general strongly-coupled sector. They were initiated for experiments at eventually not built SSC proton collider (*e.g.* Refs. [15, 39, 149, 150]). Currently, they are performed for the LHC and for future linear lepton colliders; however, only hadron-collider studies will be reviewed here.

Most studies for the LHC use model-independent EWChL formalism. There are considered resonant scenarios using appropriate unitarization procedure [97, 110, 119, 120, 151] and non-resonant ones [39, 94, 95, 152, 153, 154]. The range of chiral parameters for resonant models that will be accessible at the LHC is estimated to be increased at least one order of magnitude in respect to presently attainable range from LEP [94, 95, 96, 153]. On the other hand, detection of non-resonant models will be very difficult [39, 136].

Non-EWChL approaches are mostly model-specific, but still mostly limited to models with resonances (technicolor, BESS model) [135, 155, 156, 157].

Most of the studies are focused on specific VV final states and their decay modes. Gold-plated (purely leptonic) decay modes of VV final states are used for moderate resonance and invariant VV masses. These modes are the most popular and the cleanest way of signal detection at hadron colliders since they can be identified and reconstructed with high efficiency, and the background is very small; however, the branching ratio is low. This case was considered phenomenologically for examples in Refs. [94, 95, 96, 120, 158, 159, 160]. Like-sign $W^\pm W^\pm$ pair production with leptonic decays was considered phenomenologically in Refs. [120, 158, 160, 161, 162, 163, 164, 165]. With the use of this channel, non-resonant models can be tested.

Silver-plated (semileptonic, $V_1 \to hadrons$, $V_2 \to leptons$) decay modes of final VV states have much higher branching ratios. Thus, this channel, in analogy to heavy Higgs boson case, is especially applicable to high resonant and invariant masses. It is expected to improve the observability of very heavy scalar and vector resonances; however, phenomenological studies are rather rare [97] in contrast to frequently studied case with leptonic decays. This final state configuration is an object of much higher QCD background that should be carefully quantified with inclusion of detector reconstruction effects. Additionally, since this background has been only estimated with the use of simple $2 \to 2$ processes up to now, it is expected that current background level is undervalued and signal observability overestimated.

Most studies, especially recently, regard scattering process as an optimal experimental signal of the strongly-coupled sector. Initially, it was used in the context of Higgs production, but is also commonly studied process within EWChL approach. The VBF is usually considered using approximations[1]: effective-W approximation and ET. All other $jj \to jjVV$ $(j = q, \bar{q})$ processes of the same final state are separately treated as background. The first exact tree level calculations of generalized $jj \to jjVV$ signal processes including EWChL vertices were performed in Ref. [95]; however, this study does not consider resonances of the strongly-coupled sector. Consideration of the full even more general $jj \to q\bar{q}\mu\nu jj$ set of processes has been possible since recent appearance of the new 6-fermion PHASE generator [166, 167]. It includes interference of signal $jj \to W^+W^- jj$, $W^+W^- \to q\bar{q}l\nu$ process dependent on EWSB with all other processes leading to $qqql\nu$ final state. This program does not include gluons as initial states and is restricted only to the case of standard Higgs boson. Therefore, PHASE can not be used for the study of the strongly-coupled generalized Higgs sector.

---

[1]to be further discussed in Sec. 4.2.5.1

The $q\bar{q}$ annihilation being second popular signal process is regarded as complementary in probing the EWSB mechanism [154].

First experimental prospects for discovering EWSB strongly-coupled sector at the LHC appeared in Ref. [168] and were later presented for individual detectors in Refs. [169, 170, 171] and [152, 172] for the ATLAS and the CMS detectors, respectively. The cases of standard heavy Higgs boson and general higgs-less EWChL approach were considered. These studies were based on simplified detector simulations and considered obsolete background estimation. Only very recently appeared publications that more precisely took into account detector effects, but the background is still underestimated therein (*e.g.* Refs. [97, 173, 174]).

Recent phenomenological and experimental review, however with old results, can be found in Ref. [136].

4.2.5 Vector boson fusion as the signal process for this work

The $V_L V_L$ pair production through $q\bar{q}$ annihilation dominates over the other signal processes for low energies. It decreases much with the increase of $V_L V_L$ invariant mass, and the VBF appears as a very important process [15, 96]. The VBF is also much more useful production process since it can lead to all $V_L V_L$ final states, whereas $q\bar{q}$ annihilation contributes only to $W_L^+ W_L^-$ and $W_L^\pm Z_L$ channels. Furthermore, the VBF gives access to all three isospin $I = 0, 1, 2$ channels of $V_L V_L$ scattering and corresponding resonances, while $q\bar{q}$ annihilation is restricted only to $I = 1$ and vector resonances[1]. Thus, scattering is much more convenient process for looking for strongly-coupled V_L sector. Distinction of the VBF signal events from that happening through $q\bar{q}$ annihilation is possible either by requirement of two additional quark/jets in the final state or by exclusive study of $W^\pm W^\pm$ and ZZ final states that receive no contribution from the $q\bar{q}$ initial state. It is also expected that the background to $q\bar{q}$ annihilation is higher than that for VBF process.

All these reasons motivate the choice of the boson fusion for a study signal process in this thesis. Since this work is one of the first attempts to use detailed detector simulation and event reconstruction, such simple process is especially appreciated. More complicated signal $VVjj$ and $ffffjj$ production processes[2] being generalizations of VBF are left for future studies. Instead, the part of $jj \to VVjj$ process that is not sensitive to strong interactions in symmetry breaking sector will be separately discussed here as part of the background. This study is limited to WW pair final state (without any additional requirement on W charge combinations) with its subsequent decay to

---

[1] due to angular momentum $J = 1$ of V_T intermediate state
[2] f denotes fermion

$\mu\nu q\bar{q}$ state. The initial states are not restricted; however, it is known that the cross-section is dominated by channels with initial W's [135]. Similar choice of the final state, motivated by the largest branching ratio for $H \rightarrow WW$ and the moderate one for $WW \rightarrow \mu\nu q\bar{q}$, is made for studies on standard heavy Higgs boson case. This channel is one of the most important ones in searches with $M_H \gtrsim 600$ GeV [152, 171]. It is expected that the signal in WW final state will be also the strongest for models with the strongly-coupled sector [15].

4.2.5.1 Generation methods for vector boson fusion

Monte-Carlo generation of scattering events is usually divided into two conceptual parts. In the first part colliding particles (protons) emit vector bosons, and in the second part these bosons scatter on each other.

Spectra of initially emitted longitudinally polarized bosons are obtained with the use of effective-W approximation (EWA) [175, 176, 177]. Application of EWA to heavy Higgs boson case has been proved valid in Ref. [178], so it should still be valid for the strongly-coupled sector. The EWA works quite well with respect to matrix-element calculations for hard and central bosons [95, 179, 180]. As these requirements will be fulfilled in the event selection, this approximation is allowed for usage here.

Scattering of longitudinally polarized bosons is calculated with the use of equivalence theorem (ET) that was already mentioned in Sec. 2.2. This theorem says that at high energies (*i.e.* $\sqrt{s} \gg M_W$) scattering amplitudes can be identified with corresponding amplitudes for the underlying symmetry breaking sector. Since the ET is connected with symmetry-breaking sector, details of its application depend on the way, in which this sector is realized: whether it is linear (as for the SM with Higgs boson) or non-linear (as here for the EWChL). Formal proof of the ET applicability for the SM is presented in Ref. [15, 30, 181]. The ET has been initially proved in tree approximation [13], but later shown to be correct also to all orders in gauge interactions (g and g') and in interactions of the symmetry breaking sector (λ) [15, 30, 48, 181]. The validity to all orders in λ is crucial since theory is strongly interacting. Later on, there were found numerous problems connected with the usage of ET in processes with Higgs boson [120, 182, 183]. Special treatments and application of according K-factors are additionally required. K-factors are also needed for application of ET to calculations within EWChL [184, 185, 186]. Additionally, the EWChL must be in high-energy regime complemented with procedure ensuring unitarity (*e.g.* unitarization) [94, 182, 187].

Even though the ET approach needs slight modifications, it greatly simplifies perturbative calculations for heavy and strongly-coupled Higgs sector. For instance $V_L V_L \rightarrow V_L V_L$

requires inclusion of all leading and non-leading order diagrams, that alone have bad high-energy behavior, to finally obtain well-behaved full amplitude. On the other hand, the leading order is enough for calculations within ET because single diagrams have correct high-energy behavior, and there are no cancellations here.

Because of above mentioned limitations, simplifications and needs for corrections, the results of EWA and ET application should be (and will be later on in this thesis) cross-checked with strict (ME) calculations.

4.2.5.2 Generation process for vector boson fusion

Since scattering is effectively $2 \to 2$ process, it is attainable in PYTHIA. The EWChL amplitudes are calculated with the use of accordingly modified code responsible for $V_L V_L$ scattering within QCD-like and Higgs-like models [119][1]. After these changes amplitudes become dependent on two chiral parameters a_4 and a_5. These modifications were kindly provided by the authors of Ref. [97]. Only the $V_L V_L \to W_L W_L$ channel was taken into account.

Such obtained EWChL generator can be validated in comparison of scalar models (strongly-coupled sector with scalar resonances) with the Standard Model. The latter is treated as a prototype for models with strong VV scattering even though Standard Model with $M_H \gtrsim 800$ GeV is theoretically forbidden.

Results for $V_L V_L \to W_L^+ W_L^-$ process with scalar resonance within EWChL are compared with those for Standard Model $qq \to qqh, h \to W^+ W^-$ Higgs boson production[2] and with those for Standard Model $V_L V_L \to W_L^+ W_L^-$ process with- and without inclusion of Higgs boson. Obtained $W^+ W^-$ invariant mass distributions are shown in Figure 4.3 for 890 GeV [3] common mass of EWChL scalar resonance (model S4 [4] within EWChL) and the Higgs boson. Resonant peak are naturally very broad. Because of folding differential cross-section for VV scattering with falling-down p_L-spectrum of proton quarks, smaller invariant masses are preferred. The peaks in the distributions are thus positioned slightly at lower invariant masses than the theoretical mass of the resonance[5].

Within the limits on accuracy given in Ref. [129], there is approximate consistency between distributions of $M(W^+ W^-)$ for $V_L V_L \to W_L^+ W_L^-$ scattering within SM with Higgs boson and the one obtained for EWChL with scalar resonance. The peak is wider for SM sample, but this is in accordance with the expectations on the widths in

---

[1] in PYTHIA PYSIGH routine
[2] PYTHIA processes 123 and 124
[3] distribution for two additional masses can be found in Fig. E.5
[4] details of this signal event sample will be given in Section 6.1.1
[5] This is true both for SM $qq \to qqh, h \to W^+ W^-$ and for EWChL $V_L V_L \to W_L^+ W_L^-$ processes.

Eqs. (3.31) and (3.30). Additionally, it can be seen in Fig. 4.3 that $M(W^+W^-)$ distribution for SM $V_LV_L \rightarrow W_L^+W_L^-$ process can be approximated by the sum of distributions for SM $V_LV_L \rightarrow W_L^+W_L^-$ without the Higgs boson and for SM $qq \rightarrow qqh, h \rightarrow W^+W^-$ process. Therefore, limitation only to $V_LV_L \rightarrow V_LV_L$ amplitudes in this region of invariant masses is sufficiently enough, *i.e.* one does not need to include processes with vector bosons of the other helicities.
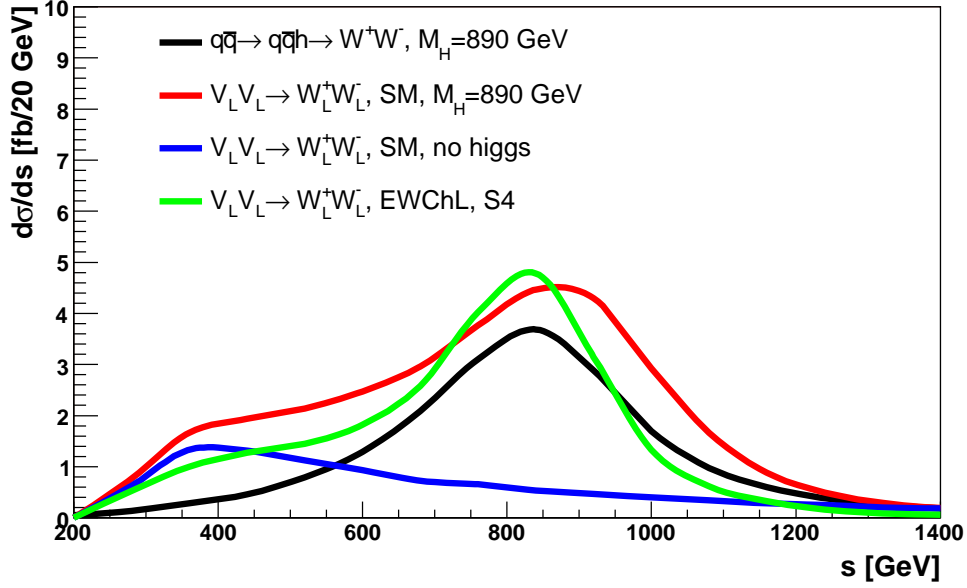
Figure 4.3: Invariant mass distribution for $V_LV_L \rightarrow W_L^+W_L^-$ scattering system simulated within various models with scalar resonance (S4 scalar resonance model within EWChL) or within the SM with M_H=890 GeV. Distributions: black - SM Higgs boson production in VBF ($qq \rightarrow qqh$ PYTHIA processes with $h \rightarrow W^+W^-$), red - $V_LV_L \rightarrow W_L^+W_L^-$ scattering within SM, blue - $V_LV_L \rightarrow W_L^+W_L^-$ scattering within SM without diagrams containing Higgs boson, green - $V_LV_L \rightarrow W_L^+W_L^-$ scattering within EWChL. Distributions are normalized to 100 fb^{-1} of integrated luminosity. Distributions for additional two signal models are presented in Figure E.5.

Distributions in Figure 4.3 allows to believe that EWChL scalar models (Higgs-like) are approximately generated in a correct way. Doubts are caused by applied simplifications in the generator (incoming W/Z bosons being on mass shell, EWA and ET) and also by the width of the resonance that is determined by the nominal resonant mass. Only in PYTHIA $qq \rightarrow qqh$ process, the Breit-Wigner resonances contain a mass-dependent width and higher-order corrections are treated more accurately.

4.2.5.3 Signal vector boson fusion characteristics

The characteristics of the expected experimental signal for $V_LV_L \rightarrow W_LW_L, W_LW_L \rightarrow q\bar{q}l\nu$ scattering within EWChL is discussed here with the use of S1, S4 and S6 scalar

models[1]. Characteristic parton-level observables are the following (their distributions can be found in Appendix E):

- p_T and η for W bosons (Figs. E.1(a) and E.1(b)),

- ΔR separation between W boson decay products (Fig. E.2(c)),

- p_T and η for W boson decay products (Figs. E.2(a) and E.2(b)),

- angular separation between W bosons (Fig. E.1(c)),

- resonant behavior in WW invariant mass (Fig. E.1(d)).

- p_T, E and η for tagging jets (Fig. E.4),

- p_T of the system composed of W bosons and tagging quarks (Fig. E.3).

Hard scattering of V bosons (formation of a heavy resonance) has its consequences on final-state W bosons. Bosons are characterized by large values of transverse momenta (Fig. E.1(a)) and are mostly proceeded in the central region (Figs. E.1(b) and E.4(b)). Boosted W bosons make their decay products (quarks and μ, ν) also boosted: escaping hard neutrino gives rise to large missing transverse energy (MET), and hard central muon is observed (Fig. E.2(a)). Decay products from the same W boson go close to each other (separation by $\Delta R{<}0.8$ for from 55% of the events in models with light resonance (S6) to 85% in models with heavy resonance (S4, S1)) (Fig. E.2(c)). This separation is not small enough to justify the assumption that undetected ν goes parallel to measured lepton. The ΔR is, however, small enough for reconstruction of hadronically decaying W with the use of a single jet. Quite large fraction of $q\bar{q}$ pairs produce a single cluster.

Both W bosons are hard, but transverse momentum of $W_L W_L$ system is small. This is a result of very low p_T of initial longitudinally polarized bosons[2]. Typically, $p_T(WW)$ is not much larger than M_W. As a result two final W_L's are very back-to-back in the transverse plane (Fig. E.1(c)). Such self-oriented and hard bosons make system of high invariant mass with resonant behavior for resonant models (Fig. E.1(d)).

The other characteristic signature of VV scattering are two quarks (jets) in forward regions (Figure E.4(b)). They are called tagging (spectator) quarks (jets). They have transverse momentum exactly equal to that of initial V bosons. It is of the order of M_W with distribution that does not peak near zero because emitted boson are massive (Fig. E.4(a)). Each jet has substantial energy (longitudinal momentum) of the order of 1 TeV (Fig. E.4(c)).

---

[1] details on generated signal event samples will be given in Section 6.1.1

[2] According to EWA the p_T-spectrum of V_L's behaves like $1/(p_T^2 + M_W^2)^2$

Two final-state W bosons and two tagging quarks make the whole final state of the scattering process. Since colliding quarks are collinear, the $\mathsf{p_T}(WWjj)$ transverse momentum should be small. This feature is not destroyed by radiation as can be seen in Fig. E.3. Similar behavior can be expected to be observed for reconstructed objects.

Summarizing, signal signature is characterized by at least 3 high $\mathsf{p_T}$ ($\mathsf{E_T}$) jets (at least one central very hard and two forward ones), one high $\mathsf{p_T}$ muon and large MET. These features will allow for efficient background reduction (see Chapter 6). The signal scattering processes are as well characterized by low LHC cross-sections (*cf.* Tab. 3.1). This causes that integrated luminosities of the order of at least 100 fb^{-1} are necessary. The high luminosity LHC runs (100 fb^{-1} of integrated luminosity per year) will thus provide the best detector conditions.

4.3   Background processes

Having defined signal process and its signature, one can determine corresponding background processes.

The candidates for background processes should contain W bosons. The examples are W, WW and $t\bar{t}$ inclusive productions, where in the latter case W bosons originate from top quark decays. Additionally, one could also consider the production of Z boson since $Z \to q\bar{q}$ can easily fake W$\to q\bar{q}$ if di-jet mass resolution is weak. Generally, hadronic W boson could even be faked by any energetic hadronic activity providing cross-section is large enough and invariant mass of 1 or 2 reconstructed jets is close to M_W. If leptonic W is concerned, $Z \to \mu^+\mu^-$ is less likely to imitate $W \to \mu\nu$ since because of Z boson boost most often both muons are simultaneously beyond or within the acceptance of the muon system ($|\eta| < 2.4$). The $Z \to \mu^+\mu^-$ can thus imitate $W \to \mu\nu$ only when it is close $|\eta| = 2.4$, what is disfavored because Z are mostly central. Generally, the muon that comes from W decay is very hard and isolated and can hardly be mimicked by other phenomena. Therefore, at least one W boson is mandatory in background process signature.

W bosons in background processes differ from final state W bosons in signal processes. Namely, at least one of the final W's produced in the background processes is transversely polarized [120], whereas both bosons are of helicity 0 in signal processes. Only in the case of background with top quark, contamination of longitudinally polarized W bosons is significant. This difference in helicity is not facilitated in current stage of this analysis.

The background processes, expected to be the most important, are the following (as before V stands for the vector boson):

1. 2→2 processes: production of VV, $t\bar{t}$ and Wj

2. real higher order QCD corrections to 2→2 processes: $Wj + (n-1) - jets$ and $t\bar{t} + n - jets$

3. $VVjj$ production processes

4. other processes: production of V+X and $t\bar{t}$+X, where X = V, W, b.

These processes are discussed in following subsections.

4.3.1   VV (VVj) production

Simple process of VV production is a subject of non-negligible NLO corrections. Consideration of these corrections by a simple rescaling is risky because necessary K-factor changes much with $\mathsf{p_T}$ of VV pair [136]. Therefore, it is better to consider VVj production instead. The VVj event sample should thus be treated as basic in inclusive VV class of background. However, VVj event signature does not provide a parton-level candidate for the second tagging jet. The probability for generating such high $\mathsf{p_T}$ candidate by parton-shower is very low and drops down with transverse momentum. The cross-section also falls very rapidly with increasing di-boson mass [15]. Therefore, VVj background process can be neglected, and will not be considered in this thesis at all.

4.3.2 $t\bar{t}$ production

Production of $t\bar{t}$ pairs[1] that goes through:

$$q\bar{q}, gg \rightarrow t\bar{t} \tag{4.1}$$

basic processes[2], is the serious background because of its large cross-section and final state (two real W bosons and bottom quark jets) that can mimic the signal signature. Hadronic activity from the b-jets is mostly in the central region. This feature can be used for reduction of this background by vetoing events with extra central hadronic activity. As a result, the weight of the events with b-jets in forward regions is increased. The other source of fake tagging jets can be radiation from initial and final states (ISR and FSR).

Event samples of $t\bar{t}$ production can be generated in both CompHEP and PYTHIA. The generation-level cut on top quark $\mathsf{p_T}$ ($\hat{\mathsf{p}}_\perp$ in the case of PYTHIA) was used in order to increase selection efficiency. The generated event samples are thus biased.

---

[1] Production of $t\bar{t}$ pair at the LHC is reviewed in Ref. [188]

[2] contributing diagrams are presented in Fig. B.2

Nevertheless, inclusion of NLO corrections is made with K=1.8 [188, 189] factor that is usually used for non-biased event samples.

4.3.3 $V + jet$ production

Production of electroweak boson together with a single hard gluon or light quark (parton-level jet)[1]:

$$qq,\ qg\ \rightarrow\ Wg,\ Wq\,,\qquad\qquad(4.2)$$

and denoted as Wj, is the first order real QCD correction to a single W production, but dominate the latter as a source of high-p_T jets.

The cross-section for Wj production is huge at the LHC (σ(Wj, W$\rightarrow \mu\nu$)=2880 pb at LO [190]). Therefore, though only one hard jet is guaranteed in the final state, this process can be an important source of background. This background is important only if W boson decays to $\mu\nu$ pair. Necessary jet activity to fake signal signature is expected to be caused by remains of parton-level jet, QCD radiation (ISR and FSR) and pile-up.

Generation of Wj process can be performed in both PYTHIA and CompHEP. The most important generation-level cut is symmetric requirement of p_T>100 GeV for W boson and a jet ($\hat{p}_\perp$>100 GeV in PYTHIA). This cut increases generation and selection efficiency. Additionally, the $W \rightarrow \mu\nu_\mu$ decay channel is forced.
The NLO corrections in the form of K-factors are available and equal 1.13 and 1.16 respectively for W^+j and W^-j [190]. Nevertheless, they are not applied here because are not significantly greater than 1.0 and because they were obtained for a very different phase space.

4.3.4 Processes with real higher order corrections (production of $Wj + (n-1) - jets$ and $t\bar{t}+n-jets$)

Most studies on the strongly-coupled sector (*e.g.* Refs. [97, 171, 173, 174]) take into account background limited only to $2 \rightarrow 2$ simple processes. Necessary extra hadronic activity has thus to be provided by parton-shower generator. However, comparison with ME generator results suggest that such procedure (with parton-shower in PYTHIA 6.2 and earlier versions) underestimates the rate of clusters with high transverse momenta [191, 192]. For clarification of this problem, specially generated event samples of final state signatures with additional jets have been considered.

Typical signal event signature consists of at least 3 hard detector-level jets. Hence, real higher order QCD corrections (processes with additional parton(s) in final state)

---

[1]contributing diagrams are presented in Fig. B.5

(a) $t\bar{t}+n-jets$ cross-sections.

(b) $W^-j+(n-1)-jets$ cross-sections.
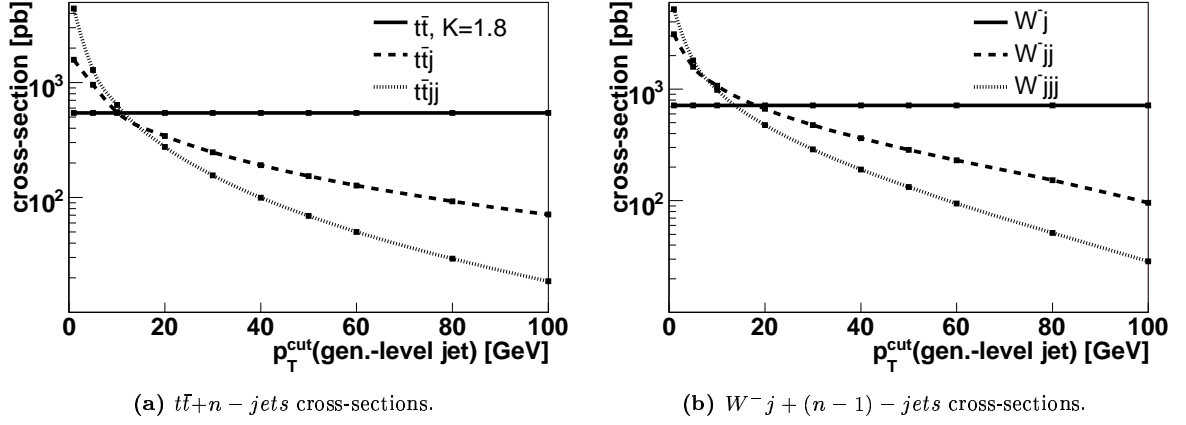
Figure 4.4: The LHC cross-sections for $t\bar{t}+n-jets$ and $Wj^-+(n-1)-jets$ event samples as a function of p_T cut on generation-level jets. Cross-section for $t\bar{t}$ event sample is multiplied by $K=1.8$ factor. CompHEP generator cuts are presented in App. G.

to $2 \rightarrow 2$ processes can be a very important source of background. The following, multi-jet, processes are taken into account:

1. $t\bar{t}+n-jets$ [193],

2. $Wj+(n-1)-jets$,

where $n = 1, 2, 3$. Example diagrams for these processes are presented in Figures B.3, B.4, B.6 and B.7. Real higher order corrections to the other $2 \rightarrow 2$ processes are not taken into account because cross-sections for these $2 \rightarrow 2$ processes are much lower than the cross-sections for Wj and $t\bar{t}$ production.

Events were generated using CompHEP. The NLO corrections exist only for W^+jj and W^-jj production in the form of K-factors that equal 0.87 and 0.88, respectively [190]. For the rest of multi-jet samples, they are not available yet, but one can expect on the basis of preliminary results [194] that they will not be significantly different from 1.0. This enables neglecting NLO corrections to all multi-jet samples in this thesis.

Event samples with additional jets[1] can be even more important source of background than basic $t\bar{t}$ and Wj processes. The first reason is the cross-section that at the LHC energies will not decrease so much with the jet multiplicity [189]. The explanation is available c.m.s. energy, which is large enough to produce extra jets with high transverse momentum and much increased number of contributing diagrams. For example for a fixed $p_T=40$ GeV cut on jet transverse momentum, ratios of cross-sections for $t\bar{t}$, $t\bar{t}j$ and $t\bar{t}jj$ exclusive processes are about $1{:}\frac{1}{2}{:}\frac{1}{3}$ and for W^-j, W^-jj and W^-jjj close to $1{:}\frac{1}{2}{:}\frac{1}{4}$. This is illustrated in Figure 4.4, where the cross-section dependence on

---

[1]The term jet, unless clearly specified, will mean in this subsection generation-level jet (parton).

(a) p_T-spectra of generation-level jets j and b quarks in $t\bar{t}$, $t\bar{t}j$ and $t\bar{t}jj$ event samples, respectively.

(b) η-spectra of generation-level jets j and b quarks in $t\bar{t}$, $t\bar{t}j$ and $t\bar{t}jj$ event samples, respectively.
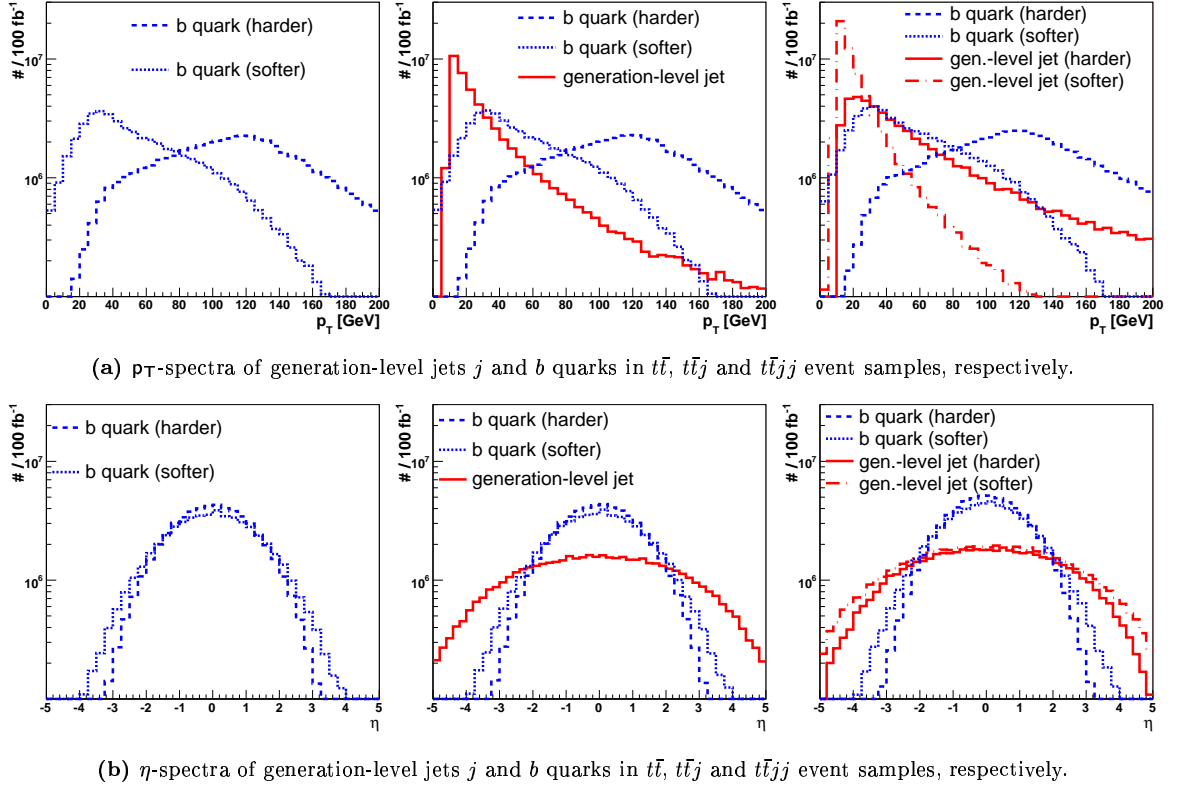
Figure 4.5: Transverse momentum p_T and pseudorapidity η spectra of generation-level jets j accompanying $t\bar{t}$ and two b quarks (harder and softer) originating from decays of top quarks in $t\bar{t}$, $t\bar{t}j$ and $t\bar{t}jj$ event samples. CompHEP generator cuts are presented in App. G. Distributions are normalized to integrated luminosity of 100 fb^{-1}.

the (generation-level) jet p_T cut is shown for $t\bar{t}+n-jets$ and $W^-j+n-jets$ samples. Quoted ratios are much different from $1{:}\frac{\alpha_s}{\pi}{:}(\frac{\alpha_s}{\pi})^2$ ratio that could be naively expected.

The second reason for importance of multi-jet processes is their kinematics. Among additional n generation-level jets in $t\bar{t}+n-jets$ event samples can be found better candidates for tagging jets than that originating from b quarks - top quark decay products. These b quarks are mostly seen in the central region of the detector (see Figure 4.5). On the other hand, whereas the hardest jet is supposed to fake hadronic W boson, the softer jets in $W^-j + (n-1) - jets$ samples are good candidates for tagging jets (see Figure 4.6).

However, in experiment one observes inclusive multi-jet events, *i.e.* events with $t\bar{t}$ and W signature and changing from event to event multiplicity of reconstruction-level jets. Having in mind that ISR and FSR are added in the step following generation, one can expect that even for a fixed number of generation-level jets, the obtained cluster multiplicity will also be variable. This is because clusters can originate from many sources: generation-level jets, ISR, FSR and fragmentation. An illustration can be found in Figure 4.7, where cluster multiplicity for individual $t\bar{t}+n-jets$ and
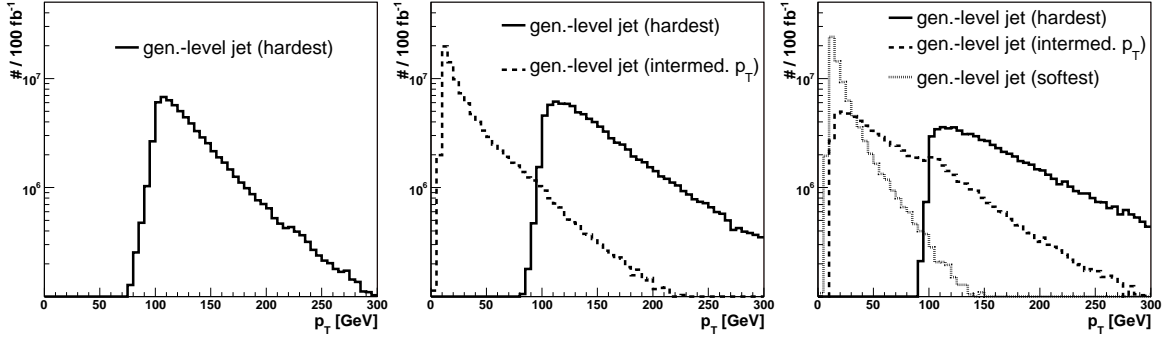
(a) p_T-spectra of generation-level jets j in $W^- j$, $W^- jj$ and $W^- jjj$ samples, respectively.
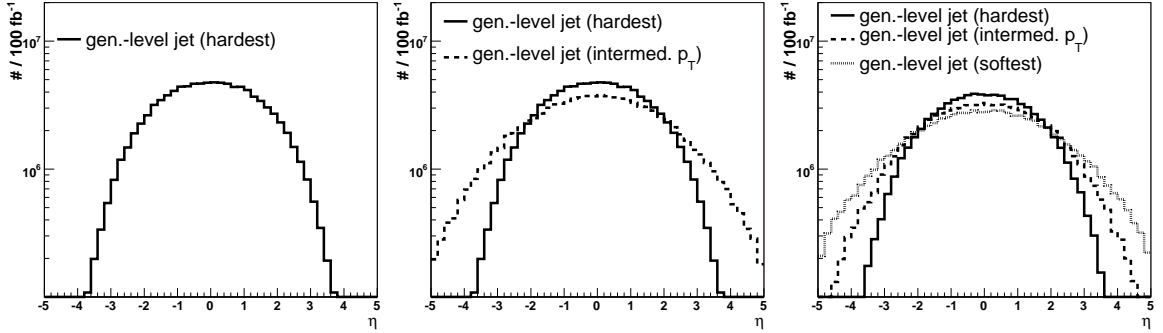
(b) η-spectra of generation-level jets j in $W^- j$, $W^- jj$ and $W^- jjj$ samples, respectively.

Figure 4.6: Transverse momentum p_T and pseudorapidity η spectra of generation-level jets accompanying W^- in $W^- j + (n - 1) - jets$ background samples. CompHEP generator cuts are presented in App. G. The most important cut is $p_T > 100$ GeV requirement on the hardest generation-level jet, which consequences are easily visible in pictures in (a). Distributions are normalized to integrated luminosity of 100 fb^{-1}.

$W^- j + (n - 1) - jets$ samples are presented with- and without addition of ISR and FSR. For the reason of limiting CPU time needed for computation, these distributions and the remaining results in this section were done at parton level, after showering but before fragmentation[1]. Clusterization takes thus into account only showered generation-level jets and ISR/FSR partons (see schemes in Figure 4.8).

Multiplicities of clusters with radiation turned off most often correspond to multiplicities of generated jets as is shown in Figures 4.7(a) and 4.7(b). It means that generation-level jets (with $p_T^{cut}(\text{jet}) > 10$ GeV cut) correspond to $p_T > 10$ GeV clusters.

The remaining pictures in Fig. 4.7 were done with ISR and FSR turned on. It is evident that given jet multiplicity n does not necessary result in cluster multiplicity equal to n. Thus, there are n possibilities of multi-cluster $t\bar{t}$ and W processes generations with the use of various $t\bar{t}+n - jets$ and $W^- j + (n - 1) - jets$ event samples, respectively. It can be interpreted as the overlap of exclusive samples with different generated jet multiplicity n. This overlapping is not an accident, but it is a result

---

[1] fragmentation was switched off in PYTHIA
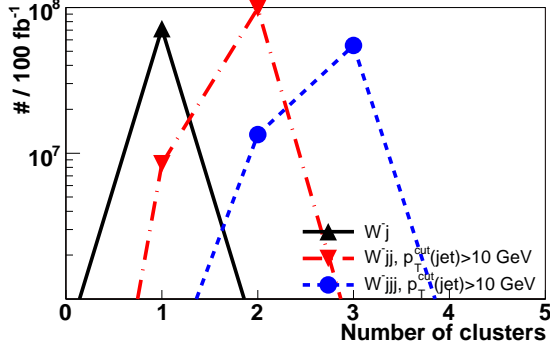
(a) Cluster multiplicities in $W^- j + (n-1) - jets$ event samples (cluster $p_T > 10$ GeV cut) without initial- and final-state radiation.
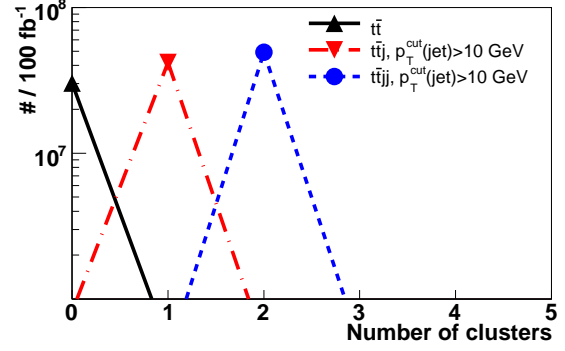
(b) Cluster multiplicities in $t\bar{t} + n - jets$ event samples (cluster $p_T > 10$ GeV cut) without initial- and final-state radiation.
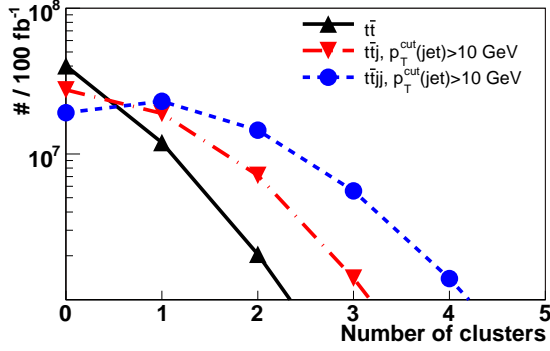
(c) Cluster multiplicities in $t\bar{t} + n - jets$ event samples (cluster $p_T > 40$ GeV cut) with initial- and final-state radiation.
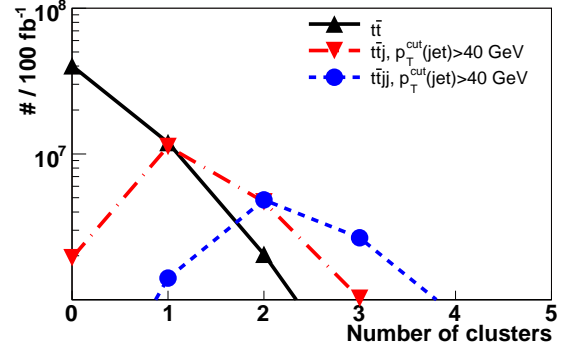
(d) Cluster multiplicities in $t\bar{t} + n - jets$ event samples (cluster $p_T > 40$ GeV cut) with initial- and final-state radiation.
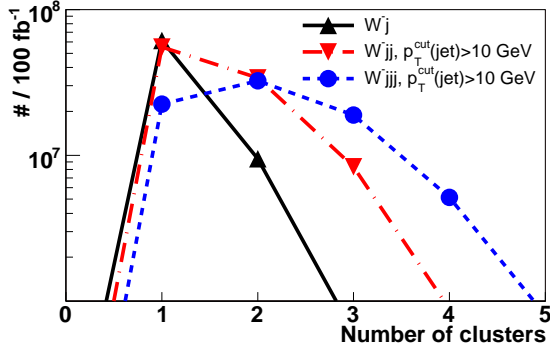
(e) Cluster multiplicities in $W^- j + (n-1) - jets$ event samples (cluster $p_T > 40$ GeV cut) with initial- and final-state radiation.
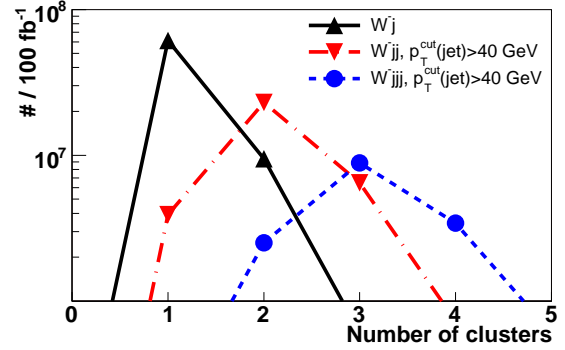
(f) Cluster multiplicities in $W^- j + (n-1) - jets$ event samples (cluster $p_T > 40$ GeV cut) with initial- and final-state radiation.

Figure 4.7: Cluster multiplicity distributions in $t\bar{t} + n - jets$ and $W^- j + (n - 1) - jets$ event samples with- and without initial- and final-state radiation. Clusterization considers partons according to Fig. 4.8 (W's and tops are not included), and cluster should fulfill certain p_T cut. Samples were generated in CompHEP with cuts listed in App. G. The cuts on p_T of generation-level jets ($p_T^{cut}(jet)$) are indicated in the figures. For $W^- j + (n - 1) - jets$ event samples, the hardest generation-level jet has always $p_T > 100$ GeV. Distribution are normalized to integrated luminosity of 100 fb^{-1}.

(a) $t\bar{t}+n-jets$ samples   **(b)** $W^- + (n-1) - jets$ samples
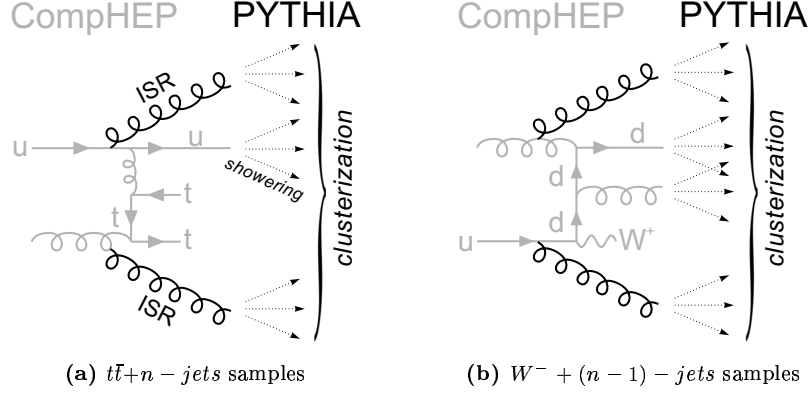
Figure 4.8: Schemes presenting the range of particles that are considered by clusterization procedure for the studies in this chapter. The process generated in CompHEP is in grey. The part performed in PYTHIA like radiation and showering of particle (excluding W bosons and t quarks) is illustrated in black. Only products of showering are clustered.

of obtaining extra clusters with the use of either radiation realized by parton-shower or extra generation-level jets generated in ME generator. Overlap may be, however, reduced if appropriate jet p_T requirement is applied. It is shown in Figures 4.7(c) and 4.7(d). On both of these pictures, only p_T>40 GeV clusters are taken into account. In the first plot, $t\bar{t}j$ and $t\bar{t}jj$ samples were generated with p_T>10 GeV requirement on jets. If this cut is increased to p_T>40 GeV, the rates for cluster multiplicities lower than jet multiplicities are much reduced (Fig. 4.7(d)). With p_T>40 GeV jet cut, the bins with the highest cluster rate correspond to the number of generated jets n. Nevertheless, the overlap between multi-jet samples is reduced only a little because $t\bar{t}$ sample still posses the same rate as $t\bar{t}j$ for $N_{cluster}$=1, and $t\bar{t}j$ sample has similar to $t\bar{t}jj$ rate for $N_{cluster}$=2. The observations for $W^-j + (n-1) - jets$ event samples (Figs. 4.7(e) and 4.7(f)) are very similar.

Summarizing, increasing the jet p_T cut will not prevent from double-counting of events if multi-jet event samples are considered together in background estimation. Even if it was possible to limit overlap between samples in this way, such obtained background would be biased and not applicable to this study. This is because soft clusters would not be produced by generation-level jets, and clusters even as soft as about 40 GeV in transverse momentum are important here because of the tagging quark spectrum in signal events (*cf.* Fig. E.4(a)).

Multi-jet inclusive background has thus to be generated in a special way that will be discussed in dedicated Section 4.3.7.

4.3.5 $VVjj$ production

The $VVjj$ production includes processes that can not be realized by showering or QCD radiation in VVj process, *e.g.* VV scattering. For this reason $VVjj$ production should be considered separately.

The most important $pp \to VVjj$ background process is $WWjj$ production. Exactly the same final state as for the searched signal makes this process irreducible background. Two other $VVjj$ production processes, $ZZjj$ and $ZWjj$, are not considered here since they are of much lower cross-section than $WWjj$ production and because of anticipated requirement of exactly one central and hard muon in the event selection.

The signal process is also $pp \to WWjj$ production, but with intrinsic $V_L V_L \to W_L W_L$ scattering. Therefore, only scatterings with at least one transversely polarized boson ($V_T V_L \to W_L W_L$, ...) and all subprocesses contributing to $pp \to W_T W_T jj$, $pp \to W_T W_L jj$ and to non-scattering $pp \to W_L W_L jj$ subprocesses[1] belong to the background. These processes are independent on strong interactions in the symmetry breaking sector.

There are differences between $V_L V_L \to W_L W_L$ signal and $pp \to WWjj$ background processes that enable discrimination between them. Since the amplitude for scattering grows faster with energy for more longitudinally polarized bosons in external lines [39], one can ignore in high energy limit the scatterings with $W_T W_T$ and $W_L W_T$ final states. This conclusion is not automatically correct for initial (radiated from colliding fermions) $V_T V_T$ and $V_L V_T$ states. The reason is negligible longitudinal boson coupling to light quarks in high energy limit (see Tab. 2.1), which consequence is much larger luminosity for transverse than for longitudinal initial bosons [15]. Nevertheless, requirement of large VV invariant masses gives preference to forward emission of initial bosons that is more likely for longitudinal bosons. The net result is that $V_L V_L \to W_L W_L$ scatterings have the biggest contribution to $\sigma(qq \to qqWW \to qqH)$ process with heavy Higgs boson [15]. Thus, consideration of scattering exclusively with longitudinally polarized bosons is a good approximation of the whole VBF process in the high-energy regime. The same conclusion for the strongly-coupled sector in Ref. [39] has been reached within EWChL language without resonances; however, should be also valid for resonant case in analogy to the SM with heavy Higgs boson. Indeed, for heavy Higgs boson the scattering amplitude in high energy limit is in resonant region totally dominated by $V_L V_L \to V_L V_L$ scattering [195]. Neglecting non-$V_L V_L \to V_L V_L$ scattering processes does not introduce additional error since is also supported by the event selection that favors

---

[1] non-scattering $pp \to W_L W_L jj$ subprocesses that go through emission of final W's from quark lines are negligible due to weak coupling of V_L to the quarks

scatterings with initial V_L's. The p_T spectra of initial transversely and longitudinally polarized bosons (emitted from quarks) are different. The V_T's are harder (spectrum goes like $p_T^2/(p_T^2 + M_W^2)^2)$[1]; therefore, transverse momentum of WW system is higher for $W_T W_T$ ($W_T W_L$) initial states. As a result tagging jets are harder and more central for this case. This behavior is employed in the selection in Section 6.3.

Scattering processes are only a part of $WWjj$ background. The $WWjj$ processes are commonly divided into two classes: processes with weak bosons as intermediate states (EW class) and processes with exchanges of gluons and quarks between initial states (QCD class) [148, 196]. Diagrams with Higgs boson appearing in the scattering are of EW type and play a special role, *i.e.* they guarantee unitarity in amplitudes for high WW invariant masses. Therefore, these diagrams can not be omitted. Common approach is including them in the EW class with very low Higgs boson mass [148]. In this method, Higgs boson resonant peak is obtained in the region much below masses characteristic for the strongly-coupled sector, whereas continuum part of $WWjj$ being almost independent on M_H is retained. This way the conflict with scattering process with heavy resonance (strongly-coupled sector resonance or heavy Higgs boson) is avoided. Such defined EW $WWjj$ background is characterized by falling down spectrum of WW invariant mass [195]. Similar behavior is expected for QCD $WWjj$ production. These classes together will be titled continuum $WWjj$ production. If one is restricted to invariant masses close to heavy resonance peak, the total rate from $V_L V_L \rightarrow V_L V_L$ highly dominates continuum $WWjj$ background, and the total rate from $pp \rightarrow WWjj$ processes can very accurately be approximated by scattering of V_L's alone [195]. Outside the heavy resonance the situation reverses. Thus, it may be expected that interference between VBF ($V_L V_L \rightarrow W_L W_L$) and continuum $WWjj$ diagrams may be neglected, and the whole $WWjj$ production can be considered with these two samples generated separately. Conclusions for $WWjj$ background and signal $V_L V_L \rightarrow V_L V_L$ scattering within SM with heavy Higgs boson are expected to be also valid for the strongly-coupled sector case.

The continuum $WWjj$ background may be, however, completely neglected if low energy tail ($M(WW)$ masses lower than the mass of the resonance) is disfavored (*e.g.* in the event selection). The rate resulting from high energy tail of continuum $WWjj$ is low comparing to the rate in resonant peak [195]. This fact and earlier reasoning allows to neglect continuum $VVjj$ and also generally all non-$V_L V_L \rightarrow W_L W_L$ scattering background processes. The $V_L V_L \rightarrow W_L W_L$ scattering will be the only part of $WWjj$ production taken into account here and even treated as the signal process.

---

[1]compare with the spectrum for V_L's in Section 4.2.5.3

4.3.6 Other background processes

There exist also other background processes with at least one W boson in the final state, *e.g.* production of W+X and t+X for X containing t, W and b. The examples are $W\bar{t}$, ttW and $Wt\bar{b}$ production processes [164, 165, 197, 198]. The $Wt\bar{b}$ production process is a special one since it contains the whole $t\bar{t}$ background and as well extra subprocesses. All these processes are regarded as less important because the cross-section of additional subprocesses that they include is much lower than the cross-section for already taken into account background samples.

4.3.7 Treatment of multi-jet background processes

This section is devoted to studies of inclusive $t\bar{t}+jets$ and $Wj+jets$ production processes. As was indicated in Section 4.3.4 they need a dedicated method of generation. Event samples that are used here were generated in CompHEP with the parameters presented in App. F and with the generation-level cuts as in App. G. For $t\bar{t}+n-jets$ samples the following requirement were used: $\mathsf{p_T}$>100 GeV for top quarks, ΔR>0.5 for jet-jet separation and various jet $\mathsf{p_T}$ cuts (ranging from 1 to 100 GeV). For $W+jets$ events only $W^-j+(n-1)-jets$ samples were used; however, the conclusions should also be valid for $W^+j+(n-1)-jets$ samples. The $W^-j+(n-1)-jets$ samples were generated with requirement of $\mathsf{p_T}$>100 GeV for W^- boson, $\mathsf{p_T}$>100 GeV cut for the hardest jet, ΔR>0.2 for all separations between jets and W^- boson and various jet $\mathsf{p_T}$ cuts (ranging from 1 to 100 GeV) applied for softer jets.

Clusterization in this section is made as in Sec. 4.3.4 and as shown in Fig. 4.8, *i.e.* clusters emerge only from showered generation-level jets and products of radiations, whereas particles originating from the decays of W bosons and top quarks are ignored.

The first candidates for representation of inclusive $t\bar{t}+jets$ and $Wj+jets$ productions are single W and $t\bar{t}$ event samples generated in any available shower generator (*e.g.* PYTHIA or CompHEP with PYTHIA). Clusters can originate only from parton-shower ISR/FSR and are rather soft with steeply going down $\mathsf{p_T}$ spectrum. Especially single W production process is thus not an efficient source of background to the signal with at least three hard jets. A more significant source of background with at least one hard cluster is Wj production process generated with high $\hat{\mathsf{p}}_\perp$ cut. The hardest cluster originates in this case from generation-level jet accompanying W boson. This process, for its huge cross-section, is very frequently taken into account as background in many analysis done for the LHC physics. Going furtherm, Wjj event sample can be regarded as even better than Wj approximation of a desired part of $Wj+jets$ background. Further on, Wjj is worse than the next in jet multiplicity $Wjjj$ production process. However, the next $Wj+(n-1)-jets$ samples for n>3 are regarded as less significant

56

because they contain higher multiplicity of hard reconstruction-level jets than typical signal event, what is disfavored by typical selection[1]. Nonetheless, one should not only take into account selection efficiency in choosing the best sample. If the hardest clusters originate from generation-level jets, the softer ones may be produced by QCD radiation and pile-up. Therefore, some contribution to the background from the samples with lower jet multiplicity is expected. However, the discussion already started in Section 4.3.4 excluded simultaneous usage of all Wj, Wjj and $Wjjj$ event samples in the background without special treatment. It is also written in Ref. [129] in Chapter 8.4.2 that W and Wj production processes overlap in region with soft clusters, and that these processes should not be used simultaneously. Similar situation and reasoning is expected for the other $Wj + (n-1) - jets$ and also for $t\bar{t}+n-jets$ event samples.

The author proposes the following method to study the overlap problem. Event samples with various multiplicities of generation-level jets n will be compared in the classes of given cluster multiplicity. The comparison will be done using cluster transverse momentum distributions. For $t\bar{t}+n-jets$ event samples these distributions are presented in Figure 4.9, and for $W^-j + (n-1) - jets$ in Figure 4.10.

If the signal event topology is taken into account (*i.e.* number of clusters), the most important background in the case of $Wj + (n-1) - jets$ process should be classes with 3 or 4 clusters and in the case of $t\bar{t}+n-jets$ processes classes without or with only one cluster.

Cluster p_T-distributions in the class with 1 cluster (Fig. 4.9(a)) are up to about 100 GeV very similar in shape for different $t\bar{t}+n-jets$ event samples. There is a little problem with normalization since the rate for $t\bar{t}$ sample is about 2 times lower (as in Figure 4.7(c)) than that for $t\bar{t}j$ and $t\bar{t}jj$ samples. The most important effect is, however, observed for transverse momenta greater than already mentioned 100 GeV, where the cluster rate in $t\bar{t}$ sample drops down significantly in comparison to the rate for $t\bar{t}j$ sample. Since in $t\bar{t}j$ sample this single cluster originates from generation-level jet obtained from ME exact calculations, distribution for this case should be regarded as the reference. In $t\bar{t}$ sample this cluster is a product of showering (ISR); therefore, the only reason of observed behavior might be inefficiency of shower generator in high p_T region. Taking into account that the rates for $t\bar{t}$ and $t\bar{t}j$ in the class with no clusters differs by only 25% (Fig. 4.7(c)), it seems to be a better choice to consider $t\bar{t}j$ instead of $t\bar{t}$ and only $t\bar{t}j$ sample.

Distributions for both $t\bar{t}j$ and $t\bar{t}jj$ samples in the class with 1 cluster follow in high-p_T region tendency from the softer region (Fig. 4.9(a)). These distributions are even very similar, what confirms that they overlap and represent the same events.

---

[1]in central jet veto and in the cut on p_T(WWjj) in Section 6.3

(a) Clusters' p_T distributions in the class of events with 1 cluster

(b) Clusters' p_T distributions in the class of events with 2 clusters

(c) Clusters' p_T distributions in the class of events with 3 clusters
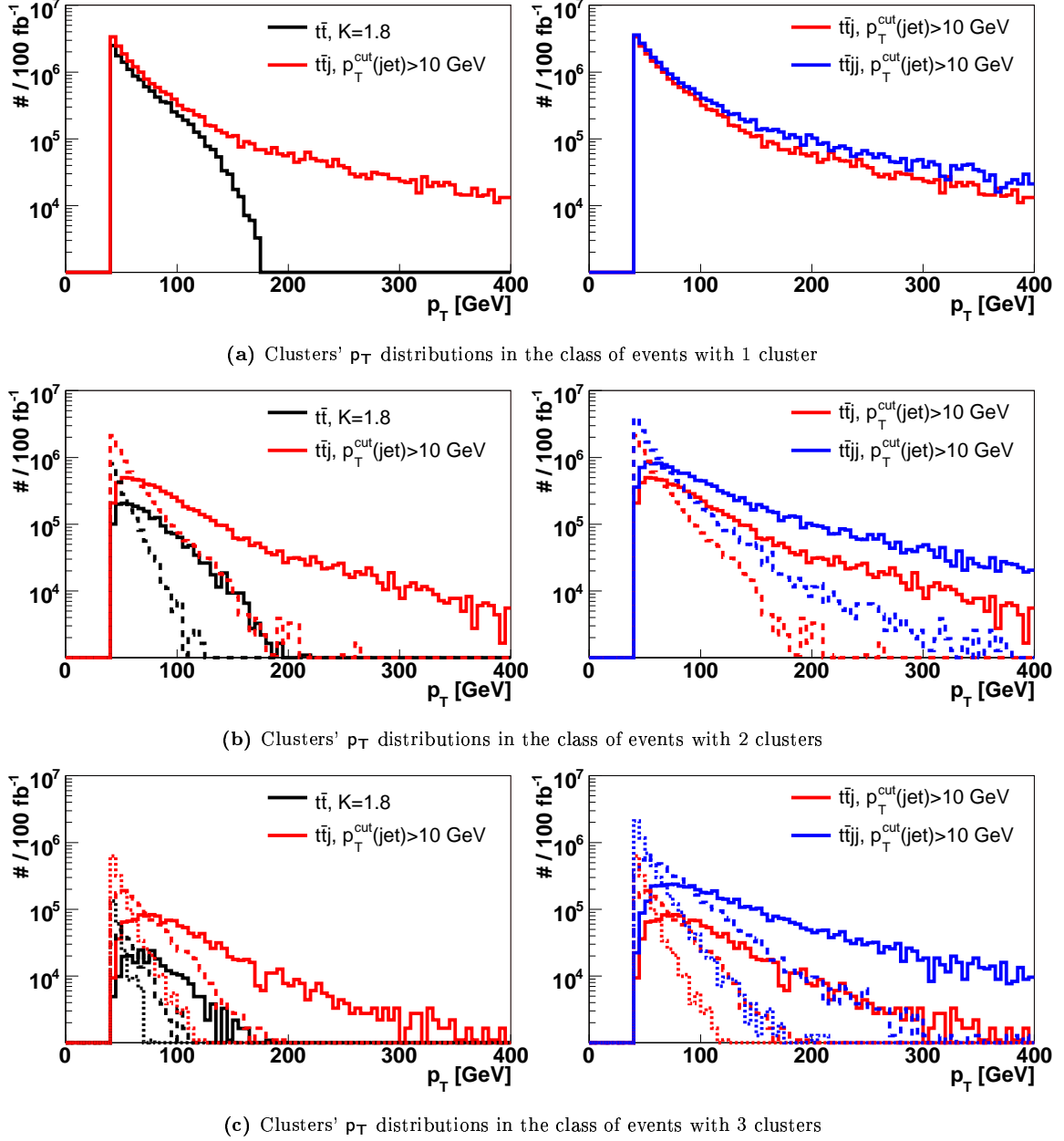
Figure 4.9: Distributions of clusters' transverse momentum in $t\bar{t}+n-jets$ event samples with $n = 0, 1, 2$. Events are divided into classes of defined number of clusters. Color determines generated sample, and the line pattern (full, dashed, dotted) orders clusters in the order from the hardest to the softest. The cut on p_T of generation-level jets ($p_T^{cut}(jet)$) is indicated in the figure. Distributions are normalized to 100 fb^{-1} of integrated luminosity and weighted by K-factors if they are available.

(a) Clusters' p_T distributions in the class of events with 1 cluster.

(b) Clusters' p_T distributions in the class of events with 2 clusters.
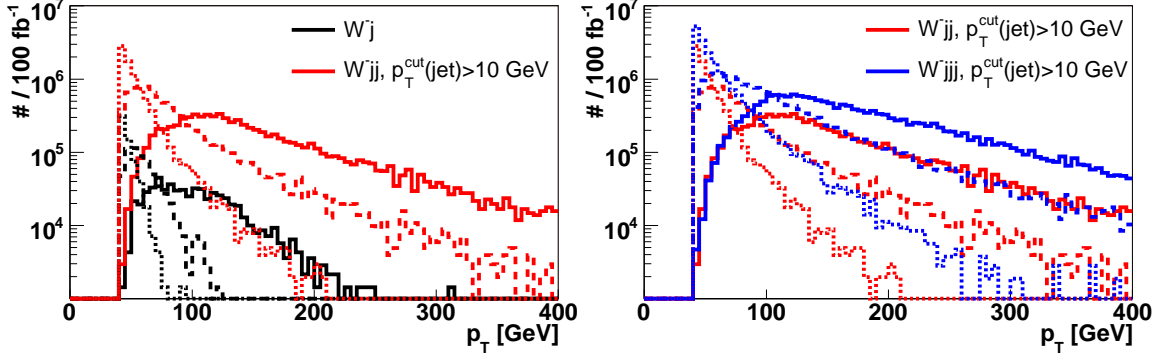
(c) Clusters' p_T distributions in the class of events with 3 clusters.

Figure 4.10: Distributions of clusters' transverse momentum in $W^-j + (n-1) - jets$ event samples with $n = 1, 2, 3$. Events are divided into classes of defined number of clusters. Color determines generated sample, and the line pattern (full, dashed, dotted) orders clusters in the order from the hardest to the softest. The cut on p_T of generation-level jets ($p_T^{cut}(jet)$) is indicated in the figure. Distributions are normalized to 100 fb^{-1} of integrated luminosity.

Therefore, inclusion of both samples would unnecessary overestimate the background. For higher values of p_T, the rates in $t\bar{t}j$ sample are a bit (approximately two times) lower than that in $t\bar{t}jj$ samples. Much differences appear eventually in classes with two and three clusters, where the rates in the whole spectrum for $t\bar{t}j$ are about two (Fig. 4.9(b)) and about three times (Fig. 4.9(c)) lower in magnitude, but the shapes of distributions for the hardest cluster are still approximately the same. It is expected that $t\bar{t}$ events with more than one cluster will be strongly suppressed in the selection. Therefore, consideration of $t\bar{t}j$ sample only seems to be enough. This sample alone is able to very well represent $t\bar{t}+jets$ background to the signal of interest.

The $W^-j + (n-1) - jets$ event samples can be analyzed in very similar manner. Distributions of cluster transverse momentum in the class with one cluster (Fig. 4.10(a)) are the same for W^-j and W^-jj samples. Discrepancy starts from the class with two clusters (*cf.* Figs. 4.10(b) and 4.10(c)). The W^-j sample lacks second generation-level jet; therefore, the rate for W^-j is much lower than that for W^-jj in the class with 2 clusters. In this class, distribution of the hardest cluster in W^-j sample goes as the one of the second hardest in W^-jj sample. Since importance of the events with 2 clusters is much enhanced, Wj sample seems to be not a good candidate for representation of $W + jets$ background. The W^-jjj sample follows the W^-jj distribution in the class with two clusters (*cf.* Fig. 4.10(b)). Significant discrepancies in distributions between W^-jj and W^-jjj appear from cluster multiplicity equal three (*cf.* Fig. 4.10(c)). This situation is similar to the one observed for W^-j and W^-jj case in the class with two clusters. Since events with at least three clusters may be very important, *i.e.* more efficiently satisfy selection requirements, it is better to use W^-jjj event sample. The next class with four clusters will be disfavored by the selection procedure presented in Sec. 6.3; therefore, there is no need for $W + 4j$ event sample consideration that is expected to be better than $Wjjj$ only in classes with $n > 3$ clusters.

It was shown above that multi-jet exclusive event samples have the same topology for certain classes. This observation and the understanding of generation and parton-showering processes let the author conclude that background events accessible with the $t\bar{t}j$ ($Wjjj$) sample very well represent contribution to the background from $t\bar{t}$ (Wjj) and $t\bar{t}jj$ ($W+4j$) samples. What are thus the reasons for differences observed between distributions in Figs. 4.9 and 4.10? The most important is inefficient parton-shower (shower ordering according to virtuality Q^2) that is used in PYTHIA 6.2. It is supposed that this parton-shower is unable to generate clusters, which could be as hard as that originating from generation-level jets. The other reasons are subprocesses that are not attainable through showering. In case of $Wj + (n-1) - jets$, it is still expected that all contributing diagrams to $Wj + (n-1) - jets$ are effectively, thanks to parton-shower ISR, included in $Wj + (m-1) - jets$ for $m < n$. On contrary, for $t\bar{t}+n - jets$

samples, there exist extra diagrams that can not be realized in this way (examples in Fig. 4.11), encouraging thus to prefer $t\bar{t}j$ sample over $t\bar{t}$. These drawbacks of parton-shower approach encourage to use multi-jet event samples generated with the use of ME generators. Besides, only in the latter approach one is able to control p_T of generation-level jets. Requiring for $Wjjj$ sample $p_T>30$ GeV cut for generated jets, one almost always obtains at least three clusters of $p_T>30$ GeV. Such control is impossible with Wj sample, and three hard clusters can be observed very rarely. Additionally, by using ME generator one takes into account the exact kinematics of multi-jet process, what is very important in events with well-separated jets (Chapter 2.2 in Ref. [129]).

Summarizing, all above observations justify usage of exclusive selected multi-jet sample generated with p_T cut as low as it is reasonable for simulation of multi-jet inclusive background. For the case of the background to strong VV scattering (and heavy Higgs boson production), event samples of $t\bar{t}j$ and $Wjjj$ (W^+jjj and W^-jjj) have been chosen for represention of $t\bar{t}+jets$ and $Wj+jets$ background processes.

Lately, an alternative shower ordering according to p_T has been developed in PYTHIA [199]. It is available starting from PYTHIA 6.3 [133] version. The new approach is found to fit better the data collected at the Tevatron [199, 200] and at the LEP collider [201] than the standard Q^2-ordered parton-shower (the old parton-shower)

(a) $t\bar{t}j$ specific diagrams

(b) $t\bar{t}jj$ specific diagrams

Figure 4.11: Additional diagrams that are present in $t\bar{t}j$ and $t\bar{t}jj$ ME samples, but that are not attainable for $t\bar{t}$ samples with parton-shower.

that has been used in this thesis up to this point. The general feature is that clusters originating from ISR, but also from generation-level jets, are harder when the new parton-shower is used. It is demonstrated in Figure 4.12, where distributions of cluster transverse momentum (in the class of events with one cluster) in $t\bar{t}$ and $t\bar{t}j$ samples for the old and the new parton-shower method are compared. For both parton-showers, the distributions for clusters in $t\bar{t}j$ sample (red lines) follow, as expected, the shape of distribution for generation-level jets (blue lines), which they originate from. On contrary, as is also shown in Fig. 4.12(a), the distribution for $t\bar{t}$ sample drops down for $p_T>100$ GeV, when the old parton-shower is used. This bad behavior is, however, not observed for $t\bar{t}$ sample with new p_T-ordered parton-shower. In the latter case, parton-shower generated cluster in $t\bar{t}$ sample has p_T-distribution shape very similar to, regarded as the reference, distribution for generation-level jet (cluster) in $t\bar{t}j$

(a) Distributions obtained with the use of old parton-shower.

(b) Distributions obtained with the use of new parton-shower.

Figure 4.12: Distributions of transverse momentum for clusters (in $t\bar{t}$ and $t\bar{t}j$ samples for one-cluster events) and generation-level jets (in $t\bar{t}j$ sample regardless the cluster multiplicity) with the use of old Q^2-ordered parton-showers in (a) and new p_T-ordered one in (b). The distribution for generation-level jet is normalized to the total cross-section. The other distributions are normalized to the rate for the class with one cluster. The cut on p_T of generation-level jets ($p_T^{cut}(jet)$) is indicated in the figure.

sample. This proves that the p_T-ordered showering is much better method, and that the configuration of parameters used here is approximately correct.

It can be expected that the differences between exclusive samples with different number of generation-level jets n will be reduced when the p_T-ordered parton-shower is used. The distributions corresponding to those in Figs. 4.9 and 4.10 were redone with PYTHIA 6.3 and new parton-shower and are presented in Figs. 4.13, 4.14 and 4.15. The set of parameters for the new parton-shower in PYTHIA 6.3 is listed in Appendix C.1. Differences between results obtained with two parton-shower generators are serious. First of all, p_T distributions of extra clusters (clusters purely originating from ISR/FSR) do not exhibit dramatic falling down that was observed when using Q^2-ordered parton-shower. Furthermore, all $t\bar{t}+n-jets$ samples are consistent with each other in the class with 1 cluster (*cf.* cluster p_T distributions in Fig. 4.13(a)). This was not the case for the old Q^2-ordered parton-shower (*cf.* Fig. 4.9(a)). In consecutive classes (higher multiplicities of clusters in Figs. 4.13(b) and 4.13(c)), the distribution shapes in individual figures are exactly the same, and only correct values of K-factors are only needed for obtaining exactly the same rates. These K-factors should be of the order of 1.2-1.3. When the new parton-shower is used, $t\bar{t}$ event sample appears to be a good approximation of $t\bar{t}+jets$ background. The agreement between $W^-j + (n-1) - jets$ samples (*cf.* Fig. 4.14) is less impressive, but the situation is much better than for results with PYTHIA 6.2. For example W^-jjj and W^-jj samples exactly overlap in the class with three jets (Fig. 4.14(c)).

The results presented in Figs. 4.13, 4.14 and 4.15 suggest not only that the new
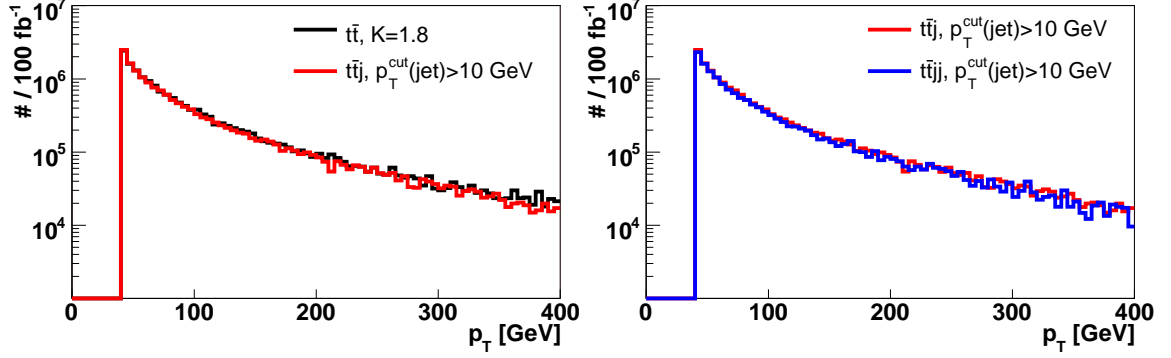
(a) Clusters' p_T distributions in the class of events with 1 cluster.
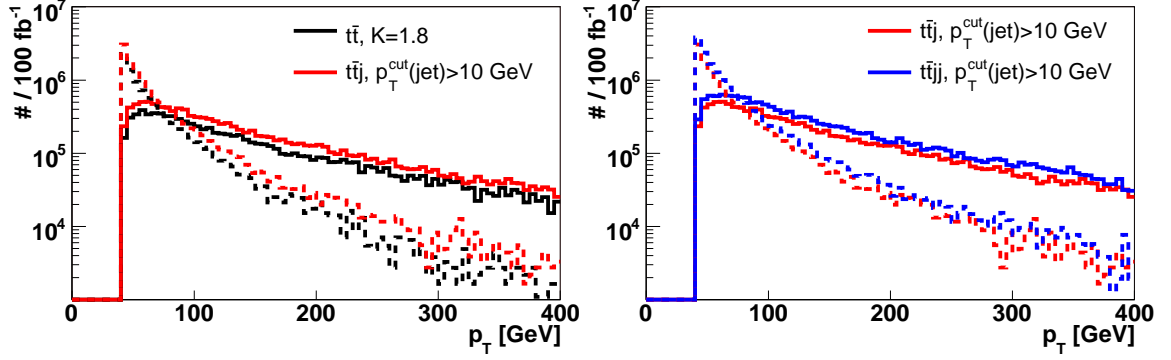
(b) Clusters' p_T distributions in the class of events with 2 clusters.
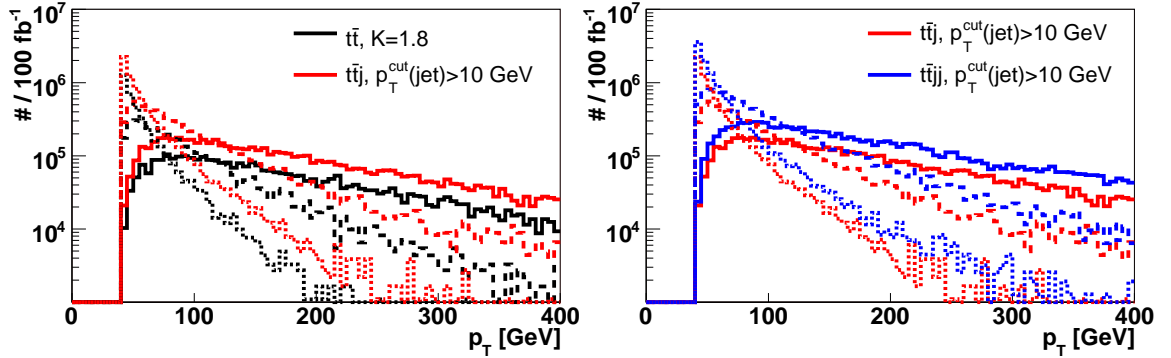
(c) Clusters' p_T distributions in the class of events with 3 clusters.

Figure 4.13: Distributions of clusters' transverse momentum in $t\bar{t}+n-jets$ event samples with $n = 1, 2$. Results are obtained with p_T-ordered parton-shower and PYTHIA 6.3. Events are divided into classes of defined number of clusters. Color determines generated sample and the line pattern (full, dashed, dotted) ranks clusters in the order from the hardest to the softest. The cut on p_T of generation-level jets ($p_T^{cut}(jet)$) is indicated in the figure. Distributions are normalized to 100 fb^{-1} of integrated luminosity and weighted by K-factors if they are available.

(a) Clusters' p_T distributions in the class of events with 1 cluster.

(b) Clusters' p_T distributions in the class of events with 2 clusters.

(c) Clusters' p_T distributions in the class of events with 3 clusters.
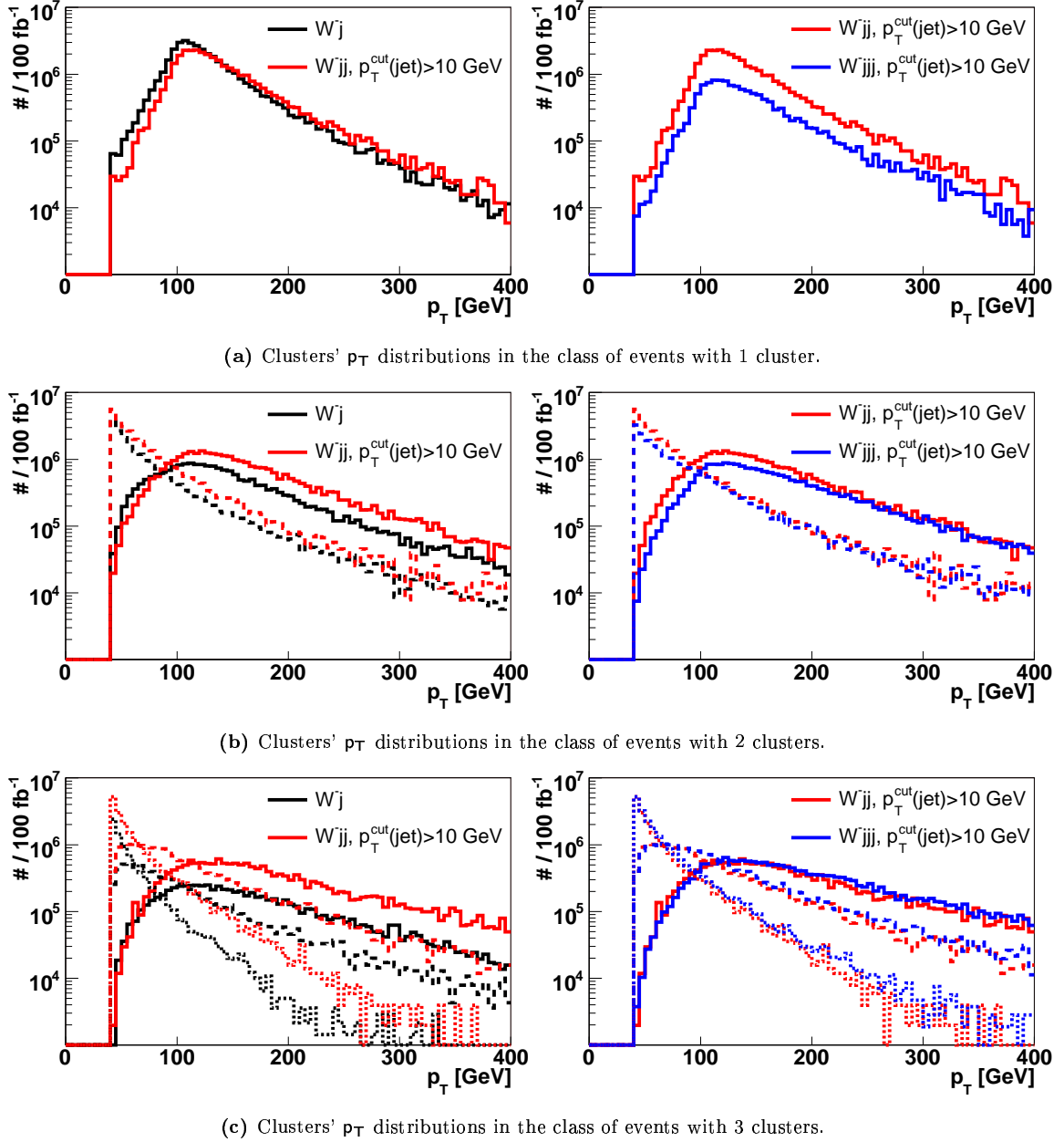
Figure 4.14: Distributions of clusters' transverse momentum in $W^- j + (n-1) - jets$ event samples with $n = 1, 2, 3$. Results are obtained with p_T-ordered parton-shower and PYTHIA 6.3. Events are divided into classes of defined number of clusters. Distributions for the class of events with 4 clusters are presented in Fig. 4.15. Color determines generated sample, and the line pattern (full, dashed, dotted) orders clusters in the order from the hardest to the softest. The cut on p_T of generation-level jets ($p_T^{cut}(jet)$) is indicated in the figure. Distributions are normalized to 100 fb^{-1} of integrated luminosity.
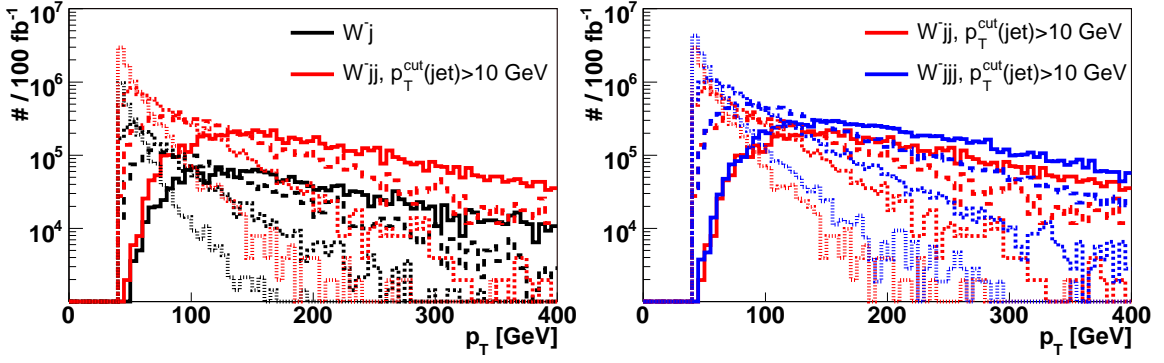
(a) Clusters' p$_T$ distributions in the class of events with 4 clusters.

Figure 4.15: Distributions of clusters' transverse momentum in $W^- j + (n-1) - jets$ event samples with $n = 1, 2, 3$. Continuation from Fig. 4.14.

p$_T$-ordered parton-shower in PYTHIA is better than the old one (at least in applied configuration). Furthermore, the new parton-shower should be regarded as the only valid since it produces results comparable with ME calculations. All of this encourages to use new p$_T$-ordered parton-shower for generation of all background and signal event samples. The decision on using $t\bar{t}j$ and $Wjjj$ samples that was made previously basing on the results obtained with the use of old parton-shower needs to be verified now. The results in this section (with new p$_T$-ordered parton-shower) suggest that it is enough to use $t\bar{t}$ sample generated with p$_T$-ordered parton-shower for representation of inclusive $t\bar{t}+jets$. The W^-jjj and W^+jjj samples obtained with the same parton-shower can, as for the case with Q^2-ordered parton-shower, be used for representation of inclusive $Wj + jets$ background process.

Results of this section demonstrated and proved that there is much overlap between event samples with different generation-level jet multiplicity. This is even more evident for samples generated with the use of new p$_T$-ordered parton-shower. Therefore, it has been proposed here to use exclusive event sample for representation of inclusive background. This way the overlap problem is solved. This method can be regarded as an alternative to specially developed procedures of matching ME calculations with parton-shower programs (matrix-element/parton-shower matching (ME/PS matching)). These procedures provide consistent addition of parton showers to a set of LO ME X, $X + jet$, $X + 2 - jets$, etc. event samples. As a result an inclusive multi-jet sample of X production is obtained. The most important studies of ME/PS matching were done by Catani, Krauss, Kuhn and Webber (CKKW) [202, 203] and by M.L.Mangano (MLM) [204] and are discussed in Ref. [205]. In these publications the authors discuss the problem of the overlap between generation of close to each other partons (generation-level jets) and subsequent fragmentation/showering of these

partons in shower programs. Both these phenomena have the same result, however, differ in contribution to the cross-section. Namely, the former phenomenon contributes to the cross-section, and the latter one should not. Very simple MLM approach examines showered events and removes the ones with not all generation-level jets having their separate matching representative among clusters. Eventually, the cross-section is reduced accordingly. Therefore, unless events were processed by this procedure, the cross-sections would be overestimated. The author expects that this overestimation can be avoided just by requiring the separation of about $\Delta R{>}0.5$ between all of the generation-level jets and reasonable value of minimal $\mathsf{p_T}$ for them. The requirement of $\Delta R{>}0.5$ separation is suggested since coincides with $R{=}0.5$ cone clusterization that was used here and also in $R{=}0.5$ cone jet algorithms that will be used later on. This requirement was imposed on all event samples used to obtain all results in this subsection[1]. The jet $\mathsf{p_T}$ cut that was used ($\mathsf{p_T}{>}10$ GeV) is low, but it is not unreasonable low since the cross-sections for generated samples in Fig. 4.4 down to about $\mathsf{p_T}{=}10$ GeV are still not divergent. Thanks to such low value of jet $\mathsf{p_T}$ cut, the exclusive samples can perfectly overlap with samples of lower number of generation-level jets and thus represent inclusive processes. Since both conditions (separation ΔR and minimal $\mathsf{p_T}$) has been set on reasonable levels, the cross-section obtained for event samples used here are physically understood and also trustworthy.

4.4 Summary on the choice of signal and background processes

Vector boson scattering (fusion) was chosen here for the process that will be used as the LHC experimental signal of the strongly-coupled sector. It will be simulated with the use of phenomenology provided by EWChL. A number of models will be considered. The background, as was argued in previous section, can be well approximated by $t\bar{t}$, W^+jjj and W^-jjj event samples. All event samples will be showered (if generated in CompHEP) in PYTHIA 6.3 with the use of $\mathsf{p_T}$-ordered parton-shower.

Simulated signal and background event samples will be discussed in Section 6.1.

---

[1] The $\Delta R{>}0.5$ separation requirement has been actually used for $t\bar{t}{+}n - jets$ event samples. For $W^-j + (n-1) - jets$ samples it has been mistakenly used rather weak $\Delta R{>}0.2$ condition, but as it is seen in the figures it does not cause blowing of cross-sections for $W^-j + (n-1) - jets$ samples in comparison to $W^-j + (n-2) - jets$ samples.

Chapter 5

The CMS detector and reconstruction of its measurements

This chapter begins with description of apparatus, *i.e.* the CMS detector, that will be used for determination if symmetry breaking by the strongly-coupled sector is realized in Nature. Later on, the main emphasis will be put on reconstruction that enables recognition and interpretation of collected events. Only appropriate to searches for signal vector boson scattering reconstruction objects (muons, MET and jets) will be defined and optimized for high luminosity conditions and given event characteristics. Reconstruction performance will be summarized with appropriate resolutions. The objects defined here will be used in Chapter 6 in analysis of physics events.

5.1 The Large Hadron Collider

The Large Hadron Collider (LHC) [206] will operate as the final stage in acceleration of protons, which collisions will be detected in the CMS detector. The protons will be accelerated in the sequence of accelerators: Liniac, Booster, Proton Synchrotron. Next, the beam will reach the energy of 450 GeV inside the Super Proton Synchrotron, and afterwards will be injected into the LHC. Here protons will be accelerated to final energy of 7 TeV.

The LHC is located in the 27-km circular tunnel at CERN near Geneva. Two beams of protons will travel in opposite directions in the same specially constructed acceleration system. Collisions will happen in the points where in underground caverns the detectors will be located. There will be two omni-purpose detectors: the ATLAS and the CMS. The other two detectors, the ALICE and the LHCb, will be dedicated to heavy ion physics and to the physics of quark b, respectively. The TOTEM detector is designed to measure the pp cross-section.

The ultimate goal of the LHC operation is 7 TeV of beam energy and high luminosity ($\mathcal{L} = 10^{34}$ cm^{-2} s^{-1}), what means around 10^9 proton-proton interactions per second[1] and effective integrated luminosity of 100 fb^{-1} per year. The beam will be formed by the bunches with 25 ns spacing and of the order of 10^{10} protons per bunch. As a result, collisions of bunches will happen every 25 ns (frequency 40 MHz). At high luminosity every collision of bunches will produce around 26 pp collisions. This means that on average 25 minimum bias pp events will "pile-up" on top of the signal high-p_T pp event.

The LHC, currently near completion, will start operation with first physics runs in 2008. High luminosity conditions that are necessary for the searches for hypothetical symmetry breaking by the strongly coupled physics will be reached around 2011.

5.2 The Compact Muon Solenoid detector

The Compact Muon Solenoid (CMS) detector [152] will be located in Point 5 of the LHC. This is an universal detector. Its detection aims range from discovery of symmetry breaking mechanism (Higgs mechanism or alternatives), discovery of supersymmetry and other exotic scenarios to precision measurements of the SM physics and heavy ion physics.

The general view of the CMS detector is shown in Figures 5.1. The detector is composed of many subdetectors (subsystems) making the whole general purpose apparatus. It possesses inner tracking system, electromagnetic and hadronic calorimeters, superconducting coil with magnet return yoke and muon system. The schematic view of one quadrant of the CMS detector with marked positions of particular subsystems is presented in Figure 5.2. The global coordinate system is started in the very center of the CMS detector and oriented as shown in this figure. The up-to-date information on the detector is presented in Ref. [207]. The detector is currently being assembled to be ready for operation in the first half of 2008. The challenging magnet system has been successfully commissioned and has reached nominal parameters in the Magnet Test and Cosmic Challenge in the second half of 2006. The other systems have been then tested as well and integrated with the use of cosmic rays.

In addition to above mentioned accelerator in-time pile-up, there is also out-of-time pile-up connected with detector time response. Most of the CMS subdetectors are sensitive to tracks produced in a number of bunch crossings both before (maximum 5) and after (maximum 3) bunch crossing containing particular event. Therefore, in high luminosity runs subdetectors are even exposed to 234 events[2] on average[3].

---

[1]assuming total inelastic pp cross-section of around 100 mb
[2](5 before + 3 after + particular bunch crossing) × 26 for in-time pile-up
[3]accident number of events is governed by Poisson distribution
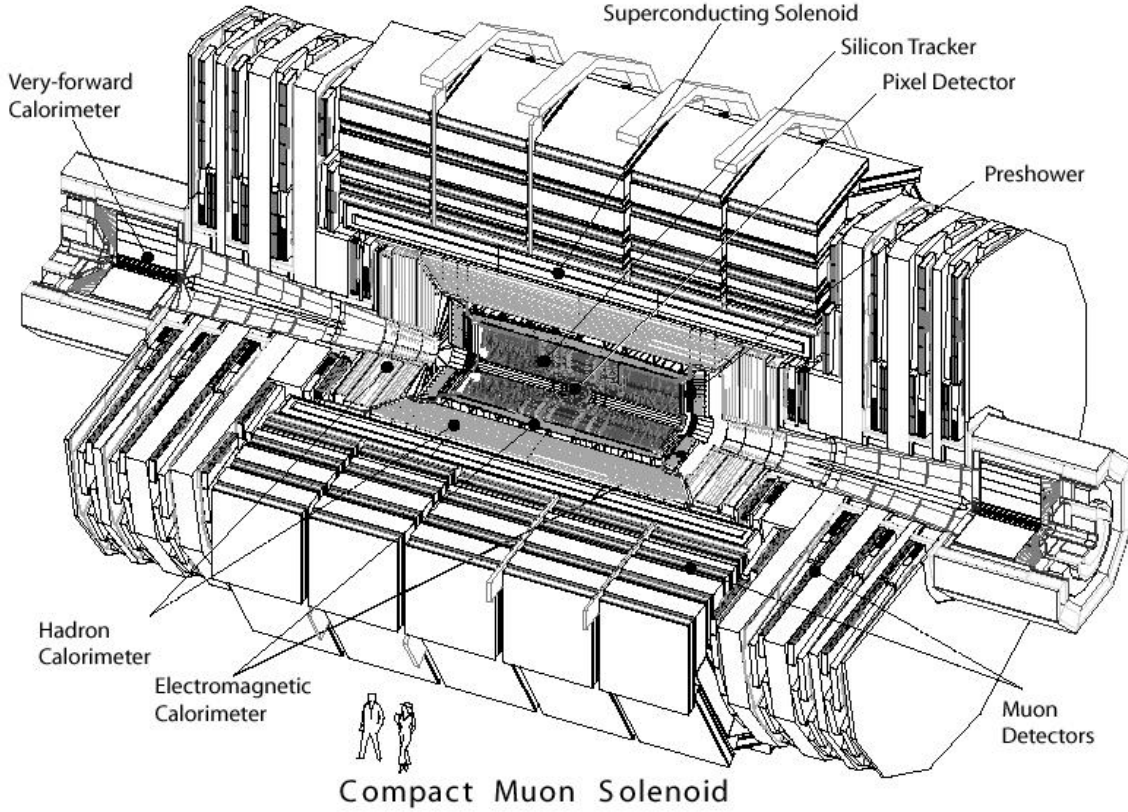
Figure 5.1: The general view of the CMS detector [207].

5.2.1 Inner tracking system

The CMS tracker system [208, 209] is composed of silicon pixel and silicon microstrip detectors. They provide coverage up to $|\eta|$=2.4.

The pixel detectors are located in the very center of the CMS. They are arranged in 3 barrel layers and 2 endcap disks on each side. They are placed inside a cylinder of approximate radius of 15 cm and height of 93 cm. The closest to the interaction vertex layer is located at mean radius of 4.4 cm. A single pixel that is the smallest read-out detector element is 100×150 μm^2 in size. The total area of pixel detectors is $\approx$1 m^2 with 66 million pixels.

The silicon microstrip detectors are located outside of the pixel detectors and extend to radius of 110 cm and $|z|$ =280 cm. A single silicon strip is of length 10-25 cm, width varying from 80 to 180 μm and a thickness of 320 and 500 μm. The total area is 200 m^2 with almost 10 million silicon strips.

Very good segmentation of the inner tracking system results in excellent performance: single-point resolution, track reconstruction efficiency and transverse momentum impact parameter resolution.
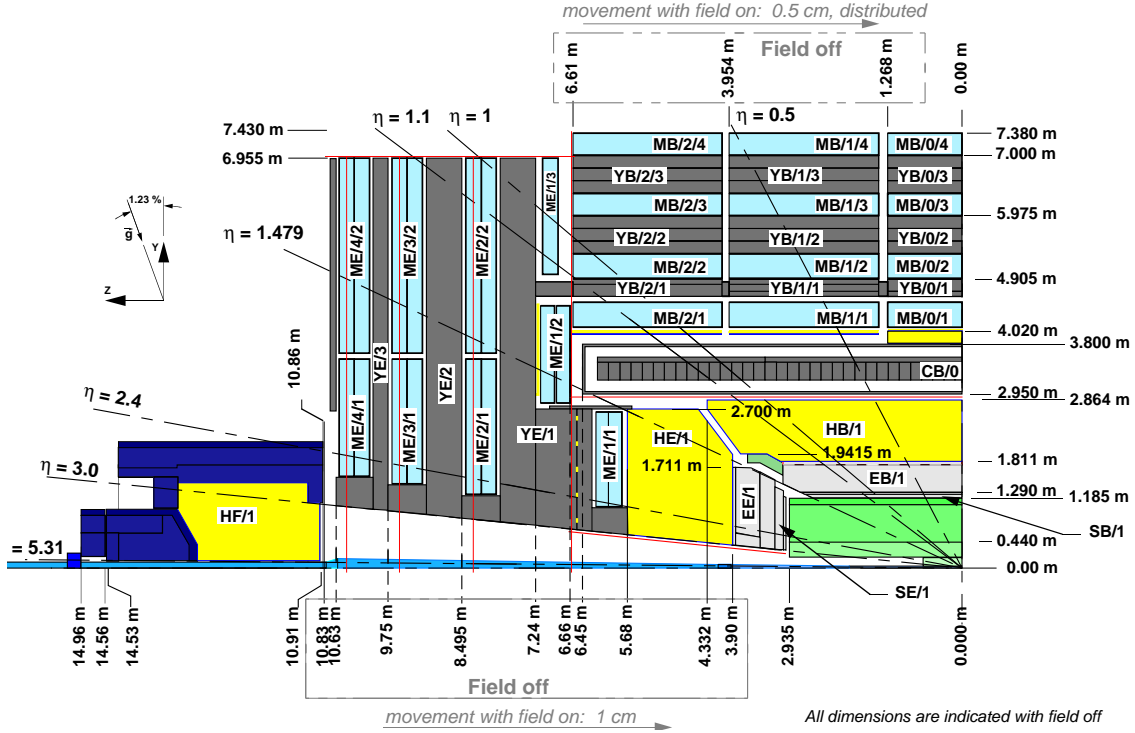
Figure 5.2: Longitudinal view of one quadrant of the CMS detector. Inner tracking system is in green, the ECAL in light grey, the HCAL in yellow, the superconducting coil is in grey and marked CB, the muon chambers are in turquoise, the magnet return yoke is in grey and marked YB and YE.

5.2.2 Calorimeter system

The CMS calorimeter system is composed of electromagnetic (ECAL) [210, 211] and hadron (HCAL) [212] calorimeters.

5.2.2.1 Electromagnetic calorimeter

The ECAL is located outside the inner tracking system and divided into the barrel section (EB) and two endcaps (EE). The coverage range is $|\eta|$<3.0. It is composed of almost 77 thousand lead tungstate ($PbWO_4$) scintillating crystals.

The barrel crystals have a front face cross-section of $\approx$22×22 mm^2 and a length of 230 mm corresponding to 25.8 X_0. They are mounted on the 129 cm radius cylinder. Thanks to being of truncated pyramid shape, they could be arranged side by side in geometry, which is off-pointing with respect to the nominal vertex, with a 3° tilt in both ϕ and η. This arrangement avoids dead regions. Crystals have dimensions $\Delta\eta \times \Delta\phi = 0.0174 \times 1^o$.

The endcap crystals are of similar sizes. They are mounted on disks at $|z|$=314 cm

distance from the vertex and, as the barrel crystals, off-point the nominal vertex. A preshower device is placed in front of the endcaps.

Particle energy lost in the ECAL is measured using collected scintillating light. Thanks to the used technology, the ECAL is compact, fast, has fine granularity and is radiation resistant.

5.2.2.2 Hadron calorimeter

The CMS hadron calorimeter system is divided into three calorimetric parts: the hadron barrel calorimeter (HB), the hadron endcap calorimeter (HE), the hadron forward calorimeter (HF) and one scintillating part: the hadron outer calorimeter (HO). Calorimeters use the sandwich (sampling) technique, *i.e.* layers of active element alternate with layers of absorber. The thickness of HCAL in interaction lengths varies from 7 to 11 λ_I depending on η.

The HB and HE surround the ECAL. Their absorber is brass (alloy of copper and zinc) and as active elements plastic scintillator tiles with wavelength-shifting fibre read-out are used.

The HF provide coverage in $3.0 < |\eta| < 5.0$ regions, thanks to which the whole CMS calorimetric system is hermetic. This calorimeter is located outside the CMS; therefore, there is a discontinuity in z position between HE and HF. Although there is an overlap in η for $|\eta| \approx 3.0$, this still may lead to the problems with reconstruction of showers starting close to this region. The HF uses steel as an absorber (composed of 5 mm thick grooved plates), and quartz fibers were chosen as the active medium.

The HO is an additional layer of scintillators lining the outside of the coil. It plays a role of a tail-catcher sampling the energy leaking from the calorimeters.

The barrel part of the HCAL is segmented into towers of dimensions $\Delta\eta \times \Delta\phi = 0.087 \times 0.087$. The segmentation of the endcap part is $\Delta\eta \times \Delta\phi = 0.087 \times 5^o$ or $\Delta\eta \times \Delta\phi = 0.09 \div 0.35 \times 10^o$. The HF is divided into 13 towers in η direction of size $\Delta\eta = 0.175$ and $\Delta\phi = 10^o$ [1]. This segmentation is used in reconstruction of hadronic activity of the physics events.

Determination of energy by sampling calorimeter is made using known relation between the collected charge in active element and incident particle energy (calibration) [213]. As a result one obtains towers with deposited energy.

5.2.3 Magnet system

The CMS detector is equipped with large (12 m in diameter and 12.9 m in length) superconducting solenoid providing 4 T magnetic field [214]. The field is parallel inside

---

[1]the exceptions are the lowest- and highest-η towers

the coil and oriented along z axis. Outside the coil, the field returns in magnet yoke composed of iron plates. The magnet system enables very good momentum resolution of charged particles in wide range of momentum and pseudorapidity. The stored energy of 2.7 GJ, large field, a current of 20 kA and stress forces required many improvements and novel technology with respect to previous developments.

5.2.4   Muon system

The CMS detector muon system [215] is composed of three types of chambers: drift tubes (DT) in the barrel region, cathode strip chambers (CSC) in both endcap regions and resistive plate chambers (RPC) in the barrel and endcaps.

The muon chambers are tracking chambers placed outside the coil and calorimeters. For this reason the only particles that reach there from the collision vertex are the muons[1]. The chambers are arranged into four stations interleaved by the return yoke iron plates. Only muons with $p_T \gtrsim 4$ GeV (softer muons are bended in the magnetic field and are not able to reach the muon chambers in the barrel) and $|\eta| < 2.4$ (maximal η coverage of muon chambers) are detected. The muon track bent in the magnetic field is used for determination of muon transverse momentum. The leading role in identification and reconstruction of muons play DT's and CSC's because of their good segmentation. The $|\eta| < 2.1$ region corresponding to the coverage of RPC and either DT (in barrel) or CSC (in endcaps) muon systems is used by the muon trigger subsystem.

5.2.5   Trigger system

The size of a single event (1 MB) and archival data transfer and storage capability (about 100 MB/s) cause that the total rate of events have to be reduced from provided by the LHC 40 MHz to about 100 Hz. For efficiency reasons, rejection of events is done in two steps. In the first step (Level-1 Trigger) [216], executed by custom electronics, the rate is reduced to about 100 kHz. The second step (High-Level Trigger (HLT)) [217, 218] leading to final rate of 100 Hz is performed on computer farm. In order to obtain more general-purpose performance, the CMS HLT is logically divided into two Level-2 and Level-3 trigger subsystems.

Trigger as a whole is also called on-line selection since it will filter events before their storage. The idea of its performance is based on setting thresholds on transverse momenta of basic reconstruction objects (jets, muons, electrons, MET) that will be discussed in Section 5.4. This action is performed by trigger subsystems, *e.g.* jet, MET and muon triggers. The cuts on the objects are deduced from results of simulations

---

[1]excluding neutrinos and other hypothetical particles that are completely directly undetected

for *pp* collisions. The values of cuts are optimized to accordingly reduce the rate of information and simultaneously keep interesting events with hard objects.

5.3   Detector simulation and digitization

In order to prepare the analysis of data with hypothetical signal of strongly-coupled symmetry breaking sector, there are used generated physics processes (Chapter 4), the CMS detector simulation, digitization and reconstruction.

Detector simulation has been performed with OSCAR (Object oriented Simulation for CMS Analysis and Reconstruction) [219] - the official detailed CMS detector simulation[1]. Version OSCAR_3_6_5 has been used. The digitization is done with ORCA (Object oriented Reconstruction for CMS Analysis) [220]. The ORCA_8_7_1 version, fully compatible with OSCAR_3_6_5, was used.

OSCAR reads in the event with particle four-momenta (*HEPEVT* ntuples) and performs the first step of detector simulation. It uses GEANT4 [221] package for the passage of particles through the CMS detector and production of hits in its sensitive parts. In the next step, done by ORCA and called digitization, simulation of the discrete detector response to a given pattern of hits is done. At this step, it is added electronic noise and hits originating from pile-up. Pile-up is realized by addition of separately simulated minimum bias events. Special care was taken here to use an appropriate configuration for high luminosity in-time pile-up and for detector out-of-time pile-up. More details on pile-up treatment and digitization can be found in Ref. [207].

The results of detector simulation and digitization are stored in `SimHits` and `Digis` files.

5.4   Reconstruction of detector measurements

The next step of event processing is reconstruction. In principle, it does not differentiate between simulated and real data. In this process detector raw data is converted into usable for physics analysis basic objects like leptons, MET and jets. These objects are expected to mimic original particles created in physics processes. Reconstruction is split between algorithms responsible for reconstruction of particular objects. The results are stored in `DST` files. The analysis of collected or simulated events operate on these files. The ORCA_8_7_1 version was used for reconstruction.

In the following subsections, there are described reconstruction algorithms, which are related to the signal process (vector boson scattering) signature listed in Section 4.2.5.3, *i.e.* jets, MET, muons and reconstruction of boosted *W* bosons. Basic

---

[1]When this thesis was being finished, OSCAR has already been replaced by CMSSW.

algorithms are described in detail in Ref. [207]. Reconstruction is optimized here to be efficient and deliver relatively pure objects in high luminosity conditions. Further optimization of reconstruction, in order to suppress the background, will be performed in Chapter 6, where the objects defined here will be extensively used.

The performance of reconstruction is discussed after Introductory Selection[1] of events that ensures presence of these objects in the event. For illustration, S4 event sample (with generation-level cuts, but without any additional preselection) will be used. The details on this event samples will be given in Section 6.2.

5.4.1   Reconstruction of jets

From the reconstruction point of view, the jets are the objects describing partonic (hadronic) activity of the event. The partons produced in the physics event fragment to particles, which in turn deposit their energies in calorimeters. Particles and their energy deposits that originate from a certain parton are typically close to each other in angle forming a group that at generation-level is called here cluster. The jets are the products of the jet algorithms performing association of input objects (generation-level clusters, particles, calorimetric towers with energy deposits). Most often one hard parton result in one cluster and one jet. However, if the parton radiates another parton, the latter may be reconstructed as an extra jet provided it is enough separated from the mother parton.

The two most popular types of jet algorithms are cone-based type (merges input objects within a cone of arbitrary size) and cluster-based type (merges input objects of small relative transverse momentum). Although the former are better motivated [222], the cone-based algorithm for its simplicity and fast operation is commonly used in hadron collider experiments, and it will be used in this analysis for jet reconstruction.

The first algorithm of cone-based type was Snowmass algorithm [223]. Its implementation in ORCA is `Iterative Cone (IC)` jet algorithm. Its operation starts from seeds selected from input objects. Hardest seeds are considered first. The proto-jet is built from the seed and input objects that are within R cone around the seed, *i.e.* with $\Delta R < R$, where $\Delta R = \sqrt{\Delta\eta^2 + \Delta\phi^2}$, and $\Delta\eta$ and $\Delta\phi$ are distances in $\eta \times \phi$ space. The angular position (centroid) of such proto-jet is calculated, and a cone is moved to this new position. This procedure is iterated until the proto-jet stops flowing. Such stable proto-jet becomes a jet. Assigned input objects (jet constituents) are removed from the list of input objects, and the process is repeated for next seeds in the list until no seeds remain.

The parameters of the jet algorithms in ORCA are the following:

---

[1] Introductory Selection, the part of the event selection chain, will be presented in Section 6.3.2

1. **jet algorithm type** - *e.g.* IC for cone-based algorithm.

2. **jet cone** - the value of jet cone R for cone-based algorithm.

3. **jet input (input objects)** - the objects that are associated to form jets (jet constituents). For calorimeter jets, these objects are calorimetric towers characterized by deposited energy and (η, ϕ) position. Energy of particular tower is obtained as a sum of corresponding energies collected in electromagnetic and hadronic calorimeters[1] in region given by particular HCAL tower. For generation-level jets input objects are stable particles in the event with exclusion of muons and neutrinos[2].

4. E_T^{cut}(tower) - minimal value of transverse energy for input objects (here for tower) (default: 0.5 GeV).

5. E_T^{cut}(seed) - minimal value of transverse energy for input objects that can seed jets (if lower than E_T^{cut}(tower) every input object can be a seed) (default: 0.0 GeV).

6. E_T^{cut}(jet) - minimal value of transverse energy for jets (default: 20 GeV).

7. **recombination scheme** - the method combining input object four-vectors to the jet four-vector.

8. **jet correction** - optional procedure correcting jet four-vector.

Electronic noise and pile-up (especially for high luminosity) can potentially influence the jets emerging from hard physics process. Since, these two phenomena are mostly responsible for tower deposits with low E_T value, in order to reduce their influence, it is enough to increase the E_T^{cut}(tower) . The E_T^{cut}(tower) value can not be too high since this could influence real jets. This effect is presented in Figure 5.3(a) for jets with $\eta < -3.1$ and in Figure 5.3(b) for jets with $|\eta| < 2.5$. Jet p_T distributions in signal samples are in these figures presented together with those in signal samples without pile-up and with transverse momentum distributions for tagging quarks and hadronic W. There are also shown distributions for so called pile-up event samples - samples of events with no hard process but only pile-up generated particles[3]. It can be seen in Figure 5.3(a) that E_T^{cut}(tower) =6.0 GeV (1.5 GeV) value is too high (too small) since resulting rates for jets are lower (higher) than that for tagging quarks. Higher values of E_T^{cut}(tower) are preferred since the rate of soft fake jets with p_T<50 GeV is lower for them. Nevertheless, down to around 50 GeV in transverse momentum all distributions

---

[1] this jet input is called `EcalPlusHcalTowerInput` in ORCA
[2] this jet input is called `GeneratorInputNoMuandNu` is ORCA
[3] one such pile-up event is made of on average 225 minimum bias events
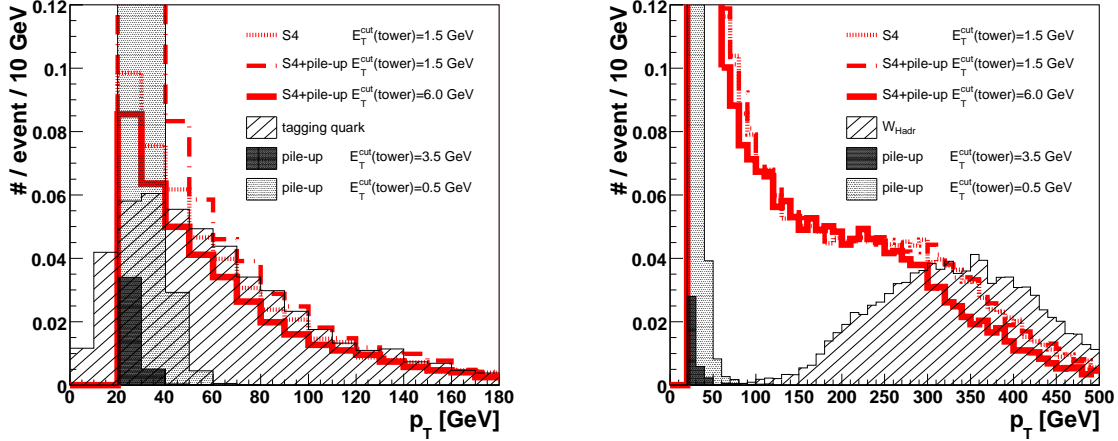
(a) The p_T distributions for calorimeter jets in $\eta < -3.1$ region.

(b) The p_T distributions for calorimeter jets in $|\eta| < 2.5$ region.

Figure 5.3: Calorimeter jet p_T distributions for various E_T^{cut}(tower) cuts in two regions in η: (a) $\eta < -3.1$ and (b) $|\eta| < 2.5$. For signal S4 event sample two cases: with- and without pile-up are considered. Distributions for jets in pile-up samples are shadowed. Jet distributions should be compared with those for their orig- inators: tagging backward quark in (a) and W boson decaying hadronically in (b). The other jet reconstruction parameters are: $R = 0.5$ cone, $E_T - scheme$, E_T^{cut}(seed) $=0.0$ GeV.

for reconstructed jets are similar to the distribution for tagging quark. This suggests that for most of the events, there is also a soft jet in addition to hard jet. Therefore, the hardest jet in appropriate region should be always considered. The comparison of transverse momentum for such jet (p_T^{rec}) with transverse momentum for forward tagging quark (p_T^{part}) is shown in Figure 5.4. For lower values of E_T^{cut}(tower) , the jet transverse momentum is on average overestimated, whereas it is underestimated for higher values. The best value for E_T^{cut}(tower) is that, for which mean value of the rel- ative difference between transverse momenta is 0. The best value is about 1.5 GeV for sample without pile-up and 3.5 GeV [1] for sample with included pile-up. These values are obtained for $R = 0.5$ cone jets. It will be shown in Sec. 5.4.2 that E_T^{cut}(tower) $=3.5$ GeV is also optimal for $R = 0.7$ cone jets. Additional optimization of E_T^{cut}(seed) value (varied from 3.0 to 15.0 GeV) does not improve the result; therefore, E_T^{cut}(seed) is set to 0.0 GeV.

This jet algorithm configuration (E_T^{cut}(tower) $=3.5$ GeV, E_T^{cut}(seed) $=0.0$ GeV) is chosen to minimize the overall impact of pile-up on jets and simultaneously to guarantee that the distributions for jets are well comparable with the distributions for parent partons.

---

[1] similar cut of 2 GeV was used in Ref.[171] for high-luminosity studies

Figure 5.4: Mean value of the relative error on transverse momentum for reconstructed hardest in $\eta > 2.5$ region jet as a function of E_T^{cut}(tower) jet algorithm parameter. The reference value is p_T of the tagging quark. Presented are the results for signal S4 samples simulated with- and without pile-up. The error is statistical root mean square deviation. The other jet reconstruction parameters are: $R = 0.5$ cone, $E_T - scheme$, variable E_T^{cut}(tower) , E_T^{cut}(seed) $=0.0$ GeV, $\gamma+jet$ correction.
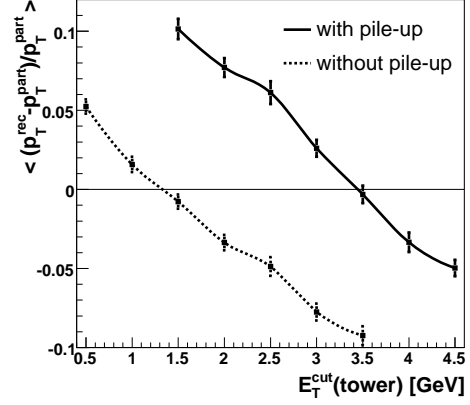
Pile-up and noise can, however, still potentially generate additional jets since deposits in calorimeter towers of these origins can be higher than E_T^{cut}(tower) . Such generated towers can produce fake jets. This has been studied with pile-up sample. The bulk of particles in pile-up event are soft (94% of pile-up generated particles poses $p_T<1$ GeV) and do not reach calorimeters. Nevertheless, calorimeter jets are still generated. The η distribution for them and the rates in particular η regions for two p_T threshold can be found in Figure 5.5. Most of the pile-up fake jets are soft, and the easiest way to get rid of them is imposing E_T^{cut}(jet) $=40$ GeV. These artificial jets were already visible in Fig. 5.3(a), where the rate of jets below around 40-50 GeV could not be explained by the rate of tagging quarks in signal event. Therefore, such soft jets should be treated with care and will be carefully studied later on in this thesis.

Figure 5.5: The rates of calorimeter jets induced by pile-up for two thresholds on jet p_T: 20 GeV, 40 GeV. Fake jets in $2.5 < |\eta| < 3.1$ intermediate region between HE and HF disappear if one selects hard jets only. Total jet rates per event in $-2 < \eta < 2$ region: 0.029 for $p_T>20$ GeV and 0.0027 for $p_T>40$ GeV are also presented. These results are obtained with the use of pile-up event sample. The other jet reconstruction parameters are: $R = 0.5$ cone, $E_T - scheme$, E_T^{cut}(tower) $=3.5$ GeV.
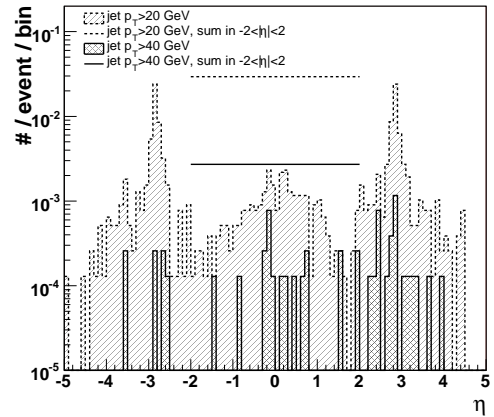
5. THE CMS DETECTOR AND RECONSTRUCTION OF ITS MEASUREMENTS

Another jet algorithm parameter is the recombination scheme. It is a method, in which the jet four-momentum $(E^J, \vec{P}^J)$ is built from four-momenta $(E^i, \vec{p}^{\,i})$ of jet constituents. Constituent (input object) is characterized by energy E^i and location: ϕ^i, η^i. Its transverse energy reads $E_T^i = E^i \sin\theta^i$. It is assumed to be massless. The two most popular recombination schemes are:

- $E - scheme$ [224] - used by CDF in RunI/II and by D0 in RunII:

$$P_\mu^J \equiv \sum_i p_\mu^i, \tag{5.1}$$

$$E_T^J \equiv E^J \sin\theta^J; \tag{5.2}$$

- $E_T - scheme$ [223] - used in Snowmass algorithm[1] and by D0 in RunI:

$$\vec{P}^J \equiv \sum_i \vec{p}^{\,i}, \tag{5.3}$$

$$E_T^J \equiv \sum_i E_T^i \Longrightarrow E^J \equiv E_T^J / \sin\theta^J. \tag{5.4}$$

Both schemes give, by definition, exactly the same result for collinear jet constituents (for very narrow jet cones). For acollinear constituents, the results should still be similar for narrow cones. However, if the cone size is increased, the results of two recombination schemes differ. It is expected that *E-scheme* would be better in reconstruction of massive, wide (*e.g.* R=0.7 cone) jet. This is because *E-scheme* directly relies on conservation of four-momentum. Such wide-cone jets are especially applicable to the case of hadronic decay of boosted W boson, where quarks are so close that they just fit into single wide cone.

Reconstructed jet variables need to be corrected in order to properly reproduce variables of the parent partons. Calibration of calorimeters itself is not enough since it deals with particular tower energies only. The sources of discrepancies are twofold. The physics effects are underlying event and pile-up (*i.e.* jet energy not coming from original parton). The detector effects are not only longitudinal (jet energy that do not fit into calorimeters) and out-of-cone leakages (jet energy that do not fit into the jet cone and soft tracks that are bended in magnetic field), but also non-uniformities and dead regions in the calorimeter response. With the future real data, so-called $\gamma + jet$ (uses exclusive events with photon and a jet with photon providing the true value of jet transverse momentum) and *jet+tracks* (out-of-cone tracks are included into a jet) corrections will be used to repair the jet variables. At present, one can

---

[1]actually original formulation of Snowmass algorithm differs a little from this definition of E_T-scheme

obtain these corrections only with simulated data. Alternative procedure is using the correspondence between reconstruction- and generation-level jets. Such corrections are called MC corrections.

The following jet collections (sets) are used in this thesis:

- `IC05ETGJ` - Iterative Cone jet collection with E_T recombination scheme and $\gamma+jet$ correction[1],

- `IC07E` - Iterative Cone jet collection with E recombination scheme and, specially designed by the author, MC correction that will be described in Sec. 5.4.2.

Their detailed configurations are presented in Table 5.1.

	`IC05ETGJ`	`IC07E`
jet algorithm	`Iterative Cone`	
jet cone	0.5	0.7
jet input	`EcalPlusHcalTowerInput`	
E_T^{cut}(tower)	3.5 GeV	
E_T^{cut}(seed)	0.0 GeV	
E_T^{cut}(jet)	20 GeV	
recombination scheme	E_T	E
jet corrections	γ-jet	MC correction in Sec. 5.4.2

Table 5.1: Configuration of the jet collections that are used in this thesis.

5.4.2 Reconstruction of boosted $W \to q\bar{q}$

This section is devoted to reconstruction of central ($|\eta| < 2.0$) and very hard ($\mathsf{p_T} >$ 200 GeV) W boson that decay hadronically and is characteristic for signal event[2]. Because of its high (transverse) momentum, the boson is very boosted. Hence, the quarks from its decay are close to each other in $\eta \times \phi$ space, their energy deposits in calorimeter overlap and could be qualified as a single jet activity. This feature was already seen in Figure 5.3(b) in quite large fraction of single $R = 0.5$ cone jets having transverse momentum comparable to $\mathsf{p_T}$ of hadronic W boson. This suggests that the standard hadronic W reconstruction using two jets can be inefficient. This subject was already discussed in Ref. [171] by ATLAS Collaboration, but was independently developed for the purpose of this work.

Eight options of hadronic W reconstruction: the usage of E and E_T schemes combined with two jet cones ($R = 0.5$ and $R = 0.7$), and with two W reconstruction ways

---

[1]standard $\gamma+jet$ correction constructed for low luminosity is used
[2]generation-level characteristics can be found in Fig. E.1
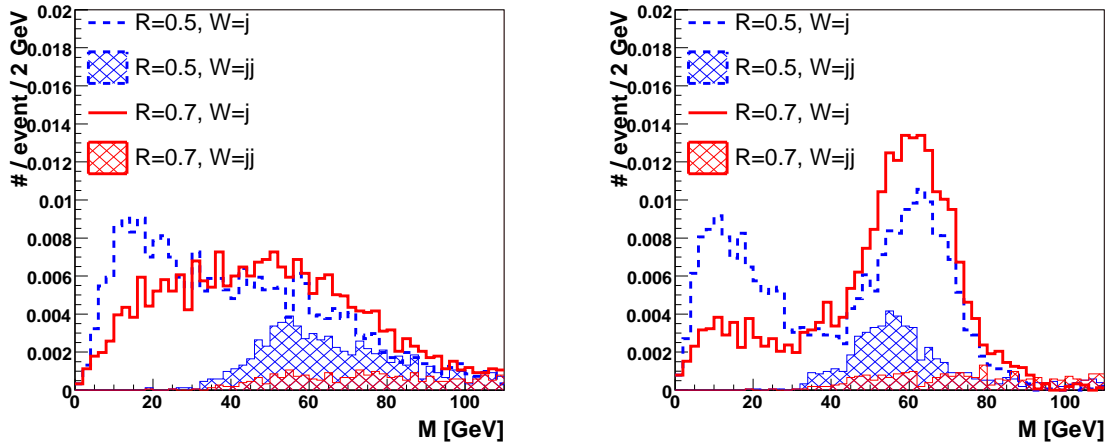
(a) Distributions of the W candidate invariant mass for E_T recombination scheme.

(b) Distributions of the W candidate invariant mass for E recombination scheme.

Figure 5.6: Distributions of the W candidate invariant masses for two recombination schemes: (a) $E_T - scheme$, (b) $E - scheme$. Two options on jet cone (R=0.5 and R=0.7) and two reconstruction methods ($W = j$ - reconstruction with the use of one jet and $W = jj$ - reconstruction with the use of two jets) are considered. Distributions are made for the candidate with invariant mass closest to M_W. Plots were made for signal S4 sample events surviving Introductory Selection that will be discussed in Section 6.3.2.

(using one and two jets) will be considered. They will be compared in the mass distributions of the candidate with mass closest to M_W. This is presented in Figure 5.6 for signal S4 event sample.

The W reconstruction with the use of two jets is highly inefficient (crosshatched histograms in Figures 5.6(a) and 5.6(b)). The requirement of two jets is itself very restrictive since most often there is only one central jet[1]. The W signal can be only observed for $R = 0.5$ cone, but with wide peak for mean mass about 55 GeV.

Reconstruction using one jet is much more efficient (empty histograms in Figures 5.6(a) and 5.6(b)). However, if $E_T - scheme$ is used, lots of jets appear for low invariant masses. If recombination scheme is changed to $E - scheme$, many jets appear for masses close to 60 GeV. The W jet seems to better fit into $R = 0.7$ cone. The evidence for this is an increase of event number at very low masses, which is more pronounced for $R = 0.5$ cone.

Hence, the best choice for hadronic W reconstruction is the reconstruction using single $R = 0.7$ cone jet recombined with $E - scheme$ (`IC07E` jet collection). However, such reconstructed W boson has a clear mass peak for value a bit lower than M_W (around 60 GeV). This problem can be repaired with the use of jet correction. Such

---

[1]The distribution of central cluster (generation-level jet) multiplicity is presented in Figure J.2(a)
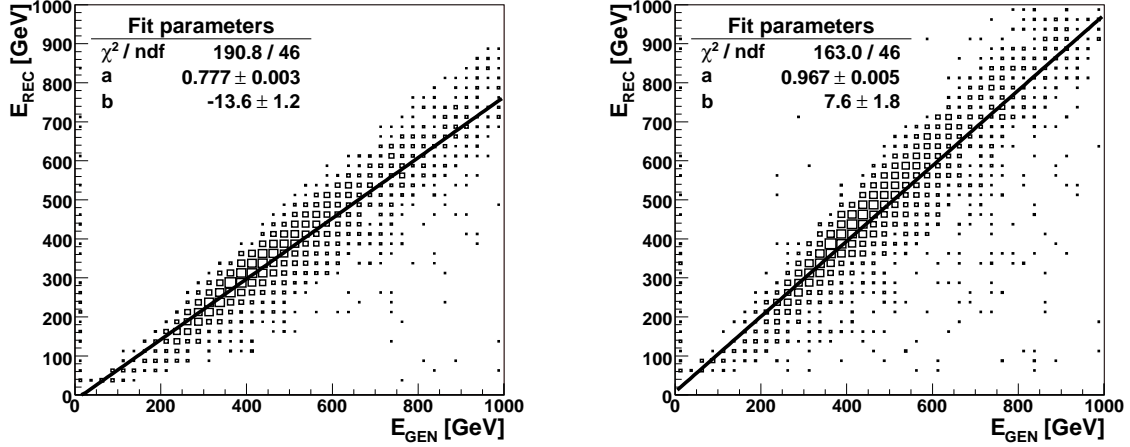
(a) Correlation between E_{GEN} and E_{REC} before correction.

(b) Correlation between E_{GEN} and E_{REC} after correction.

Figure 5.7: Correlation between generation- (E_{GEN}) and reconstruction-level (E_{REC}) energies for central jets in S4 signal sample before correction in (a) and after the correction in (b). For both cases distributions are fitted with $E_{REC} = a * E_{GEN} + b$ relation and the results are presented in the figures.

correction for $E - scheme$, $R = 0.7$ cone central jets and for high luminosity conditions was not available; therefore, dedicated MC correction has been prepared by the author himself.

The correction is based on a clear linear correlation between reconstruction- and generation-level energies of hard central jets in the signal S4 sample shown in Figure 5.7(a). The generation-level jets are found by applying the same, as for reconstruction-level jets, jet algorithm to generated stable particles. A matching criterion, based on the distance in $\eta \times \phi$ space, is used to associate generation-level jets with reconstructed jets. If there are two generation-level jets in $\Delta R = 1.5 * 0.7$ cone around reconstructed jet, the harder one is taken[1]. Linear function:

$$E_{REC} = a \ * E_{GEN} + b \tag{5.5}$$

is fitted to the mean and standard deviation of the points in every horizontal E_{GEN}-axis bin in Fig. 5.7(a). The fit result is presented in the figure. The above relation with a and b parameters can be used to obtain the true (corrected) value of jet four-momentum:

$$p^{\mu}_{true} = p^{\mu}_{REC} \times \frac{E_{REC} - b}{a * E_{REC}} \ . \tag{5.6}$$

This correction applies the factor obtained for energy to all components of jet four-momentum. Such approach is motivated by very similar correction factors for p_x and

---

[1]In 88% of events there is only one generation-level $R = 0.7$ jet.

p_y components[1] and also because it respects the old jet direction. After this correction, the W jet invariant mass clearly peaks at M_W value as is shown in Figure 5.8. Increase of the width of the mass peak is connected with a parameter being lower than unity.

This correction works very well for jets in the signal samples, but in general is applicable also to any central jets reconstructed with cone-based algorithm of the same parameters and for the same pile-up level.

The a and b correction parameters obviously depend on E_T^{cut}(tower) jet algorithm parameter. For lower values of E_T^{cut}(tower) , reconstructed jets should include (within the jet cone) more low-E_T towers and, as a result, be more energetic. Simultaneously, fit line in Figure 5.7(a) would become steeper, and a would approach unity. This behavior has been studied as a function of E_T^{cut}(tower) for ICE07 jets. As E_T^{cut}(tower) is changed from 5.5 to 1.0 GeV, the mass of the hardest central jet in $S4$ signal sample gets closer to M_W. For E_T^{cut}(tower) =1.0 GeV, mass distribution is peaked on 78 GeV. If the cut is further lowered to 0.5 GeV, very low-E_T towers are included, and the peak moves to around 90 GeV. This indicates that this cut value is too low. Correction

Figure 5.8: Invariant mass of ICO7E central jets in S4 signal event sample before and after the correction. The distribution obtained after correction is fitted with Gaussian in the region for which the curve is plotted. Obtained values of the fit parameters are presented in the figure.

with appropriate a and b parameters was applied for E_T^{cut}(tower) values in the range from 1.0 to 5.5 GeV. Obtained distributions of jet invariant mass after correction were fitted with Gaussian, and fit parameters are compared here. For E_T^{cut}(tower) between 1.0 and 3.5 GeV the standard deviations vary between 13.0 and 13.4 but are all consistent with themselves. The mean values change monotonically from 84.9±0.3 for E_T^{cut}(tower) =1.5 GeV to 78.4±0.3 for E_T^{cut}(tower) =5.5 GeV. The value E_T^{cut}(tower) that provides jet invariant mass consistent with M_W is around 3.5 GeV with estimated error of 0.3 GeV. This means that E_T^{cut}(tower) value optimal for ICET05GJ jet collection is also optimal for ICE07 collection.

Performance of the boosted hadronic W reconstruction can be summarized by the resolution and the pull in transverse momentum (the mass), defined as σ and

---

[1] and also for E_T and p_T

mean value of Gaussian fitted to:

$$\frac{\Delta p_T^{REC}(W_{Hadr})}{p_T^{REC}(W_{Hadr})} \equiv \frac{p_T^{REC}(W_{Hadr}) - p_T^{particle}(W_{Hadr})}{p_T^{particle}(W_{Hadr})} \tag{5.7}$$

distribution (for mass the distribution is analogical with p_T substituted by M). Indexes ^{REC} and ^{particle} refer to the variables for reconstruction- and particle-level (generation-level) objects. These distributions can be found in Figure I.2. The resolution in hadronic W boson transverse momentum is:

$$\frac{\sigma(p_T(W_{Hadr}))}{p_T(W_{Hadr})} = 10.9 \pm 0.2\% \ . \tag{5.8}$$

The resolution in mass reads:

$$\frac{\sigma(M(W_{Hadr}))}{M(W_{Hadr})} = 15.2 \pm 0.4\% \ , \tag{5.9}$$

i.e. 12.2 GeV[1]. This mass resolution is weak in comparison to value 6.9 GeV obtained for low luminosity conditions [171]. It is caused by specific reconstruction and wide cone. The $R = 0.7$ cone provides inclusion of the whole hadronic W activity, but results as well in big variations of reconstructed mass connected with noise and high luminosity pile-up. The W boson transverse momentum is here on average overestimated by 1.7% and the reconstructed mass overestimated by 4.3%, *i.e.* 3.5 GeV [2].

5.4.3 Reconstruction of tagging jets

Tagging jets are the next most characteristic signature of the vector boson scattering. These jets are the products of tagging quark fragmentation. They are to be observed in $|\eta| > 2$ region that is influenced by the intermediate domain between HE and HF calorimeters ($2.5 > |\eta| > 3.1$). As it was already shown in Figure 5.5, the number of jets reconstructed there is higher than expected. Therefore, one has to find a method discriminating between fake and real (tagging) jets.

In Figure 5.9(a), the p_T distribution of jets reconstructed in $-3.1 < \eta < -2.5$ region is compared with similar distribution for the right sideband region of the same length in η ($-2.5 < \eta < -1.9$). Behavior of these distributions suggests that in $-3.1 < \eta < -2.5$ region, in addition to quark jets, reconstructed are also soft jets ($p_T < 40$ GeV). As is shown in Fig. 5.9(b), the increase of rate of jets with 20 GeV$< p_T <$40 GeV in $-3.1 < \eta < -2.5$ region is significant, whereas for jets with $p_T >$40 GeV is not so much pronounced in comparison to sideband regions. The soft jets in $-3.1 < \eta < -2.5$ are obviously fake jets. This is also confirmed by integration of η distribution without p_T

---

[1]The resolution in Fig. 5.8 is different (13.5 GeV), but the other variable is fitted there.
[2]The pull in Figure 5.8 is 0.4 GeV, but the other variable is fitted there.
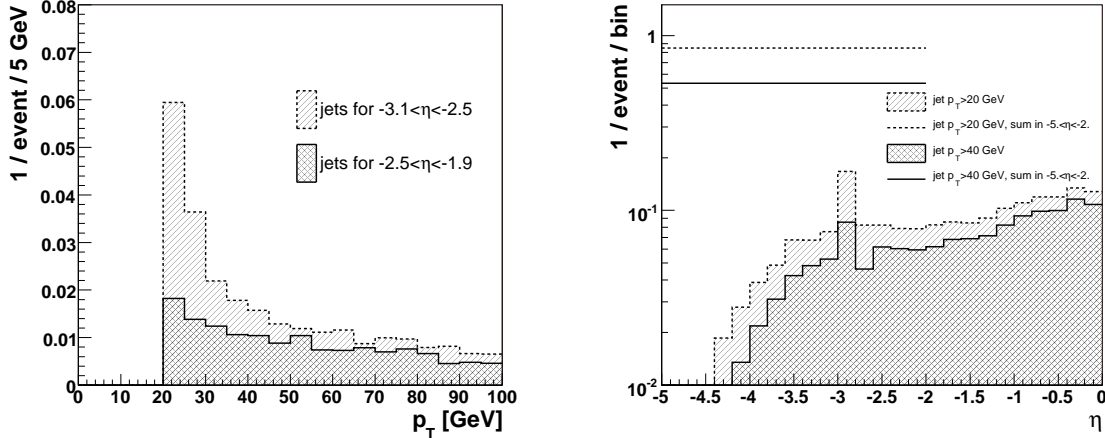
(a) The p_T distribution for jets in $-3.1 < \eta < -2.5$ and $-2.5 < \eta < -1.9$ regions.

(b) The η distribution for jets with $p_T > 20$ GeV and $p_T > 40$ GeV.

Figure 5.9: The p_T and η distributions for tagging jet candidates. The S4 signal event sample is used. The jet reconstruction parameters are: $E_T - scheme$, $R = 0.5$ cone, $E_T^{cut}(\text{tower}) = 3.5$ GeV.

cut up to $\eta = -2.0$ [1]. Probability of $p_T > 20$ GeV and $p_T > 40$ GeV jet observation in $\eta < -2.0$ region is 82% and 52%, respectively. These levels are illustrated in Fig. 5.9(b). Corresponding probability for tagging quark emission into $\eta < -2.0$ region is 66% and 52% for the same values of thresholds on quark transverse momentum. The rate of jets with $p_T > 20$ GeV is really overestimated, whereas for jets with $p_T > 40$ GeV is accurate.

These results suggest choosing the hardest jet for reconstruction of tagging quarks and imposing requirement of $p_T > 40$ GeV on this jet. This method was already used in Sec. 5.4.1 (the $2.5 > |\eta| > 3.1$ region was excluded there) with the same threshold applied to remove pile-up generated fake jets. Because $p_T > 40$ GeV cut value is in the region, for which the tagging quark p_T distribution has its maximum (*cf.* Fig. E.4(a)), this cut unfortunately will decrease the selection efficiency.

In this analysis, the candidates for tagging jets will be the hardest `ICO5ETGJ` jets in each of the two $|\eta| > 2.0$ regions. Transverse momentum resolution for such reconstructed jets was determined on the basis of curve in Figure I.3 and reads:

$$\frac{\sigma(p_T(j_{tag}))}{p_T(j_{tag})} = 17.0 \pm 0.4\% . \tag{5.10}$$

Thanks to optimization of $E_T^{cut}(\text{tower})$ the pull is consistent with 0, what means that on average transverse momentum is reconstructed with its true value.

---

[1] This upper limit is motivated by approximate lowest value of $|\eta|$ for tagging quarks.

5.4.4   Reconstruction of low-p_T central jets

The two going apart tagging quarks in signal process are not connected by the strong force; therefore, there is the rapidity gap between them [225, 226, 227]. The only hard hadronic activity in the central region is thus due to W bosons. The idea of mini-jet veto, *i.e.* utilization of jet rapidity gap, in vector boson fusion was originally intro-duced in Refs. [145, 228]. The question is whether it is still valid for high lumi-nosity condition and simulated detector effects. Thanks to the proper jet algo-rithm optimization, the jets in artificial
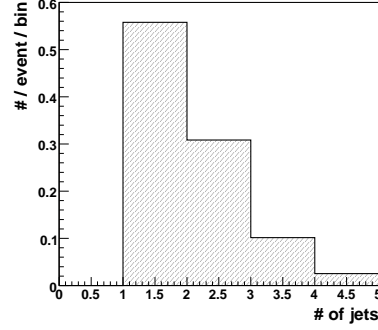
Figure 5.10: Multiplicity of central (p_T>20 GeV, $|\eta| < 2.0$) jets for the condition that both tagging quarks go to $|\eta| > 2.0$. The jet reconstruction parameters are: $E - scheme$, $R = 0.7$ cone, E_T^{cut}(tower) $=3.5$ GeV.

pile-up sample are hardly reconstructed with high p_T, as it is illustrated in Figure 5.5. The total expected in experiment rate of central pile-up generated jets with p_T>20 GeV is only about 0.028 per event. What is the central jet multiplicity in the signal event sample? Since the tagging quarks, as is shown in Figure E.4(b), can as well appear in the central region, it is better to count central jets only when tagging quark pseu-dorapidity is in absolute value greater than 2.0. For such condition, as is shown in Figure 5.10, around 56% of signal events contains only one IC07E jet with $|\eta| < 2$ and p_T>20 GeV that can identified with 1-jet hadronic W boson. The source of the extra jets is manifold: pile-up, underlying events, radiation of initial and final states and jet splitting. The extra jets appear in 44% of events. If this fraction was much higher in the background, the lack of central p_T>20 GeV jets (excluding W jet) could be a good signal signature.

5.4.5   Reconstruction of muons

The muon in signal event is hard, central and, since it originates from W decay, is also isolated, *i.e.* there are no detected charged tracks nearby it in the $\eta \times \phi$ space. The last feature can be utilized using Level-2 or Level-3 muon HLT reconstruction algorithms [207, 217] requiring *calorimetric* or *tracker isolation*, respectively. These al-gorithms were constructed for triggering purpose; however, they can be as well used to reconstruct muons in off-line analysis. The first algorithm is based on muon chambers only and is based on track fitting to the muon chamber hits and segments. The candi-dates are seeded by Level-1 muons. Additionally, one can require *calorimetric isolation*

of such muon, *i.e.* sum of calorimetric energy in the cone around the muon to be low enough. Level-3 reconstruction starts from Level-2 reconstructed muon and extrapolates its track to the tracker. This results in substantial improvement in precision of muon p_T estimation. For Level-3 muons, one can require *tracker isolation* that uses a sum of transverse momenta of the tracks in the cone around the muon. Since only tracks coming from the same collision vertex are considered, this method is less sensitive to pile-up. The thresholds for isolation are such set that the efficiency for obtaining isolated muons from W decays is 97%. More information on muon isolation can be found in Ref. [229].

Off-line Level-3 muon reconstruction should be the most adequate to signal events and it will be utilized here. Default thresholds and isolation algorithm configuration for high luminosity runs are used. The HLT p_T threshold for muons is 31 GeV; therefore, this limit is kept as minimal value for off-line muon transverse momentum. Cumulative efficiency for finding off-line isolated Level-3 muon with $|\eta| < 2.1$ and $p_T > 31$ GeV in S4 signal model events is 75.9%. This efficiency is technically obtained by requirement of at least one Level-3 muon with $|\eta| < 2.1$, $p_T > 31$ GeV and muon HLT positive decision[1] that provides isolation. Muon HLT positive decision alone is actually enough to obtain the same efficiency. Without isolation requirement (requirement of off-line Level-3 muon with $|\eta| < 2.1$, $p_T > 31$ GeV and Level-1 positive decision), the efficiency rises to 84.7%[2]. The scaling factor between these two efficiencies is 89.6%, and is much lower than efficiency of two successive isolation requirements that reads $\approx 97\% * 97\% = 94.1\%$. The difference can be explained by extraordinary transverse momentum of W bosons and muons that have not been considered in the isolation studies. As a result isolation thresholds do not provide 97%-efficiency for selection of such boosted muons, and requirement of standard isolation can lead to additional drop in efficiency. The isolation requirement is actually unnecessary since the only important source of high p_T muons, as in signal events, are leptonically decaying W bosons. Therefore, it has been decided to abandon isolation criterion in this thesis.

Muons will be reconstructed with the use of off-line Level-3 reconstruction algorithm without isolation requirement[3]. The efficiency for having at least one off-line Level-3 muon with $|\eta| < 2.1$ and $p_T > 31$ GeV (without Level-1 positive decision) is 87.8%. The transverse momentum resolution for muons in S4 signal events is 2.6% (*cf.* Fig. I.4(b)), what is consistent with the value in Ref. [207]. Such excellent resolutions are reached owing to combination on muon and tracker systems in reconstruction.

---

[1] HLT positive decision requires Level-1 decision

[2] efficiency for Level-3 muon with $|\eta| < 2.1$ and $p_T > 31$ GeV but without Level-1 positive decision is 87.8%

[3] `L3MuonReconstructor` reconstructor in ORCA

5.4.6 Reconstruction of missing transverse energy

The CMS calorimeter system is very hermetic. Therefore, the MET defined here as the minus vector sum of transverse energy of objects detected in calorimeters:

$$\overrightarrow{MET} = - \sum_{calo.\ objects} \vec{E_T} \ . \tag{5.11}$$

very well approximates the vector sum of momenta of particles escaping detection in calorimeters (neutrinos, muons[1], hypothetical sparticles, *etc.*). Since the signal events are characterized by the presence of one muon neutrino, a muon and no other escaping calorimetric detection particles, the $\overrightarrow{MET}$ reconstructs the transverse momentum of this neutrino after subtraction of muon transverse momentum.

It was chosen MET algorithm that uses calorimeter towers as *calo. objects*[2] in Eq. (5.11) [3]. The result is corrected for muons[4] and with MET type-1 correction [231, 232]:

$$\overrightarrow{MET}_{\mu,\ CORR1} = - \left[\sum_{calo.\ towers} \vec{E_T} \ + \ \overrightarrow{CORR}_{type-1} \right] + \sum_{muons} \vec{p_T} \ . \tag{5.12}$$

The MET type-1 correction is technically obtained using transverse momenta of raw (uncorrected) `ICO5ET` and corresponding corrected `ICO5ETGJ` jets:

$$\overrightarrow{CORR}_{type-1} = \sum_{p_T > 20\ GeV\ \texttt{ICO5ET}\ jets} (\vec{p_T}^{\texttt{ICO5ETGJ}} - \vec{p_T}^{\texttt{ICO5ET}}) \ . \tag{5.13}$$

The MET defined in Eq. (5.12) is found to provide the best estimate of the value and azimuthal angle ϕ of neutrino transverse momentum (see Figure I.1). The resolution for the value of MET is 25.9%, and the pull is 5.4%. The resolution for azimuthal angle ϕ is 20.4%, and the pull is consistent with 0.

5.4.7 Reconstruction of $W \to \mu\nu$

Leptonic W boson can be built from reconstructed muon and neutrino. The transverse momentum of neutrino is obtained from the MET. The only missing variable is neutrino longitudinal momentum p_z^ν. It could be potentially received from the assumption that μ and ν are collinear, but according to Fig. E.2(c) this is not the case. Alternatively,

---

[1]muons leave very small amount of energy in calorimeters and are treated as not detected in calorimeters

[2]`METfromEcalPlusHcalTower` reconstructor in ORCA

[3]The CMS MET reconstruction algorithms are described in Ref. [230]

[4]muons are reconstructed with off-line muon reconstructor that combines information from muon and tracker system `GlobalMuonReconstructor` [207, 217]

neutrino longitudinal momentum can be obtained from the requirement that invariant mass of a pair composed of the muon and the neutrino equals M_W:

$$\sqrt{(E(\nu) + E(\mu))^2 - (p_x(\nu) + p_x(\mu))^2 - (p_y(\nu) + p_y(\mu))^2 - (p_z(\nu) + p_z(\mu))^2} \equiv M_W \ . \ (5.14)$$

This problem leads to quadratic equation in $p_z(\nu)$. Real solutions exist provided determinant is positive. The efficiency of this requirement is 71% for signal S4 model events[1]. There is certainly an ambiguity between two possible solutions. Solutions with "+" and "-" signs in the formulas lead to neutrino candidates that will be called *plus* and *minus*, respectively. These two obtained candidates have different longitudinal momentum $p_z(\nu)$; however, their distances in η from the muon are the same. It means they have pseudorapidities $\eta(\mu) \pm \Delta\eta$; therefore, one can not in principle choose the candidate that is in ΔR closer to the muon.

The following recipes for neutrino candidate are considered:

1. candidate (*plus* or *minus*) with smaller $|\eta|$,

2. candidate (*plus* or *minus*) leading to more back-to-back W bosons,

3. candidate with $\eta_\nu = \eta_\mu$,

4. candidate *plus*,

5. candidate *minus*.

The first option leads to more central neutrino and leptonic W. The second one is based on the feature that leptonic and hadronic W's go back-to-back (Fig. E.1(c)). Since the ϕ angle

Figure 5.11: Distribution of the difference in η between reconstructed (ν_{rec}) and generation-level (ν_{part}) neutrino for various neutrino candidates. Plot is made after Introductory Selection to be described in Sec. 6.3.2. Distribution for "$\eta_\nu = \eta_\mu$" candidate is scaled by 1/71% factor.

of $W(Lept)$ is fixed, $W(Lept)$ is more back-to-back to $W(Hadr)$ if the value of $|\eta_{W(Lept)} + \eta_{W(Hadr)}|$ is smaller. The solution (*plus* or *minus*) leading to smaller value of this expression is chosen for the second candidate. The $\eta_\nu = \eta_\mu$ candidate means reconstruction of neutrino direction with assumption that its pseudorapidity is the same as for the muon. Two last options on neutrino reconstruction are arbitrary choices of candidates with fixed sign in the solution formula.

---

[1] This efficiency is obtained after cuts on muon and MET in Introductory Selection in Sec. 6.3.2.

All these options provide neutrinos with the same transverse momentum; however, they differ in η. Distributions of η distances from generation-level neutrino for various neutrino candidates are presented in Figure 5.11. Distributions are asymmetric for both *minus* and *plus* candidates, what disfavors these options. Distribution for the $\eta_\nu = \eta_\mu$ neutrino candidate is scaled in this figure by $1/71\%$ factor in order to take into account the fact that Eq. (5.14) has not always got a solution. Nevertheless, this option provides candidate that is much separated from the real neutrino, with two well-separated peaks in $\Delta\eta$ distribution. The other two options ("smaller $|\eta|$" and "back-to-back") provide $\Delta\eta$ distributions that are centered around zero and being statistically consistent with each other (consistent means and root mean square (RMS)'s). The "smaller $|\eta|$" candidate is chosen since its $\Delta\eta$ distribution is characterized by mean closer to 0 and lower RMS.

Leptonic W will be built from muon and neutrino candidate with smaller $|\eta|$. The proposed method for the reconstruction of leptonic W provides good transverse momentum and direction resolutions (*cf.* Fig. I.5). The resolution in transverse momentum is 10.0% and the pull is only 2.2%.

5.4.8   Reconstruction of high mass WW pair

One of the signal process signatures is high invariant mass of reconstructed W boson pair. The distribution of the error on this invariant mass is presented in Figure 5.12. The resolution:

$$\frac{\sigma(M(WW))}{M(WW)} = 10.9 \pm 0.1\% \quad (5.15)$$

is the measure of detector and reconstruction influence on reconstructed WW mass. These effects smear particle-level WW resonant distribution fitted with Gaussian of mean 828±2 GeV and $\sigma = 143 \pm 2$ GeV to distribution fitted with Gaussian of mean 815±3 GeV and $\sigma = 203 \pm 3$ GeV.
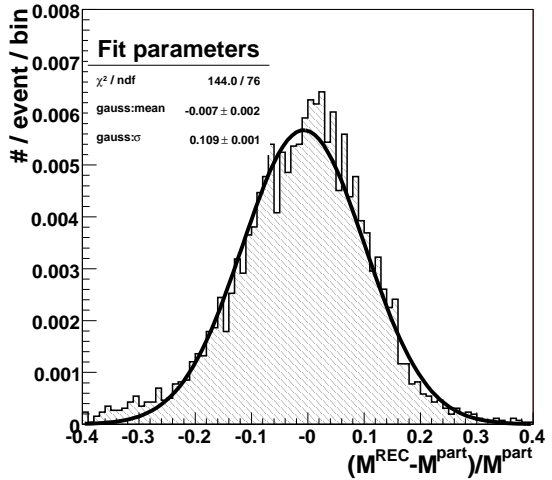
Figure 5.12: Distributions of the error on invariant mass of reconstructed WW boson pair in signal S4 event sample.

5.5   Trigger path for selecting the signal events

Trigger is by definition on-line selection; however, in simulation its action is performed on simulated and already reconstructed data. Nevertheless, its positive should be made before user dedicated selection that is called off-line selection.

5. THE CMS DETECTOR AND RECONSTRUCTION OF ITS MEASUREMENTS

Trigger path is a part of the whole trigger algorithm that can be used for selection of certain processes, here vector boson scattering. There will be considered here general trigger options, *i.e.* triggering on MET, hard jets or muon signatures. High luminosity Level-1 and HLT thresholds on these objects are listed in Table 5.2. In Level-1, events will be easily selected by "single muon" and "muon*jet" [1] algorithms (*cf.* Figs. E.2(a) and E.1(a) in App. E). In HLT exclusive "multi-jet" triggers and "jet*E_T^{miss}" triggers are useless for the purpose of these analysis since the thresholds for these triggers are much higher (or unacceptably high in the case of "jet*E_T^{miss}" trigger) than the transverse momenta of signal event jets and neutrinos. The best choice is exclusive single isolated muon trigger.

	Level-1 thresholds	HLT thresholds
single muon	20 GeV	31 GeV
1-jet, 3-jets, 4-jets	250 GeV, 110 GeV, 95 GeV	860 GeV, 326 GeV, 200 GeV
jet*E_T^{miss}	113 GeV*70 GeV	200 GeV*150 GeV
muon*jet	15 GeV*40 GeV	—

Table 5.2: High luminosity Level-1 Trigger and HLT thresholds on the transverse momentum of objects appearing in signal events. The "multi-jet" triggers requires according p_T for every jet, *e.g.* HLT "3-jets" requires 3 jets with p_T>326 GeV. The numbers are approximate. Based on [217, 218].

Level-1 muon trigger requires at least one p_T>20 GeV muon in the event. At the next step in HLT at least one off-line Level-3 muon should be harder than 31 GeV. Additionally this muon must satisfy *tracker isolation* criterion. The efficiency for finding generation-level muon with p_T>31 GeV in S4 event sample is about 97% (based on Fig. E.2(a)), and this is the upper limit on muon trigger efficiency. Additional loses of efficiency would be caused by reconstruction and isolation requirement. In Section 5.4.5 it was decided not to use isolation requirement. The efficiency of such muon HLT without isolation requirement (technically obtained by requirement of off-line Level-3 muon with $|\eta| < 2.1$, p_T>31 GeV and Level-1 positive decision) is, as was already given in Sec. 5.4.5, 84.7%. This value is acceptable for triggering; therefore, single muon trigger without isolation requirement will be exclusively used for triggering signal events, *i.e.* only events fulfilling this requirement will be taken for further analysis. Potential increase of efficiency due to the other mentioned trigger options is low. Thus, other trigger options are not taken into account.

---

[1] "muon*jet" denotes simultaneous requirement on the muon and the jet

Chapter 6

Analysis of data

This chapter is concentrated on the strategy that could lead to observation of indications of strongly-coupled electroweak symmetry breaking sector. This strategy is prepared with the use of simulated data. Event samples that are used are defined in the beginning. Next, preselection procedure that enables obtaining background samples with signature close to that for signal event is constructed. Later on, it is described the selection process of events. Selection steps are optimized to maximally increase the signal significance, *i.e.* observability of the signal model events in the presence of background. The results are summarized at the end of this chapter and discussed in the next chapter.

6.1   Simulated event samples

The strategy for selecting real events is established with simulated signal and background processes. Necessary event samples were prepared according to the results of Chapter 4.

6.1.1   Signal event samples

In order to study the LHC sensitivity to the strongly-coupled sector, representative points in the $a_4 \times a_5$ parameter space, shown in Fig. 3.1, have been chosen. Points are precisely defined in Tab. 3.1. With exception for one point (NR), they represent models containing resonance(s) with theoretical mass(es) given in this table. Thanks to the symmetries, these points represent almost the whole space presented in Fig. 3.1.

The LO calculations and cross-sections provided by PYTHIA generator are used. Calculations including NLO effects are not yet available; however, they are expected to be small since $K = 1.1$ factor is obtained for similar vector boson fusion with Higgs resonance [233]. Since this correction is not significantly greater than unity, the NLO effects can be neglected.

The signal model samples were generated in PYTHIA 6.3 using the methods described in Section 4.2.5.2. Detailed configuration of the generator can be found in App. C.1. Details of parameters for particular samples are presented in App. D. These samples were generated with- or without preselection that will be described in Sec. 6.2. Details on simulated samples are given in Tab. 6.1.

6.1.2 Background event samples

According to the results of Section 4.3.7, it is enough to use only $t\bar{t}$ and $Wjjj$ (exclusive) event samples, generated in PYTHIA with p_T-ordered parton-shower, to properly represent $t\bar{t}+jets$ and $W+jets$ (inclusive) background processes. Due to very large cross-section for those processes, the generation-level cuts (on generated partons and bosons) are implemented. These cuts are based on jet p_T thresholds, jet η range and minimum jet-jet distance ($\Delta R(j,j)$). This enables generation of events that fall within the experimentally observable region and possess signature closer to typical signal event.

The $t\bar{t}$ sample was generated in PYTHIA 6.3 (configuration can be found in App. C.1, and generator cuts in App. D) with the $\hat{p}_\perp$=100 GeV cut, which means generation of top quarks with c.m.s. transverse momentum greater than 100 GeV. The cut provides harder and more central W bosons. As a result, the cross-section for such generated sample is incompatible with standard value for LHC $t\bar{t}$ cross-section. However, the generator configuration was verified by $t\bar{t}$ generation without $\hat{p}_\perp$ cut, and good compatibility has been obtained.

Decay modes of W bosons coming from top quark decays are set to mimic the final state in signal events. It is possible with the use of PYTHIA cards to turn on only one configurations: either $W^- \rightarrow q\bar{q}$ and $W^+ \rightarrow \mu^-\bar{\nu}$, or $W^+ \rightarrow q\bar{q}$, $W^- \rightarrow \mu^+\nu$ since these bosons do not originate from the same vertex. Therefore, only $W^- \rightarrow q\bar{q}$ and $W^+ \rightarrow \mu^-\bar{\nu}$ modes are used, but the cross-section for the sample will be doubled to take into account opposite configuration as well.

The NLO effects in $t\bar{t}$ production are included with the use of K=1.8 factor.

The obtained cross-section in PYTHIA for only $W^- \rightarrow q\bar{q}$, $W^+ \rightarrow \mu^-\bar{\nu}$ mode turned on is 19 pb. If all decay modes are allowed the cross-section is thus 261 pb. It is comparable with the value obtained in CompHEP (303 pb). Corresponding horizontal line (with K=1.8 factor) is presented in Fig. 4.4(a).

The value of 19 pb for the cross-section has been obtained with m_{top}=175 GeV set in generator. Since the latest top quark mass is 171.4±2.1 [234], the cross-section needs to be corrected. Because of $\Delta\sigma/\sigma \approx -5 * \Delta m_{top}/m_{top}$ [188] dependence between $t\bar{t}$ LHC

cross-section and top quark mass, obtained cross-section should be increased by 10.3% to 21.1 pb.

The W^+jjj and W^-jjj event samples were generated in COMPHEP 4.2p1 with parameters given in App. F and generation-level cuts presented in App. H. Subsequently, these samples were processed with PYTHIA 6.3 for showering with only $W \rightarrow \mu\nu$ decay mode switched on. PYTHIA parameters can be found in App. C.1.
Generation-level jets are required to have p_T>30 GeV and $|\eta|$<5.0. The first cut enables generation of events with hard three jets. Additionally it is required p_T>100 GeV for the hardest jet that is expected to imitate signal event hadronic W. For real generation-level W boson, it is required p_T>100 GeV and $|\eta| < 3.0$ (for W^+jjj sample $|\eta| < 5.0$ cut). Minimal jet-jet ΔR distance is 0.5, and is motivated by singularity in calculations with small ΔR. This requirement allow also to avoid generation of jets that would be reconstructed within the same jet cone. This way obtained cross-section is reliable, and matching procedure is not needed. The obtained cross-section (in Tab. 6.1) for W^+jjj and W^-jjj event samples is similar to official CMS value for $Wjjj$ cross-section reading 722 fb for very similar generation-level cuts [1].

All background event samples were generated with preselection that will be described in Sec. 6.2. Summarized data for these samples can be found in Table 6.1.

6.2 Preselection procedure

Integrated luminosity of collected data in amount of at least 100 fb^{-1} is needed; therefore, a desired goal of simulation is to have all above event samples in corresponding size. However, it is almost impossible to produce them in so large statistics because full simulation and reconstruction of the CMS detector are very CPU time consuming. Even if it was feasible, most of the events would be discarded in the selection. Common approach in such cases is filtering generated events at the level of generation. This procedure is called preselection. Only accepted events are subsequently passed through the simulation and reconstruction of the detector. In this study, preselection operates on the objects obtained in the event after decaying, showering and hadronization in PYTHIA, *i.e.* muons and clusters. Clusters are obtained with parameters defined in Sec. C.3. Muons and electrons are excluded from clusterization. The preselection objects are defined as:

- central cluster: cluster with $|\eta|$<2.2 and p_T>30 GeV;

- forward/backward cluster: cluster with $|\eta|$>2.2 and p_T>30 GeV;

---

[1]can be found at https://twiki.cern.ch/twiki/bin/view/Main/Prod06

	event sample	generator	cross-section				presel. factor [%]	Number of preselected events in $\mathcal{L}_{int}$=100 fb^{-1}	Events simulated	Simulated fraction of events in $\mathcal{L}_{int}$=100 fb^{-1}
			generator level (σ_{gen}) [fb]	branching ratio not included in σ_{gen} BR($W \to$...)*combin. factor	K-factor	$\sigma_{gen}*$BR($W \to$...)$*$ combin.fac.$*K$ [fb]				
signal samples	S1 presel	P	6.5	1. * 1.	1.	6.5	64.6	420	5051	1203%
	S4	P	11.4	1. * 1.	1.	11.4	100.0	1140	25735	2257%
	S4 presel	P	11.4	1. * 1.	1.	11.4	62.3	710	5222	735%
	S6 presel	P	30.4	1. * 1.	1.	30.4	43.0	1307	5066	388%
	V1 presel	P	4.9	1. * 1.	1.	4.9	64.4	316	5500	1743%
	V2 presel	P	4.9	1. * 1.	1.	4.9	64.2	315	5332	1695%
	VS presel	P	21.9	1. * 1.	1.	21.9	48.5	1062	5861	552%
	VS1 presel	P	6.8	1. * 1.	1.	6.8	64.4	438	5698	1301%
	NR presel	P	4.3	1. * 1.	1.	4.3	63.7	274	5495	2006%
backgr. samples	$t\bar{t}$	P	21100.	1. * 2.	1.8	75960.	7.07	537037	62562	11.6%
	$W^- jjj$	C	235400.	0.102 * 1.	1.	24011.	19.7	473013	53722	11.4%
	$W^+ jjj$	C	421700.	0.102 * 1.	1.	43013.	18.4	791447	79071	10.0%

Table 6.1: Details on fully simulated event samples for signal and background processes. Samples were generated in PYTHIA 6.3 (denoted as P) and in COMPHEP 4.2p1 (C). Cross-sections are provided by the generator, so if events were generated in COMPHEP, it is necessary to take into account branching ratios since decay modes for W bosons are set in such case just in PYTHIA during showering. Combinatorial factor takes into account not included in the cross-section and not available through PYTHIA cards charge-symmetric to $t\bar{t} \to W^+ W^- \to \mu^+ \bar{\nu} q \bar{q}$ decay channel. Number of events for 100 fb^{-1} is: N=$\sigma_{gen}*$ BR $*$ combin. factor $*K*$ 100 fb^{-1}.
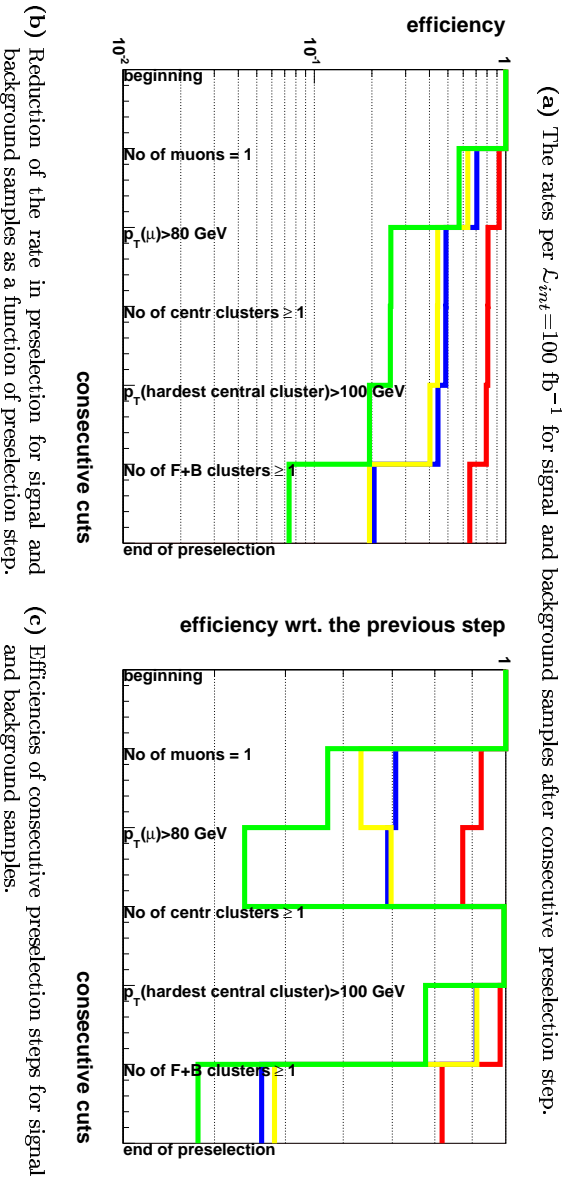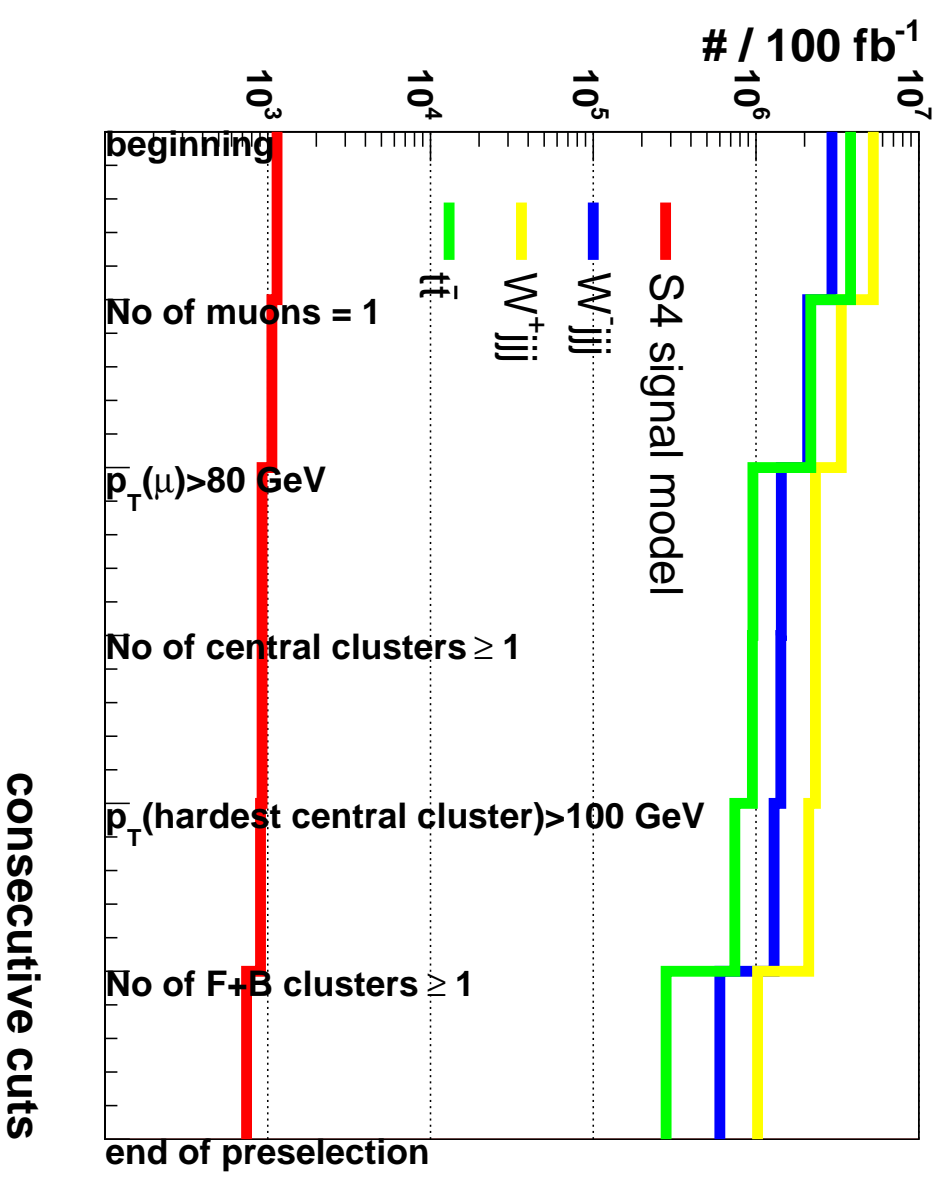
Figure 6.1: Preselection efficiencies for signal and background samples.

(a) The rates per $\mathcal{L}_{int}$=100 fb^{-1} for signal and background samples after consecutive preselection step.

(b) Reduction of the rate in preselection for signal and background samples as a function of preselection step.

(c) Efficiencies of consecutive preselection steps for signal and background samples.

- muon (μ): muon with $|\eta|$<2.5 and p_T>40 GeV.

Distributions of muon and cluster multiplicities and transverse momenta for clusters are presented in Appendix J. Relying on these distributions the following preselection criteria have been proposed:

1. number of muons = 1;

2. $p_T(\mu) > 80$ GeV;

3. number of central clusters ≥ 1;

4. p_T(hardest central cluster) > 100 GeV;

5. number of forward+backward (F+B) clusters ≥ 1.

Detailed data on the resulting preselection efficiencies for all simulated samples of background and signal can be found in Table 6.1. They are also illustrated in Figure 6.1. Thanks to the preselection, discrepancy in the rates between signal and background processes is reduced by about one order of magnitude. Another advantage of preselection is reduction of signal samples only to around 60% of their initial cross-section, whereas background samples are reduced to about 10%. Nevertheless, as is given in Tab. 6.1, it has been simulated only about 11% of background preselected events to be collected during high luminosity year of data taking.

Preselection requirements are rather loose to limit a related systematic error and to leave a room for selection operating on fully simulated events. Background samples were generated only with preselection. Because of low cross-section for signal processes, consideration of signal event samples without preselection is feasible. One signal process (S4) has been simulated with- and without preselection. These samples enable verification of preselection and estimation of preselection effect on final results. The other signal model samples were generated only with preselection.

All background and signal event samples have been treated with full simulation of the CMS detector response and next reconstructed.

6.3 Selection procedure

The aim of selection procedure is to suppress the overwhelming background with the use of signal characteristics defined in Section 4.2.5.3 and reconstruction methods described in Section 5.4.

Selection does not exactly follow real data flow, where events are first accepted by on-line selection, *i.e.* trigger algorithms, and next selected by custom off-line procedure. For the purpose of this analysis, the selection method of simulated data is

changed. First, it is applied preselection - already described in previous chapter. Next follows Introductory Selection that operates on simulated detector events and initially reduces the background. It contains trigger decision treated as an usual selection cut and introductory requirements that are necessary for the next selection part. Multiplicities of basic objects and cuts on their transverse momenta, invariant masses and pseudorapidities are among these requirements. They are arranged in 4 selection steps that are applied consecutively. The next group of requirements is the Main Selection. It consists of 6 steps that are also applied consecutively. Selection is prepared using S4 signal model sample without preselection (with generation-level cuts only) and background samples generated with preselection. As a result, the efficiencies for initial selection steps do not correspond to efficiencies for real processes. Nevertheless, the final results should be comparable with that obtained with the use of real data.

Technically, the selection is made with the use of four-momenta and multiplicities of basic reconstruction objects stored in the ROOT tree. This enables fast access to data, unrestricted ordering in Main Selection and straightforward optimization of the cuts.

The efficiencies of every selection step will be presented in Table 6.5 and illustrated in Figure 6.7 that can be found at the end of this chapter.

6.3.1   Selection optimization method

Values of cuts have been optimized using signal significance that quantifies the signal in the presence of background. Available small background samples do not enable application of more sophisticated methods. Therefore, it was decided to use very simple, but the most popular estimator using total number of signal and background events:

$$S_{c1} = \frac{N_S}{\sqrt{N_B}} \tag{6.1}$$

that says how much the signal rate is greater than the uncertainty on the background. N_S and N_B are the numbers of signal and background events collected by the experiment in the same period of time and surviving particular selection cuts. This estimator is not the most optimal (*cf.* Ref. [235] and App. A in Ref. [236]); however, for high background multiplicities (like in the case of this study) it provides the limits close to that obtained with the use of better estimators.

The greater the significance is, the lower is the probability that observed signal is background fluctuation. Signal significance can be calculated for variable value of selection cut, what enables choosing the cut (called optimal), for which S_{c1} is maximal. Such optimization can be made for every cut in sequence; however, sometimes less selective cut will be applied.

The figures presenting distributions of cut variables in signal and in background are presented in Appendix K. These distributions are normalized to unit area. They include as well the dependence of the S4 signal significance on the cut value, which is calculated for signal and background rates for $\mathcal{L}$=100 fb^{-1}.

6.3.2 Introductory Selection

Introductory selection steps are the following:

1. **Trigger decision**

   Trigger path that can be used in the on-line selection has been already described in Sec. 5.5. It has been argued that the muon HLT without requirement of muon isolation is optimal. Its efficiency (including Level-1) to select S4 signal model events is 84.7%.

   Unfortunately, the information about the Level-1 trigger decision is available only for a number of signal event samples and not for background[1]. Therefore, muon HLT must be considered without Level-1 trigger, what is equivalent to requirement of at least one off-line Level-3 muon with p_T>31 GeV and $|\eta| < 2.1$. Efficiency for this case is 87.8% and is only greater by 3.1% than nominal muon HLT (with Level-1) efficiency. It is expected that this difference will disappear for both signal and background event samples after very restrictive off-line muon cut (of the order of 100 GeV) and that not considering Level-1 trigger does not bias the results.

   Summarizing this selection step requires at list one off-line Level-3 muon with p_T>31 GeV and $|\eta| < 2.1$.

2. **Numbers of basic objects**

   In this selection step, necessary numbers of basic objects are required. Proper multiplicities will enable dealing with kinematic properties of these objects in next the steps. The requirements are the following:

   - numbers of jets
     (a) number of hard (p_T>20 GeV) and central ($|\eta|$<2.0) IC07E jets:
        $N($IC07E$) \geq 1$
     (b) number of hard (p_T>20 GeV) and forward (4.5>η>2.0) IC05ETGJ jets:
        $N($IC05ETGJ$, \eta > 0) \geq 1$

---

[1]The reason is that Digis files, where this information is stored, are no longer accessible for the background and for some of the signal samples.

(c) number of hard ($\mathsf{p_T}$>20 GeV) and backward (-4.5<η<-2.0) `IC05ETGJ` jets:

$N(\mathtt{IC05ETGJ}\ ,\ \eta < 0)\ \geq$1

- numbers of muons

(a) number of hard ($\mathsf{p_T}$>31 GeV) and central ($|\eta|$<2.1) Level-3 muons:

$N_\mu \equiv$1

Thanks to muon HLT, efficiency of this requirement is close to unity, and the only reduction is caused by reconstruction of more than one muon.

Distributions of the numbers of jets and muons can be found in Figure K.1. The cuts listed above correspond to the cuts for which the significance is high, however, not always maximal.

3. **Muon and MET**

Muon and the MET are reconstructed as described in Sections 5.4.5 and 5.4.6. The distributions of $p_T(\mu)$ and the value of MET can be found in Figures K.2 and K.3. The optimal values of $p_T^{cut}(\mu)$ and MET^{cut} obtained from significance maximization are around 150 GeV. Nevertheless, lower values are chosen:

- $p_T(\mu) > p_T^{\mathrm{cut}}(\mu)$=100 GeV,

- $MET > MET^{\mathrm{cut}}$ =100 GeV,

what results in signal significance only a bit lower than the maximal. These lower values leave more room for later-on leptonic W cut optimization.

4. **Reconstruction of selection objects**

In this step, all necessary candidates for selection objects (leptonic W, hadronic W, tagging jets) in the event are identified:

- The candidate for boosted $W \to q\bar{q}$ boson is hard ($\mathsf{p_T}$>20 GeV) and central ($|\eta| < 2.0$) `IC07E` jet with four-momentum corrected as in Section 5.4.2. The candidate with corrected mass closest to the W boson mass is chosen. This method of reconstruction (using single jet rather than two jets) is motivated by signal characteristics. Furthermore, this type of reconstruction would enables efficient reduction of the background in Main Selection. This is illustrated in Figure 6.2, where these two reconstruction methods are compared. The W bosons in $t\bar{t}$ background events are not as much boosted as in signal sample. Therefore, the mass peak in single jet reconstruction is hardly visible on top of the falling down spectrum. For both $Wjjj$ samples,

99

(a) Distribution of the invariant mass for hadronic W candidates reconstructed with the use of single `ICO7E` jet.

(b) Distribution of the invariant mass for the hadronic W candidates reconstructed with the use of two `ICO5ETGJ` jets. The bin at 0 means failed reconstruction, *i.e.* lack of two central jets.
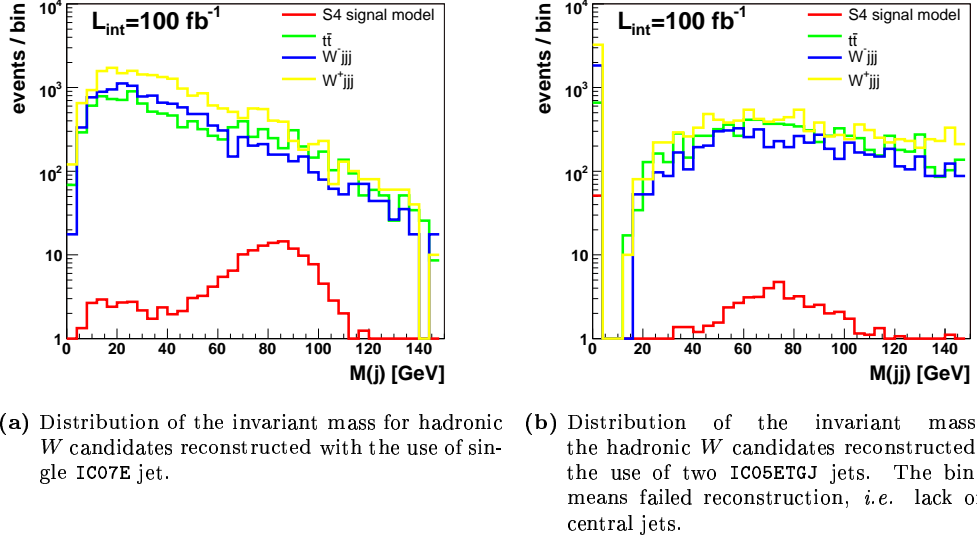
Figure 6.2: Distributions of the invariant masses for the hadronic W candidates in background and signal samples with the use of two reconstruction methods: (a) reconstruction using single jet, (b) reconstruction using two jets.

there is no W peak visible since real W boson is forced to decay leptonically, and the candidates for hadronic W boson are reconstructed from the hardest central jets.

- The $W \to \mu\nu$ is reconstructed according to procedure presented in Section 5.4.7. The efficiency of this reconstruction (with respect to the previous selection step) is 71% for signal and 61% for background events.

- Forward jets are tagged according to the recipe presented in Section 5.4.3 (hardest jets are called tagging).

Efficiency of this selection step is fully determined by $W \to \mu\nu$ reconstruction efficiency.

$t\bar{t}$	$W^- jjj$	$W^+ jjj$	whole background	signal model S4	after Introductory Selection	
					S4 signal to backgr. ratio $N_S(\text{S4})/N_B$	S4 signal significance
$2.1 \cdot 10^{-2}$	$2.1 \cdot 10^{-2}$	$2.6 \cdot 10^{-2}$	$2.5 \cdot 10^{-2}$	$1.3 \cdot 10^{-1}$	$3.4 \cdot 10^{-3}$	0.72 ± 0.01

Table 6.2: The total Introductory Selection efficiencies.

The total efficiencies of Introductory Selection are grouped in Table 6.2. Details on efficiencies for individual steps can be found in Table 6.5 that will summarize the results of the whole selection. As is seen in Tab. 6.2, the background is about 5 times more reduced than the signal S4 sample. Even so, the signal significance (with statistical

error) is only 0.72±0.01. The signal peak in WW invariant mass distribution is not visible under overwhelming background processes either (*cf.* Fig. 6.3).
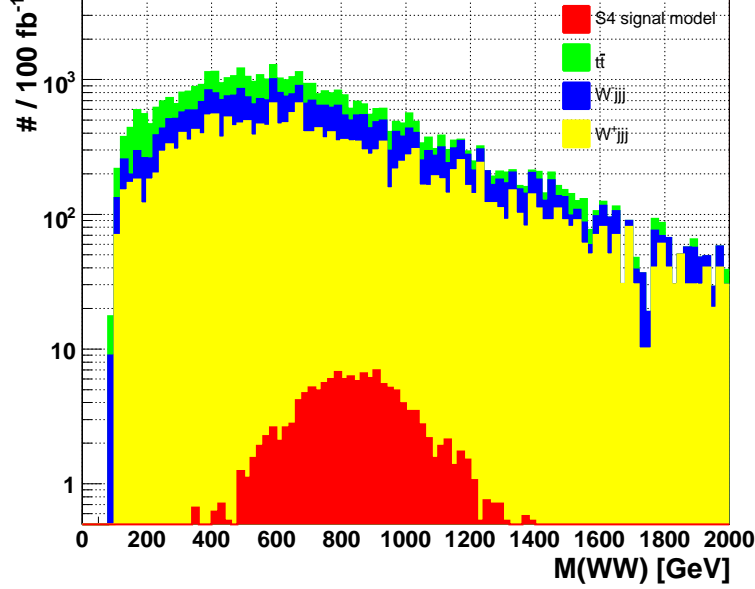
Figure 6.3: Distributions of the reconstructed WW invariant mass after Introductory Selection. There are shown distributions for signal and various background samples. Contribution from each of these samples is indicated with full color histogram and plotted on top of earlier plotted (lower) histogram. The contour of the histogram on top is the whole contribution from background and signal.

6.3.3   Loose Main Selection

Main Selection imposes requirements on kinematics of selection objects (hadronic W, leptonic W, tagging jets) and additional veto requirements. There are in total 6 steps of this selection.

It is expected that selection cuts are correlated; therefore, initially rather loose cuts are applied here in loose Main Selection. The aim is to remove the events that certainly should be discarded. After that, the selection will proceed with cut optimization that should further improve signal significance. It will be described in Section 6.3.4.

The requirements of Main Selection are applied in sequence. They are the following:

1. **Hadronic W**

   Distributions of reconstructed $M(W_{\mathrm{Hadr}})$, $\Delta M(W_{\mathrm{Hadr}}) \equiv |M(W_{\mathrm{Hadr}}) - M_W|$ mass shift, p_T and η for the candidate for hadronic W in background and signal sample are presented in the subfigures of Figure K.5. The following values of loose cuts are established:

   - $\Delta M(W_{\mathrm{Hadr}}) < \Delta M^{\mathrm{cut}}(W_{\mathrm{Hadr}}) \equiv |M(W_{\mathrm{Hadr}}) - M_W|^{\mathrm{cut}} = 40$ GeV,

- $p_T(W_{\text{Hadr}}) > p_T^{\text{cut}}(W_{\text{Hadr}}) = 150$ GeV,

- $|\eta(W_{\text{Hadr}})| < \eta^{\text{cut}}(W_{\text{Hadr}}) = 2.0$.

2. **Leptonic** W

The distributions of p_T and η for the candidate for leptonic W in background and signal sample are presented in the subfigures of Figure K.4. Because of $p_T^{\text{cut}}(\mu)$ and MET^{cut} cuts in Introductory Selection and already applied cut on hadronic W, leptonic W appears to be harder than the hadronic W (*cf.* Fig. K.5). The loose cuts on W_{Lept} are the following:

- $|\eta(W_{\text{Lept}})| < \eta^{\text{cut}}(W_{\text{Lept}}) = 2.0$,

- $p_T(W_{\text{Lept}}) > p_T^{\text{cut}}(W_{\text{Lept}}) = 200$ GeV.

3. WW **system**

Final state W vector bosons are much separated from each other in angle. This situation can be described by the following two variables:

(a) $\Delta\phi(WW)$

Separation is described using the distance in azimuthal angle between W bosons. For back-to-back W bosons, it should be close to π.

(b) $p_T(WW)$

Separation is described using transverse momentum of WW pair. For nearly back-to-back W bosons, their individual large transverse momenta should reduce to small value.

Distributions of these variables can be found in Figures K.7(a) and K.7(b). With proper $p_T^{\text{cut}}(WW)$ value, one can obtain signal significance nearly 1.11. With $\Delta\phi^{\text{cut}}(WW)^{\text{cut}}$, it is reachable $S_{c1} = 1.08$. The difference is not impressive, but enables choosing $p_T(WW)$ variable for the selection. Loose cut is set to:

- $p_T(WW) < p_T^{\text{cut}}(WW) = 400$ GeV.

4. **Tagging jets**

This selection requirement was proposed in Refs. [139, 141, 142, 144, 145] to suppress non-fusion processes.

There is at least one jet in each of the forward regions as can be seen in Figure K.6(a); therefore, as was already written earlier, the hardest candidate is chosen for tagging forward (backward) jet. Selection variables for these jets are

values of their transverse momenta (p_T) and energies (E). Distributions of minimal (of two) values of p_T and E for tagging jets can be found in subfigures of Figure K.6. Signal significance does not depend much on values of cuts on these variables; thus, exactly optimal values are not used. The following loose requirements are applied for both tagging jets:

- $p_T(\text{tag jet}) > p_T^{\text{cut}}(\text{tag jet}) = 40$ GeV,

- $E(\text{tag jet}) > E^{\text{cut}}(\text{tag jet}) = 200$ GeV,

The most costly for signal selection efficiency is high value of $p_T^{\text{cut}}(\text{tag jet})$; however, it should not be lowered for the arguments presented in Sec. 5.4.3.

5. $WWjj$ **system**

Cumulative transverse momentum of two final state W bosons and two tagging jets ($p_T(\text{WWjj})$) is small for S4 signal event. Its distribution at generation-level can be found in Figure K.8. At reconstruction level, this variable is smeared by the detector effects, but still is small (see the same figure). Nevertheless, any upper threshold on $p_T(\text{WWjj})$ greater than about 80 GeV does not improve the signal significance. Therefore, it is chosen the following loose requirement:

- $p_T(WWjj) < p_T^{cut}(WWjj) = 200$ GeV.

6. **Central jet veto**

Central jet activity, apart from that originating from bosons, is, as was argued in Section 5.4.4, very limited in scattering processes. The background final states are connected by the strong (color) interaction, what can result in appearance of extra partons in the angle between them. If these partons do not contribute to reconstructed bosons or tagging jets, they are reconstructed as extra jets. They will be looked for in `IC05ETGJ` jet collection with additional requirements: $p_T > 20$ GeV and $|\eta| < 2.0$. This jet collection ($R = 0.5$ cone) is different from collection, which W jet belongs to (`IC07E` collection). Therefore, one should omit the jet that is hadronic W representative in `IC05ETGJ` collection (closest in $\eta \times \phi$ plane to hadronic W). However, this is not enough since, as is shown in Figure K.9, extra `IC05ETGJ` jets are also very often reconstructed in $\eta \times \phi$ space close to hadronic W jet direction. This is connected with wide-cone hadronic W jet that does not fit into a single `IC05ETGJ` jet. Therefore, `IC05ETGJ` jets that are closer than $\Delta R = 0.7$ to hadronic W jet should also be omitted. The remaining jets are rather soft (Fig. K.10(a)). This is why extra central jets are called mini-jets. Distributions of the number of mini-jets is presented in Figure K.10(b). These

distributions differ much between signal and background. Whereas in the former case there are no mini-jets most often, in the latter one at least one mini-jet is usually found. Signal significance dependence on maximally allowed number of mini-jets shows that requirement of no mini-jets is almost the most optimal. Hence, the requirement is:

- $N_{mini} \equiv N_{mini}^{cut} = 0$.

This result confirms that the absence of mini-jets is one the VBF process signatures [145, 228], and central jet (mini-jet) veto still works in the case of high luminosity conditions.

Efficiency of central jet veto for the signal S4 sample is 56% (*cf.* Tab. 6.3). It is comparable with results in Ref. [237], where for the same threshold on jets it reads about 50%. On the contrary, central jet veto efficiencies for $t\bar{t}$ events differ by the factor of two (efficiency value is bigger here), but this can be easily explained by consideration of high luminosity conditions in this thesis.

Figure 6.4: Distributions of the reconstructed WW invariant mass after loose Main Selection. There are shown distributions for signal and various background samples. Notations as in Fig. 6.3.
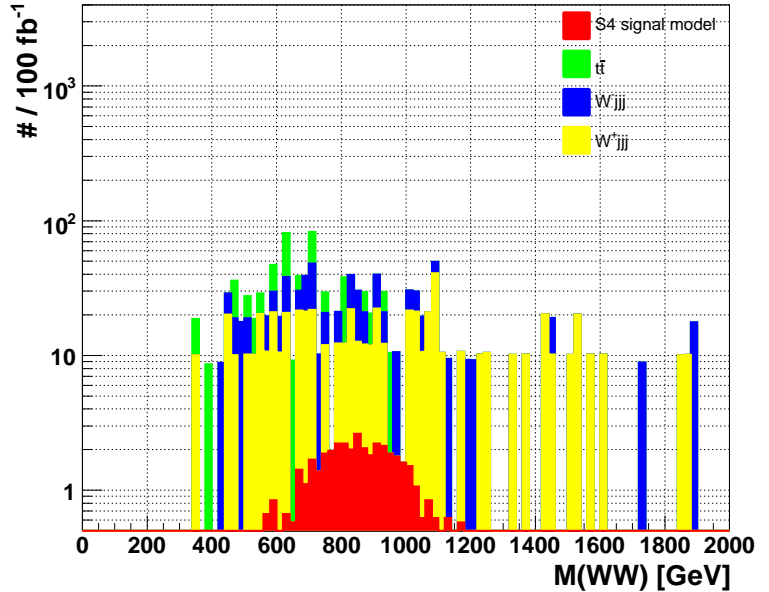
The signal significance (first bin of significance distribution in Fig. K.10(b)) is very low after loose Introductory Selection. The WW invariant mass distribution for background and scalar signal model S4 is presented in Figure 6.4. Since, there are many background events far away from the peak in signal distribution, signal significance could thus be further increased by introduction of WW invariant mass window. The window will be built here around the peak value for the signal WW mass distribution obtained from Gaussian fit. The fit parameters are: μ =863 GeV,

$\sigma =155$ GeV. Distributions of the $M(WW)$ deviation from 863 GeV is presented in Figure K.11. The width of the window is obtained from signal significance maximization. The best value of the cut is around:

- $|M(WW) - 863$ GeV$|<\Delta^{\mathrm{cut}}M(WW)=140$ GeV,

and it enables increase of the signal significance from $S_{c1}=1.32$ (after Introductory Selection) to $S_{c1}=1.62$. Although this additional selection step enables improvement in signal visibility, it is artificial (the position of the peak is assumed to be known) and is strongly dependent on particular signal model. Therefore, the cut on $M(WW)$ mass window will be only optional and will not be included in Main Selection.

selection step	efficiencies of the selection step (w.r.t. the previous step)					after the step	
	$t\bar{t}$	W^-jjj	W^+jjj	whole background	signal model S4	S4 signal to background $N_S(\mathrm{S4})/N_B$	S4 signal significance
Output of preselect.						$6.3\cdot 10^{-4}$	0.85 ± 0.01
Trigger decision	0.90	0.86	0.81	0.85	0.88	$6.5\cdot 10^{-4}$	0.81 ± 0.01
No's of basic objects	0.17	0.18	0.19	0.18	0.37	$1.4\cdot 10^{-3}$	0.70 ± 0.01
Muon and MET	0.23	0.28	0.29	0.27	0.59	$2.9\cdot 10^{-3}$	0.80 ± 0.01
Rec. of sel. objects	0.60	0.63	0.61	0.61	0.71	$3.4\cdot 10^{-3}$	0.72 ± 0.01
Hadronic W	0.43	0.37	0.40	0.40	0.84	$7.2\cdot 10^{-3}$	0.97 ± 0.02
Leptonic W	0.99	1.00	0.99	0.99	1.00	$7.3\cdot 10^{-3}$	0.97 ± 0.02
WW system	0.78	0.74	0.73	0.75	0.96	$9.4\cdot 10^{-3}$	1.08 ± 0.02
Tagging jets	0.55	0.59	0.56	0.56	0.73	$1.2\cdot 10^{-2}$	1.06 ± 0.03
WWjj system	0.72	0.75	0.73	0.73	0.91	$1.5\cdot 10^{-2}$	1.12 ± 0.03
Central jet veto	0.17	0.25	0.24	0.23	0.56	$3.7\cdot 10^{-2}$	1.32 ± 0.07
Overall efficiency	$4.5\cdot 10^{-4}$	$4.5\cdot 10^{-4}$	$7.8\cdot 10^{-4}$	$6.9\cdot 10^{-4}$	$4.1\cdot 10^{-2}$		
M(WW) window	0.29	0.29	0.17	0.23	0.59	$9.6\cdot 10^{-2}$	1.62 ± 0.16
Overall efficiency	$1.3\cdot 10^{-4}$	$1.3\cdot 10^{-4}$	$2.2\cdot 10^{-4}$	$1.6\cdot 10^{-4}$	$2.4\cdot 10^{-2}$		

Table 6.3: Efficiencies of consecutive selection steps in preselection, Initial and loose Main Selection. It is also included optional "M(WW) window" step. Overall efficiency refers to reduction of the rate from "Output of preselection" level.

Details on the loose Main Selection performance can be found in Tab. 6.3. The loose Main Selection changes the WW invariant mass distribution from that shown in Figure 6.3 to distribution in Figure 6.4. The background to signal ratio is reduced from around $1/300$ to around $1/27$. Simultaneously the signal significance improves from 0.72 ± 0.01 to 1.32 ± 0.07. Further reduction to $1/13$ ratio and significance increase to 1.62 is possible with WW invariant mass window. Nonetheless, the signal is still approximately consistent with statistical error on the background.

Distributions of all considered in Introductory and in loose Main Selection variables after loose Main Selection together with significance dependencies on the cuts are grouped in Figure K.12. It is evident that Main Selection can be optimized further since loose cuts do not maximize signal significances.

Figure 6.5: Distributions of the reconstructed WW invariant mass after optimized Main Selection. There are shown distributions for signal and various background samples. Notations as in Fig. 6.3.
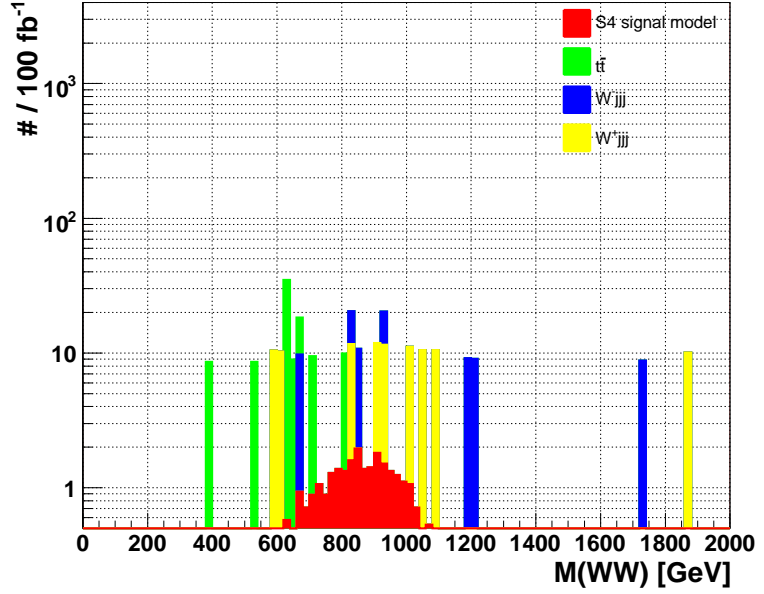
6.3.4 Optimized Main Selection

The $\Delta M(W_{\mathrm{Hadr}})$, reflecting precision of W mass reconstruction, is the variable that enables the biggest increase of the signal significance after loose Main Selection. This distribution is presented in Fig. K.13(a). The cut:

- $\Delta M(W_{\mathrm{Hadr}}) < \Delta M^{\mathrm{cut}}(W_{\mathrm{Hadr}}) = 20$ GeV,

increases the significance from 1.32 to around 1.6. After this change, the next best variable for improving significance appears to be $|\eta(W_{\mathrm{Lept}})|$, for which the distribution can be found in Fig. K.13(b). With requirement:

- $|\eta(W_{\mathrm{Lept}})| < \eta^{\mathrm{cut}}(W_{\mathrm{Lept}}) = 1.0$,

signal significance can be increased to 1.91. After these two cuts, the next significant improvement is possible only with $E(\text{tag jet})$. However, its distribution (shown in Fig. K.13(c)) suffers much from too low statistics of background event samples. With the $E^{\mathrm{cut}}(\text{tag jet})=640$ GeV, it is possible to accidentally obtain $S_{c1}=2.86$; but for neighboring values, significance falls
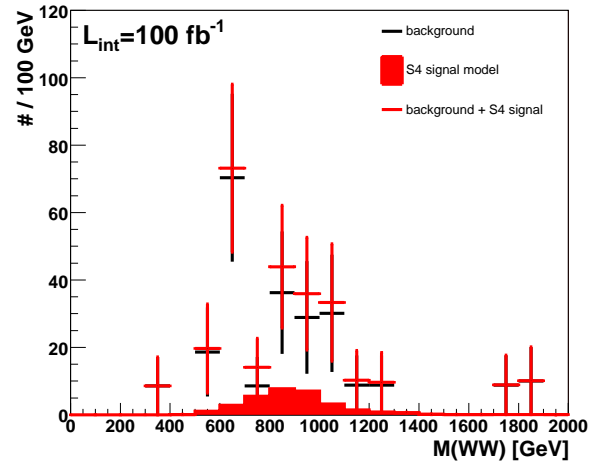
Figure 6.6: Distributions (modified distributions from Fig. 6.5) of the WW invariant mass after optimized Main Selection. Shown are histograms for summed background, background together with signal (both with statistical errors) and for signal S4 model. Distributions are normalized to $\mathcal{L}_{int}=100$ fb^{-1}.

down rapidly. Although, distributions of E(tag jet) suggest that background tagging jets are less energetic, the cut can not be reliably optimized. This is why, the cut on E(tag jet) is not optimized.

Distributions of all variables used in Introductory and Main Selections (plotted after optimized Main Selection) are grouped in Fig. K.14. It is clear that no other cut optimization is possible. The optimized Main Selection improves signal significance from 1.32 to 1.91. The background to signal ratio (for S4 signal model) is reduced from around 1/27 for loose Main Selection to around 1/8 for optimized Main Selection. Selection is very efficient. Nevertheless, the background is still not reduced enough for clear observation of the signal. The WW invariant mass distribution is changed from that in Fig. 6.4 to that shown in Fig. 6.5. After rebinning and inclusion of statistical errors the WW invariant mass distributions is shown in Fig. 6.6.

The artificial cut on WW invariant mass window[1] can further increase significance to around 2.47±0.43. The optimal cut value is:

- $|M(WW) - 865$ GeV$|<\Delta^{\mathrm{cut}}M(WW)$=180 GeV.

6.4   Summary of selection procedure

The final values of selection cuts used in Introductory and optimized Main Selection are listed in Table 6.4.

Some of the cuts, that have been used elsewhere, appeared in this analysis to be not so efficient and were eventually not used. The example is top veto (*e.g.* in Refs. [97, 173, 174]). This requirement is used therein to reduce the background from top quark production by rejecting events with $W+jet$ invariant mass close to the mass of the top quark. It has found that addition of top veto does not increase signal significance; therefore, this extra requirement is not needed.

selection step	cut variable	requirement
Trigger decision	p_T (Level-3 muon)	p_T (Level-3 muon)$>$31 GeV
No's of basic objects	No of centr jets	N(IC07E)$\geq$1
	No of forw jets	N(IC05ETGJ , $\eta > 0$)$\geq$1
	No of back jets	N(IC05ETGJ , $\eta < 0$)$\geq$1
	No of muons	$N_\mu \equiv$1
Muon and MET	$p_T(\mu)$	$p_T(\mu)>$100 GeV
	MET	$MET>$100 GeV
Rec. of sel. objects	W_{Lept} reconstruct.	$\Delta>$0
Hadronic W	$\Delta M(W_{\mathrm{Hadr}})$	$\Delta M(W_{\mathrm{Hadr}})<$20 GeV
	$p_T(W_{\mathrm{Hadr}})$	$p_T(W_{\mathrm{Hadr}}) > $ 100 GeV
	$|\eta(W_{\mathrm{Hadr}})|$	$|\eta(W_{\mathrm{Hadr}})|<$2.0
Leptonic W	$p_T(W_{\mathrm{Lept}})$	$p_T(W_{\mathrm{Lept}})>$100 GeV
	$|\eta(W_{\mathrm{Lept}})|$	$|\eta(W_{\mathrm{Lept}})|<$1.0
WW system	$p_T(WW)$	$p_T(WW)<$400 GeV
Tagging jets	p_T(tag jet)	p_T(tag jet)$>$40 GeV
	E(tag jet)	E(tag jet)$>$200 GeV
$WWjj$ system	$p_T(WWjj)$	$p_T(WWjj)<$200 GeV
Central jet veto	N_{mini}	$N_{mini} \equiv$ 0
$M(WW)$ window	$|M(WW) - 865$ GeV$|$	$|M(WW) - 865$ GeV$|<$180 GeV

Table 6.4: Values of selection cuts used in Loose and optimized Main Selection for S4 signal event sample.

tra requirement is not needed. Top veto is not the only example since also for a number

---

[1]Gaussian fit to the distribution gives μ=865 GeV and σ=144 GeV.

of other cuts (*e.g.* $p_T^{\mathrm{cut}}(W_{\mathrm{Hadr}})$, $p_T^{\mathrm{cut}}(W_{\mathrm{Lept}})$, $p_T^{cut}(WWjj)$) dummy cut values are used. Nevertheless, it is expected that these cuts should be used, and only because of limited background statistics they appear to be inefficient. General conclusion is that efficiencies of the cuts and their values are much biased by available background event samples.

selection step	efficiencies of the selection step (w.r.t. the previous step)					after the step	
	$t\bar{t}$	W^-jjj	W^+jjj	whole background	signal model S4	S4 signal to background $N_S(\mathrm{S4})/N_B$	S4 signal significance $S_{c1}(\mathrm{S4})$
Output of preselect.						$6.3 \cdot 10^{-4}$	0.85 ± 0.01
Trigger decision	0.90	0.86	0.81	0.85	0.88	$6.5 \cdot 10^{-4}$	0.81 ± 0.01
No's of basic objects	0.17	0.18	0.19	0.18	0.37	$1.4 \cdot 10^{-3}$	0.70 ± 0.01
Muon and MET	0.23	0.28	0.29	0.27	0.59	$2.9 \cdot 10^{-3}$	0.80 ± 0.01
Rec. of sel. objects	0.60	0.63	0.61	0.61	0.71	$3.4 \cdot 10^{-3}$	0.72 ± 0.01
Hadronic W	0.24	0.15	0.18	0.19	0.68	$1.2 \cdot 10^{-2}$	1.14 ± 0.03
Leptonic W	0.74	0.55	0.54	0.60	0.81	$1.7 \cdot 10^{-2}$	1.18 ± 0.04
WW system	0.75	0.73	0.64	0.70	0.97	$2.3 \cdot 10^{-2}$	1.36 ± 0.05
Tagging jets	0.55	0.58	0.54	0.55	0.73	$3.0 \cdot 10^{-2}$	1.33 ± 0.06
$WWjj$ system	0.74	0.73	0.76	0.74	0.91	$3.7 \cdot 10^{-2}$	1.40 ± 0.07
Central jet veto	0.14	0.23	0.18	0.18	0.57	$1.2 \cdot 10^{-1}$	1.91 ± 0.20
Overall efficiency	$1.6 \cdot 10^{-4}$	$1.6 \cdot 10^{-4}$	$1.5 \cdot 10^{-4}$	$1.4 \cdot 10^{-4}$	$2.7 \cdot 10^{-2}$		
$M(WW)$ window	0.20	0.38	0.40	0.33	0.74	$2.7 \cdot 10^{-1}$	2.47 ± 0.43
Overall efficiency	$3.2 \cdot 10^{-5}$	$3.2 \cdot 10^{-5}$	$5.6 \cdot 10^{-5}$	$4.6 \cdot 10^{-5}$	$2.0 \cdot 10^{-2}$		

Table 6.5: Efficiencies, signal to background ratios and S4 signal significances for consecutive selection steps in preselection, Initial Selection and in optimized Main Selection. Values of selection cuts are grouped in Tab. 6.4. Overall efficiency refers to reduction of the rate from "Output of preselection" level. Two bottom rows concern optional $M(WW)$ window selection step.

event sample	Numbers of events in $\mathcal{L}_{int} = 100$ fb^{-1}				Main Selection w.r.t. generat.-level	signal model signif. S_{c1} after Main Select.
	generat.-level	after Preselection	after Intro. Selection	after Main Selection		
S1 presel	650	420	92 ± 3	16 ± 1	$2.4 \cdot 10^{-2}$	0.99 ± 0.12
S4	1143	1143	154 ± 3	31 ± 1	$2.7 \cdot 10^{-2}$	1.91 ± 0.20
S4 presel	1144	713	144 ± 4	26 ± 2	$2.3 \cdot 10^{-2}$	1.63 ± 0.19
S6 presel	3028	1302	163 ± 6	22 ± 2	$7.3 \cdot 10^{-3}$	1.38 ± 0.20
V1 presel	492	317	70 ± 2	12 ± 1	$2.4 \cdot 10^{-2}$	0.74 ± 0.09
V2 presel	494	317	69 ± 2	11 ± 1	$2.3 \cdot 10^{-2}$	0.72 ± 0.09
VS presel	2186	1060	183 ± 6	31 ± 2	$1.4 \cdot 10^{-2}$	1.94 ± 0.24
VS1 presel	676	435	97 ± 3	17 ± 1	$2.5 \cdot 10^{-2}$	1.04 ± 0.09
NR presel	432	275	60 ± 2	10 ± 1	$2.2 \cdot 10^{-2}$	0.60 ± 0.07
$t\bar{t}$	7596504	537073	11066 ± 308	86 ± 27	$1.1 \cdot 10^{-5}$	–
W^-jjj	2401860	473167	12322 ± 329	70 ± 25	$2.9 \cdot 10^{-5}$	–
W^+jjj	4316596	794254	21837 ± 468	100 ± 32	$2.3 \cdot 10^{-5}$	–

Table 6.6: Numbers of events in $\mathcal{L}_{int} = 100$ fb^{-1} for signal and background event samples (in $WW \to \mu\nu q\bar{q}$ channel) after consecutive selection steps optimized for S4 signal model. The errors are statistical. Presented are also Main Selection efficiencies with respect to generation-level and signal significances for various models after Main Selection.
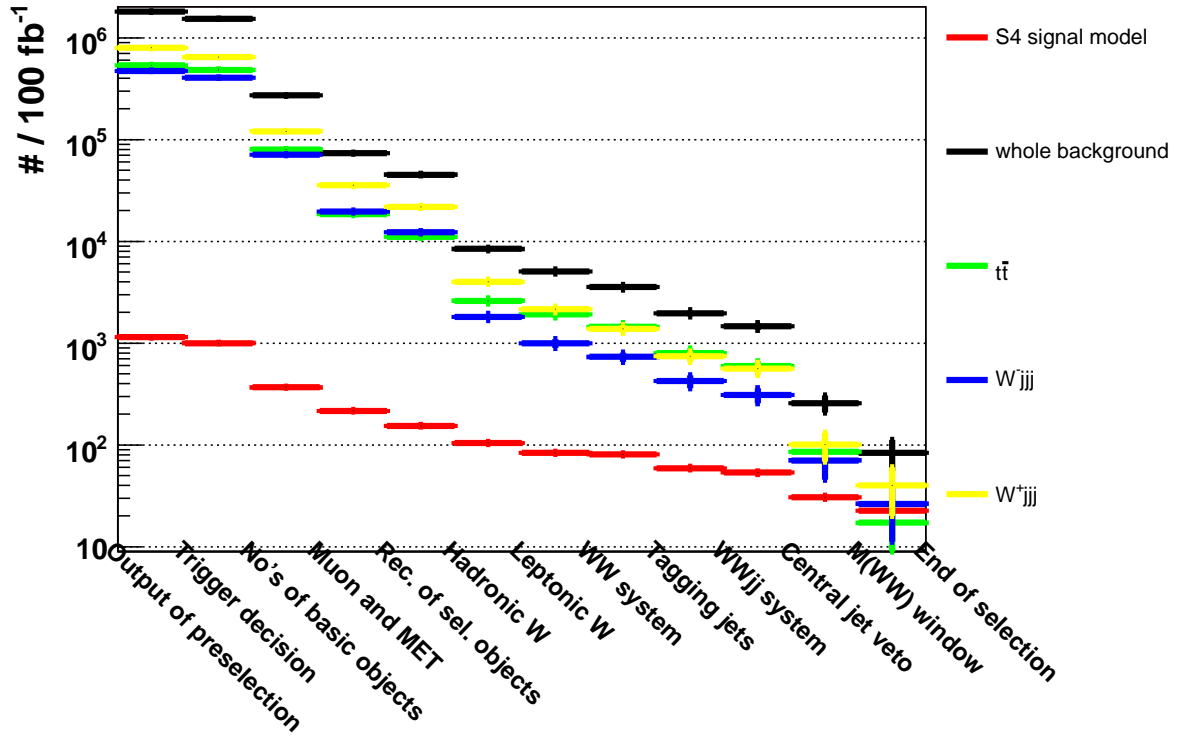
(a) The rates of signal and background samples at each of selection steps.
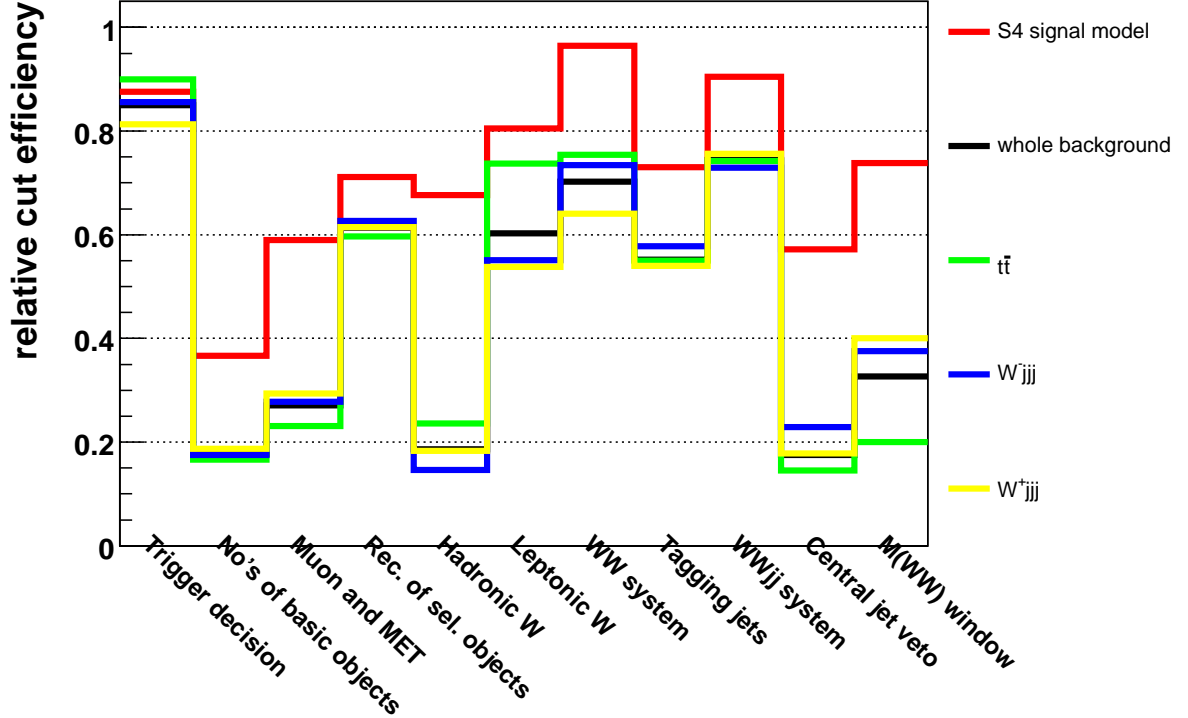
(b) Efficiencies of the selection steps for signal and background samples.

Figure 6.7: Selection efficiencies for background and signal S4 model samples. The values of selection cuts are presented in Tab. 6.4.

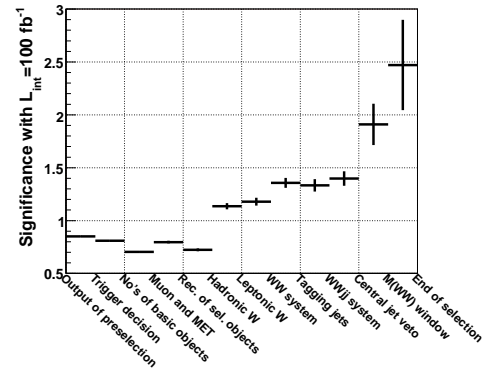| selection step	cut variable	requirement	S1 presel	S4 presel	S6 presel	V1 presel	V2 presel	NR presel
trigger decision	p_T (Level-3 muon)	p_T(Level-3 muon)>[GeV]	31	31	31	31	31	31
No's of basic objects	No of centr jets	N(IC07E) $\geq$	1	1	1	1	1	1
	No of forw jets	N(IC05ETGJ , $\eta > 0$) $\geq$	1	1	1	1	1	1
	No of back jets	N(IC05ETGJ , $\eta < 0$) $\geq$	1	1	1	1	1	1
	No of muons	$N_\mu \equiv$	1	1	1	1	1	1
muon and MET	$p_T(\mu)$	$p_T(\mu)>$ [GeV]	80	80	80	80	80	80
	MET	$MET>$ [GeV]	80	80	80	140	150	170
sel. object reco.	W_{Lept} reconstruct.	$\Delta>$	0	0	0	0	0	0
W_{Hadr}	$\Delta M(W_{\mathrm{Hadr}})$	$\Delta M(W_{\mathrm{Hadr}})<$[GeV]	25	20	20	25	25	25
	$p_T(W_{\mathrm{Hadr}})$	$p_T(W_{\mathrm{Hadr}}) >$ [GeV]	100	100	100	100	100	100
	$|\eta(W_{\mathrm{Hadr}})|$	$|\eta(W_{\mathrm{Hadr}})|<$	2.0	2.0	2.0	2.0	2.0	2.0
W_{Lept}	$p_T(W_{\mathrm{Lept}})$	$p_T(W_{\mathrm{Lept}})>$ [GeV]	270	260	150	150	150	150
	$|\eta(W_{\mathrm{Lept}})|$	$|\eta(W_{\mathrm{Lept}})|<$	1.1	1.0	0.9	2.0	2.0	2.0
WW	$p_T(WW)$	$p_T(WW)<$ [GeV]	260	260	260	260	260	260
tag jets	p_T(tag jet)	p_T(tag jet)> [GeV]	40	40	40	40	40	40
	E(tag jet)	E(tag jet)> [GeV]	400	380	360	450	450	400
$WWjj$	$p_T(WWjj)$	$p_T(WWjj)<$ [GeV]	200	200	200	200	200	200
central jet veto	N_{mini}	$N_{mini} \equiv 0$	0	0	0	0	0	0
	significance (for $\mathcal{L}_{int}$=100 fb^{-1})		1.12	1.93	1.55	1.05	1.00	0.72

Table 6.7: Values of selection cuts maximizing significance of various signal models. Resulting significance for $\mathcal{L}_{int}$=100 fb^{-1} is shown in the last row.

Efficiencies of Introductory and optimized Main Selection steps and signal significances are given in Table 6.5. The most effective requirement is the one connected with hadronic W. It is so efficient thanks to the extraordinary hadronic W reconstruction. The efficiencies for each of the background and signal event samples are also illustrated in Figure 6.7. In Fig. 6.7(a), the rates (numbers of events after collecting 100 fb^{-1} of data) after individual steps are presented. The efficiencies of each these selection steps are illustrated in Fig. 6.7(b). The background, for which the rate after preselection is around three orders of magnitudehigher than

Figure 6.8: Signal significance as a function of selection step. The error on significance is statistical. The S4 signal samples is used.

the signal, is reduced to the level only one order of magnitude higher than the signal. Improvement in the signal significance is also illustrated in Figure 6.8. Significance decreases in Introductory Selection since the background is not enough much more than the signal reduced in this part of selection[1].

The selection cuts optimized for S4 model can be as well applied to the other signal models. The results can be found in Table 6.6. It is seen that the cuts provide similar efficiencies for the rest of models with exception for S6 and VS models, for which

---

[1] According to Eq. (6.1), in order to obtain the increase of signal significance, the efficiency in the cut for the background should be lower than ε^2 if the efficiency for the signal is ε.

efficiency is significantly lower. This is caused by much lower mass of the resonance in these two models. The selection optimized with S4 model is thus only applicable to models with very heavy resonance.

Selection can be also optimized assuming the other signal models. The results for selected models (samples generated with preselection) are presented in Table 6.7. The model that is accessible with the highest value of significance is S4 model (scalar resonance of mass 900 GeV). Values of significances obtained for S4 signal samples with- and without preselection are almost identical, although they are realized with different set of cuts. Significances for the other signal models are much lower. Even though the selections were optimized for observation of these models, the improvement in significance with respect to that in Tab. 6.6 is not much. The other observation is much variation of the cut values from model to model what again supports above judgment that because of low background statistics values of cuts are poorly determined. It is seen that the discovery will be much easier in the case of scalar resonances. This is caused by initial cross-section, which is much higher for scalar resonances. It means that the VBF is not ideal process for production of vector resonances.

Chapter 7

Discussion of results

This chapter is devoted to discussion of the results obtained in Chapter 6. First, theoretical and experimental systematic errors will be estimated. Next, discovery potential of the CMS experiment in the scenario of strongly-coupled sector breaking EW symmetry will be presented. There will be also given exclusion limits for the case that this scenario is not realized. The chapter is finished with comparison with previous results and review of prospects for the LHC and other collider experiments.

7.1 Systematic uncertainties

The errors considered so far in this thesis were only statistical, *i.e.* they only took into account limited statistics of available signal and background event samples. Another subject are systematic uncertainties that appear due to theoretical and experimental limitations in precision of prediction and measurement. They are discussed here on the basis of the review made in App. B of Ref. [236][1].

7.1.1 Theoretical uncertainties

Theoretical uncertainties take into account methods of physics process simulation, unknown or approximate parts of simulation predictions and models, in which physical phenomena are described. They may cause variations of the background and signal levels; therefore, should be taken into account. The most important theoretical sources of uncertainties applicable to this study are:

1. usage of preselection,

2. MC generation uncertainties:

---

[1] alternative reference for theoretical uncertainties is Ref. [238]

(a) hard process generation: uncertainties on parameters, approximations in the calculations,

(b) usage of LO cross-sections,

(c) certain choice of and the errors due to parton distribution functions,

(d) certain choice of and the errors due to fragmentation model.

Generation-level cuts (described in Sec. 6.1) and preselection (described in Sec. 6.2) enabled study of background with reasonable statistical error. Since generation-level cuts are much less restrictive than the selection cuts, only preselection can bias final results. Such introduced extra systematic uncertainty can be rated with the use of S4 signal event samples. Comparing numbers of events after Main Selection for S4 signal event samples with- and without preselection (*cf.* Tab. 6.6), the uncertainty due to preselection may be estimated for 20%. This value will be used for all event samples produced with preselection.

Generation of $2 \to n$ hard processes uses certain models and not well known input parameters such as renormalization and factorization scales, masses, *etc.* This results in 6%-uncertainty on the $t\bar{t}$ production cross-section [239]. The uncertainties for W^+jjj and W^-jjj samples are unknown, they and will be assumed for 10%. Signal event samples are also generated with a number of approximations (equivalence theorem, effective W approximation and others). Because of that, uncertainty on their cross-sections should be estimated for 20% (value based on Fig. 4.3).

Event samples were generated using tree-level generators. Higher orders are included only for $t\bar{t}$ sample in the form of K-factors, and good compatibility with $t\bar{t}j$ sample in cluster distributions is obtained for such scaled sample. This testifies that this scaling is enough (at least for soft radiation part of NLO correction), and there is no need to introduce corresponding systematic error for $t\bar{t}$ sample. For the rest of samples ($W^\pm jjj$ and signal event samples) K-factors are unknown, but are expected to be consistent with unity within 10% (see beginning of Sec. 4.3.4 and Sec. 6.1.1), what approximates corresponding systematic uncertainty.

The next uncertainty is connected with a certain choice of set describing parton densities data[1]. Corresponding error can be estimated either by variation of parameters that are used or by comparing different sets of parton distribution functions. This study has not been done here, and 3%-uncertainty is assumed as obtained for $t\bar{t}$ production in Ref. [240].

---

[1] CTEQ5L set was used here.

Fragmentation (hadronization) uncertainty is connected with particular choice of the model that realizes non-perturbative process of hadronization. The possible error is estimated for 1% as obtained for $t\bar{t}$ production in Ref. [240].

source of uncertainty	uncertainty on cross-sections (multiplicities)				uncertainty on S4 signal significance S_{c1}
	$t\bar{t}$	W^+jjj	W^-jjj	S4 signal	
preselection	20%	20%	20%	0%	21%
hard process generation	6%	10%	10%	20%	23%
NLO	0%	10%	10%	10%	14%
parton distribution functions	3%	3%	3%	3%	4%
fragmentation model	1%	1%	1%	1%	1%
overall uncertainty	21%	25%	25%	23%	34%

Table 7.1: Estimations of theoretical systematic errors on event sample cross-sections (multiplicities) and S4 signal significance. Errors on cross-sections are added in quadrature to obtain the overall systematic theoretical uncertainty. The overall error on significance is calculated with the use of uncertainties on cross-sections (the same result is obtained from combination of consecutive uncertainties on significances).

The estimates of theoretical systematic errors in this study are summarized in Table 7.1. Most of these uncertainties will be much reduced, or will vanish, when simulation of more data is feasible, when the LHC starts its operation and eventually, when high luminosity is reached. This is because collected events will provide data for precise estimation of simulation parameters and choosing the right models. Absolute cross-sections of particular background processes will be also measured with good precision using characteristic signatures of these processes [241]. Currently, the most important sources of errors are applied preselection and uncertainties in hard process generation.

There are as well other systematic uncertainties connected with approach used to obtain the results. These errors may emerge due to limitation to certain event samples and due to the usage of p_T-ordered parton-shower. Estimation of the error introduced by these two approaches is very difficult. The author's feeling is that these uncertainties are small in comparison to the total systematic error. Nevertheless, they will be shortly discussed.

One sample ($t\bar{t}$, W^-jjj or W^+jjj) of multi-jet background samples has been used to represent the classes of processes: $t\bar{t}+jets$, $W^- + jets$ or $W^+ + jets$, respectively. As was explained in Sec. 4.3.7, the need for the other multi-jet $t\bar{t}+n - jets$ and $Wj + (n-1) - jets$ background samples is much reduced due to the usage of p_T-ordered parton-shower. Among the other background processes the most important seems to be irreducible $WWjj$ background that interferes with signal scattering. This

interference and contribution to the final number of events can, however, be neglected close to the resonance. The other background samples were not taken into account, but they are expected to be much less important (lower cross-sections and different event signatures) than the included ones. Representation of background by $t\bar{t}+jets$, $W^- + jets$ and $W^+ + jets$ processes only is thus motivated.

The chosen parton-shower model in PYTHIA results in much harder jets, which consequence is much increased level of background. This model was used with consistent set of parameters [242]; however, these parameters are not tuned yet. Because of this, parton-shower may introduce much theoretical uncertainty. Nevertheless, since the chosen parton-shower agrees with ME exact results quite well as was shown in Sec. 4.3.7, this uncertainty is much limited.

7.1.2 Experimental uncertainties

Experimental uncertainties are associated with wrong detector measurements (*e.g.* caused by uncertainty in calibration) that may influence final results. The precision of the following measurements is relevant to this study:

1. luminosity,

2. muon reconstruction,

3. the scale and the resolution of jet transverse energy,

4. the scale and the resolution of missing transverse energy.

The uncertainty on luminosity measurement will be reduced to the level of about 3% [207, 236] after collecting of $\mathcal{L}_{int}$=100 fb^{-1} and even further down with more data. Muon reconstruction uncertainties include the effects of muon detector positioning, magnetic field uncertainties influencing the muon momentum and systematics of potential muon isolation. Since all these sources of experimental uncertainties are negligible in comparison to the errors associated with calorimetric measurements, they will not be taken into account.

Uncertainties on jet energy and transverse missing energy measurements appearing due to imprecise calibration may have their impact on the level of signal and background. They are quantified by the errors on parameters of resolution curves μ and σ [1], called energy scale and resolution, respectively. The effect on final results may appear because of the cuts on transverse momenta (energies) of MET, tagging jets, reconstructed hadronic W, but also on p_T of central mini-jets. Because of very steep

---

[1]the examples are errors on fit parameters in Fig. I.2

p_T-spectra for them, even small uncertainties in p_T determination may result in large uncertainty on the number of accepted events. This concerns background as well as signal processes.

Systematic errors on the jet and MET measurements will be determined according to the official CMS recipe for low luminosity runs given in CMS Physics TDR vol. II (CMS PTDR II, [236][1]). It is explicitly assumed here that this approach may be applied to systematics of custom jet calibration for high luminosity conditions that has been made in Sec. 5.4.1 with the use of E_T^{cut}(tower) and E_T^{cut}(seed) jet parameters.

According to CMS PTDR II, the impact of jet uncertainties on the final results can be obtained by application of two consecutive smearings to the jets. Technically smearings are realized by multiplying the whole four-momentum of the jet by normal random variable of $\mu = 1$ and standard deviation σ. The first smearing, responsible for jet energy scale uncertainty, is fixed for all signal and background event samples (random variable is fixed for a particular selection of all signal and background events). The second jet-by-jet and event-by-event smearing is responsible for jet energy resolution. Parameters of these smearings as given in CMS PTDR II are used here. Smearings are applied to hadronic W jet and to both tagging jets. Similar study of uncertainty for mini-jets is not possible because jets softer than 20 GeV in transverse momentum are not reconstructed. The smearing of mini-jets' p_T can only decrease accepted number of events. Since it is expected that there are really many soft candidates for jets (*e.g.* resulting from pile-up events), uncertainty connected with mini-jets is estimated for 10%. This error will be added to the final experimental systematic error.

Recommended treatment of MET uncertainties is presented in CMS PTDR II in App. B and is based on smearing of components of the sums in Eqs. (5.12)–(5.13). Here much simpler procedures are applied. It is considered smearing of the whole MET vector (similarly as jet four-momentum is smeared) with assumed $\sigma = 7\%$ or shifting its value by $\pm 3\%$ and ± 7 %[2]. Such changed MET is not used for calculation of neutrino longitudinal momentum (finding solutions of Eq. (5.14)). It is only used in the cut on the value of MET and eventually is only included in leptonic W four-momentum.

The results of systematics study can be found in Table 7.2. Hadronic W and tagging jets were smeared according to CMS PTDR II (TDR). For MET, various options listed above were considered. Jets and MET were smeared in signal and background events in the same way. When signal and background event selection is repeated with random smearings, the results are variations of the number of selected events and variations of the signal significance. These variations were quantified by mean and σ (treated

---

[1]see App. B therein

[2]σ for smearing and shifts are expressed in percents with respect to the unchanged value

numbers of events for $\mathcal{L}_{int}=100$ fb^{-1}				significance
$t\bar{t}$	W^+jjj	W^-jjj	S4	S_{c1}
86	100	70	31	1.91

(a) Reference numbers of events (without systematics effects).

treatment of systematics			impact on numbers of events for $\mathcal{L}_{int}=100$ fb^{-1}				significance
MET	W_{Hadr}	j_{tag}	$t\bar{t}$	W^+jjj	W^-jjj	S4	S_{c1}
+7%	TDR	TDR	+6%±16%	−25%±16%	+3%±11%	+2.0%±4.5%	1.96±0.10
+3%	TDR	TDR	+6%±13%	−22%±14%	−1%±11%	−0.6%±3.5%	1.93±0.08
−	TDR	TDR	+7%±17%	−18%±14%	−9%±10%	−1.1%±3.3%	1.93±0.09
−3%	TDR	TDR	−2%±17%	−27%±14%	−9%±11%	−2.5%±4.6%	1.97±0.09
-7%	TDR	TDR	−18%±17%	−29%±14%	−8%±11%	−5.0%±5.0%	1.95±0.10
σ=7%	TDR	TDR	0%±17%	−24%±17%	−5%±11%	0.0%±4.6%	1.94±0.11

(b) Effects of combined systematics in MET and jets on numbers of events.

Table 7.2: Results for various methods treating jet and MET systematic uncertainties. Reference numbers of events and S4 signal significance without any systematics are given in (a). Impact on the numbers of events and resulting signal significances for various treatments of uncertainties in MET, hadronic W boson jet (W_{Hadr}) and tagging jets (j_{tag}) jet energies is presented in (b). Results are obtained for $\mathcal{L}_{int}=100$ fb^{-1}. Obtained distributions of the number of events are fitted with Gaussian. The mean and σ values are expressed in percents with respect to the reference numbers of events (see text for more details). Fit results for S4 signal significance distributions are presented in the last column. Results for preferred treatment of systematics is presented in the last row. Distribution of S4 signal model significance for this case can be found in Fig. 7.1.

as an error on the number of events/significance) of Gaussian fit. The mean value for the number of events distribution is expressed in the table as a percentage shift from the reference number of events. The σ value for the number of events distribution is expressed in the table in percents of reference number of events. For the case of signal significance distributions, the mean and σ are placed in the table. The mean and σ values for signal significance distributions are very similar for all options on systematics. The values in the table were obtain for 100 times repeating the selection and for $\mathcal{L}_{int}=100$ fb^{-1}.

The systematics treatment with Gaussian-smeared MET is regarded as adequate and is distinguished in the last row in Table 7.2. The significance distribution for this case is presented in Figure 7.1. The systematic error on significance due to MET, hadronic W and tagging jets can be estimated by standard deviation for the distribution

Figure 7.1: Distribution of S4 signal significance S_{c1} for $\mathcal{L}_{int}$=100 fb^{-1} after application of resolution smearings to background and signal events. The distribution was obtained for 100 times repeating the selection where in every repetition jets and MET were randomly smeared according to the smearing method in the last row of Tab. 7.2(b).
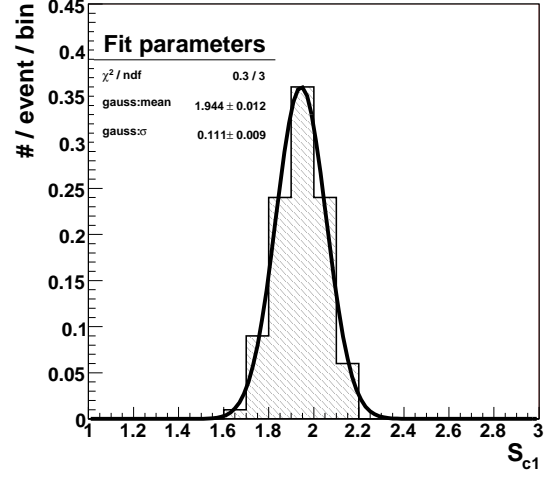
in this figure (or in the last row of Tab. 7.2):

$$0.11/1.94 = 6\% \,. \tag{7.1}$$

After addition of the error for mini-jets, the whole experimental systematic error on significance due to MET and all jets appearing in the event signature reads:

$$6\% \oplus 10\% = 12\% \,, \tag{7.2}$$

where the errors were added in quadrature.

Such obtained level of detector systematic uncertainty is only an estimate. It will be exactly known when real data is available. Similarly to theoretical error, this one will also be reduced during detector operation thanks to increasing knowledge of detector performance and improved precision of calibration.

7.1.3 Summary of systematic uncertainties

kind of uncertainty	uncertainty on numbers of events				uncertainty on S4 signal significance S_{c1}
	$t\bar{t}$	W^+jjj	W^-jjj	S4 signal	
theoretical	21%	25%	25%	23%	34%
experimental	16%	11%	14%	1%	12%
overall uncertainty	26%	27%	29%	23%	36%

Table 7.3: Summary of systematic uncertainties on event sample cross-sections and S4 signal significance. Overall uncertainties are obtained by addition in quadrature of theoretical and experimental errors.

Theoretical and experimental uncertainties are added in quadrature to obtain the overall systematic error. It is presented in Table 7.3. Overall systematic uncertainties

on the numbers of selected events vary from 23% to 29%. The error on S4 signal significance is estimated for 36%. These values determine precision of the results obtained in this thesis. This precision is currently weak.

7.2 Total uncertainty

The total relative error on significance is:

$$10\% \oplus 36\% = 37\% \ , \tag{7.3}$$

where the first error is statistical uncertainty on S4 signal significance after Main Selection (*cf.* Tab 6.5) (error due to limited number of simulated events) and the second one the total systematical error given in Tab. 7.3. Although this result has been obtained for S4 signal model, it can and will be also applied to the other signal models.

7.3 Discovery potential

In accordance with common definition, the value of significance $S = 5$ (5σ significance) is regarded as the discovery limit. For this circumstance, the probability that background imitates signal (*i.e.* for example fluctuate over expectation value for signal with background) is less than 5.7×10^{-7}. However, even for expected $S = 5$ value, the observed number of events may still have, with probability close to 50%, significance smaller than 5. It means that probability of discovery in this case is 50%. Signal with higher value of expected significance is needed to obtain discovery more probable.

Integrated luminosity needed for 5σ significance of the signal process can be deduced from the highest value of significance obtained in Tab. 6.7 for $\mathcal{L}_{int}$=100 fb^{-1} ($S_{c1}(100 \text{ fb}^{-1}) \approx$1.9). It reads:

$$\mathcal{L}_{int}(S_{c1} = 5) = \frac{25}{(S_{c1}(100 \text{ fb}^{-1}))^2} * 100 \text{ fb}^{-1} \tag{7.4}$$

for significance S_{c1} as defined in Eq. (6.1).

The conclusion is that integrated luminosity of at least

$$\mathcal{L}_{int}(S_{c1} = 5) \approx 700 \text{ fb}^{-1} \tag{7.5}$$

is needed for discovery of any model with electroweak strongly-coupled sector. The relative error on this prediction is:

$$\frac{\Delta \mathcal{L}_{int}}{\mathcal{L}_{int}} \approx 70\% \tag{7.6}$$

provided the error on significance is as given by Eq. (7.3).

Any better precision is not possible with available event samples. Given the errors and insignificant differences between the limits for different models, it is unpractical to consider discovery contours on $a_4 \times a_5$ space.

7.4 Exclusion limits

One can also ask about integrated luminosity needed for exclusion of models with strongly-coupled sector. Exclusion of models means here exclusion of these models realization in Nature. The problem can be easily understood after studying future experiment distributions of the number of events for background and for hypothetical S4 signal with background. The numbers of events in S4 signal model ($N_S(S4)$=31) and background (N_B=256) surviving the Main Selection from Table 6.6 are used for estimation of the mean values for these distributions. These distributions for various integrated luminosities, but normalized to $\mathcal{L}_{int} = 100$ fb^{-1}, are presented in Figure 7.2 for S4 signal sample. Hatched regions in this figure are the measures of probability that the number of background events alone (if no signal exists) will fluctuate over or signal with background will be below arbitrary chosen number of events (marked with the arrow in the picture). When collecting more data, hatched regions become smaller. This feature is the basis for setting limits on necessary luminosity.

Figure 7.2: Distributions of the number of observed events for the background (black) and for hypothetical signal (S4 signal sample) with background (red) in future experiment. Three integrated luminosities are taken into account (100 fb^{-1}, 300 fb^{-1} and 1000 fb^{-1}) and drawn with different line styles. They can be identified by maximum height, lowest for 100 fb^{-1}. Distributions are accordingly scaled to the expected number of events for 100 fb^{-1}, and normalized to unity. Distributions were obtained with the use of Poisson variables. Hatched regions, with the border between them marked with an arrow, are explained in the text.
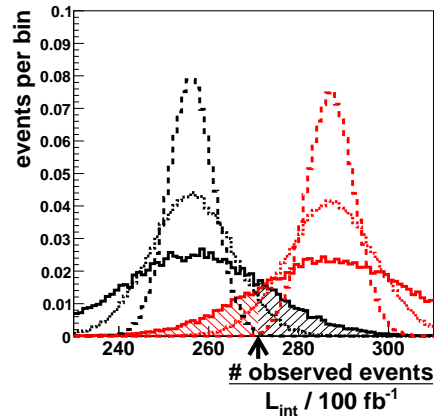
The subject of exclusion limits in planned experiments was initiated in Ref. [243]; however, the latter approach from Ref. [244] is used here. It is used estimator of the sum of probabilities that one rejects existence of the strongly-coupled sector if it

exists and accepts its existence if it does not exist. It reads [244]:

$$\hat{\kappa} = \frac{\hat{\alpha} + \hat{\beta}}{2} \tag{7.7}$$

for

$$\hat{\alpha} = \sum_{i=0}^{n_o} f(i; \mu_s + \mu_b) , \tag{7.8}$$

$$\hat{\beta} = 1 - \sum_{i=0}^{n_o} f(i; \mu_b) , \tag{7.9}$$

where μ_s and μ_b are expected multiplicities of signal and background samples, and $f(i; \mu)$ is a Poisson probability for obtaining i events for mean μ. Values of $\hat{\alpha}$ and $\hat{\beta}$ are represented by hatched regions in Fig. 7.2. The n_o is set to [244][1]:

$$n_o = Int\left(\frac{\mu_s}{\ln(\mu_s + \mu_b) - \ln(\mu_b)}\right) , \tag{7.10}$$

where $Int()$ denotes integer part of a number. For Main Selection optimized for S4 model ($\mu_b = 256$, $\mu_s = 31$) one obtains $n_o = 271$.

Requirement of

$$\hat{\kappa} < \epsilon \tag{7.11}$$

means that probability of background fluctuation over n_o ($\hat{\beta}$), and probability of having hypothetical signal with background in the number lower or equal to n_o ($\hat{\alpha}$) are simultaneously approximately lower than ϵ. This way the exclusion limit is quantified with one variable ϵ. Commonly it is used

$$\epsilon = 0.05 \tag{7.12}$$

that means excluding the signal at the 95%-C.L. The chosen approach differs from "typical experiment" approach from Ref. [245] with:

$$\hat{\kappa} = \frac{\hat{\alpha}}{1 - \hat{\beta}} \qquad \text{and} \qquad n_o = \mu_b . \tag{7.13}$$

and the natural one with:

$$\hat{\kappa} = \hat{\beta} \qquad \text{and} \qquad n_o = \mu_s + \mu_b . \tag{7.14}$$

that will be called here $S_{cl} = 2$ approach. Interpretation of $\hat{\kappa} < \epsilon$ requirement in these two approaches is straightforward. In the first one, this requirement means that

---

[1] n_o is a number, for which $f(n_o; \mu_s) = f(n_o; \mu_s + \mu_b)$

the ratio of probability that the number of signal events is below μ_b to probability that the number of background events is also below μ_b (for high values of μ the latter probability is 0.5) is lower than ϵ. In the case of $S_{c1} = 2$ approach, this requirement means that probability of background fluctuation over $\mu_b + \mu_s$ is lower than ϵ. The most important difference between these two simple approaches and the chosen one is taking into account fluctuations of both hypothetical signal and background. The chosen approach is, therefore, much more restrictive and would require higher integrated luminosity.

Figure 7.3: Estimator $\hat{\kappa}$ dependency on the integrated luminosity for S4 signal scalar model. Three approaches are presented: "typical experiment", $S_{c1} = 2$ approach and chosen approach. The 95% C.L. exclusion limit is obtained for luminosity for which $\hat{\kappa} < 0.05$.
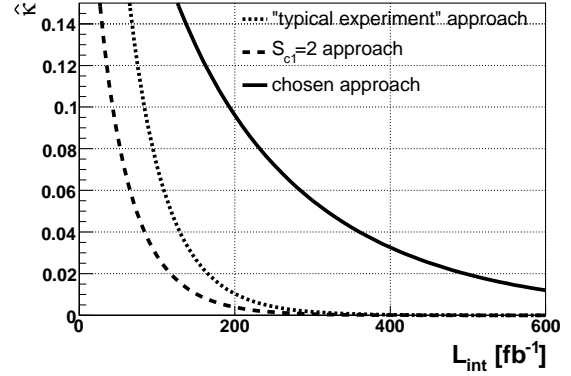
When increasing integrated luminosity, the $\hat{\kappa}$ decreases as can be deduced from Fig. 7.2. Anticipated dependency of $\hat{\kappa}$ on the integrated luminosity for S4 signal scalar model is presented in Figure 7.3. It is observed much difference in the values of $\hat{\kappa}$ between chosen approach and two other approaches. For the chosen approach exclusion is possible with $\mathcal{L}_{int}=318$ fb^{-1}, for $S_{c1} = 2$ approach with $\mathcal{L}_{int}=74$ fb^{-1}, and with "typical experiment" for $\mathcal{L}_{int}=118$ fb^{-1}. Luminosity needed for exclusion in chosen approach is thus about two times lower than required for discovery. It means that if the scenario of the strongly-coupled sector is really realized, its indications should appear after $\mathcal{L}_{int} \approx 320$ fb^{-1}, *i.e.* observed number of events should be greater than n_0 after about 3 years of running with high luminosity. If observed number of events after about 3 years of running with high luminosity is lower than n_0, the S4 signal model will be excluded.

The exclusion limit for S4 signal model can be regarded as exclusion limit for models with the strongly-coupled sector since this model is most significant and requires the lowest integrated luminosity for exclusion. Therefore, the integrated luminosity of at least of

$$\mathcal{L}_{int} \approx 320 \text{ fb}^{-1} \tag{7.15}$$

is needed for excluding existence of models with the strongly-coupled sector. With this luminosity, it is possible to exclude only S4 signal model. More data are needed for exclusion of the other less significant signal models. Because these predictions are

much uncertain according to Eq. (7.6), the exclusion limit contours on $a_4 \times a_5$ space will not be considered.

7.5 Comparison with previous results and prospects for the LHC and other colliders

The $WW \to jjl\nu$ final state appeared to be very demanding for observation of the strong VV scattering and discovery of the strongly-coupled EWSB sector. This conclusion is in contradiction with the other similar studies on this subject [97, 173, 174] and with earlier analyzes done for very heavy Higgs boson with $WW \to jjl\nu$ channel [152, 171]. The reason for much less significant signal obtained here is much increased, but at last realistic as is shown here, level of the background. Multi-jet background samples and more realistic (p_T-ordered) parton-shower in PYTHIA were used in this thesis, what makes background events not so easily rejectable in the selection procedure. These results suggest also that discovery limit for heavy Higgs boson is overrated.

Experimental signal of the strongly-coupled symmetry breaking sector is overwhelmed by the background. In order to see this signal, very restrictive selection procedure was constructed here. This procedure strongly relies on the MC simulations; therefore, it should be repeated once the presence of experimental data allows for improvement and validation of MC generators and more precise knowledge of detector response to signal and background processes. However, even before the appearance of real data, it is worth to compare the method of multi-jet background estimation proposed in this thesis with standard approach using many exclusive multi-jet event samples and ME/PS matching procedure. Additionally, background should be simulated in higher statistics for better optimization of the event selection and possible further improvement to analysis presented in this thesis. There is also a number of advances that could be introduced into the selection procedure in order to further increase signal significance. One of the option is decomposition of hadronic W jet into sub-jets, what can further suppress the QCD background [97, 222]. Another possibilities that could help in discrimination of the background are determination of helicity for the final state W bosons and assigning a distinct charge sign to the W jet (jet charge). However, as it was found in preliminary study, the latter proposal is not very promising. If the signal peak visibility increased with these improvements, it would also be realistic to use WW invariant mass window requirement leading to even further increase of the signal significance.

Results of this analysis prove that semi-leptonic channel is not so straightforward scenario for searches of heavy wide WW resonances at hadron colliders since, as was

estimated here, QCD jet activity at the LHC will be very difficult to suppress. These results suggest rather using alternative purely leptonic decay modes of final VV state. Previous studies of this case [94, 95, 96, 120, 158, 159, 160] need, however, to be repeated with more realistic simulation of background and detailed detector effects. Therefore, the limits in these references on attainable at the LHC chiral parameters should be treated as tentative. The other scattering channels ($\rightarrow ZZ, \rightarrow WZ$) can be also taken into account. Especially Z boson in leptonic decay is a clear signal and may be promising.

Strongly coupled symmetry breaking sector is according to Ref. [55, 246, 247] also within the reach of future linear electron and muon colliders. Studies to be made at these machines will be much easier because of very low hadronic activity, and the limits obtained from the LHC could be further improved.

Chapter 8

Conclusions and summary

This thesis was devoted to finding prospects for observation of hypothetical 1-TeV scale strongly-coupled sector that is able to replace light standard Higgs boson in breaking electroweak symmetry and also to naturally solve hierarchy problem. Simulation studies have been done for the CMS detector that will start data taking at the LHC at CERN laboratory in 2008.

Studies have been performed within model-independent phenomenological EWChL approach describing low-energy interactions within symmetry breaking sector. Padé unitarization procedure enables application of this approach to 1 TeV energies, where the sector is strongly coupled, and provides obeying of unitarity in $V_L V_L \to V_L V_L$ scattering. As a result, TeV scale resonant behavior, one of the characteristics of this scenario, is obtained in scattering amplitudes. Indications of strong interaction within symmetry breaking sector have been searched for, in this thesis, in vector boson fusion processes simulated with PYTHIA generator. The $WW \to \mu\nu q\bar{q}$ final state was chosen for the signal. Exclusive $t\bar{t}$ and $Wjjj$ background samples (generated respectively in PYTHIA and in CompHEP) were used for representation of multi-jet inclusive $t\bar{t}+jets$ and $W+jets$ productions being leading background processes. Novel p_T-ordered parton-shower in PYTHIA was also used. This parton-shower was found to be different and much more reliable than previously commonly used Q^2-ordered parton-shower. This way the author obtained realistic estimation of background and signal. Additionally, detailed simulation of the CMS detector and real reconstruction of simulated events were used. Reconstruction of selection objects has been discussed and optimized in high luminosity conditions to best correspond to original particles and also to suppress the background processes. Overwhelming background required construction of suitable event selection. The selection was optimized using maximization of signal process significance as an indication, what values of the cuts to choose. This selection procedure could be potentially used in the future when real data is available.

125

8. CONCLUSIONS AND SUMMARY

The final results are biased by low statistics of background samples; therefore, they only suggest that signal significance for integrated luminosity of the order of 100 fb^{-1} might be only as much as about 2.0. It has been estimated that provided the strongly-coupled sector exists, it would require at least about 700 fb^{-1} of integrated luminosity for discovery. If there were no indications of the signal of interest, the exclusion of scenarios of this kind would be possible with at least about 300 fb^{-1} of collected data. Although, as was estimated, there is much uncertainty on these limits, the results of this work indicate that the discovery of electroweak symmetry breaking scenario with the strongly-coupled sector is feasible, but will require much effort. Since main contribution to uncertainty comes from systematic theoretical error, these limits will become more certain in near future, when the first LHC data is available.

Acknowledgements

Glossary

cluster   the result of clusterization procedure; it groups $\Delta\eta \times \Delta\phi$ space cells with particle energy deposits; it is supposed to mimic a reconstruction-level jet.

generation   procedure of obtaining events (sets of final state particle four-momenta) for physics process with the use of Monte-Carlo program

generation-level jet, j, j   parton, *i.e.* q, $\bar{q}$ or g

hard   an attribute connected with high transverse momentum

higgs, H, h   Higgs boson

longitudinal   in short about polarization state of bosons with polarization three-vector (spin) parallel to the vector of momentum

reconstruction-level jet, j, j   a result of jet algorithm that combines calorimetric deposits; it is supposed to reconstruct parent generation-level jet or the event hadronic activity.

soft   an attribute connected with low transverse momentum

transverse   in short about polarization state of bosons with polarization three-vector (spin) transverse to the vector of momentum

Notation

α_s	strong interaction coupling constant,
a_{IJ}	partial wave amplitude for a given isospin I and angular momentum J,
$\mathcal{A}, \mathcal{M}$	amplitude functions,
ΔR	separation between objects in $\eta \times \phi$ plane; defined as $\Delta R = \sqrt{\Delta\eta^2 + \Delta\phi^2}$,
E	energy,
η	pseudorapidity, spatial coordinate defined as $\eta = -\ln(\tan(\theta/2))$,
$\mathsf{E_T}, E_T$	transverse energy defined as $E\sin\theta$,
$\mathsf{E_T^{cut}}$	the value of the cut on $\mathsf{E_T}$,
f_π	the pion decay constant, $f_\pi = 92$ MeV,
G_F	Fermi coupling constant, $G_F = 1.166 \cdot 10^{-5}$ GeV^{-2},
Γ	particle width,
g	gluon,
h, H	the Higgs boson,
j	a generation-level jet standing for $j = q, \bar{q}, g$, *e.g.* used to denote general processes $pp \rightarrow WWjj$; alternatively j can also denote a reconstruction-level jet,
K	multiplicative factor enabling inclusion of NLO effects to LO calculations,
Λ	the mass scale of the New Physics,
Λ_{QCD}	the mass scale of QCD condensates, $\Lambda_{QCD} \approx 210$ MeV,
$\mathcal{L}$	luminosity or notation of the Lagrangian,
$\mathcal{L}_{int}$	integrated luminosity,
μ	muon,
M_H	the mass of the Higgs boson,

M_{Planck}	the Plack mass, $M_{Planck} = 10^{19}$ GeV,
M_W	the mass of the W boson, $M_W \approx 80.4$ GeV,
M_Z	the mass of the Z boson, $M_Z \approx 91.2$ GeV,
ν	neutrino,
p	momentum,
$\mathbf{p_T}, p_T$	transverse momentum, the momentum component that is transverse to z-axis (beam axis), defined as $\sqrt{p_x^2 + p_y^2}$,
$\hat{\mathbf{p}}_\perp$	center of mass transverse momentum of partons in 2→2 processes,
$\mathbf{p_T^{cut}}$	the value of the cut on $\mathbf{p_T}$,
$q, \bar{q}$	a quark and its anti-quark, the notation is usually limited to light quarks (u, d),
r, ϕ, θ	spherical coordinates (radius, azimuthal and polar angles) in the CMS detector Cartesian coordinate system,
S	signal significance,
S_{c1}	signal significance as defined in Eq. 6.1,
$\sqrt{s}$	energy of the center of mass system,
S, T, U	oblique parameters,
s, t, u	the Mandelstam variables,
$t, \bar{t}$	top quark and its antiparticle,
V	intermediate vector boson (Z, W^+ or W^-),
v	vacuum expectation value (vev),
$V_L(V_T)$	longitudinally (transversally) polarized intermediate vector boson,
W	intermediate W vector boson appearing in two charge states: W^+, W^-,
$W_L, (W_T)$	longitudinally (transversally) polarized W boson,
x, y, z	Cartesian coordinates of the CMS detector: x-axis points towards the center of the LHC, y-axis upwards and z-axis is aligned along proton beams,
Z	intermediate Z vector boson,
$Z_L(Z_T)$	longitudinally (transversally) polarized Z boson,

List of Acronyms

ATLAS (A Toroidal LHC ApparatuS)

CERN (European Organization for Nuclear Research)

CL (confidence level)

CMS (Compact Muon Solenoid)

c.m.s. (center of mass system)

CPU (central processing unit)

ET (Equivalence Theorem)

EW (electroweak)

EWA (effective-W approximation)

EWChL (Electroweak Chiral Lagrangian)

EWSB (electroweak symmetry breaking)

FSR (final-state radiation)

GSW (Glashow-Salam-Weinberg)

HLT (High-Level Trigger)

IAM (Inverse Amplitude Method)

ISR (initial-state radiation)

LHC (Large Hadron Collider)

LO (leading-order)

List of Acronyms

MC (Monte-Carlo)

ME (matrix-element)

ME/PS matching (matrix-element/parton-shower matching)

MET (missing transverse energy)

MI (multiple interactions)

NLO (next-to-leading-order)

PU (pile-up)

QCD (Quantum Chromodynamics)

QED (Quantum Electrodynamics)

QGC (quartic gauge coupling)

RMS (root mean square)

SM (Standard Model)

TC (technicolor)

TGC (triple gauge coupling)

UE (underlaying events)

VBF (vector-boson fusion)

vev (vacuum expectation value)

Appendix A

Unitarity of scattering amplitudes

Unitarity condition forbids scattering with probability greater than unity. Its precise formulation is the condition for partial-wave amplitudes a_J:

$$|a_J(s) - 1/2\,\mathrm{i}| \leq 1/2 \,, \tag{A.1}$$

that comes from optical theorem. Relation (A.1) is often substituted by softer conditions:

$$|a_j(s)| \;\leq\; 1 \,, \tag{A.2}$$

$$\mathrm{Re}\,a_j(s)| \;\leq\; 1/2 \,. \tag{A.3}$$

For elastic scattering sign "$\leq$" is changed to "$=$" sign in preceding Eqs. (A.1), (A.2) and (A.3).

The elastic version of unitarity condition given in Eq. (A.1) is equivalent to the following two conditions:
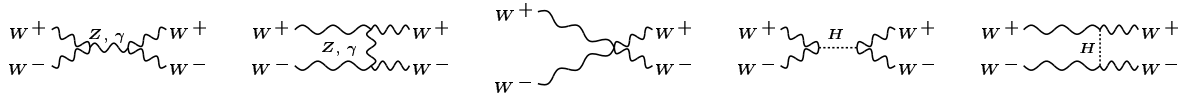
$$\mathrm{Im}\,a_{IJ}(s) = |\,a_{IJ}(s)\,|^2 \tag{A.4}$$

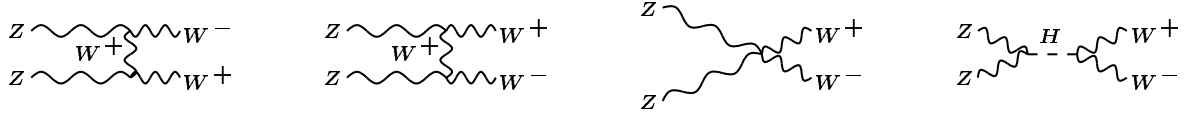and

$$\mathrm{Im}\,\frac{1}{a_{IJ}(s)} = -1 \,. \tag{A.5}$$
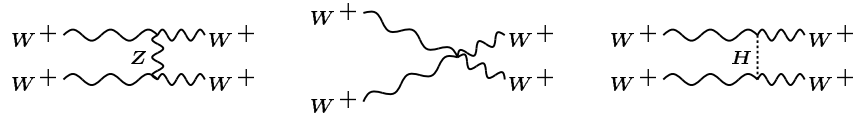
Appendix B

Feynman diagrams for considered processes

B.1 Signal scattering diagrams

(a) Diagrams contributing to $W^+W^- \to W^+W^-$ scattering.

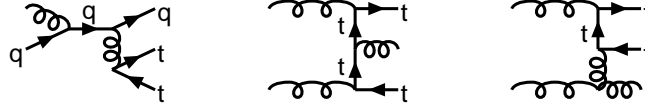**(b)** Diagrams contributing to $ZZ \to W^+W^-$ scattering.

(c) Diagrams contributing to $W^+W^+ \to W^+W^+$ $(W^-W^- \to W^-W^-)$ scattering.

Figure B.1: The Standard Model $VV \to WW$ scattering diagrams.

B.2 Diagrams for background processes

Figure B.2: Selected diagrams contributing to $t\bar{t}$ production.
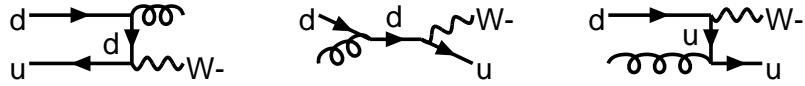

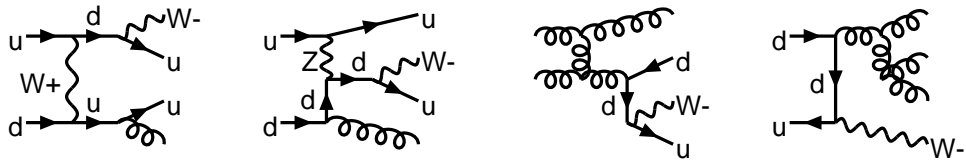**Figure B.3:** Selected diagrams contributing to $t\bar{t}j$ production.
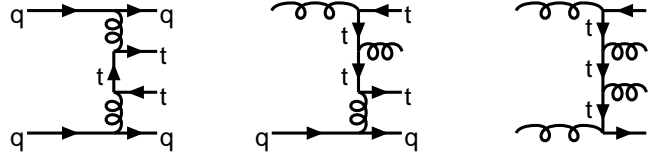
Figure B.4: Selected diagrams contributing to $t\bar{t}jj$ production.

Figure B.5: Selected diagrams contributing to W^-j production.

Figure B.6: Selected diagrams contributing to W^-jj production.

Figure B.7: Selected diagrams contributing to W^-jjj production.

Appendix C

Sets of PYTHIA 6.2 and 6.3 parameters

Listed below are the values of PYTHIA parameters used in this thesis for event generation/simulation.

C.1 General sets of PYTHIA 6.2 and 6.3 parameters

```
PMAS 5,1  = 4.6     !  b   mass
PMAS 6,1  = 175.    !  t   mass
PMAS 23,1 = 91.187  !  Z0  mass
PMAS 24,1 = 80.33   !  W   mass
```

parameter	PYTHIA 6.2 value used	default	PYTHIA 6.3 value used	origin. from	default	description	
MSTJ(11)	3	4	3		4		fragmentation function
MSTJ(22)	2	1	2		1		decay those unstable particles
PARJ(71)	10	10	10		10		for which $c\tau < 10$ mm
PARJ(81)		0.29	0.14	[242]	0.29	MI:	Λ_{FSR} scale
PARP(67)	1.	1.	1.	1.			
PARP(78)	n.a.	n.a.	1.3	[242]	0.025	MI:	
PARP(79)	n.a.	n.a.	2.0	[242]	2.0	BR:	
PARP(80)	n.a.	n.a.	0.01	[242]	0.1	BR:	
PARP(82)	2.1	1.9	2.5	[242]	2.0	MI:	pt cutoff
PARP(83)	0.5	0.5	1.8	[242]	0.5	MI:	matter overlap parameter
PARP(84)	0.4	0.2	0.4		0.2	MI:	matter overlap parameter
PARP(89)	1000.	1000.	1800.	[242]	1800.	MI:	sqrts for which PARP(82) is set
PARP(90)	0.16	0.16	0.25	[242]	0.16	MI:	power of energy-rescaling term
MSTP(51)	7	7	7		7		structure function (CTEQ5L)
MSTP(70)	n.a.	n.a.	2	[242]	1	MI:	for new model of MI, FSR and ISR
MSTP(72)	n.a.	n.a.	2	[242]	1	MI:	for new model of MI, FSR and ISR
MSTP(81)	1	1	21	[242]	1	MI:	master switch of MI, FSR and ISR
MSTP(82)	4	1	5	[242]	4	MI:	definition of the MI model
MSTP(88)	n.a.	n.a.	0	[242]	1	BR:	
MSTP(89)	n.a.	n.a.	1	[242]	1	BR:	
MSTP(95)	n.a.	n.a.	1	[242]	1	MI:	

Table C.1: Parameters used in PYTHIA 6.2 and 6.3 for generating events and for processing events from matrix-element generator. Only important parameters and with changed values are listed. Consistent sets of values were used. In PYTHIA 6.2 the default model of Q^2-ordered parton-showering is used with parameter set originating from the CMS production. This set is quite close to so-called Tune A [248, 249] set that fits CDF Run II data. In PYTHIA 6.3 it is used the new model of p_T-ordered parton-showering. PYTHIA 6.3 parameter set originates from [242], where it is discussed in Section 11.6. So-called "power" parton-shower configuration, found to be much better than Tune A for Q^2-ordered parton-showering [192], is used here.

C.2 Additional PYTHIA 6.2 and 6.3 parameters used in the studies in Sections 4.3.4 and 4.3.7

In the studies of Section 4.3.7 the parameters from Section C.1 were used. Additionally multiple interactions were switched off with the values in this table:

parameter	PYTHIA 6.2 default		PYTHIA 6.3 originated from	default	description
MSTP(81)	0	1	20 [242]	1	MI: master switch of MI, FSR and ISR

C.3 PYCELL configuration in PYTHIA used in pre-selection in Section 6.2

The following PYCELL routine parameters were used in PYTHIA during preselection of events generated in both PYTHIA and CompHEP.

```
PARU 51 = 5.0   ! maximum absolute pseudorapidity used for detector assumed in PYCELL
PARU 52 = 5     ! min Et for a cell jet initiator
PARU 53 = 20    ! min summed Et for cluster to be accepted
PARU 54 = 0.5   ! max distans in R(delta eta,delta phi) grouping cells

MSTU(51) = 60          ! N of eta bins   now roughly 0.1 * 0.1
MSTU(52) = 73          ! N of phi bins
MSTU(54) = 1           ! P 1 and 3 phi, P 2 and 4 eta, P 5 Jet ET
```

Appendix D

Details on analysis event samples generated in PYTHIA

This appendix contains specific parameters (additional to parameters listed in Section C.1) that were used in generation of samples used in analysis in Chapter 6. These samples have been generated in PYTHIA 6.3.

1. signal event samples

(a) kinematics cuts:

```
CKIN 3 = defined in the table ! PT HAT LOW CUT
CKIN 4 = -1.                   ! PT HAT UP  CUT
```

sample	presel.?	a_4	a_5	$\hat{p}_\perp$ cut [GeV]
S1 presel	yes	0.0	0.0015	200.
S1	no	0.0	0.0015	200.
S4 presel	yes	0.0	0.004	200.
S4	no	0.0	0.004	200.
S6 presel	yes	0.0	0.0090	50.
S6	no	0.0	0.0090	50.
V1 presel	yes	0.002	-0.003	200.
V2 presel	yes	0.002	-0.001	200.
VS presel	yes	0.008	0.0	50.
VS1 presel	yes	0.0025	0.0	200.
NR presel	yes	0.0	0.0	200.

Table D.1: Details on simulated signal model event samples. The cut on $\hat{p}_\perp$ is applied to remove unphysical contribution from t-channel γ exchange.

(b) process specification:

```
MSEL = 0
MSUB 72 = 1      !ZZ->W+W- (longitudinal)
MSUB 77 = 1

MSTP 45 = 3  ! (for 77: 3=all charge combinations)
MSTP 46 = 3  ! turning on EWChL approach

MSTP 2  = 1  !which order running alphaS
MSTP 33 = 0  !(D=0) inclusion of K factors in hard
MSTU 21 = 1  !Check on possible errors
                  during program execution
```

(c) W boson decay channels:

```
MSEL = 0            !(D=1)
MDME 190,1 = 4      !W decay into dbar u
MDME 191,1 = 4      !W decay into dbar c
MDME 192,1 = 4      !W decay into dbar t
MDME 194,1 = 4      !W decay into sbar u
MDME 195,1 = 4      !W decay into sbar c
MDME 196,1 = 4      !W decay into sbar t
MDME 198,1 = 4      !W decay into bbar u
MDME 199,1 = 4      !W decay into bbar c
MDME 200,1 = 4      !W decay into bbar t
MDME 206,1 = 0      !W decay into e+ nu_e
MDME 207,1 = 5      !W decay into mu+ nu_mu
MDME 208,1 = 0      !W decay into tau+ nu_tau
```

2. $t\bar{t}$

(a) process specification:

```
MSEL = 6           ! ttbar
```

(b) kinematics cuts:

```
CKIN 3 = 100.      ! PT HAT LOW CUT
CKIN 4 = -1.       ! PT HAT UP  CUT
```

(c) W boson decay channels:

```
MDME 190,1 = 3      !W decay into dbar u
MDME 191,1 = 3      !W decay into dbar c
MDME 192,1 = 3      !W decay into dbar t
MDME 194,1 = 3      !W decay into sbar u
MDME 195,1 = 3      !W decay into sbar c
MDME 196,1 = 3      !W decay into sbar t
MDME 198,1 = 3      !W decay into bbar u
MDME 199,1 = 3      !W decay into bbar c
MDME 200,1 = 3      !W decay into bbar t
MDME 206,1 = 0      !W decay into e+ nu_e
MDME 207,1 = 2      !W decay into mu+ nu_mu
MDME 208,1 = 0      !W decay into tau+ nu_tau
```

138

Appendix E

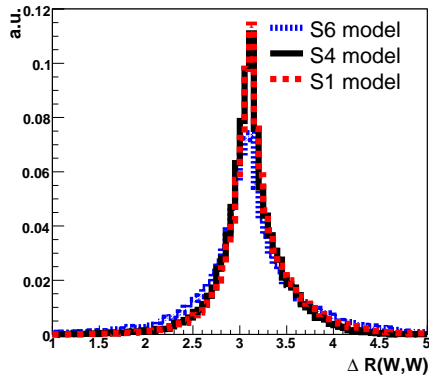# Signal characteristics at generation level

This appendix contains the figures that illustrate characteristics of signal VBF events as seen at generation level. Three signal models: S1, S4 and S6 with scalar resonances of masses varying between 650 and 1200 GeV are used. These distributions can thus be regarded as representative for models with the strongly-coupled sector.
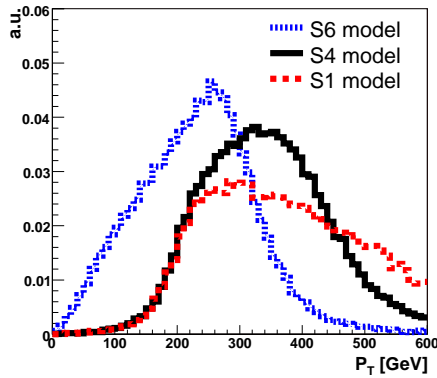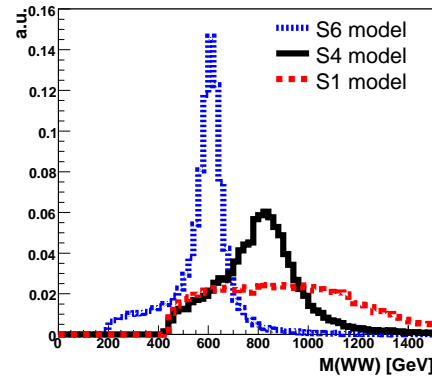

(a) Distributions of the final-state W boson transverse momentum.
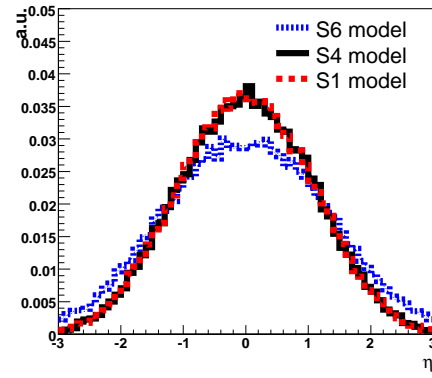
(b) Distributions of the final-state W boson pseudorapidity.
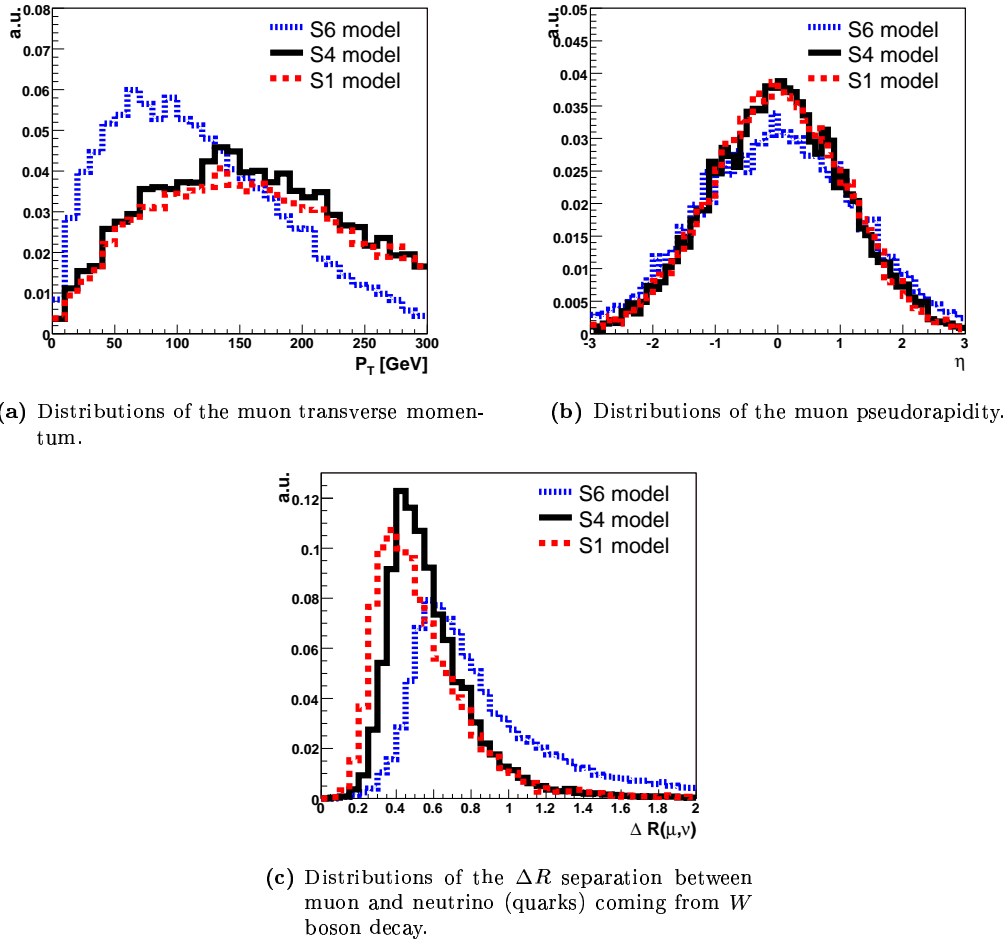
(c) Distributions of the separation ΔR between final-state W bosons.

(d) Distribution of two final-state W bosons invariant mass.

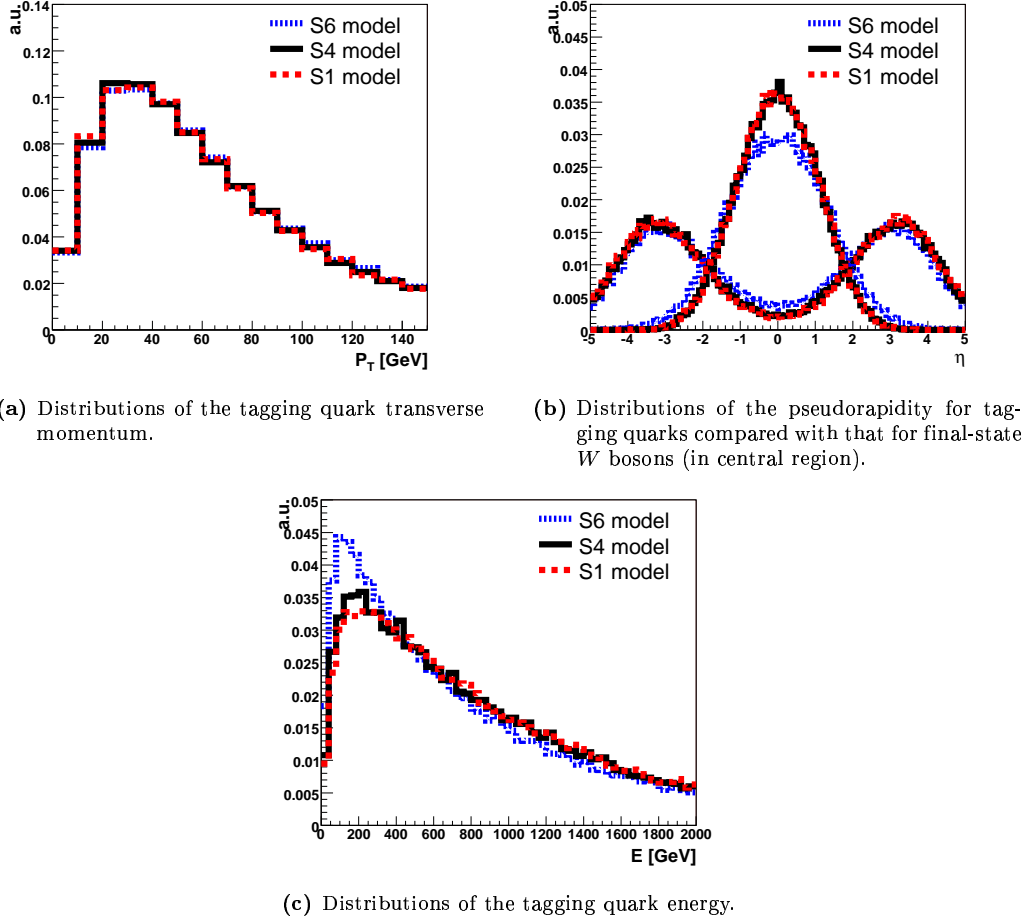**Figure E.1:** Distributions of the final-state W boson observables.

(a) Distributions of the muon transverse momentum.

(b) Distributions of the muon pseudorapidity.

(c) Distributions of the ΔR separation between muon and neutrino (quarks) coming from W boson decay.
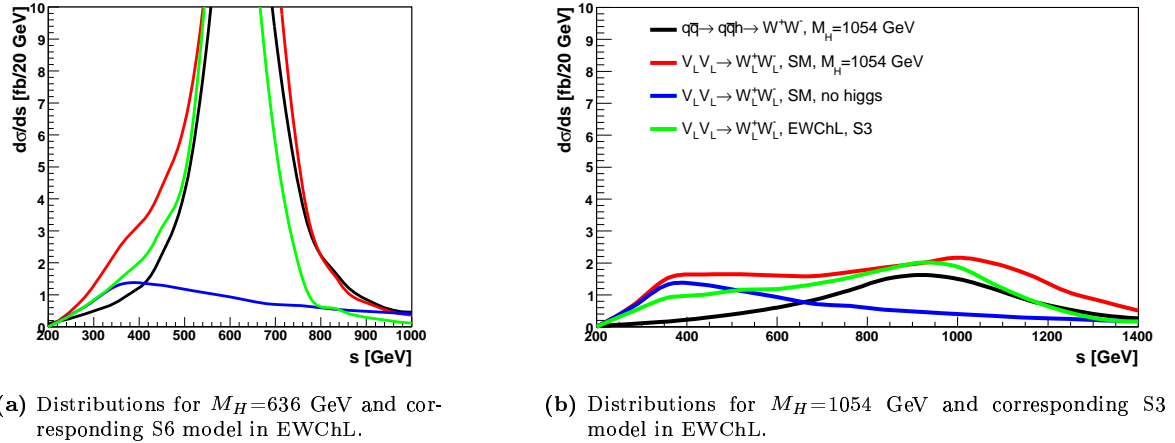
Figure E.2: Distributions of muon observables. They are universal for all W decay products (muon, neutrino and light quarks) since their masses are approximately the same and negligible in reference to the W boson mass.
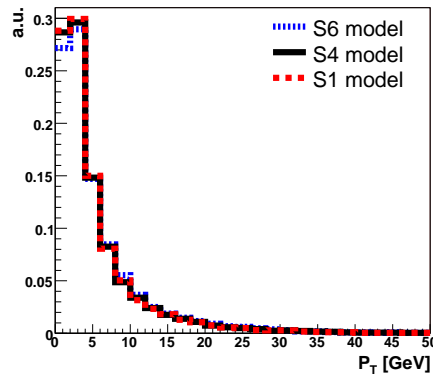
Figure E.3: Distributions of the transverse momentum of the system composed of two final-state W bosons and two tagging quarks.

140

(a) Distributions of the tagging quark transverse momentum.

(b) Distributions of the pseudorapidity for tagging quarks compared with that for final-state W bosons (in central region).

(c) Distributions of the tagging quark energy.

Figure E.4: Distributions of tagging quarks observables.

(a) Distributions for M_H=636 GeV and corresponding S6 model in EWChL.

(b) Distributions for M_H=1054 GeV and corresponding S3 model in EWChL.

Figure E.5: Invariant mass distribution for $V_L V_L \rightarrow W_L^+ W_L^-$ scattering system simulated within various models with scalar resonance (S6 and S3 scalar resonance model within EWChL) or within the SM with M_H=636 GeV and M_H=1054 GeV. For explanation please refer to Fig. 4.3. Legend is common for both pictures with exception for m_h and the name of the model.

Appendix F

Sets of parameters used in CompHEP

Event generations in CompHEP 4.2p1 [131, 132] have been performed with the use of two calculation models: "_SM_ud" and "_SM_qQ" [250] simplifying generation procedure. Their configuration is the following:

1. _SM_ud model
processes:	$pp \to W^+ j, W^- j$
	$pp \to W^+ jj, W^- jj$
	$pp \to W^+ jjj, W^- jjj$

   p, j stand for   u, $\bar{u}$, d, $\bar{d}$, g

   excluded diagrams: with photon as inter-state

   structure function for proton: CTEQ5L

   physical parameters:
   ```
   EE = 3.134500000000000E-01
   SW = 4.807600000000000E-01
   MZ = 9.118760000000000E+01
   wZ = 2.436800000000000E+00
   wW = 2.028420000000000E+00
   GG = 1.265123208342880E+00
   #QCD Lambda6 = 1.185000E-01
   Scale = 91.187
   ```

2. _SM_Qq model
processes:	$pp \to t\bar{t}$
	$pp \to t\bar{t}j$
	$pp \to t\bar{t}jj$

   p, j stand for: q, $\bar{q}$, g

   excluded diagrams: —

   structure function for proton: CTEQ5L

   physical parameters:
   ```
   Mtop = 1.750000000000000E+02
   wtop = 1.569000000000000E+00
     GG = 1.205763546298262E+00
   #QCD Lambda6= 1.185000E-01
   Scale = 175.
   ```

142

Appendix G

Details on study event samples generated in CompHEP

Here are presented the details on generated in CompHEP event samples that are used in Fig. 4.4(b) and in other studies in Sections 4.3.4 and 4.3.7.

For details on common parameters that are used for generation (parameters of the models) consult App. F.

1. $pp \to W^- j$ event sample
model: _SM_ud

Generator cuts:

variable	min. value	max. value
$p_T(j)$ [GeV]	100.	-
$p_T(W)$ [GeV]	100.	-
$\eta(j)$	-5.	5.
$\eta(W)$	-5.	5.
$\Delta R(j, W)$	0.2	-

2. $pp \to W^- j_1 j_2$ event sample
model _SM_ud

Generator cuts:

variable	min. value	max. value
$p_T(j_1)$ [GeV]	1., 5., 10., 20., 30., 40., 50., 60., 80., 100.	-
$p_T(j_2)$ [GeV]	1., 5., 10., 20., 30., 40., 50., 60., 80., 100.	-
$max\{p_T(j_1), p_T(j_2)\}$ [GeV]	100.	-
$p_T(W)$ [GeV]	100.	-
$\eta(j_1)$	-5.	5.
$\eta(j_2)$	-5.	5.
$\eta(W)$	-3.	3.
$\Delta R(j_1, j_2)$	0.2	-

3. $pp \to W^- j_1 j_2 j_3$ event sample
model: _SM_ud

Generator cuts:

variable	min. value	max. value
$p_T(j_1)$ [GeV]	1., 5., 10., 20., 30., 40., 50., 60., 80., 100.	-
$p_T(j_2)$ [GeV]	1., 5., 10., 20., 30., 40., 50., 60., 80., 100.	-
$p_T(j_3)$ [GeV]	1., 5., 10., 20., 30., 40., 50., 60., 80., 100.	-
$max\{p_T(j_1), p_T(j_2), p_T(j_3)\}$ [GeV]	100.	-
$p_T(W)$ [GeV]	100.	-
$\eta(j_1)$	-5.	5.
$\eta(j_2)$	-5.	5.
$\eta(j_3)$	-5.	5.
$\eta(W)$	-3.	3.
$\Delta R(j_1, j_2)$	0.2	-
$\Delta R(j_1, j_3)$	0.2	-
$\Delta R(j_2, j_3)$	0.2	-
$\Delta R(j_1, W)$	0.2	-
$\Delta R(j_2, W)$	0.2	-
$\Delta R(j_3, W)$	0.2	-

4. $pp \to t\bar{t}$ event sample
model: _SM_Qq

Generator cuts:

variable	min. value	max. value
$p_T(t)$	100.	
$p_T(\bar{t})$	100.	
$\eta(t)$	-5.5	5.5
$\eta(\bar{t})$	-5.5	5.5

G. DETAILS ON STUDY EVENT SAMPLES GENERATED IN COMPHEP

5. $pp \to t\bar{t}j$ event sample
model: _SM_Qq

Generator cuts:

variable	min. value	max. value
$p_T(j)$	1., 5., 10., 20., 30., 40., 50., 60., 80., 100.	-
$p_T(t)$	100.	
$p_T(\bar{t})$	100.	
$\eta(j)$	-5.5	5.5
$\eta(t)$	-5.5	5.5
$\eta(\bar{t})$	-5.5	5.5

6. $pp \to t\bar{t}j_1 j_2$ event sample
model: _SM_Qq

Generator cuts:

variable	min. value	max. value
$p_T(j1)$	10.	
$p_T(j2)$	10.	
$p_T(t)$	100.	
$p_T(\bar{t})$	100.	
$\eta(j1)$	-5.	5.
$\eta(j2)$	-5.	5.
$\eta(t)$	-5.	5.
$\eta(\bar{t})$	-5.	5.
$\Delta R(j1, j2)$	0.5	

144

Appendix H

Details on analysis samples generated in CompHEP

There are presented here the details on generated in CompHEP event samples that are used in analysis in Chapter 6. These details include: calculation model that has been used, generation-level cut and W boson decay channels used in PYTHIA during showering. Consult common parameters that are used for generation (parameters of the model) in App. F.

1. $pp \to W^- j_1 j_2 j_3$ event sample

   model: _SM_ud

Generator cuts:

variable	min. value	max. value
$p_T(j_1)$ [GeV]	30.	-
$p_T(j_2)$ [GeV]	30.	-
$p_T(j_3)$ [GeV]	30.	-
$max\{p_T(j_1), p_T(j_2), p_T(j_3)\}$ [GeV]	100.	
$p_T(W)$ [GeV]	100.	
$\eta(j_1)$	-5.	5.
$\eta(j_2)$	-5.	5.
$\eta(j_3)$	-5.	5.
$\eta(W)$	-3.	3.
$\Delta R(j_1, j_2)$	0.5	
$\Delta R(j_1, j_3)$	0.5	
$\Delta R(j_2, j_3)$	0.5	

W boson decay channels w PYTHIA:

```
MSEL = 0              !(D=1)
MDME 190,1 = 0        !W decay into dbar u
MDME 191,1 = 0        !W decay into dbar c
MDME 192,1 = 0        !W decay into dbar t
MDME 194,1 = 0        !W decay into sbar u
MDME 195,1 = 0        !W decay into sbar c
MDME 196,1 = 0        !W decay into sbar t
MDME 198,1 = 0        !W decay into bbar u
MDME 199,1 = 0        !W decay into bbar c
MDME 200,1 = 0        !W decay into bbar t
MDME 206,1 = 0        !W decay into e+ nu_e
MDME 207,1 = 1        !W decay into mu+ nu_mu
MDME 208,1 = 0        !W decay into tau+ nu_tau
```

2. $pp \to W^+ j_1 j_2 j_3$ event sample

   model: _SM_ud

Generator cuts:

variable	min. value	max. value
$p_T(j_1)$ [GeV]	30.	
$p_T(j_2)$ [GeV]	30.	
$p_T(j_3)$ [GeV]	30.	
$max\{p_T(j_1), p_T(j_2), p_T(j_3)\}$ [GeV]	100.	
$p_T(W)$ [GeV]	100.	
$\eta(j_1)$	-5.	5.
$\eta(j_2)$	-5.	5.
$\eta(j_3)$	-5.	5.
$\eta(W)$	-5.	5.
$\Delta R(j_1, j_2)$	0.5	
$\Delta R(j_1, j_3)$	0.5	
$\Delta R(j_2, j_3)$	0.5	

W boson decay channels w PYTHIA:

```
MSEL = 0              !(D=1)
MDME 190,1 = 0        !W decay into dbar u
MDME 191,1 = 0        !W decay into dbar c
MDME 192,1 = 0        !W decay into dbar t
MDME 194,1 = 0        !W decay into sbar u
MDME 195,1 = 0        !W decay into sbar c
MDME 196,1 = 0        !W decay into sbar t
MDME 198,1 = 0        !W decay into bbar u
MDME 199,1 = 0        !W decay into bbar c
MDME 200,1 = 0        !W decay into bbar t
MDME 206,1 = 0        !W decay into e+ nu_e
MDME 207,1 = 1        !W decay into mu+ nu_mu
MDME 208,1 = 0        !W decay into tau+ nu_tau
```

Appendix I

Additional plots to reconstruction

Here follows the figures illustrating reconstruction performance that is discussed in Section 5.4.
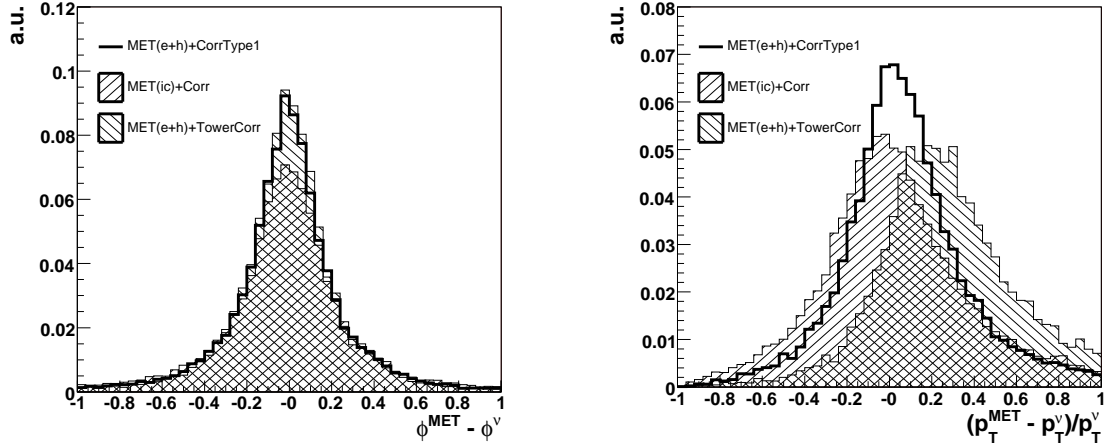

(a) Distributions of the error on ϕ angle for the MET reconstructed with various algorithms. Mean values for all distributions are consistent with zero. MET(e+h)+CorrType1 and MET(e+h)+TowerCorr provide the smallest σ's: respectively 0.204±0.002 and 0.196±0.002, whereas for MET(ic)+Corr σ=0.233±0.003 and the distribution has got long tails.

(b) Distributions of the relative error on transverse momentum for the MET reconstructed with various algorithms. MET(ic)+Corr provides the best mean value (0.005±0.003), but with large σ (0.324±0.003). MET(e+h)+CorrType1 provides mean value 0.054±0.002 not consistent with zero, but with very small σ: 0.259±0.003. Behavior of distribution for MET(e+h)+TowerCorr is unacceptable.

Figure I.1: Distributions of the errors on ϕ angle and transverse momentum for the MET reconstructed with various algorithms. Reconstructed value is compared with real neutrino. Considered are various MET algorithms: MET(e+h)+CorrType1 - the sum runs over calorimeter towers (corresponding electromagnetic and hadronic towers are summed) with MET correction type 1, MET(ic)+Corr - the sum runs over IC jets with jet corrections, MET(e+h)+TowerCorr - the sum runs over calorimeter towers with tower correction. All algorithms apply muon correction. Distributions are normalized to unity. The best algorithm is chosen basing on the mean and the standard deviation σ of the fitted Gaussian. The best behavior is observed for MET(e+h)+CorrType1 algorithm, for which the mean value of reconstructed MET is overestimated by only 5.4%, and resolution in ϕ is one of the best.
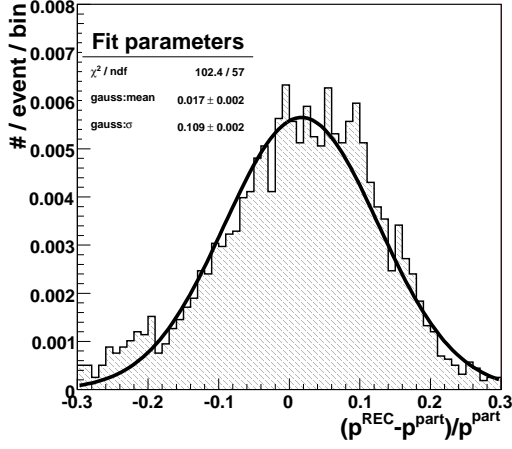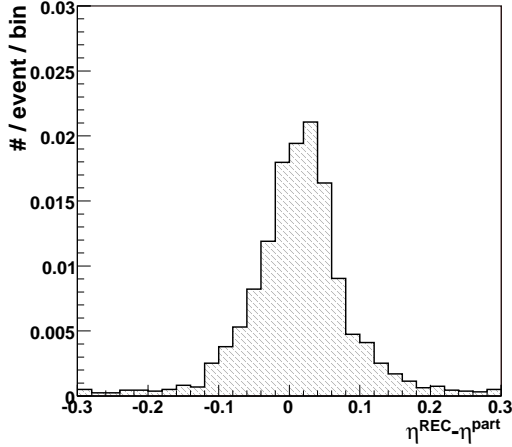
(a) Distributions of the relative error on transverse momentum for reconstructed boosted hadronic W.
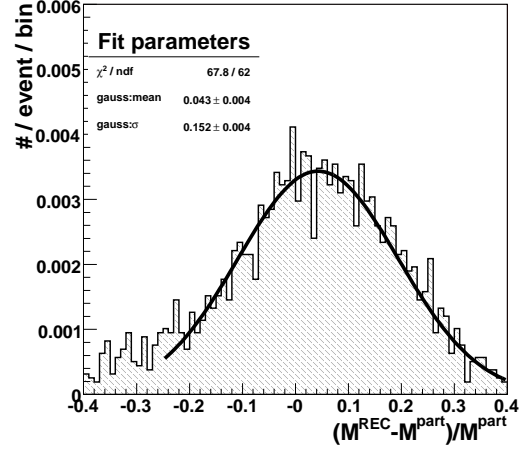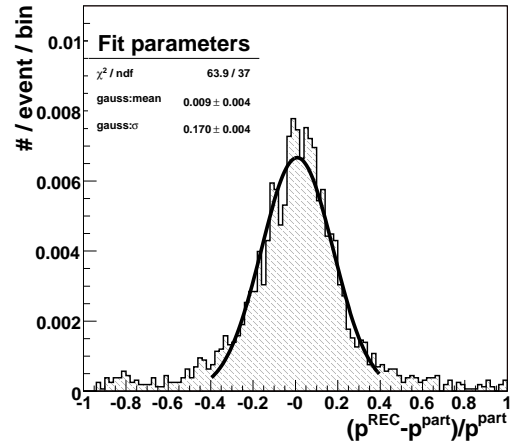

(b) Distributions of the relative error on mass for reconstructed boosted hadronic W.

Figure I.2: Distributions of the relative errors on transverse momentum and mass for reconstructed boosted hadronic W in signal S4 event sample. Resolutions are σ parameters of Gaussians fitted to these distributions. Fit is performed in the region for which the curve is plotted. The results of the fit are presented in the figures.
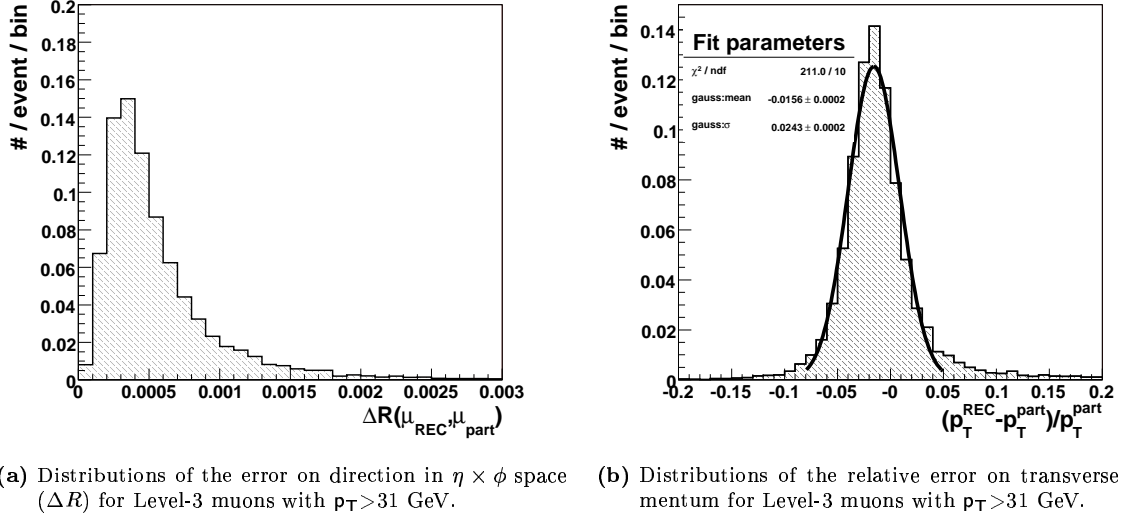

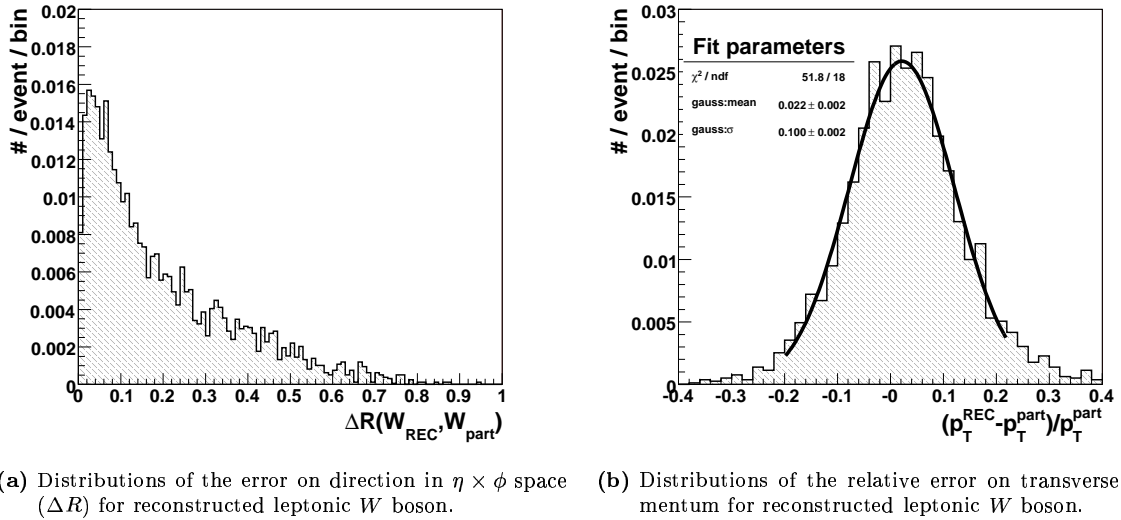**(a)** Distributions of the error on η for reconstructed tagging jet.

(b) Distributions of the relative error on transverse momentum for reconstructed tagging jet.

Figure I.3: Distributions of the errors on pseudorapidity and transverse momentum of reconstructed tagging jet in signal S4 event sample. Distributions are plotted after Introductory Selection that is defined in Sec. 6.3.2. Resolution in p_T is σ parameter of Gaussian fitted to the distribution in (b). Fit is performed in the region for which the curve is plotted. The results of the fit are presented in the figure.

147

(a) Distributions of the error on direction in $\eta \times \phi$ space (ΔR) for Level-3 muons with $p_T > 31$ GeV.

(b) Distributions of the relative error on transverse momentum for Level-3 muons with $p_T > 31$ GeV.

Figure I.4: Distributions of the errors on direction and transverse momentum for Level-3 muons with $p_T > 31$ GeV in signal S4 event sample. Resolution in p_T is σ parameter of Gaussian fitted to the distribution in (b). Fit is performed in the region for which the curve is plotted. The results of the fit are presented in the figure.

(a) Distributions of the error on direction in $\eta \times \phi$ space (ΔR) for reconstructed leptonic W boson.

(b) Distributions of the relative error on transverse momentum for reconstructed leptonic W boson.

Figure I.5: Distributions of the errors on direction and transverse momentum for reconstructed leptonic W boson in signal S4 event sample. Distributions are plotted after Introductory Selection that is defined in Sec. 6.3.2. Resolution in p_T is σ parameter of Gaussian fitted to the distribution in (b). Fit is performed in the region for which the curve is plotted. The results of the fit are presented in the figure.

Appendix J

Variables used in the preselection

This chapter contains a collection of distributions for the variables that are used in the preselection in Section 6.2. Distributions are normalized to unit area.
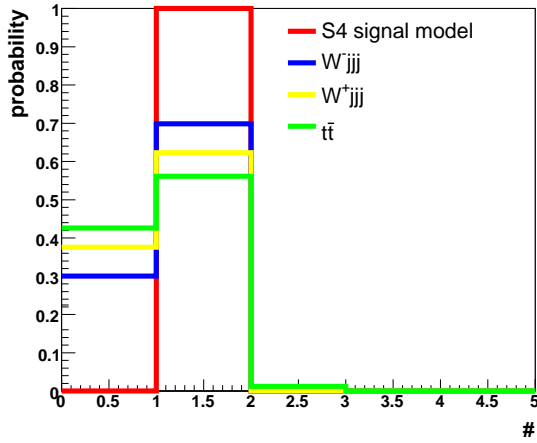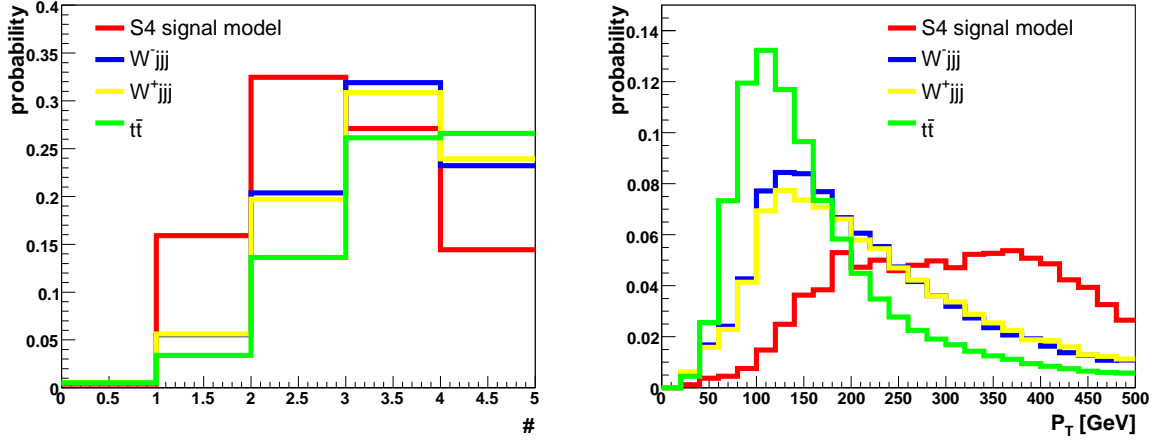

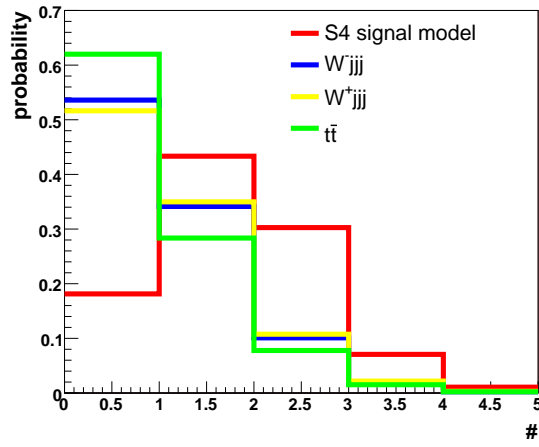(a) Distributions of the number for central muons.
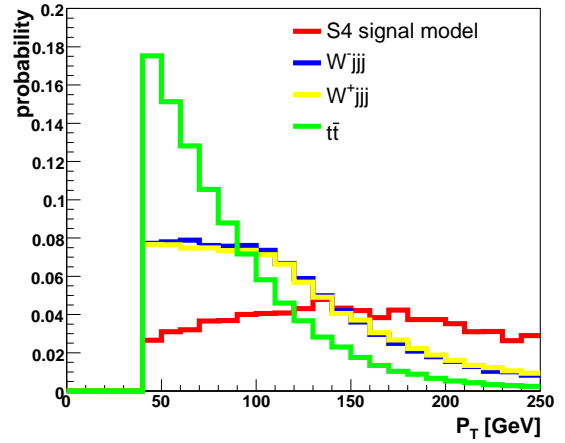
(b) Distributions of the transverse momentum for the muon for the case when only one central muon is reconstructed.

Figure J.1: Distributions of the muon variables used in the preselection. Distributions are normalized to unity.

(a) Distributions of the number for the central clusters.

(b) Distributions of the transverse momentum for the hardest central cluster.


(c) Distributions of the number for the forward+backward clusters.

Figure J.2: Distributions of the cluster variables used in the preselection. Distributions are normalized to unity.
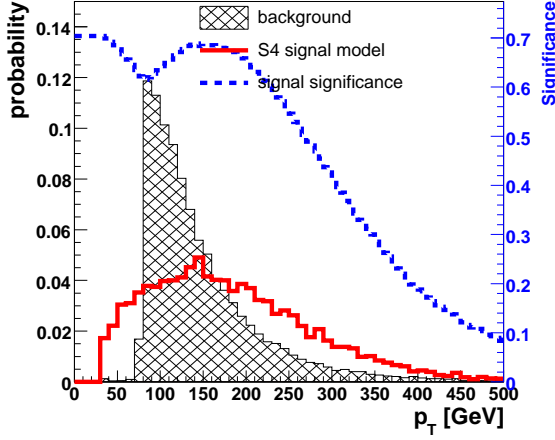
Appendix K

Variables used in the selection

This appendix contains distributions of the variables that are used in the selection in Section 6.3. Distributions are normalized to unity. The signal significance dependency on the value of the cut (superimposed in the same picture with the scale in the right) is calculated for signal and background rates in $\mathcal{L}_{int}=100$ fb^{-1}.

(a) Distributions of the number of central jets.

(b) Distributions of the number of forward+backward jets.

(c) Distributions of the number of forward (backward) jets.

(d) Distributions of the number of muons.
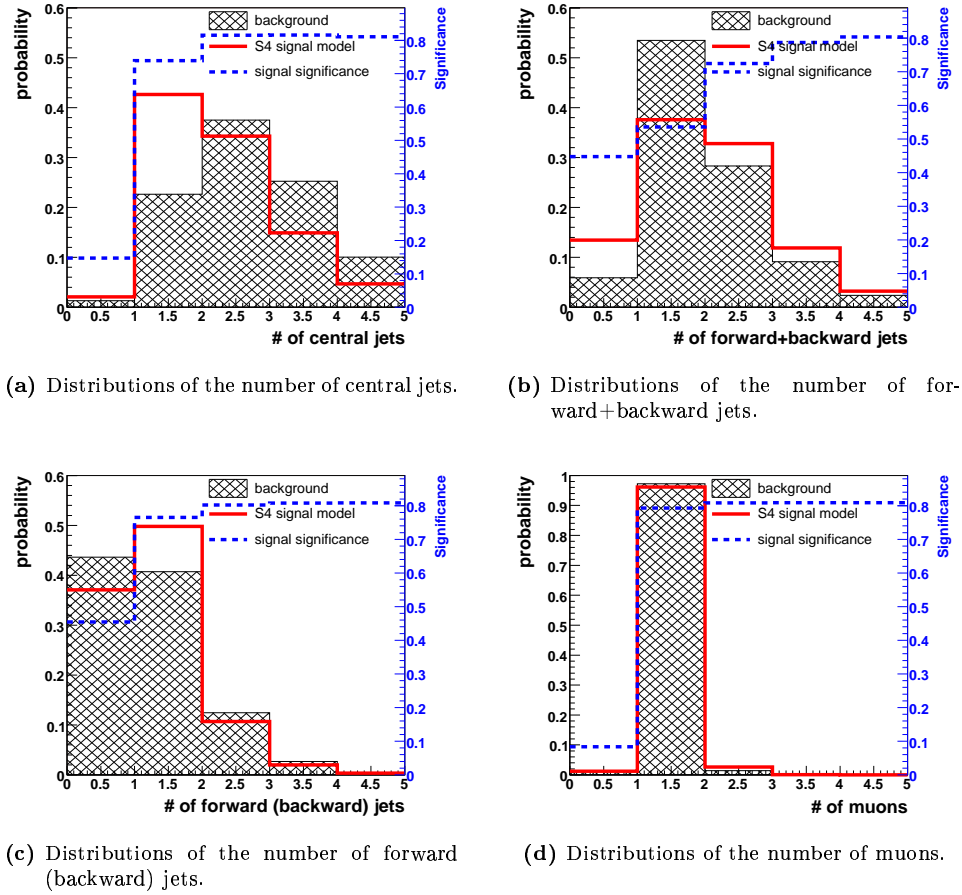
Figure K.1: Distributions of the numbers of jets and muons in background and signal sample. It is also shown the signal significance dependence on the lower cut on multiplicities.
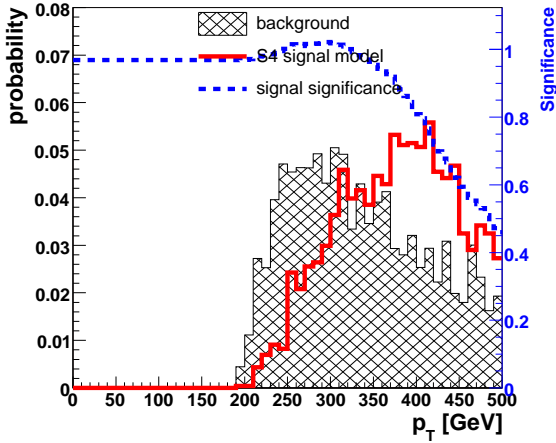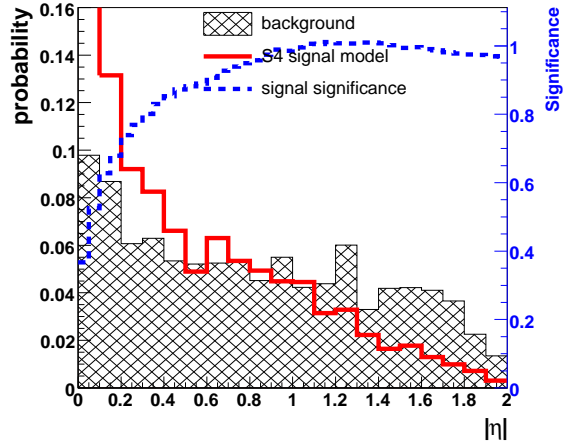
Figure K.2: Distribution of the transverse momentum of the muon in background and signal sample. Signal significance is plotted as a function of lower cut on p_T.
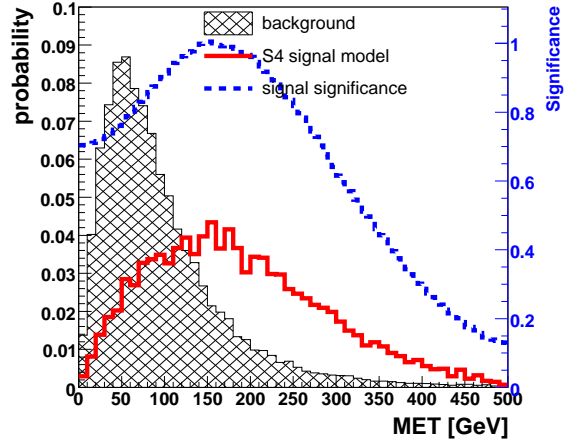
Figure K.3: Distribution of the MET in background and signal sample. Signal significance is plotted as a function of lower cut on the MET.
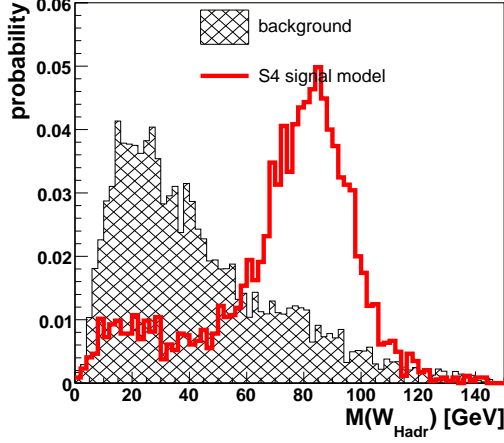

(a) Distribution of the $p_T(W_{\mathrm{Lept}})$ in background and signal sample. Signal significance is plotted as a function of lower cut on p_T.
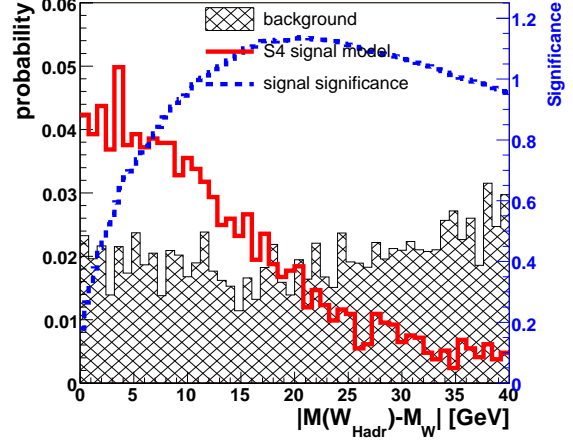
(b) Distribution of the $|\eta(W_{\mathrm{Lept}})|$ in background and signal sample. Signal significance is plotted as a function of upper cut on η.
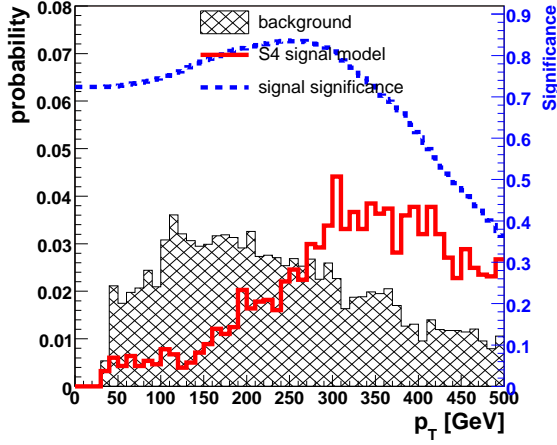
Figure K.4: Distributions of the transverse momentum and pseudorapidity of candidate for leptonic W in background and signal sample. Signal significance dependence on the cut is also shown.
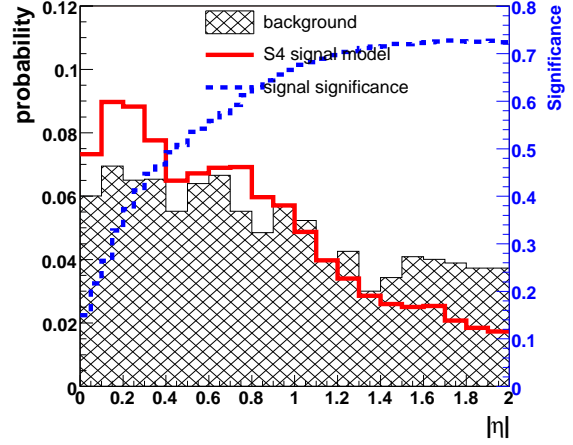
(a) Distribution of the invariant-mass for candidate for hadronic W $M(W_{\text{Hadr}})$ in background and signal sample.

(b) Distribution of the invariant-mass shift, *i.e.* $|M(W_{\text{Hadr}}) - M_W|$, for the candidate for hadronic W in background and signal sample. Signal significance is plotted as a function of upper cut on mass shift.

(c) Distribution of the transverse momentum for the candidate for hadronic W $p_T(W_{\text{Hadr}})$ in background and signal sample. Signal significance is plotted as a function of lower cut on p_T.

(d) Distribution of the absolute value for candidate for hadronic W pseudorapidity $|\eta(W_{\text{Hadr}})|$ in background and signal sample. Signal significance is plotted as a function of upper cut on $|\eta|$.

Figure K.5: Distributions of kinematic variables for candidate for hadronic W: (a) invariant-mass, (b) invariant-mass shift with respect to W mass, (c) transverse momentum and pseudorapidity in (d). Distributions are made for background and signal sample. Signal significance dependence on the cut is also shown. The plots are made before any cut on hadronic W.

153
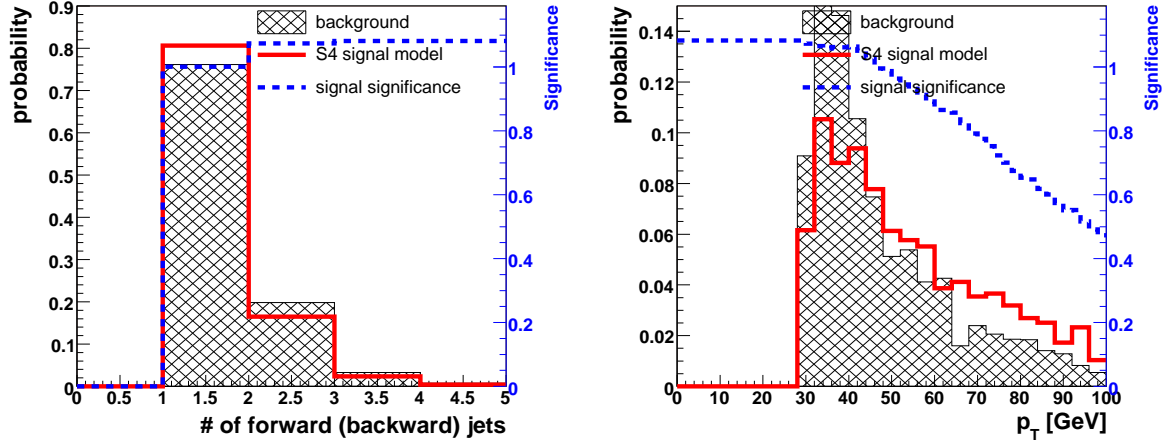
(a) Distribution of the forward (backward) jet multiplicity.

(b) Distribution of the minimal value of tagging jets' p_T.
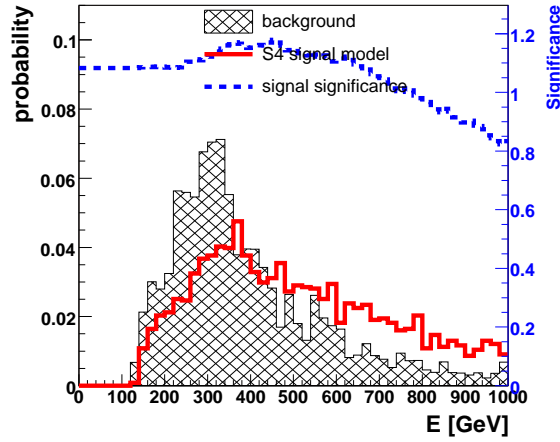
(c) Distribution of the minimal value of tagging jets' E.

Figure K.6: Distributions of reconstruction variables for forward and backward tagging jets in signal sample and background. There is also shown signal significance as a function of the lower cut on these variables.

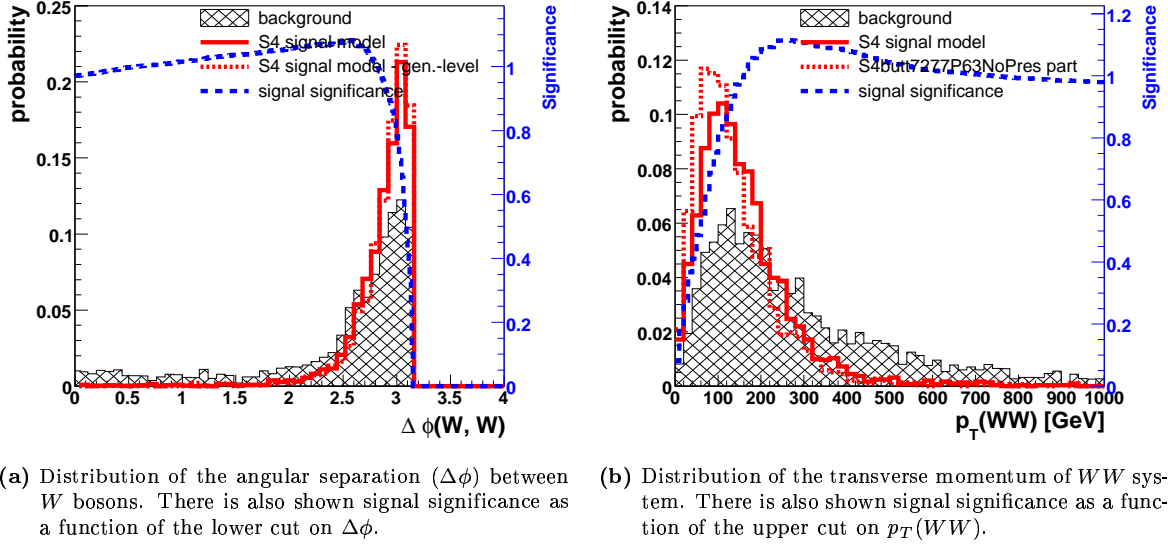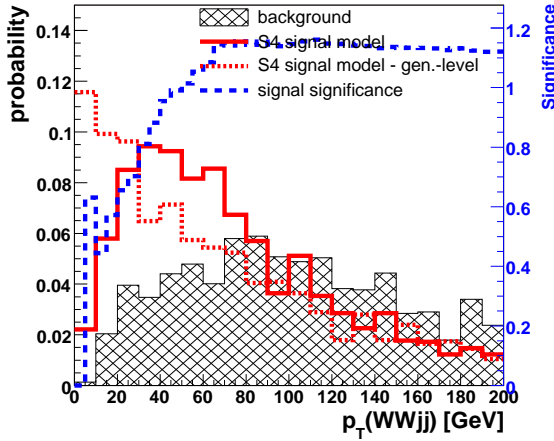**(a)** Distribution of the angular separation ($\Delta\phi$) between W bosons. There is also shown signal significance as a function of the lower cut on $\Delta\phi$.

(b) Distribution of the transverse momentum of WW system. There is also shown signal significance as a function of the upper cut on $p_T(WW)$.

Figure K.7: Distributions of reconstruction variables (angular separation and transverse momentum) for WW system in signal sample and background. They can be compared with distributions of these variables at generation-level for signal sample. There is also shown signal significance as a function of the cut on these variables.

Figure K.8: Distribution of the reconstructed $WWjj$ system transverse momentum in background and signal sample. It can be compared with distribution at generation-level. There is also shown signal significance as a function of the upper cut on $p_T(WWjj)$.
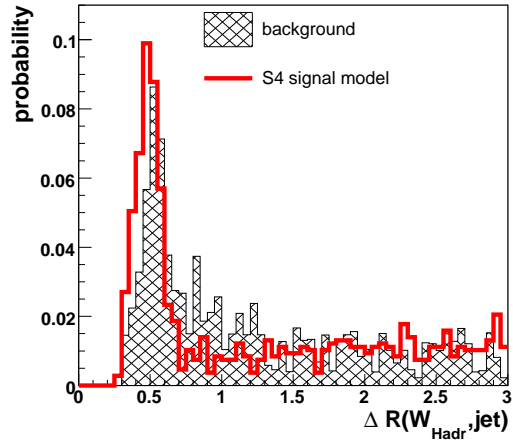
Figure K.9: Distribution of the distance between hadronic W and central ($p_T > 20$ GeV and $|\eta| < 2.0$) IC05ETGJ jets in $\eta \times \phi$ plane. Jet closest to hadronic W is omitted.
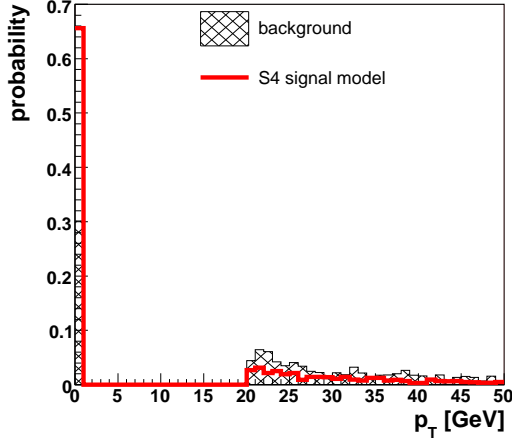
(a) Distribution of the minimal value of mini-jets' transverse momentum. Zero-bin represents events without mini-jets.
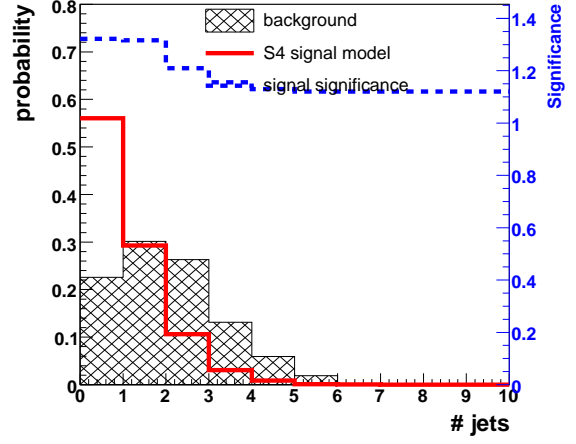
(b) Distribution of the number of central mini-jets. There is also shown signal significance as a function of the upper cut on the number.

Figure K.10: Distributions for central jets (`IC05ETGJ` jets with $p_T > 20$ GeV and $|\eta| < 2.0$) to be used in mini-jet veto. Excluded are jets that are closer than $\Delta R = 0.7$ to `IC07E` hadronic W jet.
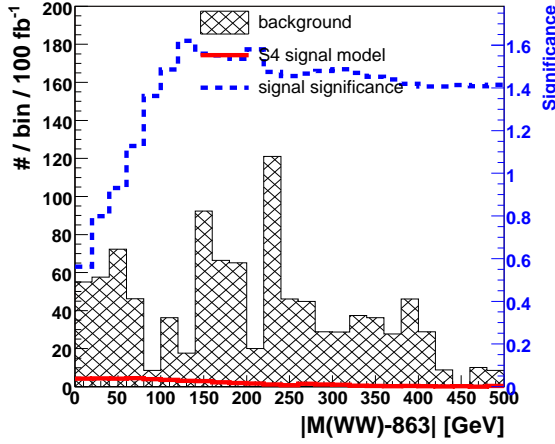
(a) Distribution of the M(WW) shift in linear scale.
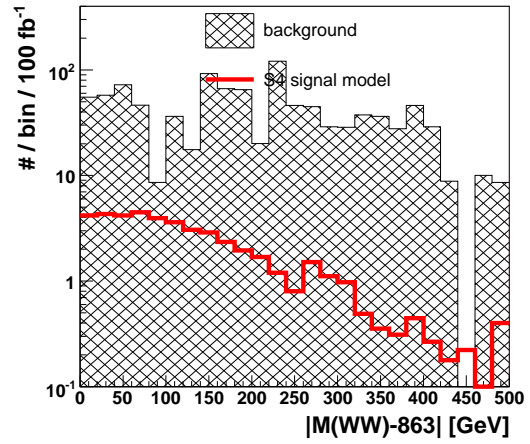
(b) Distribution of the M(WW) shift in logarithmic scale.

Figure K.11: Distribution of the shift (with respect to nominal value of 863 GeV) of the reconstructed WW invariant mass (mean of the Gaussian fitted to signal M(WW) distribution) in loose Main Selection. There are used two vertical axis scales: linear in (a) and logarithmic in (b). There is also shown signal significance as a function of the upper cut on the shift.
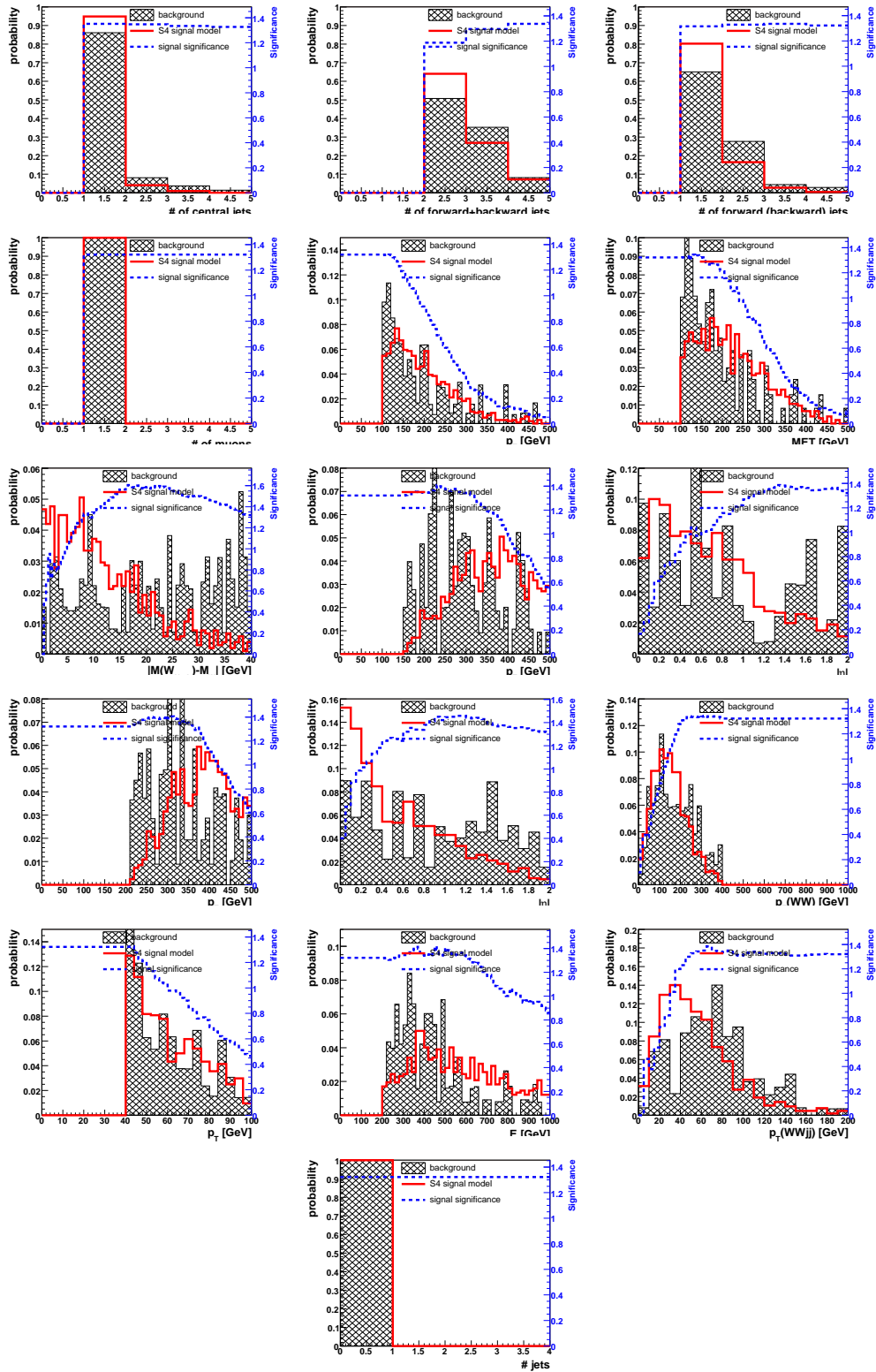
Figure K.12: Distributions of Introductory and Main Selection variables made after loose Main Selection. These plots correspond (respectively in order from the first to the last) to plots in Figs. K.1(a), K.1(b), K.1(c), K.1(d), K.2, K.3, K.5(b), K.5(c), K.5(d), K.4(a), K.4(b), K.7(b), K.6(b), K.6(c), K.8, K.10(b) that were made during Introductory and loose Main Selection (distributions of particular variables were made just before the cut on these variables).
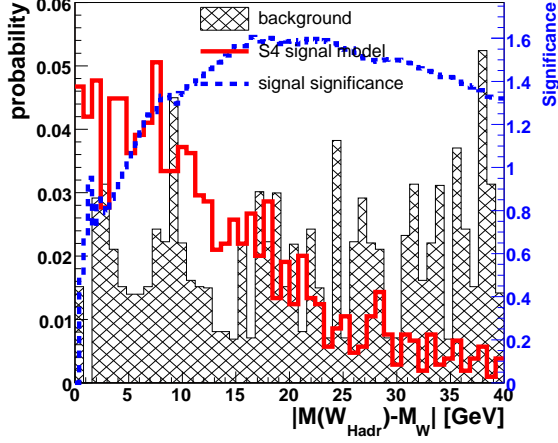
(a) Distribution of the invariant-mass shift, *i.e.* $|M(W_{\mathrm{Hadr}}) - M_W|$, for candidate for hadronic W in background and signal S4 sample. Signal significance is plotted as a function of upper cut on mass shift. Plotted after loose Main Selection.
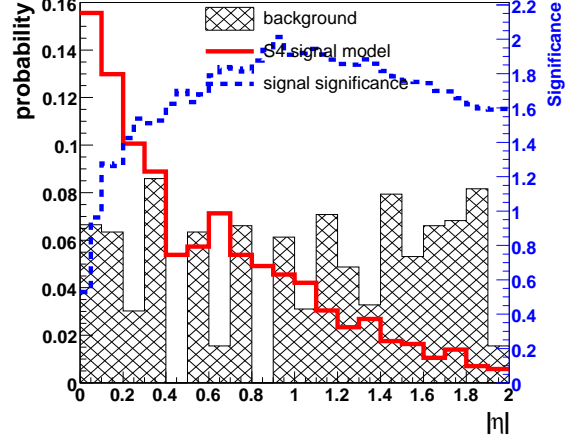
(b) Distribution of the pseudorapidity for leptonic W boson in background and signal S4 sample. Signal significance is plotted as a function of upper cut on η. Plotted after loose Main Selection and $\Delta M^{\mathrm{cut}}(W_{\mathrm{Hadr}})$=20 GeV.
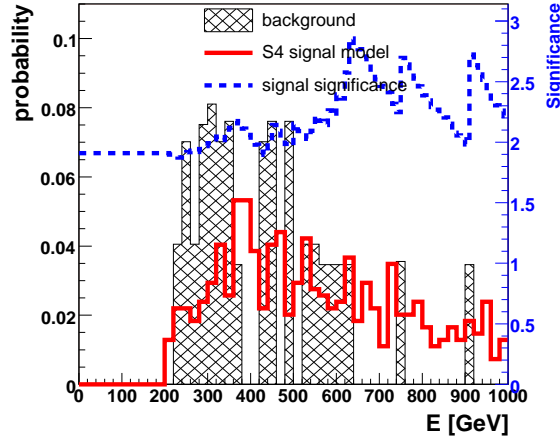
(c) Distribution of the energy for less energetic tagging jet in background and signal S4 sample. Signal significance is plotted as a function of lower cut on E. Plotted after loose Main Selection, $\Delta M^{\mathrm{cut}}(W_{\mathrm{Hadr}})$=20 GeV and $\eta^{\mathrm{cut}}(W_{\mathrm{Lept}}) = 1.0$.

Figure K.13: Distributions of the variables used to optimize Main Selection.
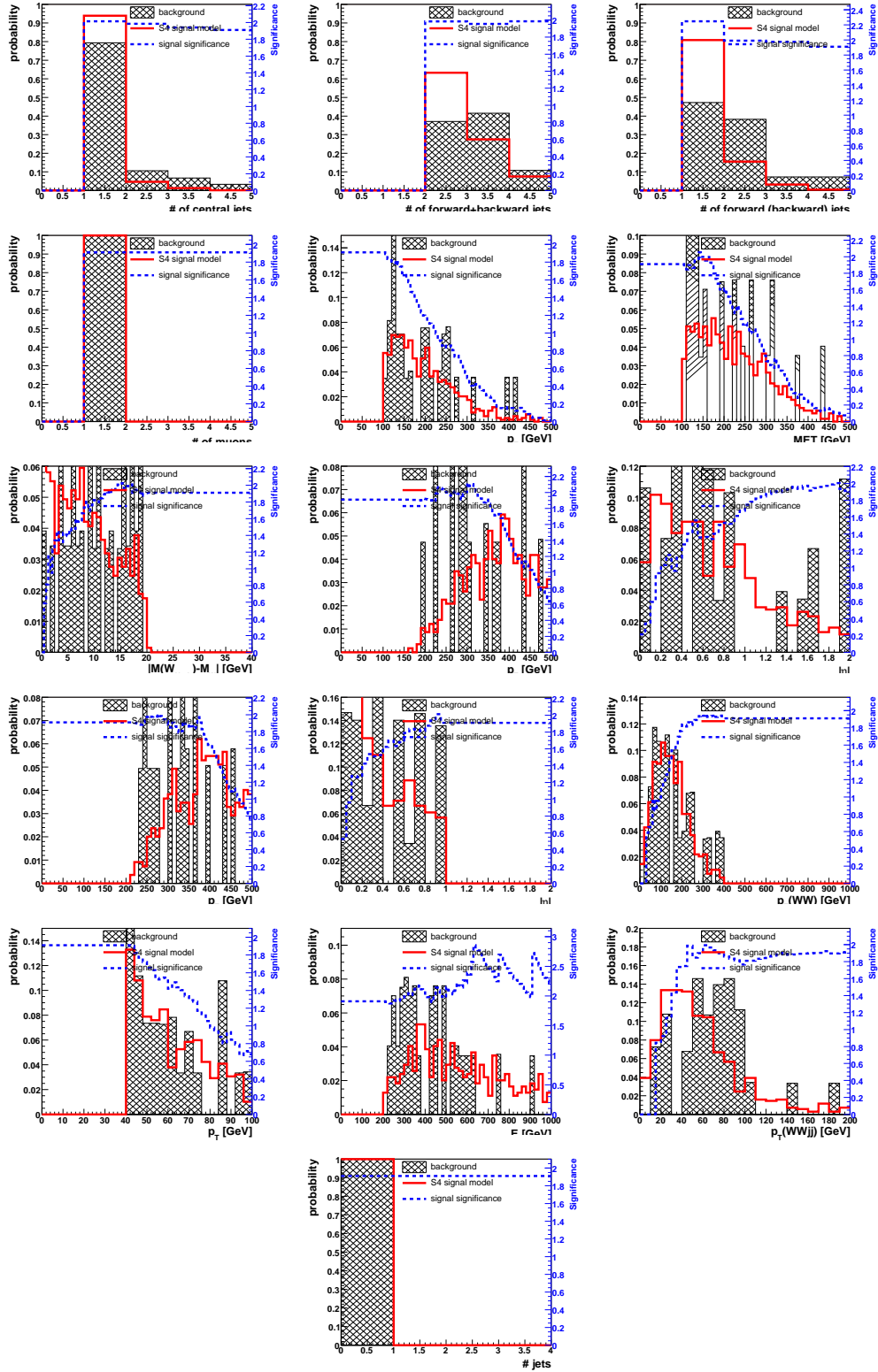
Figure K.14: Distributions of Introductory and Main Selection variables made after optimized Main Selection. See the caption to Fig. K.12 for further description.

References

[1] J. J. Thomson, "Carriers of negative electricity" *Nobel Lectures, Physics 1901-1921.*

[2] S. L. Glashow, "Partial symmetries of weak interactions" *Nucl. Phys.* **22** (1961) 579–588.

[3] S. Weinberg, "A model of leptons" *Phys. Rev. Lett.* **19** (1967) 1264–1266.

[4] A. Salam, "Weak and electromagnetic interactions". Originally printed in *Svartholm: Elementary Particle Theory, Proceedings Of The Nobel Symposium Held 1968 At Lerum, Sweden*, Stockholm 1968, 367-377.

[5] S. L. Glashow, J. Iliopoulos, and L. Maiani, "Weak interactions with lepton - hadron symmetry" *Phys. Rev.* **D2** (1970) 1285–1292.

[6] P. W. Higgs, "Broken symmetries, massless particles and gauge fields" *Phys. Lett.* **12** (1964) 132–133.

[7] P. W. Higgs, "Broken symmetries and the masses of gauge bosons" *Phys. Rev. Lett.* **13** (1964) 508–509.

[8] P. W. Higgs, "Spontaneous symmetry breakdown without massless bosons" *Phys. Rev.* **145** (1966) 1156–1163.

[9] T. W. B. Kibble, "Symmetry breaking in non-Abelian gauge theories" *Phys. Rev.* **155** (1967) 1554–1561.

[10] J. A. Bagger, A. F. Falk, and M. Swartz, "Precision observables and electroweak theories" *Phys. Rev. Lett.* **84** (2000) 1385–1388, [`hep-ph/9908327`].

[11] M. E. Peskin and T. Takeuchi, "A new constraint on a strongly interacting Higgs sector" *Phys. Rev. Lett.* **65** (1990) 964–967.

[12] M. E. Peskin and T. Takeuchi, "Estimation of oblique electroweak corrections" *Phys. Rev.* **D46** (1992) 381–409.

[13] J. M. Cornwall, D. N. Levin, and G. Tiktopoulos, "Derivation of gauge invariance from high-energy unitarity bounds on the S - matrix" *Phys. Rev.* **D10** (1974) 1145.

[14] B. W. Lee, C. Quigg, and H. B. Thacker, "Weak interactions at very high-energies: The role of the Higgs boson mass" *Phys. Rev.* **D16** (1977) 1519.

[15] M. S. Chanowitz and M. K. Gaillard, "The TeV physics of strongly interacting W's and Z's" *Nucl. Phys.* **B261** (1985) 379.

[16] F. Wilczek, "Quantum chromodynamics (QCD): The modern theory of the strong interaction" *Ann. Rev. Nucl. Part. Sci.* **32** (1982) 177–209.

[17] D. J. Gross and F. Wilczek, "Ultraviolet behavior of non-abelian gauge theories" *Phys. Rev. Lett.* **30** (1973) 1343–1346.

[18] H. D. Politzer, "Reliable perturbative results for strong interactions?" *Phys. Rev. Lett.* **30** (1973) 1346–1349.

[19] J. Alcaraz *et. al.*, **LEP** Collaboration, "A combination of preliminary electroweak measurements and constraints on the Standard Model" `hep-ex/0612034`.

[20] **LEP and SLC Groups** Collaboration, "Precision electroweak measurements on the Z resonance" *Phys. Rept.* **427** (2006) 257, [hep-ex/0509008].

[21] W. M. Yao *et. al.*, **Particle Data Group** Collaboration, "Review of particle physics" *J. Phys.* **G33** (2006) 1–1232.

[22] G. 't Hooft, "Renormalizable Lagrangians for massive Yang-Mills fields" *Nucl. Phys.* **B35** (1971) 167–188.

[23] B. W. Lee and J. Zinn-Justin, "Spontaneously broken gauge symmetries. I. preliminaries" *Phys. Rev.* **D5** (1972) 3121–3137.

[24] B. W. Lee and J. Zinn-Justin, "Spontaneously broken gauge symmetries II. perturbation theory and renormalization" *Phys. Rev.* **D5** (1972) 3137–3155.

[25] B. W. Lee and J. Zinn-Justin, "Spontaneously broken gauge symmetries. III. equivalence" *Phys. Rev.* **D5** (1972) 3155–3160.

[26] J. Goldstone, "Field theories with 'superconductor' solutions" *Nuovo Cim.* **19** (1961) 154–164.

[27] J. Goldstone, A. Salam, and S. Weinberg, "Broken symmetries" *Phys. Rev.* **127** (1962) 965–970.

[28] S. Weinberg, "The quantum theory of fields. vol. 2: Modern applications". Cambridge, UK: Univ. Pr. (1996) 489 p.

[29] C. E. Vayonakis, "Born helicity amplitudes and cross-sections in nonabelian gauge theories" *Nuovo Cim. Lett.* **17** (1976) 383.

[30] G. J. Gounaris, R. Kogerler, and H. Neufeld, "On the relationship between longitudinally polarized vector bosons and their unphysical scalar partners" *Phys. Rev.* **D34** (1986) 3257.

[31] S. Weinberg, "Implications of dynamical symmetry breaking: An addendum" *Phys. Rev.* **D19** (1979) 1277–1280.

[32] L. Susskind, "Dynamics of spontaneous symmetry breaking in the Weinberg- Salam theory" *Phys. Rev.* **D20** (1979) 2619–2625.

[33] R. A. Diaz and R. Martinez, "The custodial symmetry" *Rev. Mex. Fis.* **47** (2001) 489–492, [hep-ph/0302058].

[34] P. Sikivie, L. Susskind, M. B. Voloshin, and V. I. Zakharov, "Isospin breaking in technicolor models" *Nucl. Phys.* **B173** (1980) 189.

[35] B. W. Lee, C. Quigg, and H. B. Thacker, "The strength of weak interactions at very high-energies and the higgs boson mass" *Phys. Rev. Lett.* **38** (1977) 883.

[36] D. A. Dicus and V. S. Mathur, "Upper bounds on the values of masses in unified gauge theories" *Phys. Rev.* **D7** (1973) 3111–3114.

[37] M. Luscher and P. Weisz, "Is there a strong interaction sector in the standard lattice Higgs model?" *Phys. Lett.* **B212** (1988) 472.

[38] W. J. Marciano, G. Valencia, and S. Willenbrock, "Renormalization group improved unitarity bounds on the Higgs boson and top quark masses" *Phys. Rev.* **D40** (1989) 1725.

[39] J. Bagger, S. Dawson, and G. Valencia, "Effective field theory of anomalous gauge-boson couplings at high-energy pp colliders" *Nucl. Phys.* **B399** (1993) 364–394, [hep-ph/9204211].

[40] G. Altarelli and G. Isidori, "Lower limit on the Higgs mass in the Standard Model: An Update" *Phys. Lett.* **B337** (1994) 141–144.

[41] J. A. Casas, J. R. Espinosa, and M. Quiros, "Improved Higgs mass stability bound in the Standard Model and implications for supersymmetry" *Phys. Lett.* **B342** (1995) 171–179, [hep-ph/9409458].

REFERENCES

[42] J. A. Casas, J. R. Espinosa, and M. Quiros, "Standard Model stability bounds for new physics within LHC reach" *Phys. Lett.* **B382** (1996) 374–382, [hep-ph/9603227].

[43] K. Riesselmann, "Limitations of a standard model Higgs boson" hep-ph/9711456.

[44] L. Susskind, "The gauge hierarchy problem, technicolor, supersymmetry, and all that. (talk)" *Phys. Rept.* **104** (1984) 181–193.

[45] K. G. Wilson, "Renormalization group and critical phenomena. 2. Phase space cell analysis of critical behavior" *Phys. Rev.* **B4** (1971) 3184–3205.

[46] K. G. Wilson and J. B. Kogut, "The renormalization group and the epsilon expansion" *Phys. Rept.* **12** (1974) 75–200.

[47] e. . 't Hooft, Gerard *et. al.*, "Recent developments in gauge theories. proceedings, Nato Advanced Study Institute, Cargese, France, August 26 - September 8, 1979". New York, Usa: Plenum (1980) 438 P. (Nato Advanced Study Institutes Series: Series B, Physics, 59).

[48] M. S. Chanowitz, "Electroweak symmetry breaking: Unitarity, dynamics, experimental prospects" *Ann. Rev. Nucl. Part. Sci.* **38** (1988) 323–420.

[49] Y. A. Golfand and E. P. Likhtman, "Extension of the algebra of poincare group generators and violation of p invariance" *JETP Lett.* **13** (1971) 323–326.

[50] D. V. Volkov and V. P. Akulov, "Is the neutrino a goldstone particle?" *Phys. Lett.* **B46** (1973) 109–110.

[51] J. Wess and B. Zumino, "Supergauge transformations in four-dimensions" *Nucl. Phys.* **B70** (1974) 39–50.

[52] C. Csaki, C. Grojean, L. Pilo, and J. Terning, "Towards a realistic model of higgsless electroweak symmetry breaking" *Phys. Rev. Lett.* **92** (2004) 101802, [hep-ph/0308038].

[53] Y. Nomura, "Higgsless theory of electroweak symmetry breaking from warped space" *JHEP* **11** (2003) 050, [hep-ph/0309189].

[54] S. Weinberg, "Pion scattering lengths" *Phys. Rev. Lett.* **17** (1966) 616–621.

[55] W. Kilian, "Electroweak symmetry breaking: The bottom-up approach" *Springer Tracts Mod. Phys.* **198** (2003) 1–113.

[56] W. Kilian, "Dynamical electroweak symmetry breaking" hep-ph/0303015.

[57] S. Weinberg, "Nonlinear realizations of chiral symmetry" *Phys. Rev.* **166** (1968) 1568–1577.

[58] S. R. Coleman, J. Wess, and B. Zumino, "Structure of phenomenological Lagrangians. 1" *Phys. Rev.* **177** (1969) 2239–2247.

[59] J. Callan, Curtis G., S. R. Coleman, J. Wess, and B. Zumino, "Structure of phenomenological Lagrangians. 2" *Phys. Rev.* **177** (1969) 2247–2250.

[60] S. Weinberg, "Phenomenological Lagrangians" *Physica* **A96** (1979) 327.

[61] T. Appelquist and C. W. Bernard, "Strongly interacting Higgs bosons" *Phys. Rev.* **D22** (1980) 200.

[62] A. C. Longhitano, "Heavy Higgs bosons in the Weinberg-Salam model" *Phys. Rev.* **D22** (1980) 1166.

[63] A. C. Longhitano, "Low-energy impact of a heavy Higgs boson sector" *Nucl. Phys.* **B188** (1981) 118.

[64] M. Gell-Mann and M. Levy, "The axial vector current in beta decay" *Nuovo Cim.* **16** (1960) 705.

[65] M. J. G. Veltman, "Second threshold in weak interactions" *Acta Phys. Polon.* **B8** (1977) 475.

[66] R. Barate *et. al.*, **LEP Working Group for Higgs boson searches** Collaboration, "Search for the standard model Higgs boson at LEP" *Phys. Lett.* **B565** (2003) 61–75, [hep-ex/0306033].

[67] R. S. Chivukula and N. J. Evans, "Triviality and the precision bound on the Higgs mass" *Phys. Lett.* **B464** (1999) 244–248, [hep-ph/9907414].

[68] M. E. Peskin and J. D. Wells, "How can a heavy Higgs boson be consistent with the precision electroweak measurements?" *Phys. Rev.* **D64** (2001) 093003, [hep-ph/0101342].

[69] C. F. Kolda and H. Murayama, "The Higgs mass and new physics scales in the minimal Standard Model" *JHEP* **07** (2000) 035, [hep-ph/0003170].

[70] C. P. Burgess, "Goldstone and pseudo-goldstone bosons in nuclear, particle and condensed-matter physics" *Phys. Rept.* **330** (2000) 193–261, [hep-th/9808176].

[71] S. Weinberg, "Implications of dynamical symmetry breaking" *Phys. Rev.* **D13** (1976) 974–996.

[72] S. Weinberg, "Elementary particle theory of composite particles" *Phys. Rev.* **130** (1963) 776–783.

[73] S. Weinberg, "Quasiparticles and the Born series" *Phys. Rev.* **131** (1963) 440–460.

[74] M. Scadron and S. Weinberg, "Potential theory calculations by the quasiparticle method" *Phys. Rev.* **133** (1964) B1589–B1596.

[75] M. Scadron, S. Weinberg, and J. Wright, "Functional analysis and scattering theory" *Phys. Rev.* **135** (1964) B202–B207.

[76] B. Holdom and J. Terning, "Large corrections to electroweak parameters in technicolor theories" *Phys. Lett.* **B247** (1990) 88–92.

[77] M. Golden and L. Randall, "Radiative corrections to electroweak parameters in technicolor theories" *Nucl. Phys.* **B361** (1991) 3–23.

[78] R. S. Chivukula, "An introduction to dynamical electroweak symmetry breaking" hep-ph/9701322.

[79] K. Lane, "Two lectures on technicolor" hep-ph/0202255.

[80] S. F. King, "Dynamical electroweak symmetry breaking" *Rept. Prog. Phys.* **58** (1995) 263–310, [hep-ph/9406401].

[81] C. T. Hill and E. H. Simmons, "Strong dynamics and electroweak symmetry breaking" *Phys. Rept.* **381** (2003) 235–402, [hep-ph/0203079].

[82] C. T. Hill and E. H. Simmons, "Erratum to 'Strong dynamics and electroweak symmetry breaking' [Phys. Rep. 381 (2003) 235-402]" *Phys. Rept.* **390** (2004) 553–554.

[83] R. Casalbuoni *et. al.*, "Symmetries for vector and axial vector mesons" *Phys. Lett.* **B349** (1995) 533–540, [hep-ph/9502247].

[84] R. Casalbuoni *et. al.*, "Degenerate bess model: The possibility of a low energy strong electroweak sector" *Phys. Rev.* **D53** (1996) 5201–5221, [hep-ph/9510431].

[85] N. Arkani-Hamed, A. G. Cohen, and H. Georgi, "Electroweak symmetry breaking from dimensional deconstruction" *Phys. Lett.* **B513** (2001) 232–240, [hep-ph/0105239].

[86] N. Arkani-Hamed, A. G. Cohen, T. Gregoire, and J. G. Wacker, "Phenomenology of electroweak symmetry breaking from theory space" *JHEP* **08** (2002) 020, [hep-ph/0202089].

REFERENCES

[87] D. B. Kaplan and H. Georgi, "SU(2) x U(1) breaking by vacuum misalignment" *Phys. Lett.* **B136** (1984) 183.

[88] D. B. Kaplan, H. Georgi, and S. Dimopoulos, "Composite Higgs scalars" *Phys. Lett.* **B136** (1984) 187.

[89] M. J. Dugan, H. Georgi, and D. B. Kaplan, "Anatomy of a composite Higgs model" *Nucl. Phys.* **B254** (1985) 299.

[90] N. Arkani-Hamed *et. al.*, "The minimal moose for a little higgs" *JHEP* **08** (2002) 021, [hep-ph/0206020].

[91] N. Arkani-Hamed, A. G. Cohen, E. Katz, and A. E. Nelson, "The littlest higgs" *JHEP* **07** (2002) 034, [hep-ph/0206021].

[92] I. Low, W. Skiba, and D. Smith, "Little higgses from an antisymmetric condensate" *Phys. Rev.* **D66** (2002) 072001, [hep-ph/0207243].

[93] M. Golden, T. Han, and G. Valencia, "Strongly-interacting electroweak sector: Model independent approaches" hep-ph/9511206.

[94] A. Dobado, M. J. Herrero, J. R. Pelaez, E. Ruiz Morales, and M. T. Urdiales, "Learning about the strongly interacting symmetry breaking sector at LHC" *Phys. Lett.* **B352** (1995) 400–410, [hep-ph/9502309].

[95] A. S. Belyaev *et. al.*, "Strongly interacting vector bosons at the LHC: Quartic anomalous couplings" *Phys. Rev.* **D59** (1999) 015022, [hep-ph/9805229].

[96] A. Dobado, M. J. Herrero, J. R. Pelaez, and E. Ruiz Morales, "LHC sensitivity to the resonance spectrum of a minimal strongly interacting electroweak symmetry breaking sector" *Phys. Rev.* **D62** (2000) 055011, [hep-ph/9912224].

[97] J. M. Butterworth, B. E. Cox, and J. R. Forshaw, "W W scattering at the LHC" *Phys. Rev.* **D65** (2002) 096014, [hep-ph/0201098].

[98] M. J. Herrero and E. Ruiz Morales, "The Electroweak chiral Lagrangian for the Standard Model with a heavy Higgs" *Nucl. Phys.* **B418** (1994) 431–455, [hep-ph/9308276].

[99] M. J. Herrero and E. Ruiz Morales, "Nondecoupling effects of the SM Higgs boson to one loop" *Nucl. Phys.* **B437** (1995) 319–355, [hep-ph/9411207].

[100] D. Espriu and J. Matias, "Some remarks on the matching conditions" *Phys. Lett.* **B341** (1995) 332–341, [hep-ph/9407292].

[101] S. Dittmaier and C. Grosse-Knetter, "Integrating out the standard Higgs field in the path integral" *Nucl. Phys.* **B459** (1996) 497–536, [hep-ph/9505266].

[102] A. Nyffeler and A. Schenk, "Effective field theory for a heavy higgs: A manifestly gauge invariant approach" *Phys. Rev.* **D53** (1996) 1494–1507, [hep-ph/9507287].

[103] A. Nyffeler and A. Schenk, "The electroweak chiral Lagrangian reanalyzed" *Phys. Rev.* **D62** (2000) 113006, [hep-ph/9907294].

[104] T. Appelquist and G.-H. Wu, "The electroweak chiral Lagrangian and new precision measurements" *Phys. Rev.* **D48** (1993) 3235–3241, [hep-ph/9304240].

[105] J. Gasser and H. Leutwyler, "Chiral perturbation theory to one loop" *Ann. Phys.* **158** (1984) 142.

[106] G. Ecker, J. Gasser, H. Leutwyler, A. Pich, and E. de Rafael, "Chiral Lagrangians for massive spin 1 fields" *Phys. Lett.* **B223** (1989) 425.

[107] G. Ecker, J. Gasser, A. Pich, and E. de Rafael, "The role of resonances in chiral perturbation theory" *Nucl. Phys.* **B321** (1989) 311.

[108] A. Manohar and H. Georgi, "Chiral Quarks and the Nonrelativistic Quark Model" *Nucl. Phys.* **B234** (1984) 189.

[109] G. Valencia and S. Willenbrock, "The heavy Higgs resonance" *Phys. Rev.* **D46** (1992) 2247–2251.

[110] J. R. Pelaez, "Resonance spectrum of the strongly interacting symmetry breaking sector" *Phys. Rev.* **D55** (1997) 4193–4202, [hep-ph/9609427].

[111] J. L. Basdevant, "The Pade approximation and its physical applications" *Fortsch. Phys.* **20** (1972) 283–331.

[112] T. N. Truong, "Chiral perturbation theory and final state theorem" *Phys. Rev. Lett.* **61** (1988) 2526.

[113] T. N. Truong, "Remarks on the unitarization methods" *Phys. Rev. Lett.* **67** (1991) 2260–2263.

[114] A. Dobado, "The mass and the width of the higgs in the strongly interacting minimal Standard Model" *Phys. Lett.* **B237** (1990) 457.

[115] A. Dobado, M. J. Herrero, and T. N. Truong, "Unitarized chiral perturbation theory for elastic pion-pion scattering" *Phys. Lett.* **B235** (1990) 134.

[116] A. Dobado and J. R. Pelaez, "A global fit of pi pi and pi k elastic scattering in chpt with dispersion relations" *Phys. Rev.* **D47** (1993) 4883–4888, [hep-ph/9301276].

[117] A. Dobado and J. R. Pelaez, "The inverse amplitude method in chiral perturbation theory" *Phys. Rev.* **D56** (1997) 3057–3073, [hep-ph/9604416].

[118] D. A. Dicus and W. W. Repko, "Pade approximants and unitarity in W^+W^- and Z^0Z^0 scattering" *Phys. Rev.* **D42** (1990) 3660–3667.

[119] A. Dobado, M. J. Herrero, and J. Terron, "The role of chiral Lagrangians in strongly interacting W(L) W(L) signals at p p supercolliders" *Z. Phys.* **C50** (1991) 205–220.

[120] J. Bagger *et. al.*, "The strongly interacting w w system: Gold plated modes" *Phys. Rev.* **D49** (1994) 1246–1264, [hep-ph/9306256].

[121] J. A. Oller, E. Oset, and J. R. Pelaez, "Non-perturbative approach to effective chiral Lagrangians and meson interactions" *Phys. Rev. Lett.* **80** (1998) 3452–3455, [hep-ph/9803242].

[122] J. A. Oller, E. Oset, and J. R. Pelaez, "Erratum: Meson meson and meson baryon interactions in a chiral non- perturbative approach" *Phys. Rev.* **D60** (1999) 099906.

[123] F. Guerrero and J. A. Oller, "K anti-K scattering amplitude to one loop in chiral perturbation theory, its unitarization and pion form factors" *Nucl. Phys.* **B537** (1999) 459–476, [hep-ph/9805334].

[124] A. Brunstein, O. J. P. Eboli, and M. C. Gonzalez-Garcia, "Constraints on quartic vector-boson interactions from z physics" *Phys. Lett.* **B375** (1996) 233–239, [hep-ph/9602264].

[125] T. Han, "Strong interactions of weak bosons" hep-ph/9910495.

[126] M. A. Dobbs *et. al.*, "Les Houches guidebook to Monte Carlo generators for hadron collider physics" hep-ph/0403045.

[127] G. Arnison *et. al.*, **UA1** Collaboration, "Observation of jets in high transverse energy events at the CERN proton - anti-proton collider" *Phys. Lett.* **B123** (1983) 115.

[128] C. Albajar *et. al.*, **UA1** Collaboration, "Production of low transverse energy clusters in anti-p p collisions at s**(1/2) = 0.2-Tev to 0.9-Tev and their interpretation in terms of QCD jets" *Nucl. Phys.* **B309** (1988) 405.

[129] T. Sjostrand, L. Lonnblad, and S. Mrenna, "PYTHIA 6.2: Physics and manual" hep-ph/0108264.

REFERENCES

[130] H. L. Lai *et. al.*, **CTEQ** Collaboration, "Global QCD analysis of parton structure of the nucleon: CTEQ5 parton distributions" *Eur. Phys. J.* **C12** (2000) 375–392, [hep-ph/9903282].

[131] A. Pukhov *et. al.*, "CompHEP: A package for evaluation of Feynman diagrams and integration over multi-particle phase space. User's manual for version 33" hep-ph/9908288.

[132] E. Boos *et. al.*, **CompHEP** Collaboration, "CompHEP 4.4: Automatic computations from Lagrangians to events" *Nucl. Instrum. Meth.* **A534** (2004) 250–259, [hep-ph/0403113].

[133] T. Sjostrand, L. Lonnblad, S. Mrenna, and P. Skands, "PYTHIA 6.3: Physics and manual" hep-ph/0308153.

[134] I. Bird *et. al.*, "LHC computing Grid. Technical design report". CERN-LHCC-2005-024.

[135] T. L. Barklow *et. al.*, "Strong coupling electroweak symmetry breaking" *ECONF* **C960625** (1996) STC118, [hep-ph/9704217].

[136] S. Haywood *et. al.*, "Electroweak physics" hep-ph/0003275.

[137] M. S. Berger and M. S. Chanowitz, "Probing W boson and top quark mass generation with strong Z Z scattering signals" *Phys. Rev. Lett.* **68** (1992) 757–760.

[138] R. N. Cahn and S. Dawson, "Production of very massive Higgs bosons" *Phys. Lett.* **B136** (1984) 196.

[139] R. N. Cahn, S. D. Ellis, R. Kleiss, and W. J. Stirling, "Transverse momentum signatures for heavy Higgs bosons" *Phys. Rev.* **D35** (1987) 1626.

[140] R. N. Cahn and M. S. Chanowitz, "Detecting Higgs boson decays into Z pairs" *Phys. Rev. Lett.* **56** (1986) 1327.

[141] R. Kleiss and W. J. Stirling, "Tagging the higgs" *Phys. Lett.* **B200** (1988) 193.

[142] V. D. Barger, T. Han, and R. J. N. Phillips, "Improving the heavy higgs boson two charged lepton - two neutrino signal" *Phys. Rev.* **D37** (1988) 2005–2008.

[143] U. Baur and E. W. N. Glover, "Observability of a heavy Higgs boson at hadron supercolliders" *Phys. Rev.* **D44** (1991) 99–109.

[144] V. D. Barger, K. Cheung, T. Han, J. Ohnemus, and D. Zeppenfeld, "A comparative study of the benefits of forward jet tagging in heavy Higgs production at the SSC" *Phys. Rev.* **D44** (1991) 1426–1437.

[145] V. D. Barger, K. Cheung, T. Han, and D. Zeppenfeld, "Single forward jet tagging and central jet vetoing to identify the leptonic w w decay mode of a heavy higgs boson" *Phys. Rev.* **D44** (1991) 2701–2716.

[146] A. Erdogan, D. Froidevaux, V. Klyukhin, and V. Zmushko, "Study of H → W W → lepton neutrino jet jet and H → Z Z → lepton lepton jet jet decays for m(H) = 1- TeV at the LHC energies" *Phys. Atom. Nucl.* **57** (1994) 274–284.

[147] K. Iordanidis and D. Zeppenfeld, "Searching for a heavy Higgs boson via the $H \rightarrow l\nu jj$ decay mode at the CERN LHC" *Phys. Rev.* **D57** (1998) 3072–3083, [hep-ph/9709506].

[148] D. L. Rainwater and D. Zeppenfeld, "Observing $h \rightarrow W^{(*)}W^{(*)} \rightarrow e^{\pm}\mu^{\mp}\not{p}_t$ in weak boson fusion with dual forward jet tagging at the CERN LHC" *Phys. Rev.* **D60** (1999) 113004, [hep-ph/9906218].

[149] M. S. Chanowitz and M. K. Gaillard, "Multiple production of W and Z as a signal of new strong interactions" *Phys. Lett.* **B142** (1984) 85.

[150] J. Bagger, S. Dawson, and G. Valencia, "W(L) W(L) scattering at the SSC". JHU-TIPAC-91-002.

[151] A. Dobado, M. J. Herrero, and J. Terron, "$W^{\pm}$ Z^0 signals from the strongly interacting symmetry breaking sector" *Z. Phys.* **C50** (1991) 465–472.

[152] "CMS, the Compact Muon Solenoid: Technical proposal". CERN-LHCC-94-38.

[153] A. Dobado and M. T. Urdiales, "Determination of the electroweak chiral Lagrangian parameters at the LHC" *Z. Phys.* **C71** (1996) 659–672, [hep-ph/9502255].

[154] H. J. He, Y. P. Kuang, and C. P. Yuan, "Estimating the sensitivity of LHC to electroweak symmetry breaking: Longitudinal/Goldstone boson equivalence as a criterion" *Phys. Rev.* **D55** (1997) 3038–3067, [hep-ph/9611316].

[155] K. Cheung and R. M. Harris, "Discovering new interactions at colliders" hep-ph/9610382.

[156] E. Eichten, K. D. Lane, and J. Womersley, "Finding low-scale technicolor at hadron colliders" *Phys. Lett.* **B405** (1997) 305–311, [hep-ph/9704455].

[157] R. Casalbuoni *et. al.*, "Manifestation of a strong electroweak sector with decoupling at hadronic colliders" *Phys. Rev.* **D56** (1997) 2812–2819, [hep-ph/9702325].

[158] M. S. Chanowitz and W. Kilgore, "Complementarity of resonant and nonresonant strong W W scattering at the LHC" *Phys. Lett.* **B322** (1994) 147–153, [hep-ph/9311336].

[159] M. S. Chanowitz and W. B. Kilgore, "W+Z and W+γ^* backgrounds to strong W^+W^+ scattering at the LHC" *Phys. Lett.* **B347** (1995) 387–393, [hep-ph/9412275].

[160] J. Bagger *et. al.*, "Lhc analysis of the strongly interacting w w system: Gold plated modes" *Phys. Rev.* **D52** (1995) 3878–3889, [hep-ph/9504426].

[161] M. S. Chanowitz and M. Golden, "Like charged gauge boson pairs as a probe of electroweak symmetry breaking" *Phys. Rev. Lett.* **61** (1988) 1053.

[162] D. A. Dicus, J. F. Gunion, and R. Vega, "Isolating the scattering of longitudinal W^+'s at the SSC using like sign dileptons" *Phys. Lett.* **B258** (1991) 475–481.

[163] M. S. Berger and M. S. Chanowitz, "Strong W^+W^+ scattering at the SSC" *Phys. Lett.* **B263** (1991) 509–516.

[164] V. D. Barger, K. Cheung, T. Han, and R. J. N. Phillips, "Strong W^+W^+ scattering signals at p p supercolliders" *Phys. Rev.* **D42** (1990) 3052–3077.

[165] D. A. Dicus, J. F. Gunion, L. H. Orr, and R. Vega, "Isolating purely leptonic signals for strong W scattering using antitagging jet tagging, and lepton isolation" *Nucl. Phys.* **B377** (1992) 31–54.

[166] E. Accomando, A. Ballestrero, and E. Maina, "PHASE: An event generator for six fermion physics at the LHC" *Nucl. Instrum. Meth.* **A534** (2004) 265–268, [hep-ph/0404236].

[167] E. Accomando, A. Ballestrero, and E. Maina, "PHASE 1.0 a Monte Carlo generator for six fermion physics at the LHC". User guide. Available from URL: http://www.to.infn.it/ ballestr/phase.

[168] E. . Jarlskog, G. and E. . Rein, D., "Ecfa large hadron collider workshop, aachen, germany, 4-9 oct 1990: Proceedings.2". CERN-90-10-V-2.

[169] **ATLAS** Collaboration, "ATLAS: Letter of intent for a general purpose p p experiment at the large hadron collider at CERN". CERN-LHCC-92-04.

[170] **ATLAS** Collaboration, "ATLAS: Technical proposal for a general-purpose p p experiment at the Large Hadron Collider at CERN". CERN-LHCC-94-43.

[171] **ATLAS** Collaboration, "Atlas detector and physics performance. Technical design report. vol. 2". CERN-LHCC-99-15.

REFERENCES

[172] M. Della Negra *et. al.*, **CMS** Collaboration, "CMS: The Compact Muon Solenoid: Letter of intent for a general purpose detector at the LHC". CERN-LHCC-92-03.

[173] S. Allwood, *High Mass WW Scattering at the LHC.* PhD thesis, University of Manchester, 2006.

[174] E. Stefanidis, *Study of the WW scattering in the absence of light Higgs boson using the ATLAS Detector at LHC.* PhD thesis, University College London, 2007.

[175] S. Dawson, "The effective W approximation" *Nucl. Phys.* **B249** (1985) 42–60.

[176] Z. Kunszt and D. E. Soper, "On the validity of the effective W approximation" *Nucl. Phys.* **B296** (1988) 253.

[177] G. L. Kane, W. W. Repko, and W. B. Rolnick, "The effective $W^{\pm}$, Z^0 approximation for high-energy collisions" *Phys. Lett.* **B148** (1984) 367–372.

[178] J. F. Gunion, J. Kalinowski, A. Tofighi-Niaki, A. Abbasabadi, and W. Repko, "Comparison between an exact ff→ffWW calculation for the charged current sector and the effective w approximation". To appear in Proc. of 1986 Summer Study on the Design and Utilization of Superconducting Super Collider, Snowmass, CO, Jun 23 - Jul 11, 1986.

[179] A. Abbasabadi, W. W. Repko, D. A. Dicus, and R. Vega, "Comparison of exact and effective gauge boson calculations for gauge boson fusion processes" *Phys. Rev.* **D38** (1988) 2770.

[180] I. Kuss, "Improved effective vector-boson approximation for hadron hadron collisions" *Phys. Rev.* **D55** (1997) 7165–7182, [hep-ph/9608453].

[181] H. G. J. Veltman, "The equivalence theorem" *Phys. Rev.* **D41** (1990) 2294.

[182] Y.-P. Yao and C. P. Yuan, "Modification of the equivalence theorem due to loop corrections" *Phys. Rev.* **D38** (1988) 2237.

[183] G. Valencia and S. Willenbrock, "The goldstone boson equivalence theorem and the Higgs resonance" *Phys. Rev.* **D42** (1990) 853–859.

[184] A. Dobado and J. R. Pelaez, "The equivalence theorem for chiral Lagrangians" *Phys. Lett.* **B329** (1994) 469–478, [hep-ph/9404239].

[185] H.-J. He, Y.-P. Kuang, and X.-y. Li, "Proof of the equivalence theorem in the chiral Lagrangian formalism" *Phys. Lett.* **B329** (1994) 278–284, [hep-ph/9403283].

[186] C. Grosse-Knetter and I. Kuss, "The equivalence theorem and effective Lagrangians" *Z. Phys.* **C66** (1995) 95–106, [hep-ph/9403291].

[187] A. Dobado, J. R. Pelaez, and M. T. Urdiales, "Applicability constraints of the equivalence theorem" *Phys. Rev.* **D56** (1997) 7133–7142, [hep-ph/9702206].

[188] M. Beneke *et. al.*, "Top quark physics" hep-ph/0003033.

[189] P. Skands, T. Plehn, and D. Rainwater, "QCD radiation in the production of high $\hat{s}$ final states" hep-ph/0511306.

[190] J. Campbell, R. K. Ellis, and D. L. Rainwater, "Next-to-leading order QCD predictions for W + 2jet and Z + 2jet production at the CERN LHC" *Phys. Rev.* **D68** (2003) 094021, [hep-ph/0308195].

[191] P. Z. Skands, "QCD (and) event generators" *AIP Conf. Proc.* **792** (2005) 73–84, [hep-ph/0507129].

[192] T. Plehn, D. Rainwater, and P. Skands, "Squark and gluino production with jets" hep-ph/0510144.

[193] W. Beenakker, H. Kuijf, W. L. van Neerven, and J. Smith, "QCD corrections to heavy quark production in p anti-p collisions" *Phys. Rev.* **D40** (1989) 54–82.

168

[194] A. Brandenburg, S. Dittmaier, P. Uwer, and S. Weinzierl, "Top quark pair + jet production at next-to-leading order: Nlo qcd corrections to gg→ $t\bar{t}$g" *Nucl. Phys. Proc. Suppl.* **135** (2004) 71–75, [hep-ph/0408137].

[195] E. Accomando, A. Ballestrero, S. Bolognesi, E. Maina, and C. Mariotti, "Boson boson scattering and higgs production at the LHC from a six fermion point of view: Four jets + 1 nu processes at O(alpha(em)**6)" *JHEP* **03** (2006) 093, [hep-ph/0512219].

[196] V. D. Barger, T. Han, J. Ohnemus, and D. Zeppenfeld, "Pair production of W$^\pm$, gamma and Z in association with jets" *Phys. Rev.* **D41** (1990) 2782.

[197] R. Meng, G. A. Schuler, J. Smith, and W. L. van Neerven, "Simple formulae for the order alpha-s**3 QCD corrections to the reaction p anti-p → Q anti-Q X" *Nucl. Phys.* **B339** (1990) 325–354.

[198] G. A. Ladinsky and C. P. Yuan, "The W - top background to heavy higgs production" *Phys. Rev.* **D43** (1991) 789–793.

[199] T. Sjostrand and P. Z. Skands, "Transverse-momentum-ordered showers and interleaved multiple interactions" *Eur. Phys. J.* **C39** (2005) 129–154, [hep-ph/0408302].

[200] G. Miu and T. Sjostrand, "W production in an improved parton shower approach" *Phys. Lett.* **B449** (1999) 313–320, [hep-ph/9812455].

[201] G. Rudolph *et. al.*, "Contributions to ALEPH analysis from the Innsbruck group". Talk presented at RECFA meeting, March 26, 2004.

[202] S. Catani, F. Krauss, R. Kuhn, and B. R. Webber, "QCD matrix elements + parton showers" *JHEP* **11** (2001) 063, [hep-ph/0109231].

[203] F. Krauss, "Matrix elements and parton showers in hadronic interactions" *JHEP* **08** (2002) 015, [hep-ph/0205283].

[204] M. Mangano, "The so–called MLM prescription for ME/PS matching". Talk presented at the Fermilab ME/MC Tuning Workshop, October 4, 2004.

[205] S. Mrenna and P. Richardson, "Matching matrix elements and parton showers with HERWIG and PYTHIA" *JHEP* **05** (2004) 040, [hep-ph/0312274].

[206] **LHC Study Group** Collaboration, "The Large Hadron Collider: Conceptual design". CERN-AC-95-05-LHC.

[207] **CMS** Collaboration, "CMS physics : Technical Design Report v.1 : Detector performance and software". CERN-LHCC-2006-001.

[208] **CMS** Collaboration, "The CMS tracker system project : Technical Design Report". CERN-LHCC-98-006.

[209] **CMS** Collaboration, "Addendum to the CMS Tracker TDR by the CMS Collaboration". CERN-LHCC-2000-016.

[210] **CMS** Collaboration, "The CMS electromagnetic calorimeter project : Technical Design Report". CERN-LHCC-97-033.

[211] **CMS** Collaboration, "Addendum to the CMS ECAL technical design report: Changes to the CMS ECAL electronics". CERN-LHCC-2002-027.

[212] **CMS** Collaboration, "The CMS hadron calorimeter project : Technical Design Report". CERN-LHCC-97-031.

[213] D. Green, "Calibration of the CMS calorimeters". FERMILAB-FN-0704.

[214] **CMS** Collaboration, "The CMS magnet project : Technical Design Report". CERN-LHCC-97-010.

[215] **CMS** Collaboration, "The CMS muon project : Technical Design Report". CERN-LHCC-97-032.

REFERENCES

[216] **CMS** Collaboration, "CMS. The TriDAS project. Technical design report, vol. 1: The trigger systems". CERN-LHCC-2000-038.

[217] **CMS** Collaboration, "CMS: The TriDAS project. Technical design report, Vol. 2: Data acquisition and high-level trigger". CERN-LHCC-2002-026.

[218] W. Adam *et. al.*, **CMS Trigger and Data Acquisition Group** Collaboration, "The CMS high level trigger" *Eur. Phys. J.* **C46** (2006) 605–667, [hep-ex/0512077].

[219] **CMS** Collaboration, "Object oriented Simulation for CMS Analysis and Reconstruction". http://cmsdoc.cern.ch/oscar.

[220] **CMS** Collaboration, "Object oriented Reconstruction for CMS Analysis". http://cmsdoc.cern.ch/oscar.

[221] S. Agostinelli *et. al.*, **GEANT4** Collaboration, "GEANT4: A simulation toolkit" *Nucl. Instrum. Meth.* **A506** (2003) 250–303.

[222] M. H. Seymour, "Searches for new particles using cone and cluster jet algorithms: A comparative study" *Z. Phys.* **C62** (1994) 127–138.

[223] J. E. Huth *et. al.*, "Toward a standardization of jet definitions". Presented at Summer Study on High Energy Physics, Reaearch Directions for the Decade, Snowmass, CO, Jun 25 - Jul 13, 1990.

[224] G. C. Blazey *et. al.*, "Run II jet physics" hep-ex/0005012.

[225] Y. L. Dokshitzer, S. I. Troian, and V. A. Khoze, "Collective QCD effects in the structure of final multi - hadron states. (in Russian)" *Sov. J. Nucl. Phys.* **46** (1987) 712–719.

[226] Y. L. Dokshitzer, V. A. Khoze, and T. Sjostrand, "Rapidity gaps in higgs production" *Phys. Lett.* **B274** (1992) 116–121.

[227] J. D. Bjorken, "Rapidity gaps and jets as a new physics signature in very high-energy hadron hadron collisions" *Phys. Rev.* **D47** (1993) 101–113.

[228] V. D. Barger, R. J. N. Phillips, and D. Zeppenfeld, "Mini - jet veto: A tool for the heavy higgs search at the LHC" *Phys. Lett.* **B346** (1995) 106–114, [hep-ph/9412276].

[229] N. Amapane, M. Fierro, and M. Konecki, "High Level Trigger Algorithms for Muon Isolation". CMS-NOTE-2002-040.

[230] H. Pi *et. al.*, **CMS** Collaboration, "Measurement of missing transverse energy with with the CMS detector at the LHC". CMS Note 2006/035.

[231] A. N. Nikitenko, R. Kinnunen, and S. Kunori, "Missing transverse energy measurement with jet energy corrections". CMS-NOTE-2001-040.

[232] A. Kalinowski private communication.

[233] D. L. Rainwater, M. Spira, and D. Zeppenfeld, "Higgs boson production at hadron colliders: Signal and background processes" hep-ph/0203187.

[234] E. Brubaker *et. al.*, **Tevatron Electroweak Working Group** Collaboration, "Combination of cdf and d0 results on the mass of the top quark" hep-ex/0608032.

[235] S. I. Bityukov and N. V. Krasnikov, "New physics discovery potential in future experiments" *Mod. Phys. Lett.* **A13** (1998) 3235–3249.

[236] **CMS** Collaboration, "CMS physics : Technical Design Report v.2 : Physics performance". CERN-LHCC-2006-021.

[237] **ATLAS** Collaboration, "ATLAS: Detector and physics performance technical design report. Volume 1". CERN-LHCC-99-14.

[238] P. Bartalini, R. Chierici, and A. De Roeck, "Guidelines for the estimation of theoretical uncertainties at the LHC". CMS-NOTE-2005-013.

[239] F. Maltoni, "Top physics: theoretical issues and aims at the Tevatron and LHC". Talk presented at Hadron Collider Physics Symposium, July 4-9, 2005.

[240] J. D'Hondt, J. Heyninck, and S. Lowette, "Measurement of the cross section of single leptonic t anti- t events". CERN-CMS-NOTE-2006-064.

[241] H. Pi, P. Avery, J. Rohlf, C. Tully, and S. Kunori, "Search for Standard Model Higgs boson via vector boson fusion in the H $\to$ W$^+$W$^- \to \ell^\pm \nu jj$ with 120<m$_h$<250 Gev/c^2". CMS-NOTE-2006-092.

[242] T. Sjostrand, S. Mrenna, and P. Skands, "PYTHIA 6.4: Physics and manual" `hep-ph/0603175`.

[243] J. J. Hernandez, S. Navas, and P. Rebecchi, "Estimating exclusion limits in prospective studies of searches" *Nucl. Instrum. Meth.* **A378** (1996) 301–304.

[244] N. V. Krasnikov and S. I. Bityukov, "Incorporating systematics and statistical uncertainties into exclusion limits". Prepared for PHYSTAT2003: Statistical Problems in Particle Physics, Astrophysics, and Cosmology, Menlo Park, California, 8-11 Sep 2003.

[245] T. A. Tabarelli de Fatis, T., "Expectation values of exclusion limits in future experiments" *Nucl. Instrum. Meth.* **A403** (1998) 151–152.

[246] T. Han, "Strong W W scattering physics: A comparative study for the LHC, NLC and a muon collider" `hep-ph/9704215`.

[247] W. Kilian, "Strongly interacting W bosons at e- e- colliders" *eConf* **C010630** (2001) E3052.

[248] R. D. Field, **CDF** Collaboration, "The underlying event in hard scattering processes" `hep-ph/0201192`.

[249] R. Field and R. C. Group, **CDF** Collaboration, "PYTHIA Tune A, HERWIG, and JIMMY in Run 2 at CDF" `hep-ph/0510198`.

[250] E. E. Boos, V. A. Ilyin, and A. N. Skachkova, "Simplification of flavour combinatorics in evaluation of hadronic processes" *JHEP* **05** (2000) 052, [`hep-ph/0004194`].